

Effect of Proximity of Sheet Pile Walls on the Apparent Capacity of Driven Displacement Piles, Task 2 Deliverable Report

September 2015

TASK 2 DELIVERABLE REPORT BRIDGE SOFTWARE INSTITUTE

Sponsor:

Florida Department of
Transportation (FDOT)

Project Manager:

Juan Castellanos

Principal Investigator:

Jae H. Chung, Ph.D.

Co-Principal Investigators:

Michael C. McVay, Ph.D.

Michael T. Davidson, Ph.D., P.E.

Research Assistants:

Vinh Q. Le, Nikhil Mishra,

Michael A. Faraone, Ph.D.

Address:

Bridge Software Institute (BSI)
Engineering School of
Sustainable Infrastructure and
Environment (ESSIE)
College of Engineering
University of Florida (UF)
1949 Stadium Rd. Room 365
Gainesville FL 32611

Contract:

FDOT Contract No. BDV31 TWO
977-26

UF Project No. 01525015

DISCLAIMER

The opinions, findings, and conclusions expressed in this publication are those of the authors and not necessarily those of the State of Florida Department of Transportation.

SI (MODERN METRIC) CONVERSION FACTORS (from FHWA)

APPROXIMATE CONVERSIONS TO SI UNITS

SYMBOL	WHEN YOU KNOW	MULTIPLY BY	TO FIND	SYMBOL
LENGTH				
in	inches	25.4	millimeters	mm
ft	feet	0.305	meters	m
yd	yards	0.914	meters	m
mi	miles	1.61	kilometers	km

SYMBOL	WHEN YOU KNOW	MULTIPLY BY	TO FIND	SYMBOL
AREA				
in²	square inches	645.2	square millimeters	mm ²
ft²	square feet	0.093	square meters	m ²
yd²	square yard	0.836	square meters	m ²
mi²	square miles	2.59	square kilometers	km ²

SYMBOL	WHEN YOU KNOW	MULTIPLY BY	TO FIND	SYMBOL
VOLUME				
fl oz	fluid ounces	29.57	milliliters	mL
ft³	cubic feet	0.028	cubic meters	m ³
yd³	cubic yards	0.765	cubic meters	m ³

NOTE: volumes greater than 1,000 L shall be shown in m³

SYMBOL	WHEN YOU KNOW	MULTIPLY BY	TO FIND	SYMBOL
MASS				
oz	ounces	28.35	grams	g
lb	pounds	0.454	kilograms	kg
T	short tons (2,000 lb)	0.907	megagrams (or "metric ton")	Mg (or "t")

SYMBOL	WHEN YOU KNOW	MULTIPLY BY	TO FIND	SYMBOL
TEMPERATURE (exact degrees)				
°F	Fahrenheit	5 (F-32)/9 or (F-32)/1.8	Celsius	°C

SYMBOL	WHEN YOU KNOW	MULTIPLY BY	TO FIND	SYMBOL
ILLUMINATION				
fc	foot-candles	10.76	lux	lx
fl	foot-Lamberts	3.426	candela/m ²	cd/m ²

SYMBOL	WHEN YOU KNOW	MULTIPLY BY	TO FIND	SYMBOL
FORCE and PRESSURE or STRESS				
lbf	pound force	4.45	newtons	N
kips	kips	4,448.22	newtons	N
lbf/in²	pound force per square inch	6.89	kilopascals	kPa
ksi	kips per square inch	6,894.76	kilopascals	kPa
tsf	tons (short) per square foot	95.67	kilopascals	kPa
pcf	pound force per cubic foot	156.967	newtons per cubic meter	N/m ³

APPROXIMATE CONVERSIONS TO SI UNITS

SYMBOL	WHEN YOU KNOW	MULTIPLY BY	TO FIND	SYMBOL
LENGTH				
mm	millimeters	0.039	inches	in
m	meters	3.28	feet	ft
m	meters	1.09	yards	yd
km	kilometers	0.621	miles	mi

SYMBOL	WHEN YOU KNOW	MULTIPLY BY	TO FIND	SYMBOL
AREA				
mm²	square millimeters	0.0016	square inches	in ²
m²	square meters	10.764	square feet	ft ²
m²	square meters	1.195	square yards	yd ²
ha	hectares	2.47	acres	ac
km²	square kilometers	0.386	square miles	mi ²

SYMBOL	WHEN YOU KNOW	MULTIPLY BY	TO FIND	SYMBOL
VOLUME				
mL	milliliters	0.034	fluid ounces	fl oz
L	liters	0.264	gallons	gal
m³	cubic meters	35.314	cubic feet	ft ³
m³	cubic meters	1.307	cubic yards	yd ³

SYMBOL	WHEN YOU KNOW	MULTIPLY BY	TO FIND	SYMBOL
MASS				
g	grams	0.035	ounces	oz
kg	kilograms	2.202	pounds	lb
Mg (or "t")	megagrams (or "metric ton")	1.103	short tons (2,000 lb)	T

SYMBOL	WHEN YOU KNOW	MULTIPLY BY	TO FIND	SYMBOL
TEMPERATURE (exact degrees)				
°C	Celsius	1.8C+32	Fahrenheit	°F

SYMBOL	WHEN YOU KNOW	MULTIPLY BY	TO FIND	SYMBOL
ILLUMINATION				
lx	lux	0.0929	foot-candles	fc
cd/m²	candela/m ²	0.2919	foot-Lamberts	fl

SYMBOL	WHEN YOU KNOW	MULTIPLY BY	TO FIND	SYMBOL
FORCE and PRESSURE or STRESS				
N	newtons	0.225	pound force	lbf
N	newtons	0.000224809	kips	kips
kPa	kilopascals	0.145	pound force per square inch	lbf/in ²
kPa	kilopascals	0.000145	kips per square inch	ksi
kPa	kilopascals	0.000145038	kips per square inch	ksi
N/m³	newtons per cubic meter	0.0104526	pound force per cubic foot	pcf

*SI is the symbol for International System of Units. Appropriate rounding should be made to comply with Section 4 of ASTM E380. (Revised March 2003)

1. Report No.	2. Government Accession No.	3. Recipient's Catalog No.	
4. Title and Subtitle Effect of Proximity of Sheet Pile Walls on the Apparent Capacity of Driven Displacement Piles, Task 2 Deliverable Report		5. Report Date September 2015	
		6. Performing Organization Code	
7. Author(s) Chung, J. H., Davidson, M. T., Le, V., Mishra, N., Faraone, M., McVay, M. C.		8. Performing Organization Report No.	
9. Performing Organization Name and Address Bridge Software Institute University of Florida 1949 Stadium Rd. Room 365 P.O. Box 116580 Gainesville, FL 32611		10. Work Unit No. (TRAIS)	
		11. Contract or Grant No. BDV31 977-26	
12. Sponsoring Agency Name and Address Florida Department of Transportation 605 Suwannee Street, MS 30 Tallahassee, FL 32399		13. Type of Report and Period Covered Task 2 Deliverable Report 9/01/2014 - 6/30/2015	
		14. Sponsoring Agency Code	
15. Supplementary Notes			
16. Abstract The current research report is submitted as part of a larger research undertaking, with the overall objectives of: (1) Quantifying the effects that sheet pile wall (SPW) installations have on nearby displacement-driven pile resistance, where the influence of both friction and bearing components are evaluated; (2) Identifying and evaluating the influence that relevant physical parameters have on driven pile resistance, including: soil characteristics, pile size, sheet pile sectioning, and relative positioning between SPW and driven pile members; (3) Quantifying the effect of sheet pile extraction with respect to changes in pile capacities; (4) Cultivating design-oriented practical recommendations to account for SPW-associated changes in driven pile resistance; and (5) Cultivating design-oriented practical recommendations to minimize SPW-associated pile capacity reduction. Further, the current report documents those efforts made toward satisfying Task 2 (of 5) toward completion of the current study. Accordingly, this Task 2 deliverable report documents the following research efforts: (1) Investigation of fundamental behaviors of discrete spherical elements (DSE); (2) Development of a numerical model and procedure for simulation direct shear tests on DSE assemblies; (3) Development of a numerical model and procedure for triaxial compression testing on DSE assemblies; and (4) Validation of the numerical models developed for simulating the direct shear test and triaxial compression test against physical test measurements; and (5) Use of the numerical models in forming a catalog of numerical parameters, which in turn, constitute a library of DSE for simulating assemblies of granular materials			
17. Key Words Bearing capacity; Dislocation (Geology); Pile driving; Resistance (Mechanics); Sheet pile walls; Soil mechanics		18. Distribution Statement No restrictions.	
19. Security Classif. (of this report) Unclassified	20. Security Classif. (of this page) Unclassified	21. No. of Pages 184	22. Price

ACKNOWLEDGEMENTS

The authors would like to thank the Florida Department of Transportation (FDOT) for providing the funding that made this project possible.

EXECUTIVE SUMMARY

The process of installing sheet pile walls (SPWs) in the ground can potentially cause significant changes in the stress states and density conditions of soil materials that fall within the vicinity of said SPW. In addition, further disturbances to soil material in the proximity of SPWs can occur during subsequent SPW removal (which typically involves vibratory processes). It follows that the capacities of any nearby displacement-driven pile objects may be affected by the presence (and removal) of SPW objects. Such phenomena are not well understood, and the need to characterize the effect that SPWs can have on proximally-near displacement-driven pile objects motivates the current research. Conducting a strictly physical, experiment-based parametric study to evaluate the influence of SPW on nearby pile members would be cost prohibitive given the setup time and costs involved in physical testing of displacement-driven piles. As an alternative, relatively novel computational simulation methodologies are identified and adopted in the current study to perform (otherwise cost-prohibitive) assessments of SPW, pile, and granular soil behavior. Namely, a long-standing numerical approach for analyzing continuous media, the finite element method (FEM), is utilized in a complimentary manner with a relatively more recently developed analysis approach for investigating discontinuous media (i.e., the discrete element method, DEM) to simulate interactions between driven objects (modeled using the FEM) and granular soil media (modeled using the DEM), respectively.

The combined DEM-FEM approach, as applied in the current study, is justified by the physical nature of the phenomena being modeled. More specifically, the physical system being studied contains separate structural objects (SPWs and driven piles) that interact with one another indirectly via disturbances in the surrounding granular material. For the numerical modeling of these structural objects, it is most efficient to apply a continuum hypothesis; for this reason it is best to model these structures using the FEM. In contrast to this, the influence of SPWs on the resistance and bearing capacity of neighboring piles is a function of the micromechanical phenomena taking place in the soil media between them; for this reason, the discrete nature of the particle constituents of the soil bodies is of critical importance to this study. Hence, in the current study, the DEM is combined with the FEM in order to capture the interactions between the structural elements and granular material.

The strategy of developing novel numerical approaches to explore SPW-associated changes in soil states, and corresponding changes in pile capacities, has a number of benefits. In particular, the use of simulation to explore such phenomena corresponds to reduced development and physical testing costs as well as more rapid generation of soil and pile response predictions. Importantly, the numerical approaches adopted in the current study do not diminish the potential for generating research findings that can lead to improved reliability of foundation design. However, far fewer cycles of development and testing are required if simulation results can be relied upon to identify both design parameters that improve design robustness, and design flaws that degrade foundation performance. Evaluating zones of influence of SPWs on the resistance and capacity of neighboring driven piles is of particular interest in the current study.

Small-scale physical testing (e.g., laboratory tests) remains necessary in validating and qualifying the integrity of the computational tools. Towards this end, the Task 2 deliverable report focuses on the development of numerical counterparts to the laboratory tests and modeling of

discrete spherical element (DSE) assemblies at the macroscopic scale. Typically, the Task 2 deliverable report encompasses an investigation into the fundamental behaviors of discrete spherical elements (DSEs); the development and benchmarking of numerical models for carrying out laboratory test simulations on DSE assemblies; and, the calibration of DSE rheological properties for the purpose of characterizing macroscopic properties of DSE assemblies. Accordingly, the focus of this report is concerned with satisfying the four following objectives:

1. Development of a numerical model that is capable of simulating direct shear tests on granular soil;
triaxial
2. Development of a numerical model that is capable of simulating ~~direct shear~~ tests on granular soil; and,
3. Creation of a standardized DSE library that represents a range of macroscopic properties (e.g., internal friction angle, relative density);
4. Evaluation of Mohr-Coulomb failure envelopes based on numerical simulations of granular soil types.

As a necessary precursor in satisfying these four objectives, the rheological components making up the DSEs used in the current study are comprehensively subjected to both conceptual and quantitative investigations. In this way, novel insights are made regarding the fundamental behaviors of DSEs. Additionally, the bounds of numerical parameter values for each rheological component are quantified. Concerning the aforementioned objectives one and two, DEM-FEM modeling efforts dedicated to both the development and validation of numerical models are documented for the direct shear test and triaxial compression testing apparatuses. In particular, concerted efforts are made to ensure that the apparatuses do not unduly influence the DEM samples as the samples are being manipulated during the (numerical) test procedures. Also, the numerical models are shown to produce simulation results that are in line with (physical) test measurements made in laboratory settings. By making use of the numerical bounds of parameter values for modeling DSE rheological components in conjunction with the validated (numerical) laboratory test apparatuses, a library of DSE is developed in satisfaction of objective three. Throughout the Task 2 deliverable report numerical data directly pertaining to the evaluation of Mohr-Coulomb failure envelopes are presented, as obtained from use of the direct shear and triaxial compression test numerical models, in satisfaction of objective four.

TABLE OF CONTENTS

DISCLAIMER	i
SI (MODERN METRIC) CONVERSION FACTORS (from FHWA).....	ii
ACKNOWLEDGEMENTS.....	v
EXECUTIVE SUMMARY	vi
LIST OF FIGURES	x
LIST OF TABLES	xix
1. INTRODUCTION	1
1.1 Introduction.....	1
1.2 Background and Motivation	2
1.3 Scope of Report.....	4
2. FORMATION OF A DISCRETE SPHERICAL ELEMENT (DSE) LIBRARY FOR THE NUMERICAL MODELING OF PILE DRIVING INTO GRANULAR MEDIA	6
2.1 Friction.....	6
2.1.1 Historical Review.....	6
2.1.2 Scale-Dependent Coefficient of Friction	8
2.1.3 Cold Welding: Theory of Bowden and Tabor	12
2.1.4 JKR Theory	14
2.1.5 Grain Surface Texture and Frictional Resistance	16
2.1.6 Factors Affecting Frictional Resistance at Macroscopic Scales	35
2.1.7 Discrete Spherical Elements (DSEs) and Model Parameters	38
2.1.8 Macroscopic Modeling Concepts	51
2.2 Numerical Method for Soft Particle Dynamics	61
2.2.1 The Discrete Element Method (DEM).....	62
2.2.2 Advantages of Combined DEM-FEM	63
2.2.3 Utility of DSE Libraries.....	64
2.3 Governing Equation and Solution Approaches.....	64
2.3.1 Equation of Motion	64
2.3.2 Conceptual Remarks on Geometry, Contact Mechanics, and Rheology	67
2.3.3 Microscopic Constitutive Models and Parameters	67
2.4 Detailed Description of Rheological Model	70
2.4.1 Microscopic Contact Parameters of LS-DYNA DSE Analysis.....	70
2.4.2 Hertzian Normal Contact Stiffness	76
2.4.3 Tangential Contact and Coulombic Friction.....	78
2.4.4 Natural Frequencies and Critical Damping of Two Spheres in Contact.....	81
2.4.5 Restitution Coefficients	85

2.4.6 Detailed Description of Rheological Model	90
2.4.7 Boundary Model of Capillary Suction Pressure	93
3. NUMERICAL MODELING OF STANDARD LABORATORY TESTS FOR ASSESSING MACROSCOPIC PROPERTIES OF DSE ASSEMBLIES	98
3.1 Overview	98
3.2 Direct Shear Test.....	98
3.2.1 Description of Physical Test Procedure	99
3.2.2 Numerical Model of Test Apparatus.....	100
3.2.3 Numerical Test Procedure.....	100
3.2.4 Validation.....	103
3.2.5 Shearing Resistance of Geometric Packings	105
3.2.6 Apparent Cohesion.....	109
3.3 Triaxial Compression Test.....	111
3.3.1 Description of Physical Test Procedure	112
3.3.2 Numerical Model of Test Apparatus.....	113
3.3.3 Numerical Test Procedure.....	115
3.3.4 Validation.....	119
3.3.5 Preliminary Investigation of Scale Invariance with respect to DSE Size	121
3.4 Calibration of DSE Library Rheological Components	123
3.4.1 Simulation of Macroscopic Granular Behaviors using Monodisperse Systems	123
3.4.2 Simulation of Shear Jamming Effects on Macroscopic Granular Behaviors using Binary Systems.....	129
3.4.3 Representative DSE Models for Relative Density States	137
3.4.4 Summary of Numerical Results	141
4. SUMMARY AND CONCLUSIONS	144
4.1 Summary of Task 2 Work Completed	144
4.2 Conclusions.....	145
4.3 Preliminary Progress for Task 3	146
5. REFERENCES	154

LIST OF FIGURES

<u>Figure</u>	<u>Page</u>
Figure 2.1.1.1. Coulomb’s original sketch of interaction between roughnesses as the origin of frictional resistance (Popov 2010)	6
Figure 2.1.1.2. Simplified conceptualization of dry friction: a) Point mass under force equilibrium on an inclined surface; b) Free body diagram (Popov 2010)	7
Figure 2.1.1.3. Macroscopic simplification for a maximum (dry) frictional resistance on slip planes	8
Figure 2.1.2.1. Geometrically regular packings: a) Close-packed tetrahedral spheres at the theoretical maximum bulk density of $\pi/(3\sqrt{2})$ (~74%) in a volume; b) An equivalent 2-D planar packing of discs at the theoretical maximum bulk density of $\pi/(2\sqrt{3})$ (~91%) (Israelachvill 2011)	8
Figure 2.1.2.2. Pictorial surface texture of close-packed spheres: a) Microroughness of a spherical particle; b) Macroroughness of 2-D corrugated surface; c) Representation of a periodic surface with corrugations on the two scales	9
Figure 2.1.2.3. Dimensional representation of the surface random packings of multi-disperse systems: a) Close random packing of monodisperse system (Israelachvill 2011); b) Height (peak) distribution on a stochastic surface (Greenwood and Williamson 1966); c) 1-D representation of macroscopic surface roughness (from Adams and Nosonovsky 2000)	10
Figure 2.1.2.4. Idealized macroroughness with periodic corrugation: a) Corrugated surface with intrinsic coefficient of friction, μ_0 ; b) Free-body diagram of a body on a corrugated surface with coefficient of friction, μ_0	11
Figure 2.1.3.1. Depiction of microscopic contact area between two spherical grains (the rightmost illustration is from Bromwell 1966)	13
Figure 2.1.3.2. Cold welding mechanism (from Bromwell 1966)	14
Figure 2.1.4.1. Formation of a characteristic “neck” during adhesive contact (Popov 2010)	14
Figure 2.1.4.2. Contact force and pressure: a) Dependence of normal contact force on penetration depth at the microscopic contact (Eqn. 2.1.4.3); b) Hertzian contact pressure distribution in an adhesive contact (Johnson 1985)	16
Figure 2.1.5.1. Grain surface topography: a) Mechanically crushed pure quartz with sharp edges and clean faces with minimal surface texture; b) Diagenetic quartz with euhedral crystal growths formed naturally by deposition under high pressure. Minimal transportation of the grains is	

evident from lack of edge abrasion; c) Semi-round grains with characteristic surface fractures (Konopinski et al. 2012)	18
Figure 2.1.5.2. Dimensional representation of the grain surface (from Konopinski et al. 2012): a) 3-D elevation map of Fig. 2.1.5.1b; b) 3-D representation of the microscopic surface texture of a grain; c) Counting estimate of fractal dimension for a 20 μm AFM scan	19
Figure 2.1.5.3. Two spherical asperities in contact (Popov 2010).....	20
Figure 2.1.5.4. A schematic of three deformation stages of contact asperities at the microscopic scale: a) Initial contacts take place within frictional asperity bodies undergoing elastic deformation; b) Further deformation occurs conjointly; c) Final stage of seizure, where conjoint deformation of all the asperities occurs at all sites of seizure (Bhushan 2013).....	23
Figure 2.1.5.5. Indentation test results: a) Young’s modulus of sand grains as a function of depth, obtained from 33 indentation tests; b) Indentation hardness of sand grains from 33 tests on 11 sand grains (Huron River and Ottawa 20-30 sand) (Nadukuru 2013).....	25
Figure 2.1.5.6. 2-D Fourier transformation analysis on the surface of an Ottawa 20-30 sand grain: a) Surface texture; b) Waviness of the surface (low frequency components); c) Roughness of the surface due to asperities (high frequency components) (Nadukuru 2013)	28
Figure 2.1.5.7. Schematic sketches of frictional phenomena at three scales for $R_1 \gg R_2 \gg R_3$ (left) and measured tomographic data for the sand grain from Fig. 2.1.5.5 (right)	29
Figure 2.1.5.8. AFM analysis on a grain of Fig. 2.1.5.5: a) 3D AFM image of a 2 x 2 μm area on grain surface; b) Statistical distribution of asperity heights for the entire scan surface; c) Statistical distribution of slopes of asperities for the entire scan surface (Nadukuru 2013).....	30
Figure 2.1.5.9. SEM analysis of quartz grains: a) Diameter \sim 0.55 mm (scale bar = 100 μm) with rough surface texture (scan size = 10 μm); b) Diameter \sim 0.8 mm with fairly smooth surface texture; c) Diameter \sim 0.6 mm (scale bar = 100 μm) with smooth surface (scale size = 25 μm)...	31
Figure 2.1.5.10. Shear strength ratio versus coefficient of friction (after Bowden and Tabor 1954, Bromwell 1966)	33
Figure 2.1.6.1. Alternative definitions of particle diameter (Santamarina et al. 2001)	35
Figure 2.1.6.2. Particle roundness and sphericity: a) Illustration of Wadell’s (1932) evaluation of particle roundness (from Sukumaran, and Ashmawy 2001); b) Relationship between roundness and sphericity with visual estimation of particle silhouettes (Krumbein and Silos 1963).....	36
Figure 2.1.6.3. Example of particle shape characterization (from Powers 1953): a) Roundness grades; b) Roundness scale	37

Figure 2.1.7.1. Irregularly shaped grains represented by spheroids: a) Circumscribing diameter (note that the volume of the inner sphere drawn on the larger grain is approximately the same as the volume of the particle); b) Equivalent diameters (note that the surface of the sphere drawn on the smaller grain is approximately the same as the surface area of the particle).....	38
Figure 2.1.7.2. Formation of irregular shapes of discrete elements: a) Clustered discrete element (the solid line inscribing the clustered circles represents a silhouette surface of a grain; b) Discrete volume of superimposed spheres.....	39
Figure 2.1.7.3. Correlations between the fractal dimension and interparticle friction angle (Chan and Page 1997): a) Particle characteristics; b) Direct ring shear test results	41
Figure 2.1.7.4. Correlation between angularity and the interparticle friction angle; for Ottawa sands, see the linear trend of the numbers, i.e., 1, 2, 4, and 5 (from Sukumaran and Ashmawy 2001): a) Material types; b) Relationship between large-strain friction angles (drained triaxial tests), shape, and angularity factors (materials labeled with numbers given in Fig. 2.1.7.4a)	42
Figure 2.1.7.5. Variations in measured internal angles of friction at constant volume per angularity and roughness: a) Linear correlation between angle of repose and roundness (Santamarina and Cho 2004) (note: angle of repose was assumed equal to angle of friction at constant volume); b) Exponential correlation for coupled effects including surface roughness and angularity (Sukumaran and Ashmawy 2001)	43
Figure 2.1.7.6. Grain shape influence on macroscopic friction (from Mair et al.2002): a) Schematic diagram of direct shear apparatus: the 100 x100 mm, 3-mm-thick granular layers sandwiched between rough steel blocks. The orientations of shear and normal stresses are specified; b) Friction as a function of shear displacement for angular and spherical grains at normal stress = 5 MPa. Spherical grains show a lower value of friction coefficient and exhibit stick-and-slip behavior, whereas angular gouge slides stably with higher friction.	44
Figure 2.1.7.7. SEM images of particulate fabrics on shear surface planes (from Mair et al.2002): a) SEM photomicrograph of angular gouge deformed at normal stress = 50 MPa. Slip is 20 mm in both cases; b) SEM photomicrograph of spherical gouge deformed at normal stress = 50 MPa. Note development of the fabric at the shear plane due to particle size distribution	45
Figure 2.1.7.8. Rolling displacement caused by pure rolling motion of two elastic spheres with equal radius R	46
Figure 2.1.7.9. Effect of particle shape on particle rotation in force equilibrium under a lateral load.....	46
Figure 2.1.7.10. Rolling resistance as a shape parameter in sheared granular media (From Estrada 2013): a) Trajectory of the center of mass (dashed line) and definition of the mean dilatancy angle; b) Shear strength (q/p) and volume fraction of solid particles (v) shown in a function of μ_r for the discs and $(1/4) \tan \bar{\psi}$ for the polygons	48

Figure 2.1.7.11. Simplification of creep phenomenon in rolling (based on Popov 2010).....	49
Figure 2.1.7.12 Schematic of random assembly of eight angular particles (left) and transformed equivalent DSEs (right).....	51
Figure 2.1.8.1. Polar histogram of coordination (from Mitchell and Soga 2005): a) 3D orientation of a crushed basalt particle (top); Frequency histogram of axis orientations (middle); b) Polar diagram of crushed basalt in a sample prepared by pouring (relative density is 62%); c) Polar diagram of crushed basalt in a sample prepared by dynamic compaction (relative density is 90%).....	52
Figure 2.1.8.2. Physical representations of idealized packings (John 1982): a) Spheroids in cubic packing; b) Spheroids in tetragonal-spheroidal packing; c) Prolate spheroids in cubic packing; d) Prolate spheroids in tetrahedral packing.....	53
Figure 2.1.8.3. Evolution of pore size distribution with confinement: larger pores collapse before smaller pores (Santamarina et al. 2001).....	55
Figure 2.1.8.4. Force chains and granular fabrics: a) Force chains of the shaded particles carry larger contact forces than an average contact force. The remaining unshaded particles act as supports, playing a secondary yet important role in load-carrying mechanism (Santamarina et al. 2001); b) Photoelastic demonstration of force chains: Contact forces tend to be higher along particle chains. Particles that are not part of the force chains play the role of boundary supports preventing the chains from buckling (Mitchell and Soga 2005); c) Development of column-like force chains in 2D numerical tests on rolling resistance (left: free rolling, right: active rolling friction, Iwashita and Oda 1998)	56
Figure 2.1.8.5. Illustration of possible force chain geometries for a granular layer subjected to shear. Solid lines indicate optimal chain orientation and dotted lines denote ranges of possible stable orientations; ϕ_c defines a critical angle of local dilatancy for stress chains; outside this range, stress chains fail by interparticle slip or rolling. Note that parts c and d have larger ϕ_c than that of part b. a) Force chains of a monodisperse system subjected to external shear forces (from Mair et al. 2002): dark gray particles bear high load; light gray particles carry moderate load; and white particles indicate spectators that do not contribute to appreciable load-carrying capacity; b) Force chain of uniform size DSEs; c) Multi-grain fabrics per particle size distributions; d) Modeling of jamming per binary mixtures of DSEs.....	57
Figure 2.1.8.6. Comparison of mobilized macroscopic friction angles (from Yang et al. 2012): It is evident that polygonal discrete elements tend to produce shear jamming even with low values of interparticle friction coefficient. In contrast, uniform-size spherical and clustered discrete elements exhibit limited macroscopic mobilization of greater shear strengths regardless of the value of the coefficient. The effect of shear jamming phenomena needs to be simulated in spherical discrete element analysis	59
Figure 2.1.8.7. Jamming phase diagrams (from Bi et al. 2011): a) Original Liu–Nagel jamming phase diagram. The boundary between unjammed and jammed regions is the yield stress line.	

Unjamming can be induced by decreasing the packing fraction or increasing the shear stress; b) Generalized jamming diagram including the shear-jammed (SJ) and fragile (F) states. Along the ϕ axis, there are two special densities: ϕ_s , below which there is no shear jamming, and ϕ_j , above which isotropically jammed states exist. For $\phi_s \leq \phi \leq \phi_j$, jamming can occur with application of shear stress	60
Figure 2.1.8.8. Relationship between tensile strength and particle size (Lee 1992).....	61
Figure 2.3.3.1. Particle-particle linear contact force model.....	68
Figure 2.4.1.1. Example grain size distribution for a granular soil (Nielsen 2004).....	72
Figure 2.4.1.2. Tangential coefficient of restitution (e_T) versus stiffness ratio (k_T to k_N).....	75
Figure 2.4.2.1. Contact between two spheres: a) With shared contact point O; b) With overlapping regions.....	77
Figure 2.4.4.1. Solutions to the characteristic equation plotted in the complex plane	83
Figure 2.4.4.2. Displacement responses at the contact interface as damping is varied for two overlapping spheres	84
Figure 2.4.5.1. Schematic of ball-drop simulations	86
Figure 2.4.5.2. Time-varying vertical position of sphere over the range of damping values considered	87
Figure 2.4.5.3. Coefficient of normal restitution versus normal damping.....	87
Figure 2.4.5.4. Schematic of oblique collision simulations	88
Figure 2.4.5.5. Tangent of effective recoil angle versus tangent of effective incident angle for a ratio of rolling to sliding friction equal to 0.1.....	89
Figure 2.4.5.6. Tangent of effective recoil angle versus tangent of effective incident angle for a ratio of rolling to sliding friction equal to 0.5.....	89
Figure 2.4.5.7. Tangent of effective recoil angle versus tangent of effective incident angle for a ratio of rolling to sliding friction equal to 1.0.....	90
Figure 2.4.6.1. Nonlinear stiffness and Hertz secant stiffness for modeling normal contact between spheres	91
Figure 2.4.6.2. Nonlinear tangential stiffness per Mindlin's Theory and an approximate secant stiffness approach for use in tangential contact modeling between DSE	92

Figure 2.4.7.1. Schematic of the liquid bridge concept for two neighboring spheres (Rabinovich et al. 2005)	94
Figure 2.4.7.2. Schematic representation of capillary force model (LSTC 2014b).....	96
Figure 2.4.7.3. LS-DYNA model to study the effects of capillary suction force	97
Figure 2.4.7.4. Sphere-sphere distance versus capillary suction force	97
Figure 3.2.1.1. Schematic of a direct shear test (ASTM 2012)	99
Figure 3.2.2.1. Combined DEM-FEM model of direct shear test apparatus	100
Figure 3.2.3.1. Initial configuration with unpacked specimen	101
Figure 3.2.3.2. Application of acceleration field	101
Figure 3.2.3.3. Application of normal pressure	102
Figure 3.2.3.4. Prescribed horizontal translation of top half of apparatus.....	102
Figure 3.2.4.1. Shear stress versus horizontal displacement for direct shear test simulations using random packings of stainless steel spheres	104
Figure 3.2.4.2. Peak shear stress versus normal stress for direct shear test simulations using random packings of stainless steel spheres	104
Figure 3.2.5.1. Geometric packings considered: a) Face-centered cubic; b) Rhombic; c) Simple cubic binary; d) AB binary	105
Figure 3.2.5.2. Numerical simulation of direct shear tests for rhombic packings $FRIC = 0.3$: a) Shear stress versus shear strain; b) Peak shear stress versus normal stress	108
Figure 3.2.5.3. Parametric results from direct shear test simulations of idealized packings	108
Figure 3.2.6.1. States of saturation in for granular soils (Kim 2001): a) Capillary; b) Funicular; c) Pendular	110
Figure 3.2.6.2. Direct shear test simulations with and without use of capillary force calculations	111
Figure 3.3.1.1. Schematic of a triaxial compression test (ASTM 2011) with indication of numerical model scope for the current study	112
Figure 3.3.2.1. Combined DEM-FEM model of triaxial compression test apparatus	114

Figure 3.3.3.1. Unpacked specimen within a rigid cylinder	115
Figure 3.3.3.2. Packed specimen within a rigid cylinder	115
Figure 3.3.3.3. Random packing of specimen into the test chamber	117
Figure 3.3.3.4. Introduction of bonded DSE membrane	118
Figure 3.3.3.5. Application of confining (hydrostatic) pressure to bonded DSE membrane, bottom plate, and top plate	118
Figure 3.3.3.6. Prescribed motion of apparatus top and bottom plates	119
Figure 3.3.4.1. Triaxial compression testing of plastic pearls: a) Physical specimen prior to shearing; b) Physical specimen after shearing (Cil and Alshibli 2014); c) Numerical model prior to shearing; d) Numerical model after shearing (displacement field shown)	120
Figure 3.3.4.2. Comparison between numerical simulation and physical triaxial compression tests using random packings of plastic pearls	121
Figure 3.3.5.1. Comparison of numerical results for triaxial compression tests of 5 mm and 25 mm DSE assemblies: a) Deviatoric stress versus shear strain; b) Volumetric strain versus shear strain	122
Figure 3.4.1.1. A DEM-FEM model for generating various density states of monodisperse systems: a) Isometric view; b) Wireframe view	124
Figure 3.4.1.2. Illustration of deviatoric stress and volumetric strain per relative density states (Belheine et al. 2009)	126
Figure 3.4.1.3. Deviatoric stress versus axial strain for triaxial compression test simulations on monodisperse systems	127
Figure 3.4.1.4. Volumetric stress versus axial strain for triaxial compression test simulations on monodisperse systems	128
Figure 3.4.1.5. Void ratio versus axial strain for triaxial compression test simulations on monodisperse systems	128
Figure 3.4.2.1. A DEM-FEM model for generating density states of binary-sized sphere systems: a) Isometric view; b) Wireframe view	129
Figure 3.4.2.2. Random packings of DSE assemblies: a) Binary system (with a cut plane across the center of the section, Plane A); b) Monodisperse system created via removal of smaller spheres (with a cut plane across the center of the section, Plane B)	130

Figure 3.4.2.3. Triaxial compression test simulations of monodisperse and binary systems: a) Deviatoric stress versus axial strain; b) Volumetric strain versus axial strain	131
Figure 3.4.2.4. Evolution of particle rearrangement and in-plane displacement using the cut planes from Fig. 3.4.2.2: a) Sequence of shear deformation patterns in the binary system; b) Formation of homogeneous deformation fields in the monodisperse system.....	134
Figure 3.4.2.5. Development of force chains in the cut planes of Fig. 3.4.2.2: networks in color of blue are strong contact forces; green and red particles are spectators: a) Vertical force chains in the binary system; b) Weaker force chains in the monodisperse system.....	135
Figure 3.4.2.6. Comparison of elasticity and stress paths for the monodisperse and binary systems: a) Compression (and extension) moduli; b) Stress paths	136
Figure 3.4.3.1. Ordered packings of monodisperse systems: a) Simple cubic assembly; b) Hexagonal assembly	137
Figure 3.4.3.2. Deviatoric stress versus axial strain for DSE assemblies under initial numerical density states	140
Figure 3.4.3.3. Volumetric strain versus axial strain for DSE assemblies under initial numerical density states	140
Figure 3.4.4.1 Linear regression of flow rule	143
Figure 4.3.1.1. Simulation of geostatic stresses in a megascopic DSE assembly: a) Isometric view of model; b) Application of acceleration field; c) Cataloging of stresses.....	147
Figure 4.3.1.2. Locations of REV's in the random packings of DSE assemblies (plan view)	148
Figure 4.3.1.3. Macroscopic horizontal stresses over the range of Coulombic friction coefficients considered	149
Figure 4.3.1.4. Macroscopic vertical stresses over the range of Coulombic friction coefficients considered	149
Figure 4.3.1.5. Macroscopic horizontal versus vertical stresses over the range of Coulombic friction coefficients considered.....	149
Figure 4.3.1.6. Combined DEM-FEM model for demonstrating simulated driving of pile objects into granular media	150
Figure 4.3.1.7. Vertical compressive stresses (0 MPa to 1 MPa) that arise due to gravitational acceleration and driving of the pile object: penetration due to self weight	151

Figure 4.3.1.8. Vertical compressive stresses (0 MPa to 1 MPa) that arise due to gravitational acceleration and driving of the pile object: onset of driving force transfer151

Figure 4.3.1.9. Vertical compressive stresses (0 MPa to 1 MPa) that arise due to gravitational acceleration and placement of the pile object: increased transfer of driving force152

Figure 4.3.1.10. Vertical compressive stresses (0 MPa to 1 MPa) that arise due to gravitational acceleration and driving of the pile object: peak transfer of driving force152

Figure 4.3.1.11. Vertical compressive stresses (0 MPa to 1 MPa) that arise due to gravitational acceleration and placement of the pile object: onset of rebound153

Figure 4.3.1.12. Vertical compressive stresses (0 MPa to 1 MPa) that arise due to gravitational acceleration and driving of the pile object: maximum rebound153

LIST OF TABLES

<u>Tables</u>	<u>Page</u>
Table 2.1.5.1. Mean surface roughness values of quartz grains (Lieu 2013)	26
Table 2.1.5.2. Surface energies of quartz (Parks 1984)	26
Table 2.1.5.3. Elastic properties of mineral granules (Santamarina et al. 2001)	26
Table 2.1.5.4. Values of microscopic angles of friction for various minerals (Mitchell and Soga 2005)	27
Table 2.1.5.5. Angles of friction (microscopic) for minerals (Mitchell and Soga 2005)	34
Table 2.1.6.1. Rounded particle slenderness and eccentricity (Santamarina et al. 2001).....	36
Table 2.1.7.1. Fractal dimensions of granular particle shapes (Arasan et al. 2011).....	40
Table 2.1.8.1. Properties of uniform size sphere packings (from Santamarina et al. 2001).....	54
Table 2.1.8.2. Compositional factors of granular soil (Mitchell and Soga 2005).....	61
Table 2.3.3.1. Contact parameters available in LS-DYNA for modeling sphere-sphere interactions	69
Table 2.4.7.1. LS-DYNA input parameters for modeling capillarity	97
Table 3.2.4.1. Numerical parameters listed for DSEs in O’Sullivan et al. (2004b)	103
Table 3.2.5.1. Properties of geometric packings.....	106
Table 3.2.5.2. DSE Parameters for direct shear testing of idealized packings in LS-DYNA.....	106
Table 3.2.6.1. DSE parameter values for direct shear test simulations	110
Table 3.2.6.2. Direct shear test simulation results	111
Table 3.3.2.1. Numerical parameters for the bonded DSE membrane (adapted from Cil and Alshibli 2014)	114
Table 3.3.4.1. Numerical parameters for DSEs representing the plastic pearls (after Cil and Alshibli 2014)	120
Table 3.3.5.1. Properties of DSE used in demonstrating scale invariance	122

Table 3.4.1.1. Parameter values for random packing simulations and resulting void ratios	125
Table 3.4.1.2. Summary of input parameter values for triaxial compression tests simulations ..	126
Table 3.4.2.1. Summary of input parameters used for comparing behaviors between monodisperse and binary systems.....	130
Table 3.4.3.1. Numerical characteristics of DSE assemblies across descriptive density categories and angles of internal friction	139
Table 3.4.4.1 Library for discrete element analysis models with simulated macroscopic behaviors	141
Table 3.4.4.2. Simulation of random packing of spherical particles with two different size distributions (top: packing density, bottom: coordination number) (Shi and Zhang 2006)	142
Table 4.3.1.1. Input parameter values for modeling megascopic DSE assemblies	147
Table 4.3.1.2. Volumetric properties of the random packings of DSE assemblies over the range of Coulombic friction coefficients considered.....	148

CHAPTER 1

INTRODUCTION

1.1 Introduction

The overall objective of the current research is to study the effect of driven sheet pile walls (SPWs) on the resistance of subsequently driven piles in a granular medium by utilizing a combination of novel computational methods and physical laboratory testing. In order to fulfill the overall study objective, it is required to develop a working, critical knowledge of the numerical modeling of soil behavior, structural behavior, and the interaction between soil and structural objects. In addition, the current project requires the modeling of fundamentally different types of materials (e.g., steel, medium-dense sands), which necessitates the combined use of two separate modeling procedures. For modeling of members composed of manufactured materials such as cement and steel, and for applications in which a continuum hypothesis is satisfactory, the finite element method (FEM) is employed. For granular material (e.g., medium-dense sands), in which the discontinuous nature of the constituent material grains is of predominant importance to mechanical interactions, the discrete element method (DEM) is employed. Simultaneous use of both methods within a model is referred to in the current study as the combined discrete-finite element method (DEM-FEM).

The current report is submitted as the Task 2 deliverable and addresses the development of combined DEM-FEM models for use in simulating the response of granular soils to controlled quasi-static loading. Herein, numerical models are developed for simulation of granular materials subjected to direct shear testing and triaxial testing (and the associated conditions imposed on the test specimens). As a critical first step in ensuring proper modeling of discrete spherical element (DSE) assemblies within the test apparatuses, a comprehensive investigation is carried out, in exploration of each rheological component of a given DSE. Additionally, the formulation of rheological components of the DEM, as used in numerical modeling of inter-particle contacts, is investigated. The numerical models and simulation stages developed in simulating the direct shear and triaxial compression tests are validated against physical test measurements obtained from the literature. Along these lines, the (numerical) test apparatuses are shown to be capable of making meaningful assessments of macroscopic properties for random packings of DSE assemblies.

As a culmination of the investigation into the fundamental behaviors (and interactions) of DSE rheological components, and by making use of the validated (numerical) test apparatuses, a catalog of DSE parameter values is created. This catalog, or library, constitutes a significant enhancement to the extant capabilities related to modeling of granular material. By sampling from this library, assemblies of DSEs can be formed such that the macroscopic properties of said assembly are known a priori. As part of the larger, ongoing research project (i.e., as part of Task 3), a library such as the one presented in the current (Task 2) report will be drawn from in populating megascopic DSE assemblies. Once formed, the megascopic assemblies can then be used to simulate granular soil under geostatic stress states. Furthermore, the megascopic assemblies (built up using macroscopic volumes per the library of rheological parameter values) permit direct examinations of changes in stress states that arise due to the installation (or removal) of structural objects (e.g., piles, SPW).

1.2 Background and Motivation

Over the past three decades, technological and computational advances have corresponded to enhanced capabilities for assessing the behaviors of piled foundations. As a result, it is now recognized that the process of pile construction or installation in the ground can cause major changes in the stress state and density conditions of soil in the vicinity of the pile. Such recognition signifies the value of basic research, which has enabled geotechnical engineers to depart from the historical approach of employing empirical constants to modify theoretical predictions, where corresponding design predictions were not capable of allowing engineers to reliably account for residual stresses induced during pile installation or SPW construction. Examples of the more historical, empirical approach include: an averaging of empirical coefficients in Skempton (1959) through translation of undrained shear strength of stiff clays into 'average' adhesion values for bored piles; Meyerhof's (1959, 1963) estimation of the extent of zones of increased soil density and shear strength near pile tips; and, Kishida's (1967) linear interpolation of internal friction angles within an empirically calculated zone in the vicinity of driven piles. Despite the abundance of empirical methods (which were obtained from observational experiments and in-situ testing), numerous uncertainties remain regarding soil densification (or loosening) and its influence on the stress states that arise in vicinity of piled foundations. Indeed, uncertainties abound for construction operations involving the use of SPWs (e.g., in association with cofferdam construction, piled foundation construction).

Changes in soil conditions may also be associated with use of SPWs when groups of piles are driven into the ground. For example, the ultimate load capacity of the pile group may be either greater or less than the sum of the capacities of the individual piles, depending on whether or not the soil undergoes compaction (or, alternatively, loosening) during pile driving. For scenarios where driving-induced soil compaction occurs, piles driven in the vicinity of SPW or adjacent piles can develop greater load capacities relative to those piles driven in virgin ground. The phenomenon that individual pile stress states are dependent upon the proximity of other pre-driven structural members is further complicated for those scenarios where pile driving into dense soil causes loosening rather than compaction. Subsequent to installation of driven piles, removal (pull-out) of any nearby SPW may well further alter the pile-soil stress states, due to soil disturbances that occur during extraction of the SPW. Such disturbances can lead to reductions in frictional resistance at pile-soil interfaces, and thus, overestimation of pile design capacities (and group efficiencies).

Most of the early research carried out on the phenomenological behavior of soils under the action of shear stresses was primarily restricted to the study of residual loads (or residual compression and tension) in relation to peak strength conditions (and failure criteria). Based on results from laboratory testing of slender model piles in sand, Hanna and Tan (1973) demonstrated the effects of residual compression as a combined result of negative skin friction developing in the upper portions of piles, whereas positive shaft resistances can develop in the lower pile portions. Through investigation of the slope of pile load-deformation curves up to failure, they quantified the effects that residual loads have on pile capacities. Residual load phenomena were later expanded upon in establishing the theory of residual loads on piles for both compression and tension loads (e.g., Holloway et al., 1978, Briaud and Tucker, 1985) such that only extremely small relative movements between piles and the surrounding soil are required to mobilize maximum shaft frictional resistances. It was believed that lock-in stresses along the pile shaft are near yield

stresses. In support of the theory of residual loads, additional studies investigated limit pressures of spherical and cylindrical cavity formation that can occur during pile installation, where the stress states in shear zones of pile-soil interfaces approach critical states of volumetric strain in preloading conditions (Vesic, 1972; Randolph et al., 1979; Yu and Holsby, 1991; Collins et al., 1992; Carter and Kullhawy, 1992; Randolph et al., 1994).

Based on numerous previous studies, it is evident that residual compression and tension loads of driven piles (prior to being exposed to in-service conditions) result from the effects of residual stresses developed in surrounding soil during pile installations. Despite this long-standing finding, little success has been achieved in the rigorous prediction of residual stress states, partly because: (1) Analysis of pile installation in soil is a large strain problem, which involves predominant constitutive and kinematic nonlinearities; and (2) Penetration of an object into particulate materials is a boundary-value problem, where the continuum hypothesis is not valid. Consequently, design practice concerning pile installation has been based on general engineering and mechanics principles, previous design experience, and engineering judgment. Given the limitations associated with extant pile-driving analysis tools, several cycles of design, fabrication, and load testing may typically be required to arrive at reliable, safe foundation designs. Furthermore, design optimization—which requires that the sensitivity of foundation response to changes in key design parameters be evaluated—can be costly if physical testing is the sole assessment-mechanism available.

In the current study, steps are taken toward an alternative methodology, wherein a portion of the assessment can be performed using computational simulation (combined DEM-FEM). Use of such novel simulation methodologies can result in more rapid analysis, improved reliability of foundation design, and reduced development costs. Small-scale physical testing (e.g., centrifuge and laboratory tests) remains necessary in validating and qualifying the integrity of the computational tools. However, far fewer cycles of development and testing are required if simulation results can be relied upon to identify both design parameters that improve design robustness, and design flaws that degrade foundation performance. Evaluating zones of influence of SPWs is of particular interest in the current study. Given the setup time and costs involved in physical testing of pile driving, conducting a strictly physical-experiment based parametric study to evaluate the influence of SPW would be cost prohibitive.

Through complimentary utilization of combined DEM-FEM and laboratory testing, the principal mechanisms behind pile driving that induce changes in soil microstructure of granular soils can be investigated in an efficient manner. Three-dimensional combined discrete and finite element analysis is to be carried out to investigate and evaluate the particulate nature of soil systems subjected to penetration by hardened objects through simulation of the mechanical interaction between penetrator (e.g., SPW or pile) and soils, as well as sequentially combined driven pile and SPW systems. Taking into account the proximity of SPW members, the study employs explicit modeling of soil particle-structure dynamic interactions and residual stress zone of influence resulting from both pile driving and pulling out behavior. Further, this study enables quantification of particle-to-particle contact forces in soil densification (or loosening).

Primary motivations for use of the combined DEM-FEM numerical procedures to the SPW-soil-pile boundary value problem are: (1) To capture the intrinsic features of geo-materials

(geostatic stress states; dilatancy; and, stress dependencies of kinematic response to the complex phenomena of particle crushing and damage during cavity expansion and contraction processes associated with pile driving); and, (2) To simulate lock-in stress through inter-particulate contacts and associated densification of soil clusters by non-conservative forces acting on particle boundaries in the microstructures. In contrast to the conventional continuum-hypothesis-based numerical methods (e.g. finite difference method; smooth particle hydrodynamics, SPH; hybrid Lagrangian SPH Method), the numerical approach discussed herein is capable of simulating: (1) Realistic in-situ stress state initialization of preloading conditions; (2) Stochastic characterization of particle distribution (e.g., relative density); (3) Pulverization of particulate clusters at the tips of penetrators; (4) Explicit occurrence of cavity expansion and contraction; and, (5) Effective stress developed across particulate contact discontinuities.

As a result of employing the above approach, the effects of pile driving at megascopic scales can be assessed (as part of research efforts carried out in satisfaction of Task 3) via fully-coupled particle-structure interactions. In addition, statistical estimates can be made for those geophysical parameters relevant to granular soils at the macroscopic scale (e.g., parameterized values of internal friction angle). Therefore, the goal of this study is to identify those parameters which hold greatest significance in the assessment of pile design capacity by: (1) Tabulating numerical predictions of pile-SPW system response alongside model input values (generated as part of parametric study); and then, (2) Identifying trends in the tabulations of input values with respect to the response quantities. Those parameters that retain significance (i.e., give indications of meaningful input-response trends) when processed in this way can then be directly packaged (via flowcharts and/or graphs) into graphical design-oriented tools for use by geotechnical engineers.

The content of the remainder of the Task 2 deliverable report deals with documenting a comprehensive investigation into the fundamental behaviors of DSEs; numerical models for assessing macroscopic properties of DSE assemblies; and, the calibration of numerical parameters for modeling DSE rheological components. Collectively, these advances are used in forming a library of parameter values for modeling DSE assemblies such that the assemblies exhibit pre-determined macroscopic properties. Importantly, as a favorable outcome of satisfying the objectives specific to Task 2, the associated numerical models and parameter library will be used (as part of the Task 3 research activities) to begin the process of ascertaining the influence of in-situ pile-SPW systems. More specifically, the computational modeling methodologies introduced and documented as part of the Task 2 deliverable report will be used to form prototypes of soil-pile and SPW-soil-pile systems based on use of modular “soil unit” numerical models, rigorous verifications of laboratory-scale experimentations, and a parametric study using the calibrated computational entities.

1.3 Scope of Report

The purpose of the Task 2 deliverable report is to: 1) Demonstrate an understanding of the fundamental behavior of DSE rheology, interactions, and motions; 2) Document the development and validation of numerical models for conducting laboratory testing of DSE assemblies; and, 3) Establish a library of parameter values for constituent DSEs for use in forming DSE assemblies

with known macroscopic properties. The scope of this report involves the following major considerations:

- In Chapter 2, focus is given toward a comprehensive investigation into the numerical formulation and fundamental behaviors of DSEs;
- In the first part of Chapter 3, the numerical modeling of standard laboratory tests is reported, namely for the direct shear and triaxial compression tests. Benchmark scenarios are detailed and used in showcasing the numerical model capabilities, with demonstrated agreement between numerical results and previously measured physical laboratory testing.
- The latter portions of Chapter 3 are dedicated to the calibration of DSE rheological components, followed by the presentation of a “soil unit” library.
- Summaries of the efforts carried out in satisfaction of Task 2 are given in Chapter 4, and a repository of report-wide reference citations is listed in Chapter 5.

CHAPTER 2

FORMATION OF A DISCRETE SPHERICAL ELEMENT (DSE) LIBRARY FOR THE NUMERICAL MODELING OF PILE DRIVING INTO GRANULAR MEDIA

2.1 Friction

Interactions between granular surfaces, and the intimacy of contact between them, are profoundly complicated physical phenomena. These processes encompass elastic and plastic deformations of the surface layers of the contacting microscopic-scale bodies; asperity interlocking and wearing processes at sub-microscopic scales; micro-fracture; chemical reaction; and, lubrication due to water adsorption on grain surfaces and/or surface contamination. Interestingly, a relatively simplistic formulation of the law for dry friction, i.e., a first order approximation of proportionality between the frictional force and the normal force, has been quite sufficient to model (in an approximate manner) several of these phenomena in many engineering applications. The notion of the coefficient of friction in the aforementioned first order approximation originated from a seemingly intrinsic property of dry friction between two macroscopic contacting bodies, which in turn, appeared to be dependent neither on observational (macroscopic) contact area nor on contact surface roughness. In Ch. 2, the intrinsic properties of dry friction are examined from a multi-scale perspective, and in the context of the observational shear strength of granular materials.

2.1.1 Historical Review

Based on the seminal experimental observation that frictional resistance is proportional to the weight and independent of contact area by Leonardo da Vinci (1452-1519), Amontons (1663-1706) confirmed the velocity independence of the friction force (Dowson 1979). Later, Coulomb (1736-1806) determined through detailed experimental investigations the following empirical relationship, known as Coulomb's law of static friction:

$$F_s = \mu_s F_N \quad (2.1.1.1)$$

where the frictional force F_s between two bodies pressed together with a normal force F_N is defined as the proportionality constant μ_s , referred to as the coefficient of static friction. The coefficient of static friction was presented to be independent of macroscopic ("apparent") contact area and relative motion (sliding velocity). Interestingly, Coulomb suggested the physical origin of friction to be the influence of the roughness of the surfaces. To explain the micro-roughnesses of both contacting surfaces, Coulomb depicted surface roughness as a corrugated surface in his original sketch (Fig. 2.1.1.1), and without the aid of a microscope.

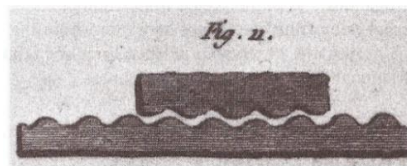


Figure 2.1.1.1. Coulomb's original sketch of interaction between roughnesses as the origin of frictional resistance (Popov 2010)

Coulomb's view on the physical origin of friction became the simplest description of the coefficient of friction as the measurement of the inclination angle at which a body lying on an inclined plane begins to slide. The force equilibrium conditions for the free body diagram between the corrugated surface and the point mass (Fig. 2.1.1.2) is expressed as:

$$R \cos \theta = F_N, \quad R \sin \theta = F \rightarrow F = F_N \tan \theta \quad (2.1.1.2)$$

where R is the resultant force between the mass and incline, and θ is the inclination angle. The force of static friction F_s is (by definition) equal to the maximum force F_{\max} (and maximum inclination angle θ_{\max}) at which the force equilibrium can remain satisfied:

$$F_s = F_{\max} = F_N \tan \theta_{\max} \quad (2.1.1.3)$$

Therefore, the coefficient of friction is equal to the maximum slope of the inclined plane:

$$F_s = F_{\max} = F_N \tan \theta_{\max} \quad (2.1.1.4)$$

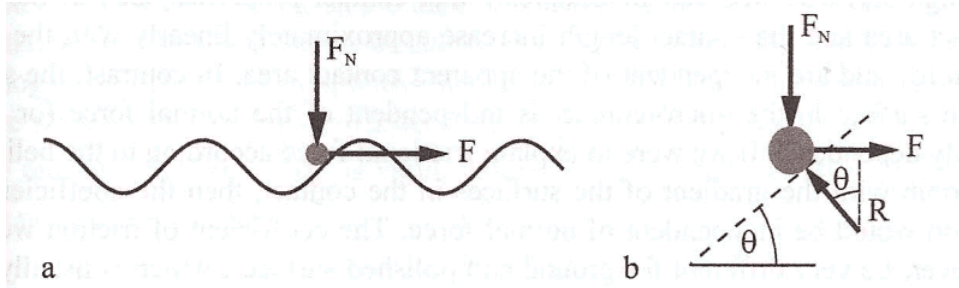


Figure 2.1.1.2. Simplified conceptualization of dry friction: a) Point mass under force equilibrium on an inclined surface; b) Free body diagram (Popov 2010)

The concept of dry friction, as conceptualized by Coulomb, has been widely adopted in the field of engineering. Particularly, in soil mechanics, a maximum inclination angle is called the angle of friction φ , which is typically illustrated as shown in Fig. 2.1.1.3: a block with mass m on an inclined plane is at force equilibrium under gravitational acceleration (g). At the angle of friction, the static force reaches its maximum value $F_s = \mu_s F_N$. The equilibrium of the forces (in the coordinate system shown) yields in this critical state:

$$\begin{aligned} x: \quad mg \sin \varphi - \mu_s F_N &= 0 \\ y: \quad F_N - mg \cos \varphi &= 0 \end{aligned} \quad (2.1.1.5)$$

Thus, the coefficient of friction is equal to the tangent of the angle of friction according to the macroscopic simplification:

$$\mu_s = \tan \varphi \quad (2.1.1.6)$$

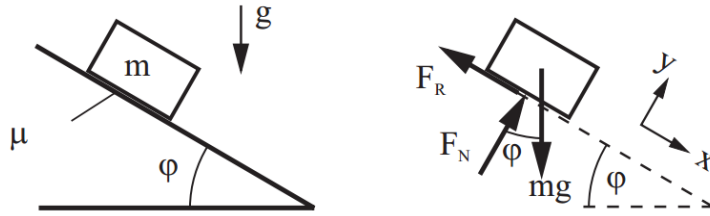


Figure 2.1.1.3. Macroscopic simplification for a maximum (dry) frictional resistance on slip planes

2.1.2 Scale-Dependent Coefficient of Friction

Note that the macroscopic model of Fig. 2.1.1.3 is applied to sufficiently large *continua* with micro-scale “surface roughness” as in Coulomb’s original sketch (recall Fig. 2.1.1.1). In contrast, consider an assembly of idealized discrete granules as depicted by spheres in a three-dimensional (3-D) volume, and discs in a two-dimensional plane (Fig. 2.1.2.1a and Fig. 2.1.2.1b, respectively).

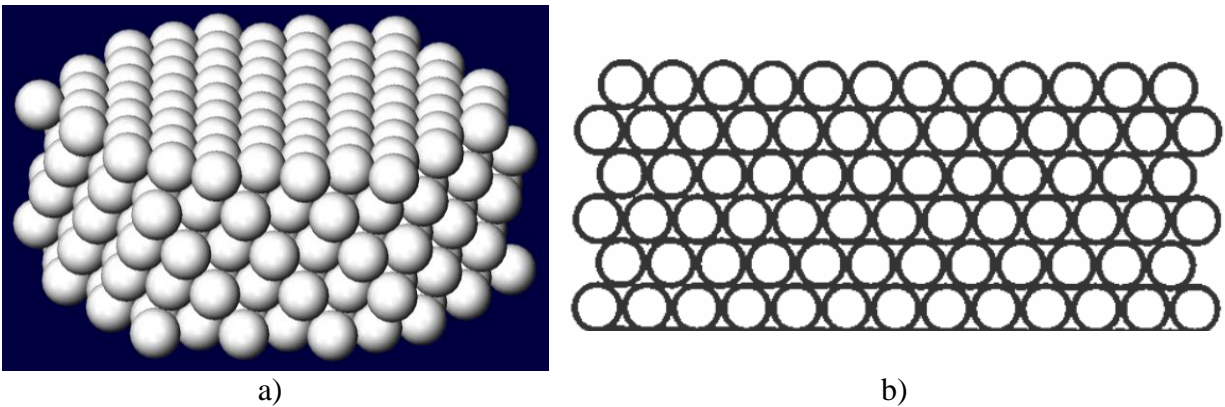


Figure 2.1.2.1. Geometrically regular packings: a) Close-packed tetrahedral spheres at the theoretical maximum bulk density of $\pi/(3\sqrt{2})$ (~74%) in a volume; b) An equivalent 2-D planar packing of discs at the theoretical maximum bulk density of $\pi/(2\sqrt{3})$ (~91%) (Israelachvill 2011)

The repetitive (or randomly ordered) particle arrangement from the contact normal surface forms the 3-D topology of the surface, which is called *surface texture*. For example, consider a uniform dispersion of spherical particles, as shown in Fig. 2.1.2.1. The collection of spheres form a solid-like lattice, which produces a surface texture that includes: roughness (nano- and microroughness) of the constituent particle surfaces (Fig. 2.1.2.2a); and, waviness of contact surface, with macroscopic corrugations (Fig. 2.1.2.2b).

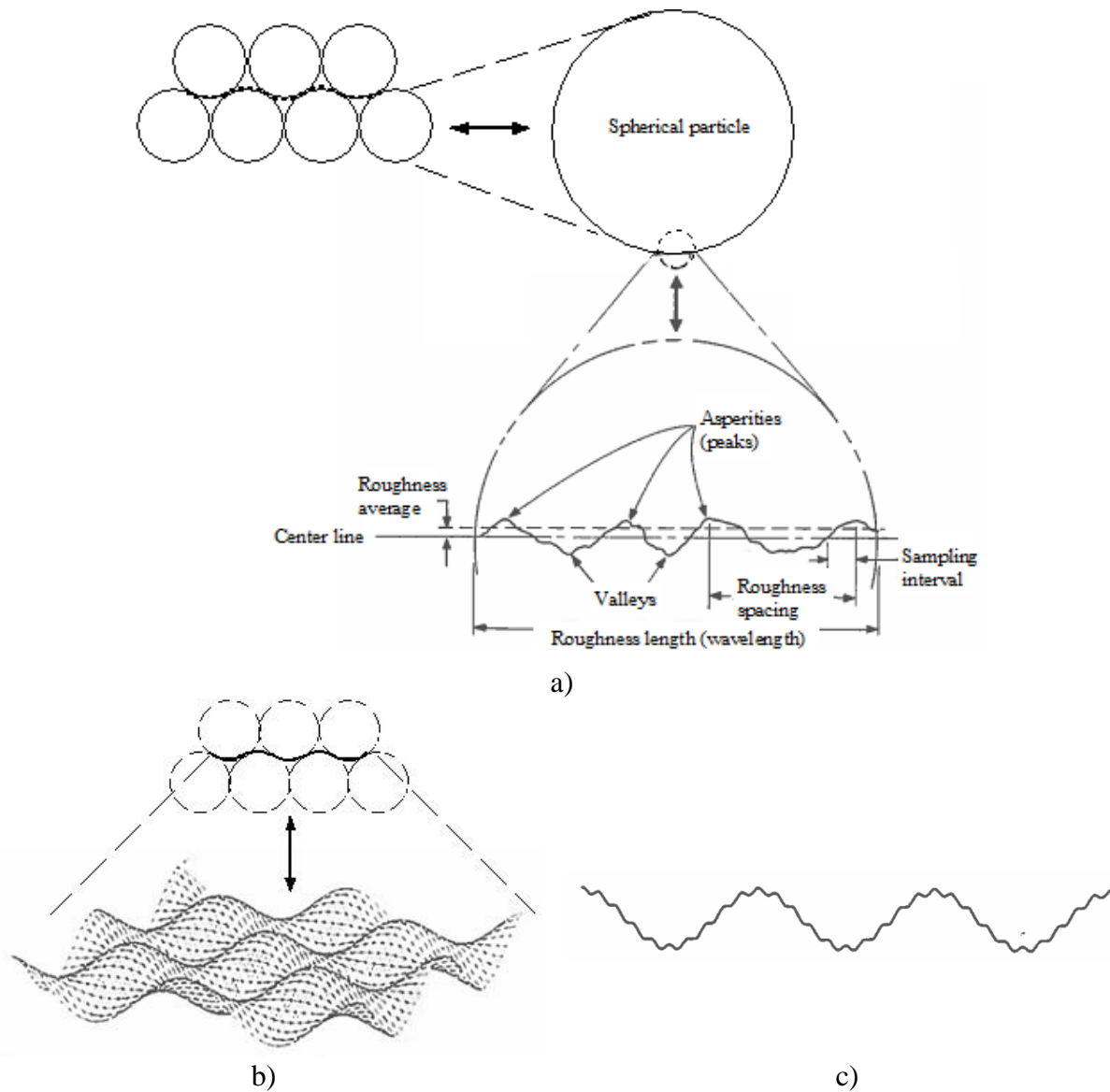


Figure 2.1.2.2. Pictorial surface texture of close-packed spheres: a) Microroughness of a spherical particle; b) Macroroughness of 2-D corrugated surface; c) Representation of a periodic surface with corrugations on the two scales

Nano- and microroughness are formed by fluctuations (e.g., irregularities) of short wavelength across a given surface, where the fluctuations are characterized by asperities (local maxima) and valleys (local minima) of varying amplitudes and spacings, and these are small compared to the granule dimensions. Waviness is the surface irregularity of longer wavelengths, and is referred to as macroroughness. All irregularities in macroroughness can be described in terms of the sampling spacing, which is of much greater magnitude than the microroughness sampling length and less than (or presumably equal to) the size of a laboratory test sample (e.g., for triaxial compression tests). In tribology, random surface variations in space are very similar to randomness of microroughness, and are characterized using macroscopic amplitude probability

distributions and autocovariance functions (refer to Fig. 2.1.2.3c). Surface roughness, thus, is by definition non-uniform with respect to scale (e.g., from the nano/micro to macro-scale).

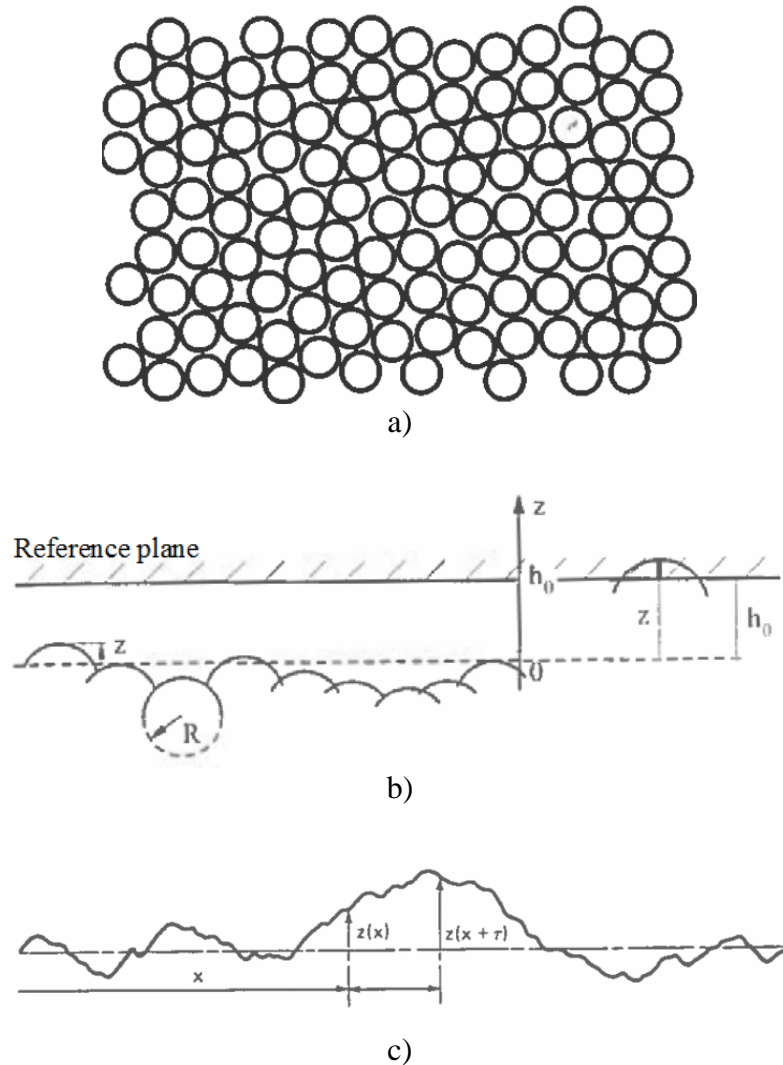


Figure 2.1.2.3. Dimensional representation of the surface random packings of multi-disperse systems: a) Close random packing of monodisperse system (Israelachvill 2011); b) Height (peak) distribution on a stochastic surface (Greenwood and Williamson 1966); c) 1-D representation of macroscopic surface roughness (from Adams and Nosonovsky 2000)

It must be noted that the physical macroroughness is being depicted herein solely to provide a simple uniform pattern for visualization purposes (e.g., Figs. 2.1.2.2a and 2.1.2.2b show idealized cubic closest packings and a simple one-dimensional topographical mapping, respectively). More importantly, the deterministic surface texture of Figs. 2.1.2.2b will be used to derive scale-dependency of the coefficient of friction using a relatively simple analytical method in the following. However, the principal direction of predominant surface patterns and gross deviations from nominal shapes of the macro wavelength (e.g., Fig. 2.1.2.3c) are parts of the surface texture, known as an anisotropic fabric tensor in continuum mechanics, and these geometrical features will

be assessed together by means of loose or close random packing or bi-disperse packing in Chapter 3 of the current report.

Consider Fig. 2.1.2.4 where two different scales of frictional angles are illustrated. The presence of “microscopic friction angle” is characterized as an intrinsic coefficient of friction μ_0 . This way, a single corrugated surface with coefficient of friction μ_0 can be drawn with a maximum slope of $\mu_1 = \tan \theta_1$. Based on the free body diagram of a body in force equilibrium at contact with the surface, the following equilibrium equations are written in the local x' - and l' -direction:

$$\begin{aligned} l': \quad F_N \cos \theta_1 + F \sin \theta_1 &= R \\ x': \quad F_N \sin \theta_1 + \mu_0 R &= F \cos \theta_1 \end{aligned} \quad (2.1.2.1)$$

From which, it follows that:

$$\frac{F}{F_N} = \frac{\mu_0 + \tan \theta_1}{1 - \mu_0 \tan \theta_1} = \frac{\mu_0 + \mu_1}{1 - \mu_0 \mu_1} \quad (2.1.2.2)$$

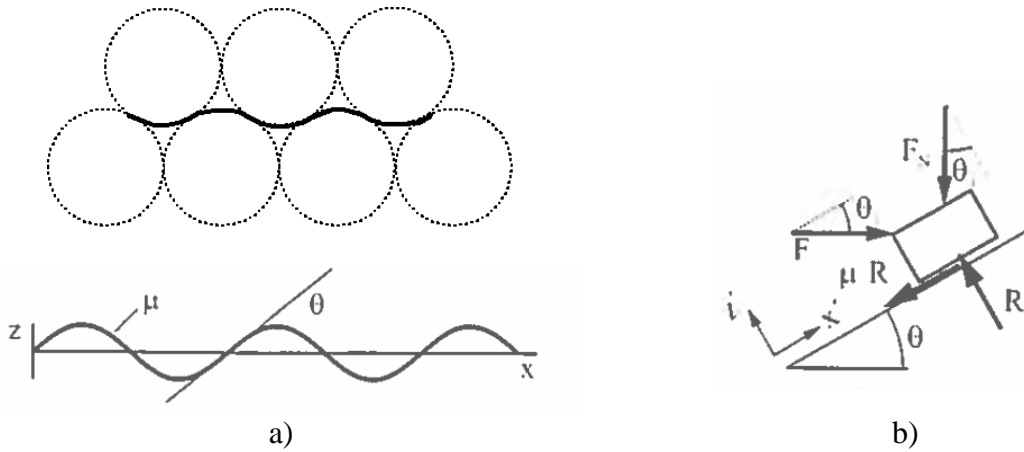


Figure 2.1.2.4. Idealized macroroughness with periodic corrugation: a) Corrugated surface with intrinsic coefficient of friction, μ_0 ; b) Free-body diagram of a body on a corrugated surface with coefficient of friction, μ_0

Note that this “superposition” has a simple interpretation for coefficient of friction on the two different scales, and for which the friction angles are summed on the scales of interest (e.g., $\theta = \theta_0 + \theta_1$). Thus, the coefficient of friction μ can be accounted for by defining a total frictional resistance, which simultaneously provides a general rule to superimpose coefficients of friction at a given scale:

$$\mu = \tan \theta = \frac{\sin(\theta_0 + \theta_1)}{\cos(\theta_0 + \theta_1)} = \frac{\sin \theta_0 \cos \theta_1 + \cos \theta_0 \sin \theta_1}{\cos \theta_0 \cos \theta_1 - \sin \theta_0 \sin \theta_1} = \frac{\tan \theta_0 + \tan \theta_1}{1 - \tan \theta_0 \tan \theta_1} = \frac{\mu_0 + \mu_1}{1 - \mu_0 \mu_1}$$

In general,

$$\mu = \tan \left(\sum_i \arctan \mu_i \right) \quad (2.1.2.3)$$

Therefore, the tangent of angles due to scale-dependent surface irregularities would then give the coefficient of friction. Specifically, frictional strength of a volume of granular mass, which is measurable in laboratory settings, is characterized by frictional processes on the micromechanical scale. Further, a discrete multi-body representation of the granular mass enables the inclusion of scales when considering friction angles (as opposed to relegating the treatment to that of two continuous bodies, Eqn. 2.1.1.6). In the following, a theoretical basis is established for determining those factors that contribute to an intrinsic coefficient of friction at the microscopic scale.

2.1.3 Cold Welding: Theory of Bowden and Tabor

Throughout the history of tribology, several attempts have been made to explain the universality and simplicity of Coulomb's law of friction, based on the proportionality of the frictional force to the normal force. The contact properties investigated typically derive from the interlocking of projections on surface roughness. One such attempt is found in the work of Sir Thomas Hardy, who examined wear track on sliding glass surfaces in 1919. Per observation of tearing, Hardy concluded that sliding friction was due to cohesive forces between contacting surfaces, where the actual area of contact was only a fraction of the total contact area. Thus, the cohesive forces on a unit area basis were quite large. Several years later, as cited by Bromwell (1966), Terzaghi (1925) presented the first quantitative description of the adhesive frictional processes at the microscopic scale, as shown in Fig. 2.1.2.4a. His reasoning was that the normal load N acting on a very small area of actual contact would cause yielding of the microscopic contact asperities (refer to Fig. 2.1.3.1). The contact area A_c would be given by:

$$N = A_c q_u \quad (2.1.3.1)$$

where q_u is the normal stress required to cause plastic flow. Note that early theoretical work used yield stress σ_y as the indentation hardness. The quantity q_u is essentially a bearing capacity, which is the indentation hardness of asperity and tends to be greater than the yield stress (e.g., $q_u = \sigma_0 = 3\sigma_y$). Adhesion would occur over the regions of actual contact where the junctions should be sheared before sliding takes place, i.e., stick conditions. If the grain material has a shear strength, τ_m , then the maximum tangential force F_{\max} is defined as:

$$F_{\max} = A_c \tau_m \quad (2.1.3.2)$$

Thus, an inter-particle coefficient of friction μ_i is written as:

$$\mu_i = \frac{F_{\max}}{N} = \frac{\tau_m}{q_u} = \frac{\tau_m}{\sigma_0} \quad (2.1.3.3)$$

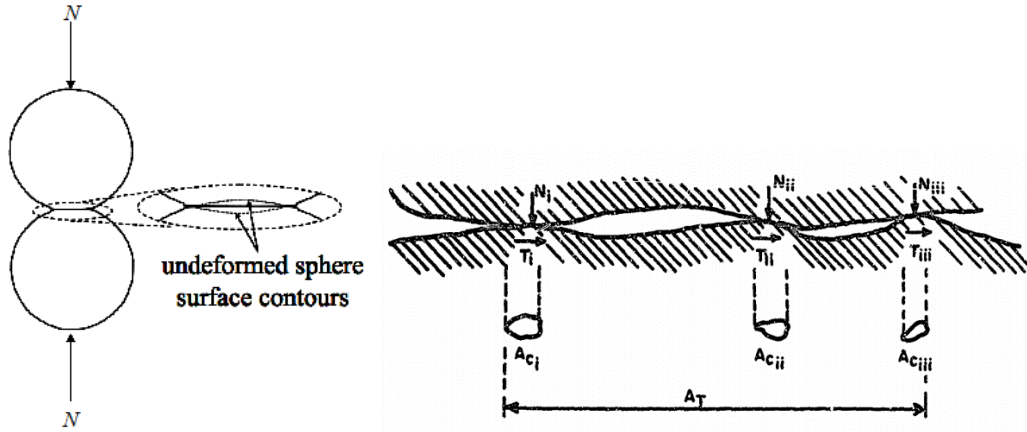


Figure 2.1.3.1. Depiction of microscopic contact area between two spherical grains (the rightmost illustration is from Bromwell 1966)

Independent from Terzaghi's analysis, Bowden and Tabor (1950) presented a theory to explain frictional behaviors for a wide variety of materials. Namely, the Adhesion Theory of Friction explains phenomena such as kinetic friction between pure metallic surfaces through the formation of cold-weld junctions, and more generally, where friction is treated as cohesive bonds at points of contact between two objects. As a novel facet of the theory, strong adhesion due to microscopic interlocking exists for contacts in compression A_{comp} and tension $A_{tension}$:

$$\begin{aligned} F_{\max} &= \tau_c (A_{comp} + A_{tension}) \\ N &= \sigma_c (3A_{comp} - \xi A_{tension}) \end{aligned} \quad (2.1.3.4)$$

where F_{\max} is the static force of friction if all of the cold welds are sheared; the maximum normal stress compressive area per normal load N is roughly equal to the indentation hardness ($3\sigma_c$); and, for tensile areas, a ratio ξ of the hardness to the maximum normal stress is defined (which is generally less than 3). Thus, the intrinsic coefficient of friction at adhesive contact surfaces is then:

$$\mu_0 \approx \frac{F_{\max}}{N} = \frac{\tau_c (A_{comp} + A_{tension})}{\sigma_c (3A_{comp} - \xi A_{tension})} \quad (2.1.3.5)$$

Explanation of this adhesive bonding called "cold-welding" is illustrated per Von-Mises yield criterion in Fig. 2.1.3.2. As the asperities are initially loaded to the yield stress (step 1), application of a small shear stress would require that applied normal stresses are less than the yield stress (step 2). As the shear stress increases, the contact area must continually increase in order to maintain the plastic equilibrium. If the junction does not shear until $\tau = \tau_m$, then normal stress must decrease to zero (step 3). That is, either an infinite area of contact or gross seizure over the entire area takes

place in the process of junction growth that produces cold welding, and further, can correspond to extremely large coefficients of friction (Bowden and Tabor 1950).

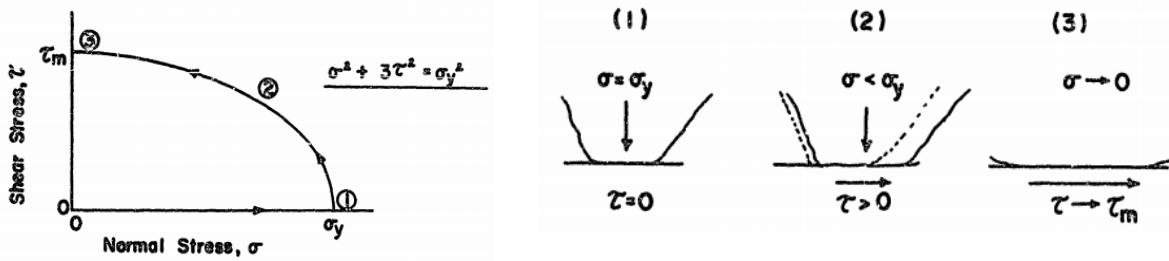


Figure 2.1.3.2. Cold welding mechanism (from Bromwell 1966)

If the maximum shear stress is less than the uniaxial compressive strength by (approximately) a factor of $\sqrt{3}$, then $\tau_c \approx \sigma_c / \sqrt{3}$. Also, for this condition, plastic substances can undergo isotropic hardening. If $A_{comp} \approx A_{tension}$ (e.g., perfectly conformal contact) and $\xi \approx \sqrt{3}$, then

$$\mu_0 = \frac{2}{\sqrt{3}(3 - \sqrt{3})} = 0.91.$$

For quartz with an indentation hardness of about 1100 kg/mm² (10 GPa), stress levels must exceed the yield limit of approximately 10.3 GPa to cause plastic deformation in the asperities in contacts. It is a matter of debate whether or not this level of stress is reached for a significant number of asperities engaged in surface contacts among grains. Nevertheless, adhesion of brittle granular materials can be a significant factor contributing to the intrinsic coefficient of friction at the microscopic scale. Therefore, a quantitative description of the coefficient of friction at the microscopic scale is investigated later for brittle granular materials, and particularly for quartz.

2.1.4 JKR Theory

A treatment of adhesive normal contact between elastic bodies was proposed by Johnson, Kendall, and Roberts in 1971, and is known as JKR Theory. This theory prevalently serves as the starting point for essentially all frictional studies in modern granular physics. Consider an elastic sphere with radius R in contact with a rigid, planar surface. Because of the attractive forces between two solid bodies (known as van der Waals forces), an elastic sphere (Fig. 2.1.4.1) deforms through depth d due to contact with a plane, and forms a characteristic “neck” across contact area a .



Figure 2.1.4.1. Formation of a characteristic “neck” during adhesive contact (Popov 2010)

As part of the deformation due to contact, the points on the contact surface of the sphere displace through a certain depth, which can be written in terms of vertical displacement u_z (Johnson 1985):

$$u_z = \frac{\pi}{4E^*a} p_o(2a^2 - r^2) \quad (2.1.4.1)$$

where p_o is a contact pressure at the centroid of the contact area; and, an elasticity constant for the sphere is defined using Young's modulus E and Poisson's ratio ν as $E^* = E / (1 - \nu^2)$. A derivation can be carried out using the energy principle for determining a critical radius, where this radius corresponds to development of a maximum adhesive force. As a result, the absolute values of the force F_a (the adhesive force) are given in terms of a critical contact radius a_{crit} and a critical penetration depth d_c (e.g., the maximum displacement on a single asperity):

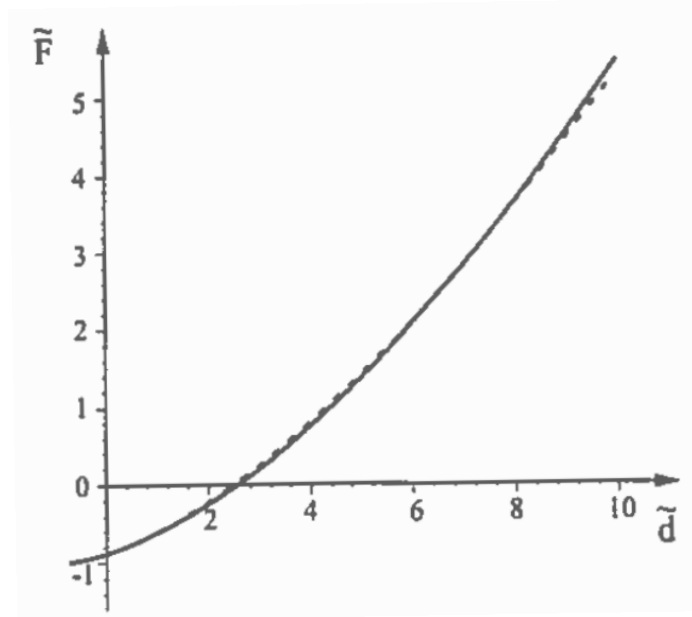
$$F_a = -\frac{3}{2}\gamma_{12}\pi R \quad \text{when} \quad a = a_{crit} = \left(\frac{9}{8}\frac{\gamma_{12}\pi R^2}{E^*}\right)^{1/3} \quad \text{and} \quad d = d_c = -\left(\frac{3}{64}\frac{\gamma_{12}^2\pi^2 R}{(E^*)^2}\right)^{1/3} \quad (2.1.4.2)$$

where γ_{12} is the surface tension under force equilibrium (at the microscopic scale). Note that the interactive forces between solid surfaces will be further discussed in the presence of small amounts of water in Chapter 3, where capillarity is modeled to simulate apparent cohesion of drained, dense granular mass. Using dimensionless variables: $\tilde{F} = F / |F_a|$, $\tilde{a} = a / a_{crit}$ and $\tilde{d} = d / |d_{crit}|$, we write:

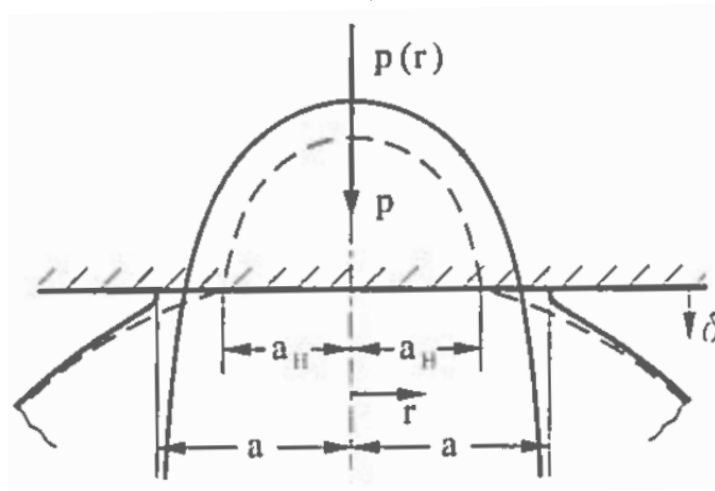
$$\tilde{F} = \tilde{a}^3 - 2\tilde{a}^{3/2} \quad \text{and} \quad \tilde{d} = 3\tilde{a}^2 - 4\tilde{a}^{1/2} \quad (2.1.4.3)$$

which defines a parametric form of the dependence of the dimensionless force on the dimensionless penetration depth. A physical interpretation of the equation is: adhesive forces formed at contacts of multiple asperities can provide substantial resistance, as the asperities engaged in the surface contact must be sheared in the tangential direction. Adhesive normal stresses (as analogous to prestressed conditions) can reach very large values at the edges of the contact area between two contact asperities. A graphical illustration is given in Fig. 2.1.4.2. Assuming that the penetration depth is of the same order of magnitude as d_c , the dimensionless force can be approximated (dashed line in Fig. 2.1.4.2b) as:

$$\tilde{F} = -1 + 0.12(\tilde{d} + 1)^{5/3} \quad (2.1.4.4)$$



a)



b)

Figure 2.1.4.2. Contact force and pressure: a) Dependence of normal contact force on penetration depth at the microscopic contact (Eqn. 2.1.4.3); b) Hertzian contact pressure distribution in an adhesive contact (Johnson 1985)

2.1.5 Grain Surface Texture and Frictional Resistance

Having reviewed JKR Theory, which describes adhesive contact between two elastic bodies (i.e., a pair of contact asperities at the microscopic scale), attention is shifted to estimating an intrinsic coefficient of friction between two rough surfaces containing multiple contacts among asperities. More specifically, forensic casework studies for the latest quartz grain surface texture analysis using scanning electron microscopy (SEM) and atomic force microscopy (AFM) are used

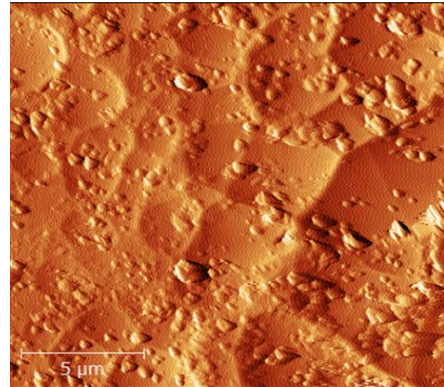
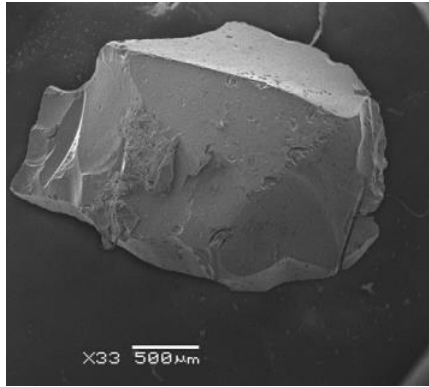
as the basis of analytical calculation. SEM can produce very high-resolution images of a sample surface, revealing details at the nanoscale. SEM micrographs can also have a depth of field yielding a characteristic three-dimensional appearance, which is useful for understanding the surface texture of a grain over a wide range of magnifications (from 10x to 500,000x; which, is approximately 250 times greater than the magnification limit of high-end microscopes). According to Konopinski et al. (2012), the AFM is:

“A form of scanning probe microscope utilizing an ultra-sharp tip micro-fabricated on a cantilever to image a sample. When in close proximity with the sample, the deflection of the cantilever, due to interaction with intermolecular forces between the tip and the sample surface, is detected by reflecting a laser beam off the top of the cantilever onto a position-sensitive photodiode. Given a known deflection and spring constant for the cantilever, the interaction force between tip and sample can be obtained using Hooke’s law. Feedback circuitry controls the tip-sample distance to remain small, but also avoids damaging the sample. Positioning of the tip is precisely controlled with piezoelectric elements in the x, y, and z axes, and during analysis the tip is scanned across the sample surface in a raster scan, building up an image of the surface topography.”

As a compliment to SEM techniques, the AFM offers a quantitative means of analyzing mappings generated at the nanoscale. Consider the three SEM images of quartz grains shown in Fig. 2.1.5.1. In Fig. 2.1.5.1a, a mechanically crushed (angular) granule is displayed. In Fig. 2.1.5.1b the natural crystalline growth formed by deposition under high pressure (sub-rounded) is displayed, whereas Fig. 2.1.5.1c depicts the effects of abrasion wearing on a granule. Topographical images of multiple sets of these grain samples (totaling 24 grains, using AFM, Konopinski et al. 2012) revealed that surface textures on grains are highly disparate from one another. Such variability is indicative of the topological evolution that takes place on granular surfaces subjected to the myriad paths of loading over time.

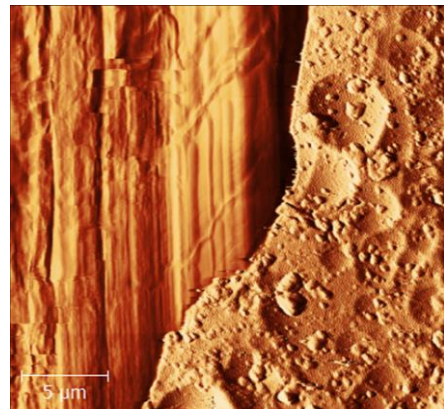
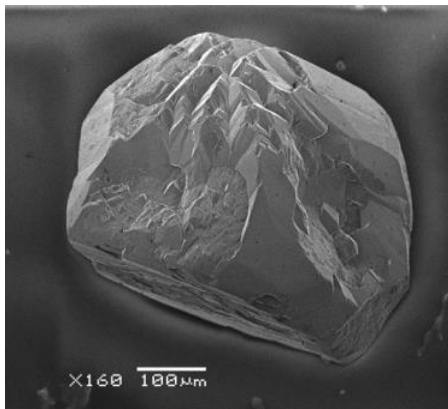
Surface roughness measured at the microscopic scale (amplitudes and periods of asperities) can vary significantly, given some degree of surface abrasion and crystalline growth. To investigate this phenomenon, Konopinski et al. (2012) also reconstructed 3D elevation maps from the topographic data. Amplitudes among the three sets were found to vary in 0.63, 1.6, and 4.5 μm for scan sizes of 10 by 10, 25 by 25, and 30 by 50 (μm by μm), as shown in Fig. 2.1.5.2a. Based on a statistical analysis of amplitude and surface roughness, Konopinski et al. (2012) concluded that it is possible to construct a histogram of the heights of the surface boundaries. Applying a Gaussian low-pass filter to smooth the results, the resulting height distribution histogram gives the relative frequency of specific height data obtained from the surface.

Given the scope of the current FDOT research project, a detailed review of topographical analyses from the literature is not conducted. Instead, identification of the range of values of amplitudes (asperities) and the corresponding standard deviations (i.e., the root mean square of the height distributions) pertaining to quartz grains is focused upon. In this way, an intrinsic coefficient of friction (using an averaging method) can be developed and applied to the modeling of granular materials, as discussed below.



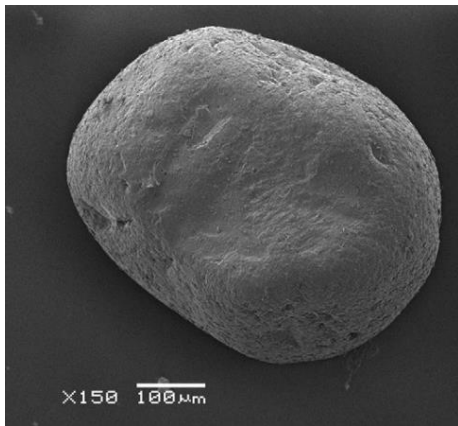
SEM (left) and AFM (right) scan size $17.5 \times 17.5 \mu m^2$

a)



SEM (left) and AFM (right) scan size $25 \times 25 \mu m^2$

b)



SEM (left) and AFM (right) scan size $10 \times 10 \mu m^2$

c)

Figure 2.1.5.1. Grain surface topography: a) Mechanically crushed pure quartz with sharp edges and clean faces with minimal surface texture; b) Diagenetic quartz with euhedral crystal growths formed naturally by deposition under high pressure. Minimal transportation of the grains is evident from lack of edge abrasion; c) Semi-round grains with characteristic surface fractures (Konopinski et al. 2012)

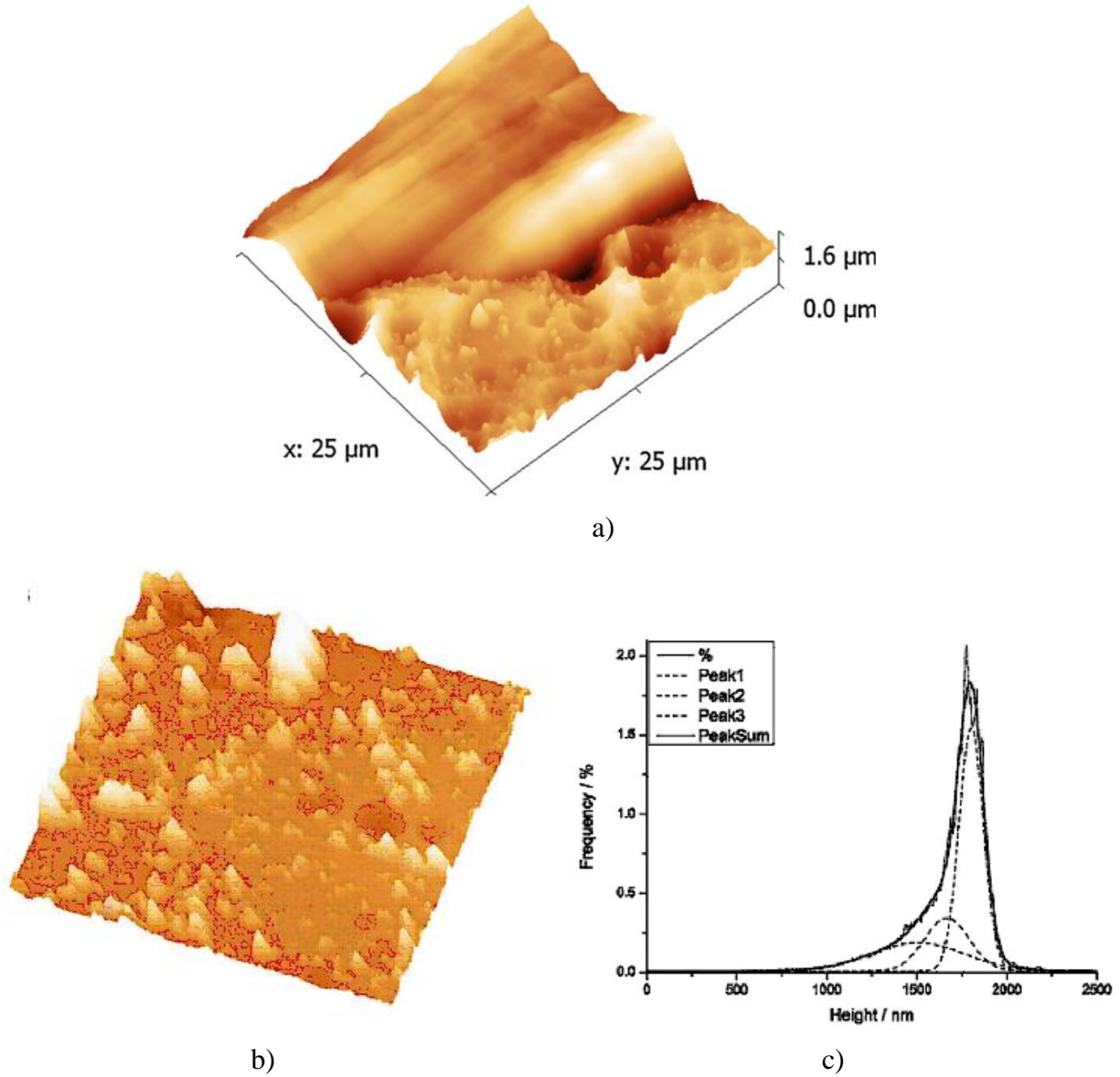


Figure 2.1.5.2. Dimensional representation of the grain surface (from Konopinski et al. 2012): a) 3-D elevation map of Fig. 2.1.5.1b; b) 3-D representation of the microscopic surface texture of a grain; c) Counting estimate of fractal dimension for a 20 μm AFM scan

Let the height distributions (amplitudes) of two contacting granular surfaces be given by a Gaussian distribution, with standard deviation l . We assume that the surfaces are pressed together under the action of a normal force F_N . Subsequent to being pressed together, granular surfaces are translated relative to one another in the tangential direction. The resulting friction force that arises is due to the asymmetry of the loading processes occurring during the formation and destruction of adhesive contacts: two approaching asperities first come into contact when their undeformed geometric contours intersect. Conversely, the surface localities separate only after some finite

distance between the two has been achieved. The strength of adhesion can be characterized by the critical distance at which the separation of the surfaces occurs (recall the critical depth calculation in Eqn. 2.1.4.2) where $R^* = \frac{R}{2}$ and $E^* = \frac{E}{1-\nu^2}$. Note that the surface radius of curvature and elastic property of both the contacting asperities are assumed to be identical, purely for simplicity in deriving an analytical solution. Then, the problem basically deals with three statistical parameters, each with dimension of length: the radius of curvature, the height distribution, and the critical distance. For contact between a single pair of asperities (with an average height, measured over a sampling length), the three following conditions are imposed as part of a statistical parametrization: $d_c < l$, $d_c / R^* \ll 1$, and $l / R^* \ll 1$. A physical description of the three imposed geometric conditions is as follows: the critical distance is less than the standard deviation of the height distribution (to ensure inclusion of only a single pair of asperities); the critical distance has to be much smaller than the radius (in consideration of the ratio of amplitude to particle radius); and thus, the height distribution must be much smaller than the radius. Under these conditions, we first investigate contact between the two asperities and, thereafter, expand the solution by means of an averaging over the statistical distribution of multiple contact asperities.

Consider a schematic sketch of two asperities with equal radii of curvature, as shown in Fig. 2.1.5.3. The form of the asperities is described by:

$$z_1(x) = z_1 - \frac{x^2}{2R} \quad \text{and} \quad z_2(x) = z_2 - \frac{(x - x_0)^2}{2R} \quad (2.1.5.1)$$

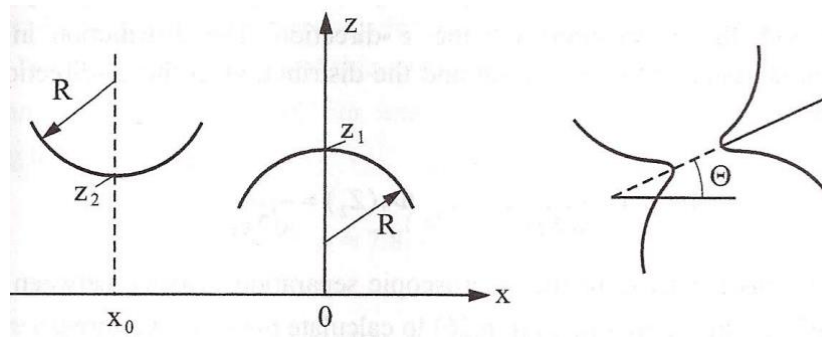


Figure 2.1.5.3. Two spherical asperities in contact (Popov 2010)

While the surfaces remain in contact, the penetration depth is given by:

$$d = z_1 - z_2 - \frac{x_0^2}{2R} \quad (2.1.5.2)$$

and the tangent of the contact angle is then:

$$\tan \theta \approx \theta = \frac{x_0}{2R} \quad (2.1.5.3)$$

For the first contact ($d = 0$) and the last contact ($d = -d_c$) just before separation, we can obtain minimum and maximum values of x_0 from Eqn. 2.1.5.2:

$$x_{0,\min} = -2\sqrt{R(z_1 - z_2)} \quad \text{and} \quad x_{0,\max} = 2\sqrt{R(z_1 - z_2) + Rd_c} \quad (2.1.5.4)$$

If we denote the contact force between the asperities as F , then the z-component and x-component of the contact force can be written using Eqn. 2.1.5.3:

$$F_N = F \quad \text{and} \quad F_R = -F \frac{x_0}{2R} \quad (2.1.5.5)$$

Thus, the intrinsic coefficient of friction can be calculated as:

$$\mu_0 = \frac{\langle\langle F_R \rangle\rangle}{\langle\langle F_N \rangle\rangle} \quad (2.1.5.6)$$

where the notation $\langle\langle \dots \rangle\rangle \equiv \langle \dots \rangle_x \langle \dots \rangle_z$ denotes an average over the asperity distribution (macroscopic roughness) in both the x-direction and the z-direction. For simplicity in numerical quantification, the distribution in the x-direction is assumed to be uniform over a finite sampling length, and the height distribution in the z-direction is defined (with respect to functional form) using a normal distribution (Greenwood and Williamson 1966):

$$\Phi_1(z_1) = \frac{1}{\sqrt{2\pi}l} \exp\left[-\frac{z_1^2}{2l^2}\right] \quad \text{and} \quad \Phi_2(z_1) = \frac{1}{\sqrt{2\pi}l} \exp\left[-\frac{(z_2 - z_0)^2}{2l^2}\right] \quad (2.1.5.7)$$

Based on Eqn. 2.1.4.4, we approximate the adhesive force:

$$F \approx F_c \left[0.12 \left(\frac{d}{d_c} + 1 \right)^{5/3} - 1 \right] \quad \text{for} \quad -1 \leq \frac{d}{d_c} \leq 10 \quad (2.1.5.8)$$

where $F_c = \frac{3}{2} \pi \gamma_{12} R$ (refer to Eqn. 2.1.4.2). Averaging the forces F_N and F_R in the x-direction, over the length of sliding surface (L), we write:

$$\begin{aligned}
\langle F_R \rangle_x &= -\frac{1}{L} \int_{x_{0,\min}}^{x_{0,\max}} F \frac{x_0}{2R} dx_0 \approx \frac{F_c d_c}{2 L} \\
\langle F_N \rangle_x &= \frac{1}{L} \int_{x_{0,\min}}^{x_{0,\max}} F dx_0 \approx F_c \frac{\sqrt{Rd_c}}{L} \left[1.2(1 + \xi)^{13/6} - \sqrt{\xi} - \sqrt{\xi + 1} \right]
\end{aligned} \tag{2.1.5.9}$$

where $\xi = \frac{3}{4} \frac{l}{d_c}$ and $l = \sqrt{\langle z^2 \rangle}$. Therefore:

$$\mu_0 \approx \frac{\langle F_R \rangle_x}{\langle F_N \rangle_x} = \frac{0.5 \sqrt{(d_c/l)} \nabla_z}{1.2(1 + \xi)^{13/6} - \sqrt{\xi} - \sqrt{\xi + 1}} \tag{2.1.5.10}$$

where $\nabla_z = \sqrt{\left\langle \left(\frac{1}{L} \int_0^L \frac{dz(x)}{dx} \frac{dz(x)}{dx} dx \right) \right\rangle} = \sqrt{\left\langle \left(\frac{dz}{dx} \right)^2 \right\rangle}$.

Thus, the intrinsic coefficient of friction is proportional to the root mean square of the surface gradient. For small values of d_c/l , Eqn. 2.1.5.10 can be simplified to:

$$\mu_0 \approx 7.8 \left(\frac{d_c}{l} \right)^{8/3} \nabla_z \tag{2.1.5.10}$$

Defining ∇_z as being approximately equal to the tangent of average angle of asperities in the x-direction, i.e., $\langle \theta \rangle_x$, then:

$$\mu_0 \approx 7.8 \left(\frac{d_c}{l} \right)^{8/3} \tan(\langle \theta \rangle_x) \tag{2.1.5.11}$$

For example, for mild steel, with $\left\langle \frac{d_c}{l} \right\rangle_x < 0.1$, $\mu_0 \approx (0.017) \tan(\langle \theta \rangle_x) \rightarrow 0$. The adhesive contribution to friction in a pairing of steel-to-steel contact surfaces is negligibly small (and can approach zero if the surface roughness is very small, e.g., by means of lubrication). As another example, for viscoelastic materials such as rubber, with $\left\langle \frac{d_c}{l} \right\rangle_x \geq 0.48$, $\mu_0 \approx 1.12 \cdot \tan(\langle \theta \rangle_x)$. The adhesive contribution to friction in a pairing of steel-to-steel contact surfaces is negligibly small (and can approach zero if the surface roughness is very small, e.g., polished). For viscoelastuc materials such as rubber with $\left\langle \frac{d_c}{l} \right\rangle_x \geq 0.7$, $\mu_0 \approx 3.0 \cdot \tan(\langle \theta \rangle_x)$.

Of relevance to the current study, consider quartz. More specifically, consider coarse grains with a radius of 1.5 mm; surface roughness l (9.37 nm from Table 2.1.5.1; Lieu 2013); surface

energy γ_{12} (1.2 J/m² from Table 2.1.5.2; Parks 1984); Young's modulus E for E^* (76 GPa from Table 2.1.5.3 from Santamarina et al. 2001); and, Poisson's ratio ν for E^* (0.3 from Table 2.1.5.3 of Santamarina et al. 2001). Then, the following can be calculated using Eqns. 2.1.4.2 and 2.1.5.11:

$$d_c = \left(\frac{3 \gamma_{12}^2 \pi^2 R}{64 (E^*)^2} \right)^{1/3} = \left(\frac{3 (1.2)^2 \pi^2 (0.0015)}{64 (83.5E9)^2} \right)^{1/3} = 5.233 \times 10^{-9} \text{ m} \approx 5.233 \text{ nm} \quad (2.1.5.12)$$

$$\mu_0 \approx 7.8 \left(\frac{5.233}{9.37} \right)^{8/3} \tan(\langle \theta \rangle_x) = 1.65 \tan(\langle \theta \rangle_x)$$

That is, development of adhesive contacts of asperities (as shown in Fig. 2.1.5.4) can quite noticeably contribute to the frictional force if the ratio of maximum penetration depth to the height distribution (i.e., roughness of microscopic surface) is relatively large. The surface energy of the grain is the controlling factor for this ratio. As for formation of young quartz in place, the height distribution tends to increase by an order of magnitude, and the specific surface and surface energy increase almost proportionally. In contrast, mechanical weathering causes surface abrasion and reduces the critical penetration depth by an order of magnitude. Likewise, mechanical weathering reduces values of the height distribution by a factor of two (or three), ultimately leading to a very low coefficient of friction.

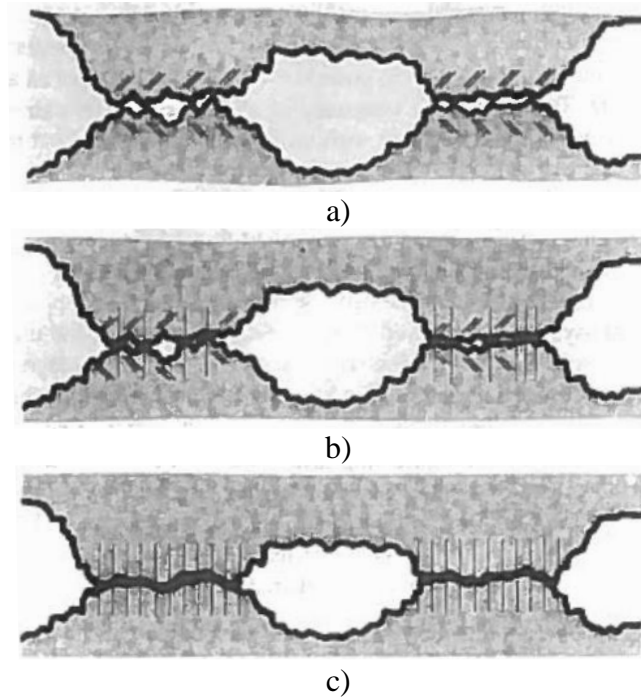


Figure 2.1.5.4. A schematic of three deformation stages of contact asperities at the microscopic scale: a) Initial contacts take place within frictional asperity bodies undergoing elastic deformation; b) Further deformation occurs conjointly; c) Final stage of seizure, where conjoint deformation of all the asperities occurs at all sites of seizure (Bhushan 2013)

The values of Young's modulus and hardness appear to be a function of penetration depth. For relatively small indentation depths, a wide range of these two values is observed, whereas such scattering becomes moderately predictable for increasing indentation depths (Fig. 2.1.5.5, Nadukuru 2013). As part of preparing samples for testing in Nadukuru (2013) grain surfaces were polished using polishing compounds to achieve average particle sizes of 250 nm. These sizes were assumed to be of the same order of magnitude as the mean average height of asperities.

The data of Fig. 2.1.5.5, for indentation depths less than 250 nm, may not be representative of the material properties of the quartz. As the indentation depths approach the scale of microscopic asperity (~1 nm), the values tend to be in agreement with test data reported in other studies. For example, Daphalapurkar et al. (2011) performed 500 nanoindentation tests on 250 quartz grains collected from Stillwater Lake in Oklahoma: mean values of Young's modulus, hardness, and fracture toughness were found to be 91.1 GPa, 10.7 GPa, and 1.77 MPa-m^{0.5}, respectively.

Fracture toughness is the ability of a material with a crack to resist fracture. The low fracture toughness value for quartz indicates that the grains are more susceptible to undergo brittle fracture rather than ductile failure. For comparison, the fracture toughness of mild steel is 50 MPa-m^{0.5}, and that of normal strength concrete is 1.4 MPa-m^{0.5}. Considering force-deformation relationships to be scale-dependent, nanoindentation techniques for determining elastic properties of granular particles are valuable in capturing deformation at the microscopic scale. At grain-size scales, the tensile strengths of grains tend to decrease as the sizes of grains increase (Table 2.1.5.4).

Because capturing the behaviors associated with contact between two grains is central to the proposed hypothesis of DEM in modeling at the grain-size scale, the variability in grain minerals (specifically, quartz) mechanical properties and the complexity of the surface morphology are not further investigated. Nonetheless, qualitative quantification of the grain surface morphology is performed over a range of values to explore the intrinsic coefficient of friction in relation to contact loading. Whether or not the asperities on grain surfaces are prone to plastic deformation or brittle failure is still a matter of debate. Further, in-depth data analysis on SEM and AFM of microscopic surface textures seems to be necessary to stochastically determine the degrees of adhesion through shearing mechanisms. Exploring these contributing factors to the intrinsic coefficient of friction, as more data become available from the literature, is beyond the scope of the current study.

Ongoing efforts to advance the modeling of granular materials using the DEM are maintained by researchers in the Computer Laboratory for Granular Physics Studies (CL-GPS) at the University of Florida, where such efforts are currently aimed at conducting detailed stochastic analysis of intrinsic friction on various types of sand grains. As facilitation of these efforts, CL-GPS possesses priority access to 256 processing cores of the 21,000 core UF HPC cluster. Currently, these cores draw upon 16-core AMD Opteron 6378 processors, and 2 GB of RAM is available per core. The CL-GPS collaborates with the developers of LS-DYNA (LSTC 2014b) to test new DEM-specific features within the LS-DYNA multi-physics simulation software.

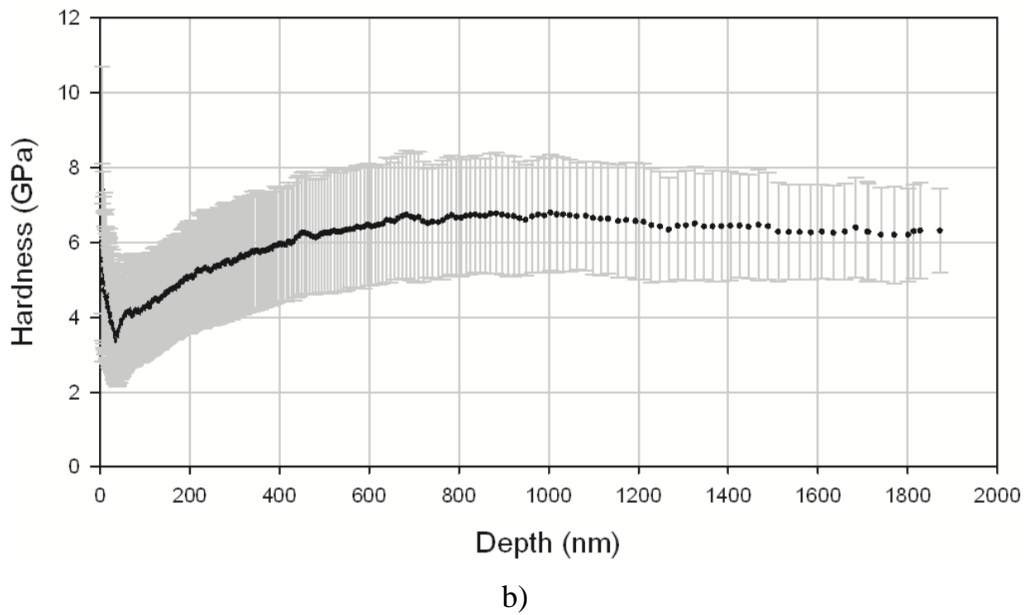
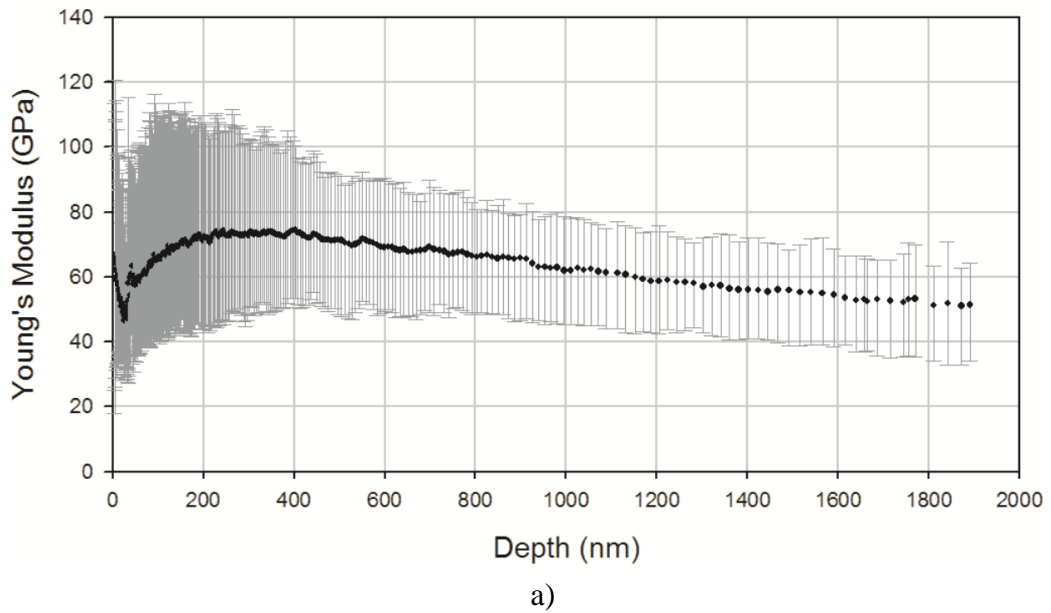


Figure 2.1.5.5. Indentation test results: a) Young's modulus of sand grains as a function of depth, obtained from 33 indentation tests; b) Indentation hardness of sand grains from 33 tests on 11 sand grains (Huron River and Ottawa 20-30 sand) (Nadukuru 2013)

Table 2.1.5.1. Mean surface roughness values of quartz grains (Lieu 2013)

Order	Type	Mean value (nm)	Standard deviation (nm)	Min value (nm)	Max value (nm)
1	illite-chlorite	34.03	27.88	2.42	134
2	chlorite	22.4	8.49	6.22	30.7
3	illite	18.44	11.31	2.24	46.1
4	authigenic quartz	35.63	26.62	12.26	92
5	quartz	14.19	9.37	3.62	29.3
6	calcite	45.62	31.39	15.4	89
7	halite-illite	28.72	22.74	10.5	61.5
8	anhydrite	24.55	5.44	20.7	28.4

Table 2.1.5.2. Surface energies of quartz (Parks 1984)

Sample Description ^a	Method ^b	Environment	Temperature °C	P ^c	Q _f , J m ⁻²	Source
Natural Quartz (Brazil, B; Madagascar, M)						
B {11 $\bar{2}$ 0}	OGC	air	RT	--	0.76	Brace and Walsh [1962]
{10 $\bar{1}$ 1}	OGC	air	RT	--	0.28 to 0.57	
{ $\bar{1}$ 011}	OGC	air	RT	--	0.46 to 0.53	
{10 $\bar{1}$ 0}	OGC	air	RT	--	0.83 to 1.2	
? {? }	Tn	air	25	--	2.	Ball and Payne [1976]
M {? }	Hz	air	20	100	--	Hartley and Wilshaw [1973]
B {? }	Hz	air	20	485	--	
Synthetic Quartz						
{10 $\bar{1}$ 1}	3PB	air	20	--	11.5	Hartley and Wilshaw [1973]
n {01 $\bar{1}$ 1} ^e	DT	air?	20	--	3.49	Atkinson [1979]
n {10 $\bar{1}$ 1}	DT	air	20	--	4.83	
{1010}	VI	air	20	--	1.34	Atkinson [this issue]
{0001}	VI	air	20	--	0.46	

Table 2.1.5.3. Elastic properties of mineral granules (Santamarina et al. 2001)

Material	Young's Modulus (GPa)	Shear Modulus (GPa)	Poisson's Ratio
Quartz	76	29	0.31
Limestone	2 – 97	1.6 – 38	0.01 – 0.32
Basalt	25 – 183	3 – 27	0.09 – 0.35
Granite	10 – 86	7 – 70	0.00 – 0.30
Hematite	67 – 200	27 – 78	—
Magnetite	31	19	—
Shale	0.4 – 68	5 – 30	0.01 – 0.34

Table 2.1.5.4. Values of microscopic angles of friction for various minerals (Mitchell and Soga 2005)

Mineral	Type of Test	Conditions	ϕ_r (deg)	Comments	Reference
Quartz	Block over particle set in mortar	Dry	6	Dried over CaCl ₂ before testing	Tschebotarioff and Welch (1948)
		Moist	24.5		
		Water saturated	24.5		
Quartz	Three fixed particles over block	Water saturated	21.7	Normal load per particle increasing from 1 g to 100 g	Hafiz (1950)
Quartz	Block on block	Dry	7.4	Polished surfaces	Horn and Deere (1962)
		Water saturated	24.2		
Quartz	Particles on polished block	Water saturated	22–31	ϕ decreasing with increasing particle size	Rowe (1962)
Quartz	Block on block	Variable	0–45	Depends on roughness and cleanliness	Bromwell (1966)
Quartz	Particle–particle	Saturated	26	Single-point contact	Procter and Barton (1974)
		Particle–plane	22.2		
		Particle–plane	17.4		
Feldspar	Block on block	Dry	6.8	Polished surfaces	Horn and Deere (1962)
		Water saturated	37.6		
Feldspar	Free particles on flat surface	Water saturated	37	25–500 sieve	Lee (1966)
Feldspar	Particle–plane	Saturated	28.9	Single-point contact	Procter and Barton (1974)
Calcite	Block on block	Dry	8.0	Polished surfaces	Horn and Deere (1962)
		Water saturated	34.2		
		Dry	23.3		
Muscovite	Along cleavage faces	Dry	16.7	Oven dry	Horn and Deere (1962)
		Saturated	13.0	Air equilibrated	
Phlogopite	Along cleavage faces	Dry	17.2	Oven dry	Horn and Deere (1962)
		Dry	14.0	Air equilibrated	
		Saturated	8.5		
Biotite	Along cleavage faces	Dry	17.2	Oven dry	Horn and Deere (1962)
		Dry	14.6	Air equilibrated	
		Saturated	7.4		
Chlorite	Along cleavage faces	Dry	27.9	Oven dry	Horn and Deere (1962)
		Dry	19.3	Air equilibrated	
		Saturated	12.4		

A more general expression of Eqn. 2.1.5.12 can be rewritten as:

$$\mu_0^i = \lambda_i \tan(\langle \theta \rangle_i) \quad (2.1.5.13)$$

where μ_0^i is the intrinsic coefficient of friction in the directions of sliding ($i = x, y$) on the contact surface (Fig. 2.1.5.6a); λ_i is defined as the adhesion factor of the i th-direction, per the statistical distribution of asperity heights for the contact surface (Fig. 2.1.5.6b); and, $\langle \theta \rangle_i$ is the mean average value of the statistical distribution of slopes of asperities for a scan surface, and represents microscopic angles of friction per directional roughness (Fig. 2.1.5.6c).

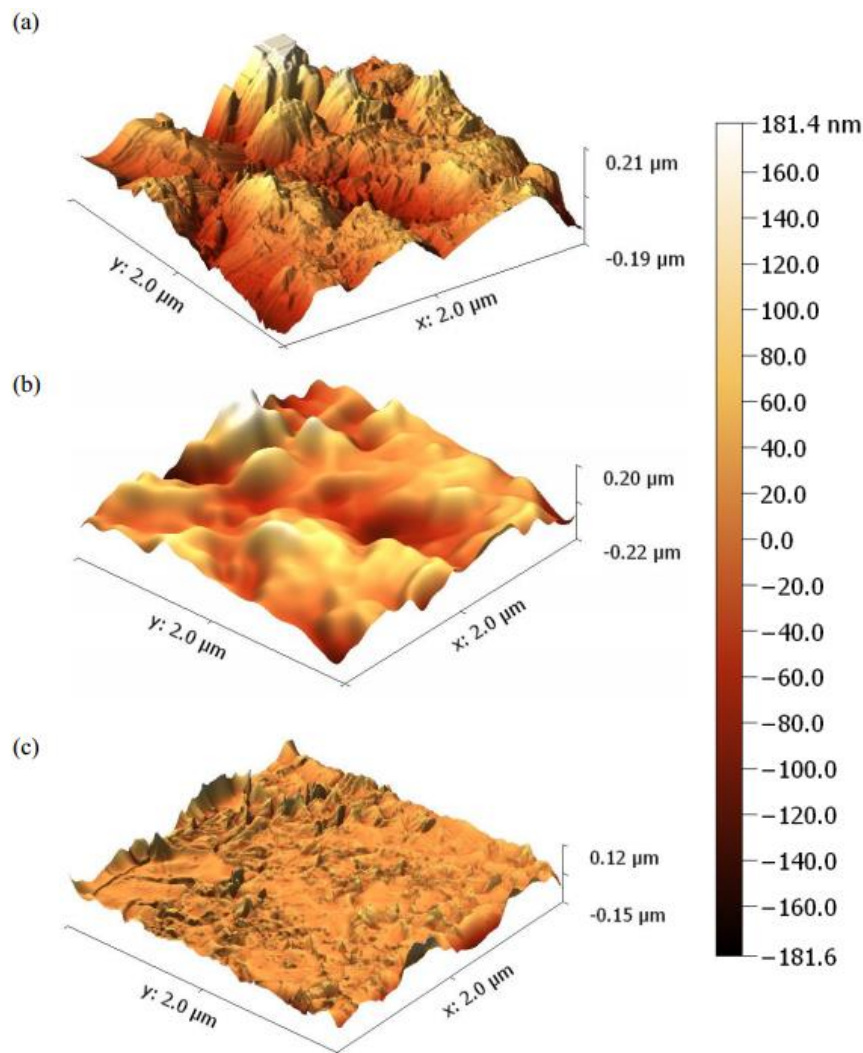


Figure 2.1.5.6. 2-D Fourier transformation analysis on the surface of an Ottawa 20-30 sand grain: a) Surface texture; b) Waviness of the surface (low frequency components); c) Roughness of the surface due to asperities (high frequency components) (Nadukuru 2013)

To facilitate physical interpretation of Eqn. 2.1.5.13, the authors use Archard's schematic sketch of surface protuberances (Archard 1957) in combination with measured data on a sand grain (Nadukuru 2013) as shown in Fig. 2.1.5.7. Consider a body of granular mass conforming a spherical volume with an average radius of curvature R_1 . More specifically, the macroscopic surface texture of the spherical body is represented by an amplitude of R_1 , with a (macroscopic) surface potential described by Prandtl-Tomlinson Theory of Dry Friction (Popov and Gray 2012).

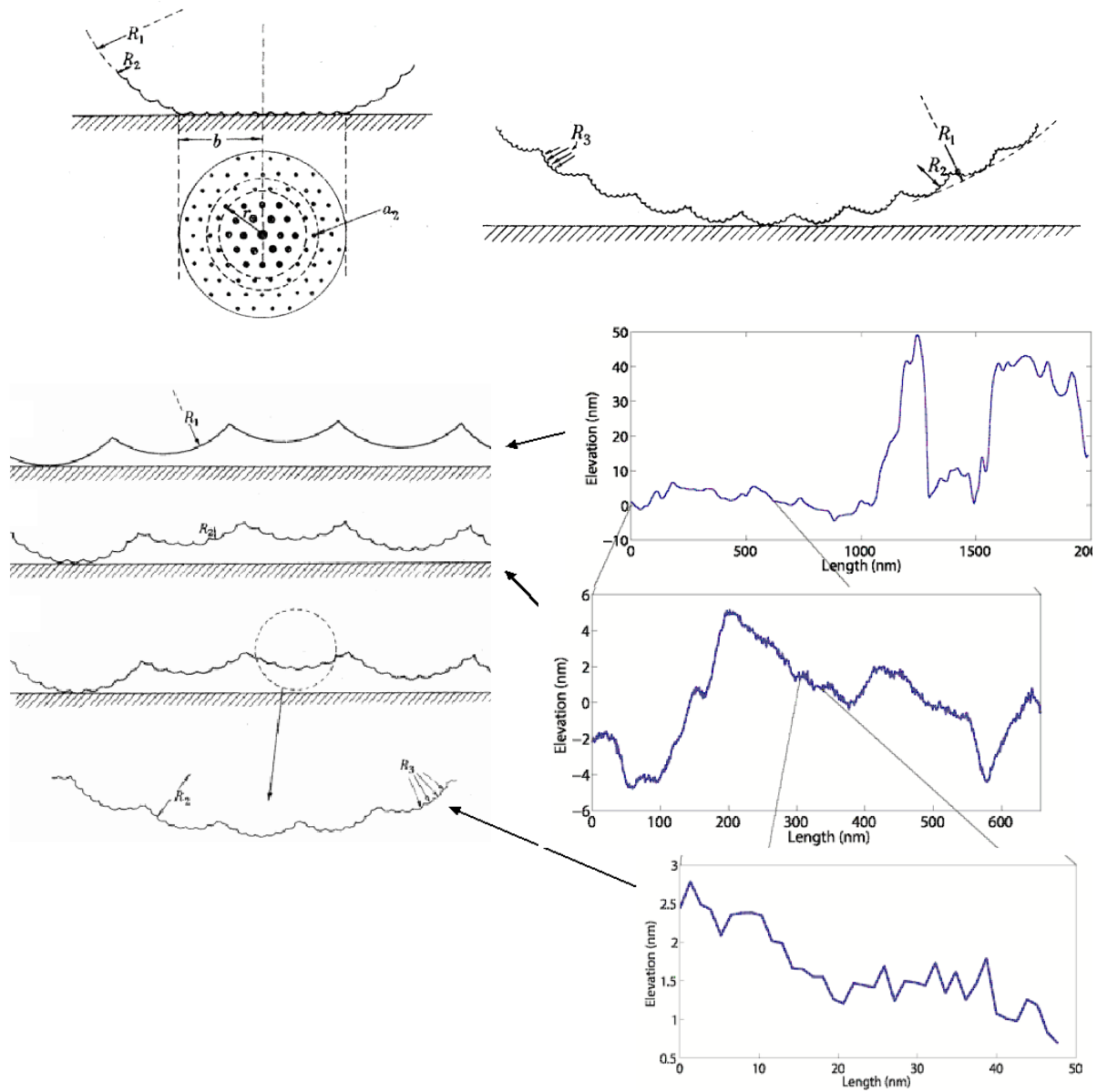


Figure 2.1.5.7. Schematic sketches of frictional phenomena at three scales for $R_1 \gg R_2 \gg R_3$ (left) and measured tomographic data for the sand grain from Fig. 2.1.5.6 (right)

On the macroscopic surface, an intrinsic radius of curvature R_2 is perturbed to represent the mean average value of microscopic angles of friction. In other words, the microscopic angles of friction are represented by $\langle \theta \rangle_i$ from Eqn. 2.1.5.13, and the mean average angle of AFM data (e.g., Fig. 2.1.5.8). The grain surface contains even smaller protuberances, with radius of curvature R_3 , which can either deform plastically or undergo brittle fracture in modes of shear failure. The third radius of curvature produces the effect of energy dissipation, and contributes to the intrinsic coefficient of friction.

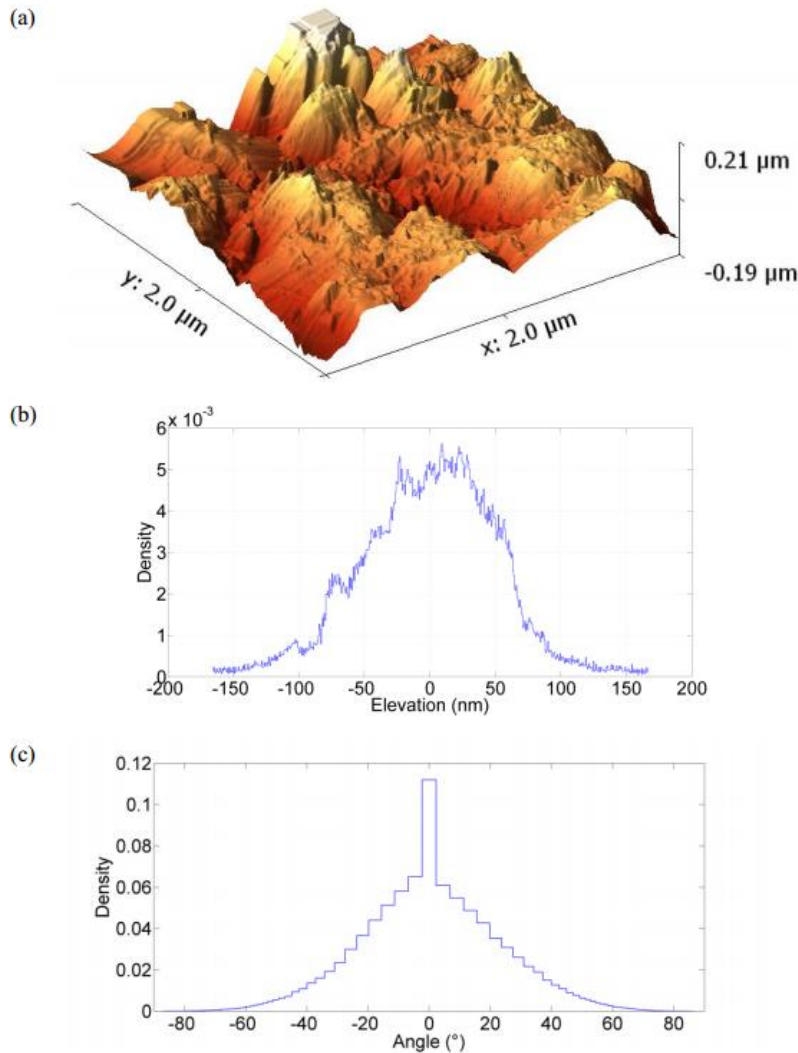


Figure 2.1.5.8. AFM analysis on a grain of Fig. 2.1.5.6: a) 3D AFM image of a 2 x 2 μm area on grain surface; b) Statistical distribution of asperity heights for the entire scan surface; c) Statistical distribution of slopes of asperities for the entire scan surface (Nadukuru 2013)

Based on a review of the morphology of types of sand grains, it appears that differences in micro surface textures may stem from mineralogy (crystalline growth as shown in Fig. 2.1.5.1b) and/or due to the process of weathering (abrasion fatigue). It is evident that weathering processes produce

microscopic abrasions on asperities, which significantly lowers the value of λ_i , and effectively reduces $\langle \theta \rangle_i$. The effects of weathering, in this context, are shown in Fig. 2.1.5.9a (Helland and Homes 1997) and Fig. 2.1.5.9b (Krinsley et al. 2015). These effects lead to smoother, smaller and more rounded grains (Fig. 2.1.5.9c, Helland et al. 1997) as compared to young, fresh quartz grains (e.g., crushed from sandstone, Ottawa types) (Krinsley and Doornkamp 1973, Lieu 2013, Nadukuru 2013).

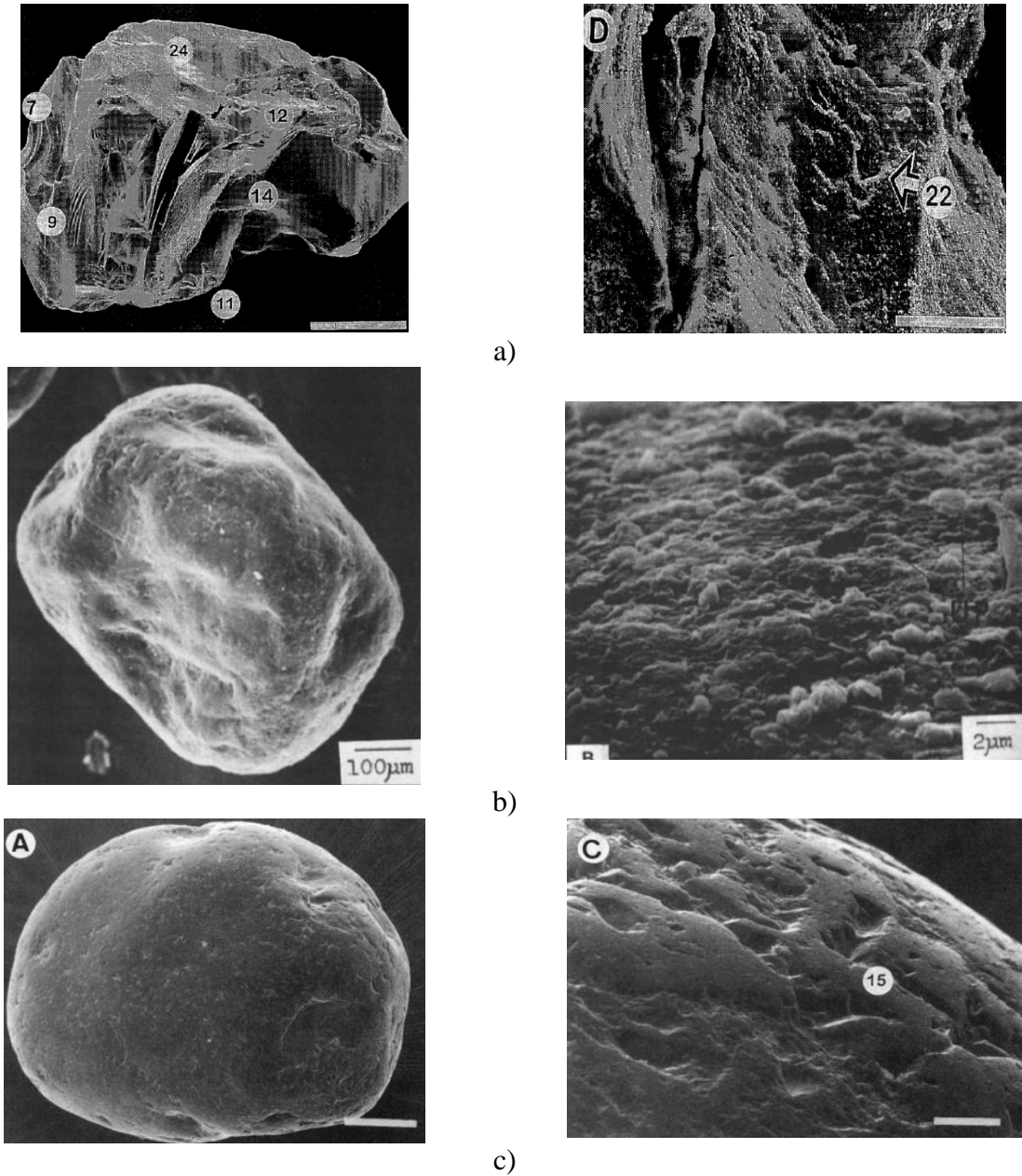


Figure 2.1.5.9. SEM analysis of quartz grains: a) Diameter ~0.55 mm (scale bar = 100 μm) with rough surface texture (scan size = 10 μm); b) Diameter ~0.8 mm with fairly smooth surface texture; c) Diameter ~0.6 mm (scale bar = 100 μm) with smooth surface (scale size = 25 μm)

In summary, factors affecting frictional phenomena at the microscopic and nanoscopic scales are:

1. *Levels of Normal Force Acting on Granules' Contacts*: Per Amonton's first law of friction, wherein the friction force is considered to be proportional to the normal force, it has been assumed that a constant friction coefficient is independent of normal load. However, degrees of plastic deformation at the contacts of asperities may define a microscopic contact area between two grains. In the preceding analysis, we focused on averaged frictional resistance due to adhesion (shearing multiple asperities in contacts). Accordingly, two scenarios involving micro contact mechanisms arise. First, as the contact normal load increases, the number of contacting asperities remains constant and the elastic deformation of each asperity increases. Further, in this first scenario, the contact area of the pairing grains is proportional to $N^{2/3}$ (Archard 1957 and Radchik et al. 2002) per Hertzian Contact Theory (note that the contact theories of Hertz and Mindlin are discussed in detail later in Ch. 2). In the second scenario, as the contact normal load increases, the number of contacting asperities increases proportionally, and the deformation of each asperity remains virtually constant. As a result, the contact area is proportional to N . If we write the contact area to vary as N^n , then the contact area of quartz grains may be expected to fall within the range of $n = \{2/3, 1\}$ for either elastic-plastic and perfectly elastic deformation of asperities, respectively. For instance, analysis of plastic behaviors of asperities is not correct for a perfectly elastic solid such as diamond, and would be more appropriate for metals. Apparently, the behavior of quartz falls somewhere between these two extremes.
2. *Surface Conditions on Granules*: Microscopic surfaces can become contaminated by adsorbed gases, dust, and organic compounds. At contact surfaces, the deformation of asperities, i.e., the shear strength of the contact, will be influenced by the type and degrees of contaminants adsorbed onto the surfaces. Also, loading history (wind and water loads) on granules affects surface roughness of grains (i.e., the height distribution of asperities). Thus, measured values of the intrinsic coefficient of friction can vary widely depending upon surface cleanliness, sedimentary history, and environmental conditions to which grains may have been exposed.
3. *Hardness and Adhesion of Quartz and Brittle Materials*: Brittle materials do not possess appreciable tensile strength. Therefore, indentation hardness tests are relevant to the geometric contacts of the contacting asperities. Indentation hardness is measured as the normal force divided by the residual area of deformation after the indenter is removed. For contact normal stress less than the indentation hardness, asperities deform elastically. When the stress exceeds the hardness, the asperities in contact deform plastically. For quartz, yield stresses on coarse grains with diameters greater than 100 μm and less than 2 mm can be approximated to be equal to one third of the mean tensile strengths, ranging from 40 MPa to 150 MPa (Table 2.1.5.1). However, at the microscopic scale (sizes of asperity), the indentation hardness can reach 10 GPa. Thus, "cold welding" phenomena would probably not be prevalent on shearing in the contact surface of quartz granules, unless the granules were subjected to an ultra-high pressure (to cause yielding) and/or high temperatures (to cause softening). Instead, brittle fracture

around, within, and between asperities would probably be a predominant shearing mechanism, which may have been previously viewed to be yielding on the contact surface of grains from a macroscopic perspective.

The coefficient of friction of quartz can be very low, ranging from 0.1 to 0.2, when surfaces are polished and measured under dry conditions (Horn 1961). When the surfaces are submerged in water, the coefficient increases by a factor of three to four (Horn and Deere 1962). For example, measured friction coefficients were 0.53 for air-dried conditions and 0.71 for submerged conditions. According to Horn (1961), the prevalence of smooth surfaces under air-dried conditions was the result of adsorbed molecules of air acting as a highly effective lubricant. Water can disrupt the orientation of this boundary layer, leading to higher values of the coefficient (Bromwell 1966). Sjaastad (1963) reported similar experimental results such that the coefficient of dry quartz was found to vary from 0.33 (at ambient conditions) to 0.6 (measured in a vacuum). One difference in sample preparation between the tests conducted by Horn (1961) relative to those of Sjaastad (1963) was that Sjaastad soaked quartz grains in benzene and acetone, whereas Horn wiped the surfaces with an acetone-soaked piece of cotton. Presumably, Sjaastad's granules had a higher degree of surface cleanliness. The highest measured values of the coefficient in the air-dried conditions was 0.77 for quartz and 0.94 for glass (Hardy and Doubleday 1922). Rougher surface textures resulted in development of greater shear stresses. Thus, higher values of μ_0 were observed, which is a function of maximum shear stress acting on an actual contact area (i.e., total area of all contact surfaces among asperities), as shown in Fig. 2.1.5.10.

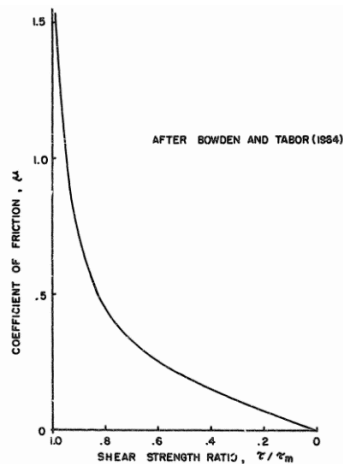


Figure 2.1.5.10. Shear strength ratio versus coefficient of friction (after Bowden and Tabor 1954, Bromwell 1966)

Other historical measured values of angle of friction for earth minerals are summarized in Table 2.1.5.5, where the arctangent of μ_0 is referred to as ϕ_μ . This quantity (ϕ_μ), has been used in many soil mechanics textbooks as if it were an intrinsic friction parameter associated with the surface roughness of grains. However, empirical values of ϕ_μ have been estimated under various levels of normal loads applied on contacting grains, height distributions of asperities, degrees of surface contamination, degrees of weathering, and thus, the measured values of ϕ_μ listed in the Table 2.1.5.5 vary over a wide range ($0 \leq \phi_\mu \leq 45^\circ$). A physical maximum of the coefficient appears to

be, thus, approximately on the order of unity. However, for scenarios where significant plastic deformation takes place (in contact asperities subjected to high normal pressures), the value can exceed the order of unity, which was experimentally tested in the recent years (Shellenberger and Logan 2002). In the following section, we discuss macroscopic surface texture formed by multiple grain contacts and how such textures may also contribute to the scale-dependent coefficient of friction. Subsequently, we will evaluate a range of values of the macroscopic factors for later use in determining frictional input parameters for use in conjunction with the DEM.

Table 2.1.5.5. Angles of friction (microscopic) for minerals (Mitchell and Soga 2005)

Mineral	Type of Test	Conditions	ϕ_{μ} (deg)	Comments	Reference
Quartz	Block over particle set in mortar	Dry	6	Dried over CaCl ₂ before testing	Tschebotarioff and Welch (1948)
		Moist	24.5		
		Water saturated	24.5		
Quartz	Three fixed particles over block	Water saturated	21.7	Normal load per particle increasing from 1 g to 100 g	Hafiz (1950)
Quartz	Block on block	Dry	7.4	Polished surfaces	Horn and Deere (1962)
		Water saturated	24.2		
Quartz	Particles on polished block	Water saturated	22–31	ϕ decreasing with increasing particle size	Rowe (1962)
Quartz	Block on block	Variable	0–45	Depends on roughness and cleanliness	Bromwell (1966)
Quartz	Particle–particle	Saturated	26	Single-point contact	Procter and Barton (1974)
		Particle–plane	22.2		
		Particle–plane	17.4		
Feldspar	Block on block	Dry	6.8	Polished surfaces	Horn and Deere (1962)
		Water saturated	37.6		
Feldspar	Free particles on flat surface	Water saturated	37	25–500 sieve	Lee (1966)
Feldspar	Particle–plane	Saturated	28.9	Single-point contact	Procter and Barton (1974)
Calcite	Block on block	Dry	8.0	Polished surfaces	Horn and Deere (1962)
		Water saturated	34.2		
Muscovite	Along cleavage faces	Dry	23.3	Oven dry	Horn and Deere (1962)
		Dry	16.7	Air equilibrated	
		Saturated	13.0		
Phlogopite	Along cleavage faces	Dry	17.2	Oven dry	Horn and Deere (1962)
		Dry	14.0	Air equilibrated	
Biotite	Along cleavage faces	Saturated	8.5		Horn and Deere (1962)
		Dry	17.2	Oven dry	
Chlorite	Along cleavage faces	Dry	14.6	Air equilibrated	Horn and Deere (1962)
		Saturated	7.4		
		Dry	27.9	Oven dry	
		Dry	19.3	Air equilibrated	
		Saturated	12.4		

2.1.6 Factors Affecting Frictional Resistance at Macroscopic Scales

The macroscopic texture of the granular mass stems from its particulate nature, which represents collective geometric particle characteristics and the resulting arrangements of particles. The most important macroscale characteristic is the volumetric density distribution, which relates to the statistics of particle shape, size distribution, and spatial arrangement of particles (Santamarina et al. 2001). These geometric parameters are briefly reviewed in order of significance, with respect to macroscopic surface texture. The corresponding relevance of each parameter (in transitioning to considerations for numerical modeling of DSEs) is discussed afterward.

Size

Quantifying representative grain sizes has previously been carried out in many ways, for example, by making use of the: 1) Diameter of a circle with equal projected area; 2) Dimensions of the grain in several directions; 3) Opening of the finest sieve that a grain passes through; and, 4) Mean diameter. Grain size is often used to classify soils as gravels, sands, silts, or clays although various classification systems, which mutually differ in the particle sizes categorization, as part of assigning soil denominations. A statistical means of characterizing granule diameters has also been used (Fig. 2.1.6.1).

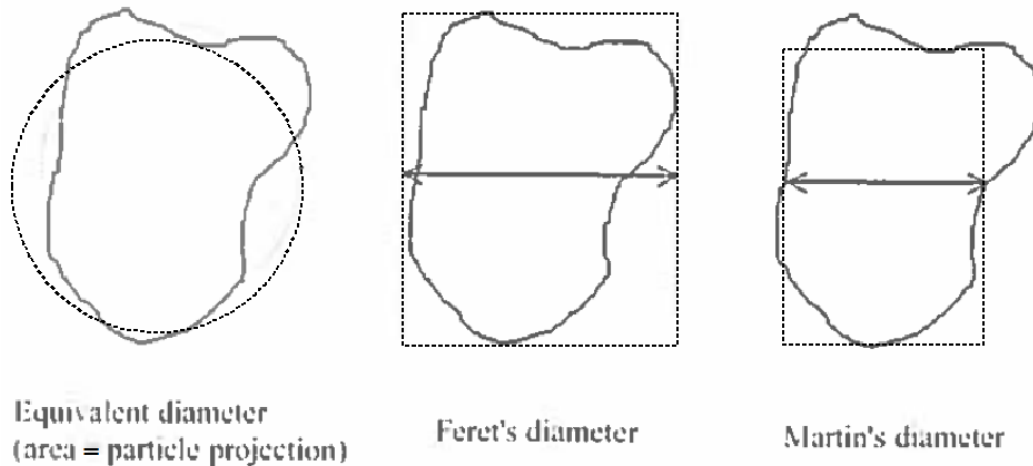


Figure 2.1.6.1. Alternative definitions of particle diameter (Santamarina et al. 2001)

Sphericity, Roundness, and Angularity

Sphericity is an index that indicates the extent to which dimensions of the particle are of the same order of magnitude in projected planes, for three orthogonal directions. Physical quantification is the ratio of the surface area of a sphere of equal volume to the surface area of the particle. Based on the definition of particle size using an equivalent diameter, a definition of sphericity could be given as the ratio of the area of the particle projection to the area of the circle with diameter equal to the longest length of projection called 'projection sphericity'. Elliptical particles can be further characterized by eccentricity and slenderness. In 3-D, elongation and

flatness per axis ratios are additionally needed to characterize preferential directions of anisotropic particle assembly, which will be discussed after a brief summary of the geometric characteristics of grains. Note that an ellipsoid has higher degrees of roundness yet lower sphericity. Pictorial comparisons between roundness and sphericity are shown in Table 2.1.6.1.

Table 2.1.6.1. Rounded particle slenderness and eccentricity (Santamarina et al. 2001)

Shape					
Slenderness	5.0	2.5	1.67	1.25	1.0
Eccentricity	0.67	0.43	0.25	0.11	0

The roundness of a particle is a measure of the curvature of the corners and edges expressed as a ratio of the average curvature of the particle as a whole, independent of its form. For practical purposes, an average of radius of curvature is used in terms of the inscribed circle drawn on a projection of the particle over a maximum radius that can be inscribed in a plane (Fig. 2.1.6.2).

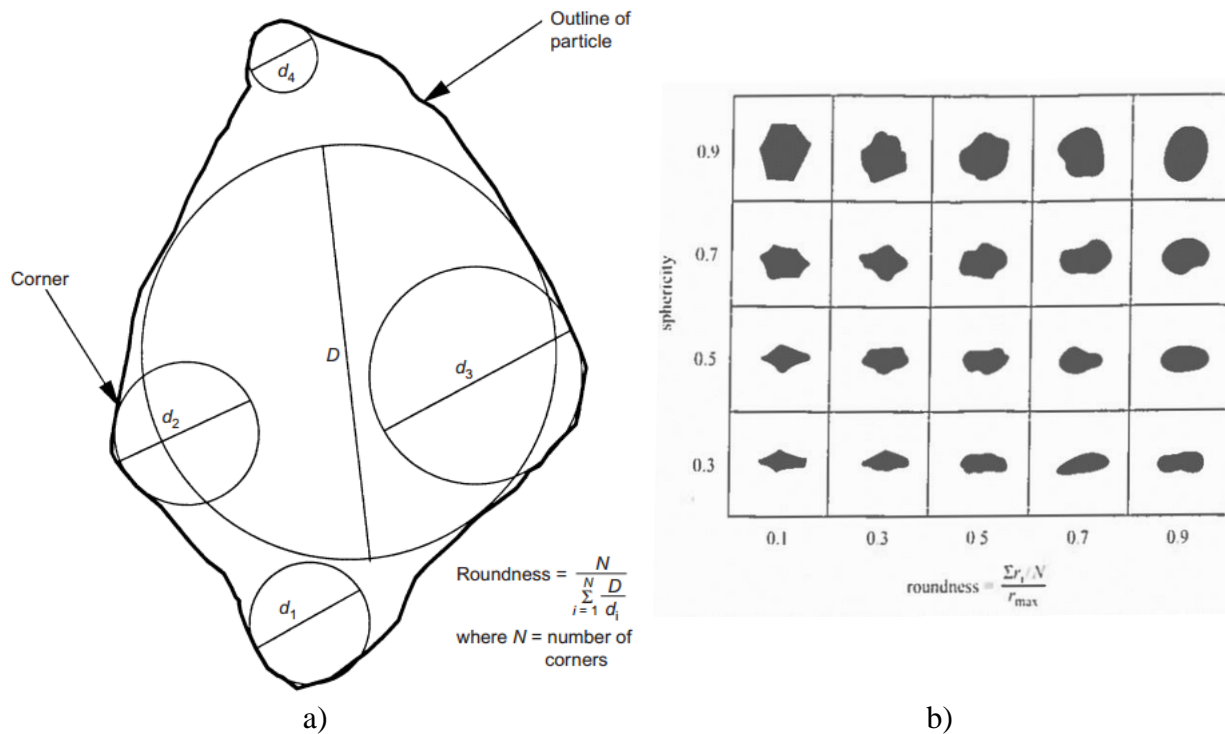


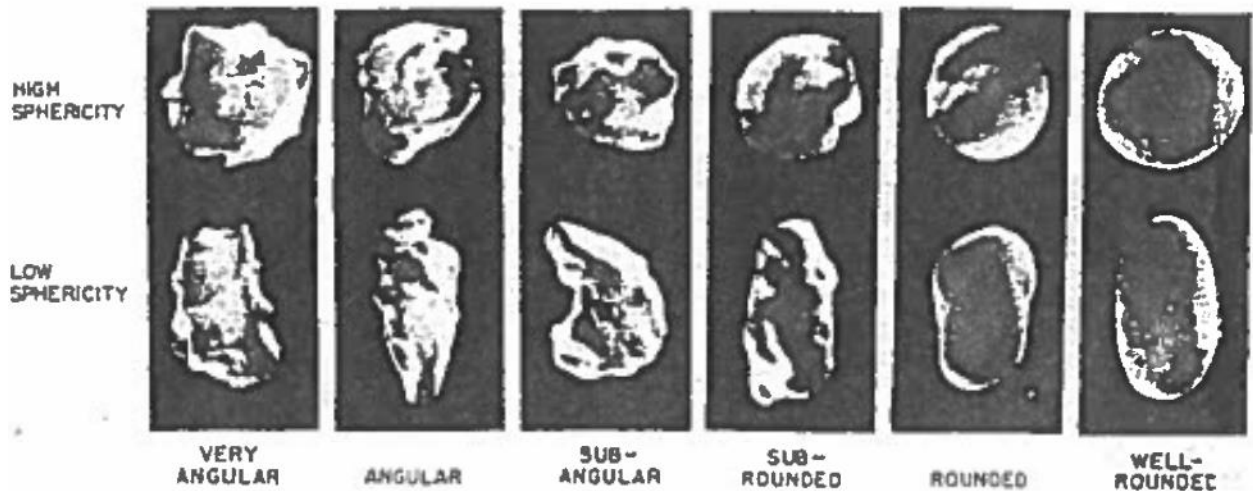
Figure 2.1.6.2. Particle roundness and sphericity: a) Illustration of Wadell's (1932) evaluation of particle roundness (from Sukumaran, and Ashmawy 2001); b) Relationship between roundness and sphericity with visual estimation of particle silhouettes (Krumbein and Silos 1963)

Wadell (1932) was the first to use a mathematical expression to quantify 'shape', which he coined as 'sphericity'. Note that terms 'shape' and 'sphericity' are distinct from the term 'roundness'. The shape of a particle is its form, entirely independent of whether the edges or corners are sharp or round. Fundamentally, the shape is a measure of the ratio of the surface area of a particle to its volume. This ratio reaches at a minimum for spheres. Also, the ratio indicates how closely or remotely the particle approaches the form of a sphere. For practical purposes, the ratio is difficult to measure, and thus, the actual measurement is taken as the ratio of the volume of the particle to the volume of its circumscribing sphere. The cube root of this ratio is called the 'sphericity' of the particle (Krumblein 1941).

Recall that 'roundness' is distinct from 'sphericity'. When roundness equals to 1.0, the particle is a sphere. Angularity is opposite to roundness, and as particles become more angular, roundness approaches zero (Fig. 2.1.6.3a). Fig. 2.1.6.3b shows differences in the particle profiles with respect to sphericity, angularity, and roundness.

Grade term	Russell and Taylor		Pettijohn	
	Class Limits	Arithmetic Mid-Point	Class Limits	Geometric Mid-Point
Angular	0 to 0.15	0.075	0 to 0.15	0.125
Subangular	0.15 to 0.30	0.225	0.15 to 0.25	0.200
Subrounded	0.30 to 0.50	0.400	0.25 to 0.40	0.315
Rounded	0.50 to 0.70	0.600	0.40 to 0.60	0.500
Well rounded	0.70 to 1.00	0.850	0.60 to 1.00	0.800

a)



b)

Figure 2.1.6.3. Example of particle shape characterization (from Powers 1953): a) Roundness grades; b) Roundness scale

2.1.7 Discrete Sphere Elements (DSEs) and Model Parameters

The application of soft particle dynamic analysis models to granular soil mechanics (referred to as the discrete element method, DEM, Cundall and Strack 1979) is based on spherical discretization of individual particles. The method has been widely adopted in modeling and understanding granular materials in engineering applications, where knowledge of the static and dynamic behavior of discontinuous multiple bodies is important. An in-depth description of DEM is presented later in Ch. 2.

In the DEM simulations and numerical tools developed for use in the current study, complex body shapes of individual grains (particles) of granular media are discretized (approximated) by spheroids (spherical elements), as shown in Fig. 2.1.7.1. The main criticism would appear to focus on a morphological discrepancy between a physical grain and a sphere, and resulting topological changes in the internal structure. Fundamentally, contact forces of spherical bodies may differ from variations of the contact mechanisms of irregular granular bodies, not only at the level of individual grains, but also as an assembly. Prior to rebuttal discussion, we first review the latest developments of shape descriptors as one possible alternative to modeling DSEs.

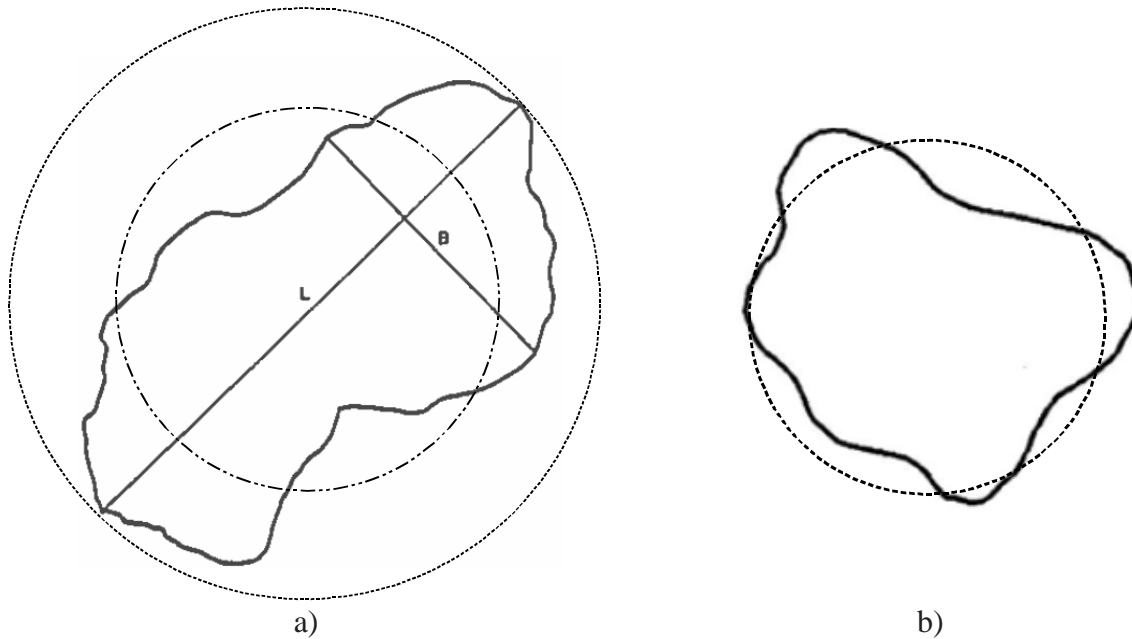


Figure 2.1.7.1. Irregularly shaped grains represented by spheroids: a) Circumscribing diameter (note that the volume of the inner sphere drawn on the larger grain is approximately the same as the volume of the particle); b) Equivalent diameters (note that the surface of the sphere drawn on the smaller grain is approximately the same as the surface area of the particle)

Improved geometric descriptors to represent complex bodies have recently been proposed. For example, composite approaches have been proposed, where simple spherical geometries or sharp-edged polygons are clustered to describe more complex shapes, and thus, result in irregular macro textures. One such approach is to only examine the portions of a given surface that conform to simple geometries, in forming complex clustered particles (Fig. 2.1.7.2a). Another example

approach is to superimpose several spherical bodies to approximate a desired irregular shape, Fig. 2.1.7.2b, per Fourier transformation analysis. By overlapping several spheres, tablet shaped particles can be created. A cylindrical main body, with attached spheres at both ends or ellipsoid-like particles (via replacing the cylinder with a torus), has also been investigated for use in discrete element analysis. Summarily, if a more general shape descriptor is desired, then various geometries (comprised of several constrained spherical elements) may be superimposed to form a new complex particle. Moreover, composite discrete elements that vary in size can be applied to the generation of macro contact surfaces, which in turn, exhibit local variations in element-level density allocation.

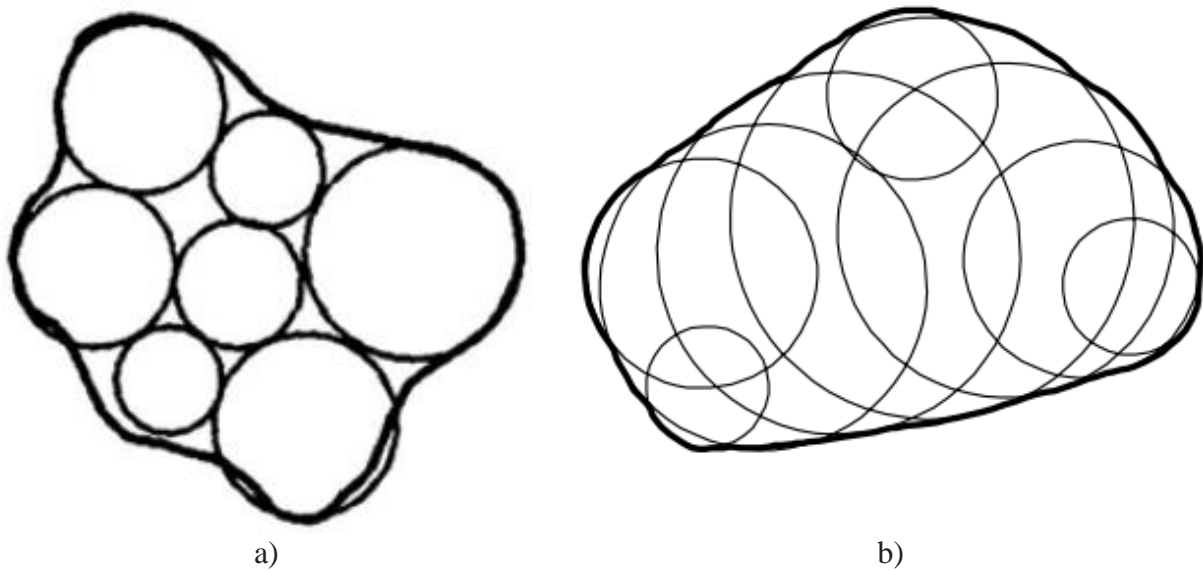


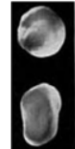
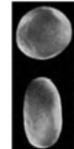
Figure 2.1.7.2. Formation of irregular shapes of discrete elements: a) Clustered discrete element (the solid line inscribing the clustered circles represents a silhouette surface of a grain; b) Discrete volume of superimposed spheres

Advancement on shape descriptors of DEM permits unanswered questions to be addressed, and can enhance the fidelity of results obtained from DSE simulations. However, careful consideration must be given to the application of multiple-composite discrete elements for modeling large-scale (megascopic) assemblies in civil engineering and design applications. Namely, the multiple-composite modeling is: 1) Computationally expensive; and, 2) Susceptible to hardware limitations. For example, if a particle size distribution of coarse-grained soil is represented for the volume of a 100 mm by 200 mm cylinder by using four different sizes of DSEs, then the total number of DSE required is approximately 3 million to 4 million. As a separate scenario, even if uniform DSEs with diameters of 5 mm were to be employed, then the total number of DSEs required to populate a volume of 6 m x 6 m x 10 m would exceed one hundred million. A factor (with value greater than unity) is, then, multiplied to the total number of DSEs required to account for composite construction of representative particle shapes. Even if possible, numerical simulation of 1 sec, for a model representing in-situ field conditions, would require several months of massively parallel processing (MPP) on the state-of-art supercomputer, and several billion DSEs. Usage of such complex shape descriptors is impractical for the purpose of this study, and unrealistic in consideration of available resources to the research team.

In order to (practically) achieve the objectives pertaining to the current numerical study, and to quantify the influence of particle shape on the intrinsic angle of friction (corresponding to R_2 of Fig. 2.1.5.6), previous experimental work has been reviewed and synthesized. Particular importance on data collection is to decouple the particle shape and size effects on shear behaviors of the granular soil. As a theoretical basis of such decoupling was established in the above portions of Ch. 2, we now specifically examine particle shape effects by comparing similar sized sieve fractions of particles chosen for their inherent morphology. In this way, a correlation of particle shape to the intrinsic angle of friction (as a function of particle shape indexes) can be drawn upon, and generalizations can be made for grains over a wide range of grain sizes.

Particle shape is a distributed parameter. As shown in Fig. 2.1.7.2, complexity of shape necessitates more laborious derivations for the corresponding descriptors, where the descriptors are needed if it is desired to more directly model surface contours to a greater degree of accuracy. Particle shape is commonly quantified in terms of two-dimensional shapes in the powder industry. One shape measure of particular interest (for simplicity and generality) is the boundary fractal dimension, which constitutes a measure of surface geometry unconstrained by the length scale. Higher angularity and lower roundness values represent higher particle surface irregularities (Russell and Taylor 1937; Krumbein 1941; Powers 1953; Alshibli and Alsaleh 2004). Also, it is well known that increasing particle irregularities increases fractal dimension (Vallejo 1995, Kolay and Kayaball 2006). Based on reviews of the aforementioned studies, the fractal dimension appears to be affected by the particle shape; fractal dimensions increase with increasing angularity or decreasing roundness of the particles. Table 2.1.7.1. is given as a reference for making correlations between fractal dimension of particles and particle shape indexes (i.e., sphericity, roundness, and angularity) per Fig. 2.1.6.3b. As a fractal dimension approaches unity, roundness increases.

Table 2.1.7.1. Fractal dimensions of granular particle shapes (Arasan et al. 2011)

Particle Images	Unnatural Particles						
Roundness Class		Very Angular	Angular	Sub-Angular	Sub-Rounded	Rounded	Well Rounded
Roundness - Cox (1927)*	< 0.50	0.5-0.65	0.65-0.70	0.70-0.75	0.75-0.77	0.77-0.80	0.80-1.00
Roundness – Russell and Taylor (1937)	-	-	0.00-0.15	0.15-0.30	0.30-0.50	0.50-0.70	0.70-1.00
Roundness – Krumbein (1941)	< 0.10	0.10-0.20	0.20-0.30	0.30-0.50	0.50-0.60	0.60-0.80	0.80-1.00
Roundness – Pettijohn (1949)	-	-	0.00-0.15	0.15-0.25	0.25-0.40	0.40-0.60	0.60-1.00
Roundness - Powers (1953)	0.00-0.12	0.12-0.17	0.17-0.25	0.25-0.35	0.35-0.49	0.49-0.70	0.70-1.00
Roundness - Al-Rousan (2004)	> 2.00	1.54-2.00	1.43-1.54	1.33-1.43	1.29-1.33	1.25-1.29	1.00-1.25
Roundness – Alshibli and Alsaleh (2004)	-	> 1.50	1.40-1.50	1.30-1.40	1.20-1.30	1.10-1.20	1.00-1.10
<i>Fractal Dimension</i>	1.70-2.00	1.55-1.70	1.40-1.55	1.30-1.40	1.25-1.30	1.15-1.25	1.00-1.15

Chan and Page (1997) reported isolated shape effects of powder particles with sizes ranging 0.1 mm to 0.2 mm, and for average boundary fractal dimensions of three unique shapes (spherical, 1.0367; irregular, 1.1173, with sub-angularity; and, dendritic 1.1618, with multiple protrusions on the surface), as shown in Fig. 2.1.7.3a. Due to the fineness of the powder particles, they considered microscopic surface roughness to be consistent among all three sampling groups.

Powder	AL180	US180	PO125
Flow rate (s per 50 g) ^a	14.5	20.5	31.5
Apparent density (g cm ⁻³) ^a	4.85	3.46	2.48
Tap density (g cm ⁻³) ^a	5.42	3.96	2.96
Hausner ratio	1.12	1.14	1.19
Average fractal dimension	1.0367	1.1173	1.1618

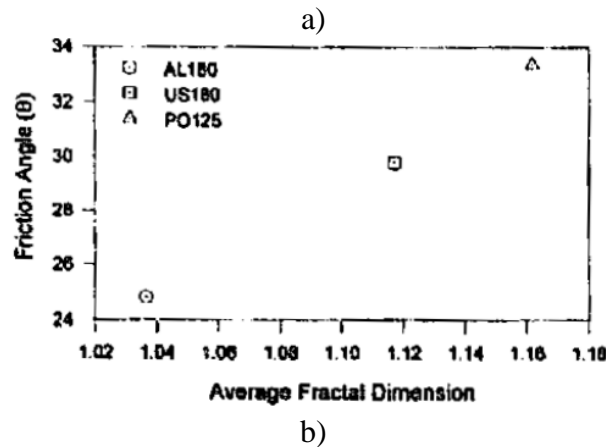


Figure 2.1.7.3. Correlations between the fractal dimension and interparticle friction angle (Chan and Page 1997): a) Particle characteristics; b) Direct ring shear test results

Based on a linear correlation between the fractal dimensions and frictional parameters in the direct ring shear cell tests of Chan and Page 1997, we write:

$$\mu_1 = \tan(\phi_{cs}^a) - \tan(\phi_{cs}^{sp}) \quad (2.1.7.1)$$

where μ_1 is a numerical friction coefficient for shape effects, ϕ_{cs}^a represents an internal friction angle of granular packing with irregular particle shapes, and ϕ_{cs}^{sp} denotes an internal friction angle of granular packing with uniform size DSE at a constant volume. Alternatively stated, μ_1 is used as a numerical parameter to simulate shape effects in scale-dependent friction (in addition to the intrinsic coefficient of friction μ_0). It is noted that the modeling concept expressed in Eqn. 2.1.7.1 is used in engineering analysis to minimize morphological errors due to spherical representation of soil grains.

Sukumaran and Ashmawy (2001) reported an observational relationship between particle shape factor and large-strain friction angles for drained specimens. Based on SEM analyses: Daytona Beach sand particles have distinct cleavage planes; Syncrude Tailings sand has a very rough texture, and is composed of irregularly shaped particles; and, Ottawa sand #60/80 particles are more rounded and less angular than the other two materials. It was further reported in Sukumaran and Ashmawy (2001) that considerable variation exists between particles in each type

of sands. From the SEM photomicrographs, Sukumaran and Ashmawy indicated that, in addition to shape and angularity, quantitation of surface texture of particles may ultimately be necessary as it varies significantly between the various materials. Their correlation between angularity factors (AF%, Fig. 2.1.7.4) in test results from Ottawa sand is consistent with the work of Chan and Page (1997).

Material	Label	D_{50} : mm	C_u	e_{max}	e_{min}
Ottawa #20/70	1	0.53	2.4	0.78	0.47
Ottawa #60/80	2	0.21	2.4	0.85	0.55
Ottawa #15 (angular)	3	1.46	1.5	1.06	0.72
Ottawa #45 (angular)	4	0.57	2.1	1.11	0.75
Ottawa #90 (angular)	5	0.27	2.2	1.10	0.73
Glass ballotini #140	6	0.17	1.4	0.72	0.34
Glass beads #10/20	7	1.18	1.0	—	—
Daytona Beach sand	8	0.23	1.4	1.00	0.64
Syncrude Tailings sand	9	0.18	2.5	1.14	0.59
Michigan Dune sand	10	0.33	1.5	0.80	0.56
Fraser River sand	11	0.30	1.9	1.13	0.78

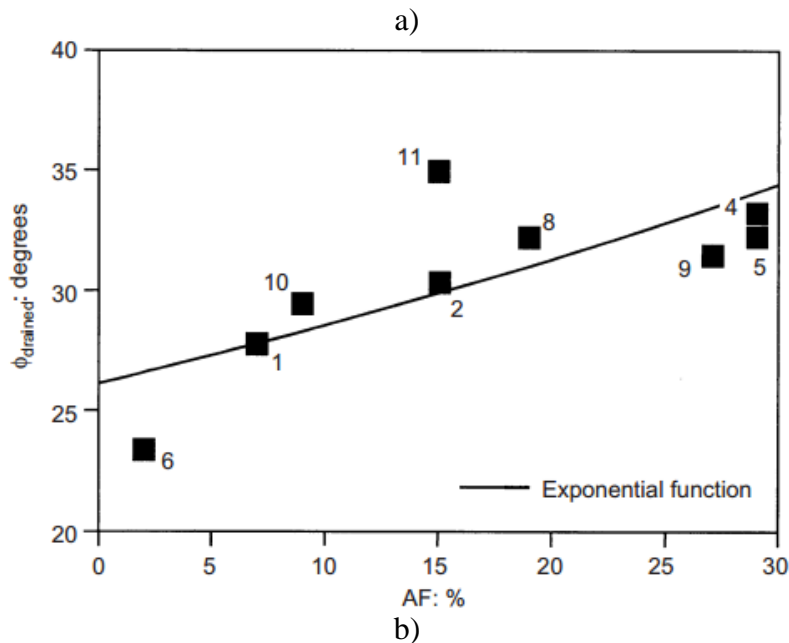


Figure 2.1.7.4. Correlation between angularity and the interparticle friction angle; for Ottawa sands, see the linear trend of the numbers, i.e., 1, 2, 4, and 5 (from Sukumaran and Ashmawy 2001): a) Material types; b) Relationship between large-strain friction angles (drained triaxial tests), shape, and angularity factors (materials labeled with numbers given in Fig. 2.1.7.4a)

In other geotechnical applications, Santamarina and Cho (2004), Fig. 2.1.7.5a, have proposed a correlation of which a greater degree of shape effects is implied:

$$\phi_{cv} = 42 - 17 \cdot R \quad (2.1.7.2)$$

where ϕ_{cv} is the internal angle of friction at constant volume, and R is a value of roundness. However, Santamarina and Cho (2004) actually used values of the angle of repose versus

roundness. As a result, Eqn. 2.1.7.2 represents a combined (coupled) effect of both shape and surface roughness, which Sukumaran and Ashmawy (2001) has also observed in correlation with shape factors (SF, an inclusive factor of angularity and surface roughness) in Fig. 2.1.7.5b.

Therefore, it is assumed, for values of μ_1 utilized in the current study, that μ_1 is bounded between 0 and 0.19, based on the correlation between angularity and constant-volume angles of friction as shown in Fig. 2.1.7.3. Anthony and Marone (2005) also reported essentially the same bound per percentage of angular grains, and the corresponding increment in the peak friction coefficient.

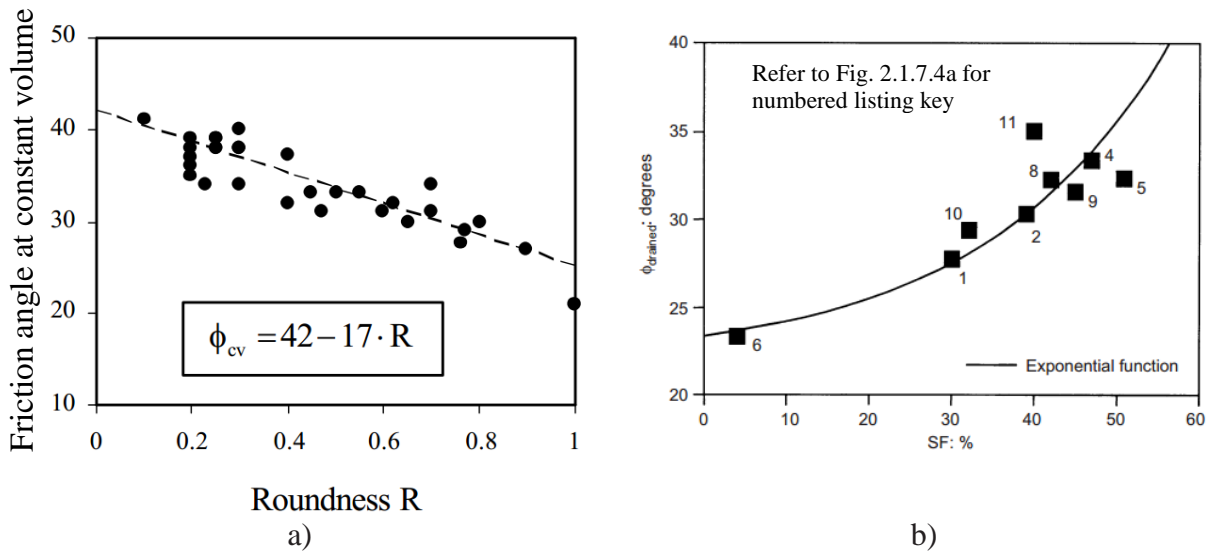


Figure 2.1.7.5. Variations in measured internal angles of friction at constant volume per angularity and roughness: a) Linear correlation between angle of repose and roundness (Santamarina and Cho 2004) (note: angle of repose was assumed equal to angle of friction at constant volume); b) Exponential correlation for coupled effects including surface roughness and angularity (Sukumaran and Ashmawy 2001)

In laboratory experiments, Mair et al. (2002) investigated the influence of grain shape, roughness, and particle size distribution on the frictional strength and stability of granular layers between roughened steel blocks. Using a controlled direct shear apparatus (Fig. 2.1.7.6a), Mair et al. (2002) observed that the macroscopic coefficient of friction varies (rather significantly) between 0.6 for angular quartz sand and 0.45 for granular materials of spherical grain (Fig. 2.1.7.6b). The friction levels of spherical beads with both narrow and broad particle size distributions were reported to be identical.

Mair et al. (2002) additionally suggested that the kinematics of angular and spherical particles behave in distinctively different manners. The associated reasoning was that spheres are highly efficient in translational movement due to preferential rolling. In contrast, angular grains at contact prohibit one another from rolling over by interlocking at the interfaces, leading to intensive tangential contact forces at sliding (refer to Fig. 2.1.7.7). The pronounced kinematical differences of granules necessitate a qualitative discussion of the process of rolling contacts, which is given below.

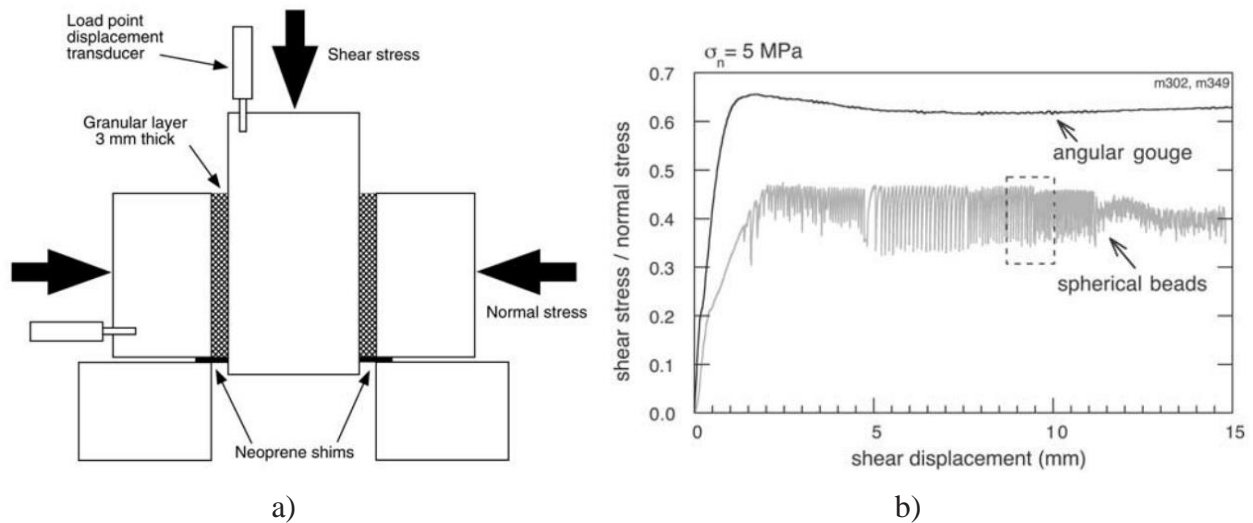


Figure 2.1.7.6. Grain shape influence on macroscopic friction (from Mair et al.2002): a) Schematic diagram of direct shear apparatus: the 100 x100 mm, 3-mm-thick granular layers sandwiched between rough steel blocks. The orientations of shear and normal stresses are specified; b) Friction as a function of shear displacement for angular and spherical grains at normal stress = 5 MPa. Spherical grains show a lower value of friction coefficient and exhibit stick-and-slip behavior, whereas angular gouge slides stably with higher friction.

Based on both experimental data and laws of physics, the origin of friction of grain contacts has been analytically reasoned from: 1) The dominant mechanism of adhesion (due to interlocking asperities) is sliding at the microscopic scale; and, 2) Frictional resistance (deriving from granular morphology) is sliding at the intermediate (grain) scale. Unlike a solid (continuum) treatment of friction, which is mainly a surface property, it is also known, both experimentally and theoretically, that shear strength increases with μ . Shear strength also mobilizes gradually in a loose packing such that mobilization appears to be independent of μ . This behavior confirms the fact that, even though sliding friction is the dominant source of dissipation in plastic flow within a bulk volume of grains, the main grain-scale mode of displacement can be the rolling of grains over one another. In turn, this rolling limits mobilized sliding friction to relatively low levels. Numerical simulations (presented in Chapter 3) also indicate that, in granular media modeled using DSEs, more pronounced tangential (sliding) contact forces occur when DSE are frustrated in rolling. These observations further suggest that the prediction of the macroscopic shear strength is substantially affected when the relative rolling is restrained by a mechanism of interlocking between the grains (or in very dense packing scenarios).

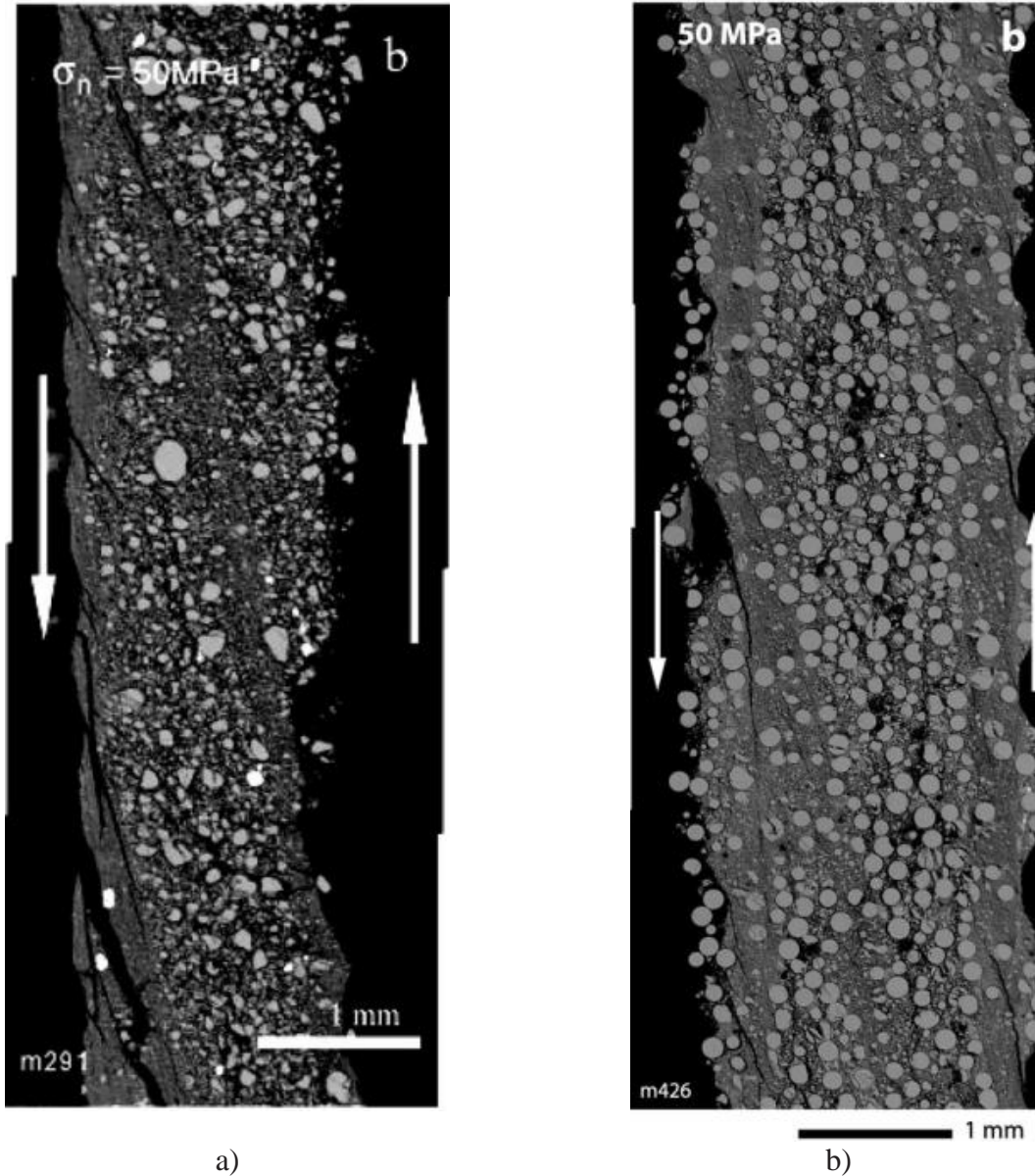


Figure 2.1.7.7. SEM images of particulate fabrics on shear surface planes (from Mair et al.2002):
 a) SEM photomicrograph of angular gouge deformed at normal stress = 50 MPa. Slip is 20 mm in both cases; b) SEM photomicrograph of spherical gouge deformed at normal stress = 50 MPa. Note development of the fabric at the shear plane due to particle size distribution.

A model of interlocking in the framework of the contact dynamics method is introduced through a *rolling friction* law. Along these lines, the relative rotations of grains correspond to the generation of a contact torque, which is proportional to the normal force. To facilitate expression of the model, a rolling friction coefficient μ_r is introduced, and is analogous to the coefficient of (sliding) friction μ . In order to simulate interlocking between DSEs, we replace the effect of non-spherical grain shapes (convex or angular) by a contact law of rolling resistance. Let us define

local kinematic variables for the relative angular velocity ω_r at the contact between two adjacent DSEs, referred to as *Particle 1* and *Particle 2* (Fig. 2.1.7.8), with angular velocities of ω_1 and ω_2 :

$$\omega_r = \omega_1 - \omega_2 \quad (2.1.7.3)$$

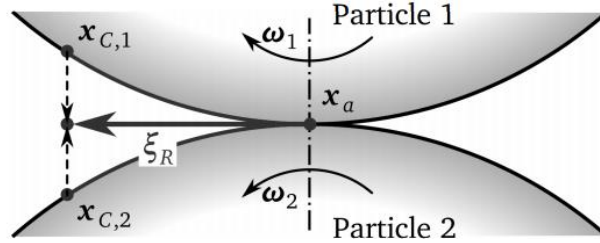


Figure 2.1.7.8. Rolling displacement caused by pure rolling motion of two elastic spheres with equal radius R

The interlocking between grains corresponds to $\omega_r = 0$. This condition requires that the torque M at the contact point does not exceed the elastic threshold of T_R (Estrada et al. 2008):

$$\begin{aligned} \omega_r > 0 & \text{ if } T = -T_R \\ \omega_r = 0 & \text{ if } -T_R < T < T_R \\ \omega_r < 0 & \text{ if } T = T_R \end{aligned} \quad (2.1.7.4)$$

Further, this mechanism allows the transmission of a torque, which can be described as rolling resistance (analogous to Coulombic sliding resistance). To determine rolling resistance with an elastic limit, we consider the effect of particle shapes in force equilibrium (Fig. 2.1.7.9).

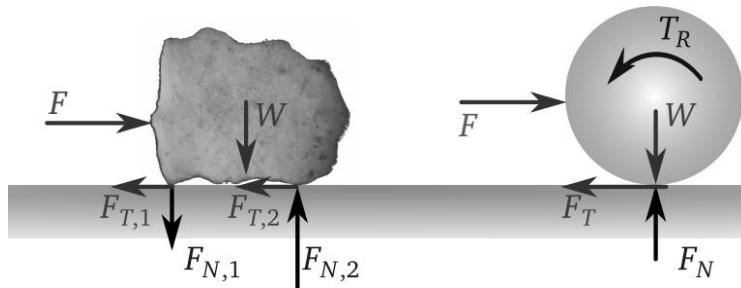


Figure 2.1.7.9. Effect of particle shape on particle rotation in force equilibrium under a lateral load

For the non-spherical particle, a force couple $F_{N,i}$ resists rolling motion of the particle. For spherical bodies, this force effect has to be imitated by a rolling resistance torque T_R . The elastic limit would be enforced by restricting the magnitude of the rolling deformation vector (Obermayr et al. 2013) to:

$$\|\xi_r\| = |\omega_r| R \Delta t = \frac{x_{c,2} + x_{c,1} - x_a}{2} \leq c_R \mu \frac{F_N}{k_T} = \mu_r \frac{F_N}{k_T} \quad (2.1.7.5)$$

where c_R is the dimensionless rolling resistance coefficient; μ_r denotes the coefficient of rolling friction; and, the normal force and the tangential contact stiffness are denoted by F_N and k_T , respectively. Refer to Iwashita and Oda (1998) and Obermayr et al. (2013) for additional details of the derivation. If $c_R = 1$, then the rolling resistance matches the torque produced by the Coulombic friction force; the particle is sliding over the surface without any rotation. This is because the torque from the friction is completely compensated by the rolling resistance. As an analogy, consider a sphere sliding over a flat frictional surface. The sphere will not rotate due to the friction force for $c_R = 1$, just as if its contact surface were flat (e.g., such as that of a sliding block, Plassiard et al. 2009).

Estrada et al. (2013) carried out a numerical study to quantify the effect of angularity in rolling resistance in granular systems composed of regular polygonal particles. The numerical study of Estrada et al. (2013) for the mechanical behavior of discs versus that of polygonal particles (each having the same volume fractions per particle size in a volume of 7,500 particles) revealed that the influence of particle shapes on the rolling resistance could be identified with a statistical number of sides (n_s) of polygonal particles. Based on the work-energy principle, Estrada et al. (2013) proposed a correlation between μ_r and n_s :

$$\mu_r = \frac{1}{4} \tan \bar{\psi} \quad (2.1.7.6)$$

where $\bar{\psi} = \frac{\pi}{2n_s}$ is the mean dilatancy angle of the trajectory of the center of mass of the polygon (see Fig. 2.1.7.10). The perimeter of polygonal particle, as generated from a particle size distribution, is assumed to be equal to $R \frac{(\pi/n_s)}{\sin(\pi/n_s)}$, which corresponds to a spherical particle (of radius R) multiplied by a statistical factor of $\frac{(\pi/n_s)}{\sin(\pi/n_s)}$. Based on p-q diagrams obtained from the

numerical simulations, Estrada et al. (2013) concluded that a packing of regular polygons of n_s sides produces both the volume fraction of solid particles and macroscopic shear strength equivalent to a packing of discs with μ_r , approaching a constant value, i.e., $\mu_r = \frac{1}{4} \tan \bar{\psi} \approx 0.1$.

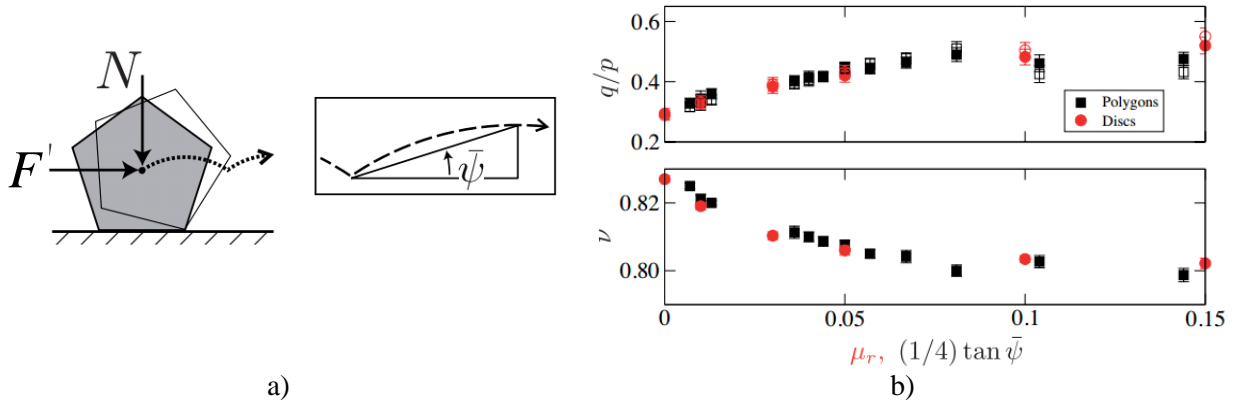


Figure 2.1.7.10. Rolling resistance as a shape parameter in sheared granular media (From Estrada 2013): a) Trajectory of the center of mass (dashed line) and definition of the mean dilatancy angle; b) Shear strength (q/p) and volume fraction of solid particles (ν) shown in a function of μ_r for the discs and $(1/4) \tan \bar{\psi}$ for the polygons.

As introduced above, a rolling motion is that in which no tangential (friction) force or sliding (slip) can occur at the contact. Specifically, when rolling occurs without sliding or spinning, the motion of the contacting bodies is referred to as ‘pure rolling’. As a minimal tangential force Q , which is less than the limiting Coulombic friction, *may* act on the contact surface, partial slip may take place in the contact zone. To differentiate pure rolling without any partial sliding, we will use the terms *free rolling* and *tractive rolling*, instead, where the tangential force is zero and non-zero (yet less than the limiting friction), respectively. As the normal load induces elastic deformation of the contacting bodies over a finite area in tractive rolling, the influence of incipient sliding on rolling contact produces two distinct areas of the contact zone, and is governed by a states known as ‘stick’ and ‘slip’. Major differences among the tangential strains developed in the ‘stick’ area of the contacting bodies induces a small apparent slip, referred to as *creep*. Johnson (1985) explains creep phenomena (first discovered by Reynolds in 1875) using an analogy to a deformable wheel rolling on a relatively rigid plane surface:

“If, owing to elastic deformation under load, the tangential (circumferential) strain in the wheel is tensile. The (contact) surface of the wheel is stretched where it is in sticking contact with the plane. The wheel then behaves as though it had an enlarged circumference and, in one revolution, moves forward a distance greater than its undeformed perimeter by a fraction known as the creep ratio.”

Let us qualitatively discuss the processes that transpires for a rolling wheel, as depicted in the schematic sketches of Fig. 2.1.7.11. More specifically, Fig. 2.1.7.11 shows a simplified model of an elastic wheel, with a radius of R , that is composed of a rigid inner ring and a series of spring elements. Between the spring elements and the base, friction develops in accordance with the coefficient of friction. If we initially press the wheel onto the rigid base (Fig. 2.1.7.11b) and subsequently apply a moment (Fig. 2.1.7.11c), then the springs to the right of the contact area are in compression and the springs to the left are in tension.

As the wheel rolls to the right (i.e., transitions from the state shown in Fig. 2.1.7.11c to that of Fig. 2.1.7.11d), the inner rigid ring rotates across a finite angle, which is dependent on the number and stiffness of the springs engaged in contact with the base. The elements that have not yet contacted the base enter the contact area. In contrast, the elements already making contact reach the trailing edge (where the normal force decreases). Further, as the elements slip out of the contact area towards the rear, the wheel undergoes an additional finite rotation. This kinematic ‘stick’ and ‘slip’ phenomenon in a stationary rolling contact is essentially the source of rotational resistance. For every rotation of an angle corresponding to an individual spring element, the wheel experiences an “elastic rotation” in addition to the “rigid-body rotation (free rolling).” Because of this differential rotation, the circumferential speed of the wheel is faster than the translational speed. If the wheel brakes in its motion, traction moment acts in the opposite direction of rolling, which results in the circumferential speed less than the translational speed. The difference in speed is called creep: $v_\xi = v - \omega R$, where v is the translational speed and ω is an angular velocity. By normalizing creep velocity by translational velocity, we define the creep ratio ξ as:

$$\xi = \frac{v_\xi}{v} = \frac{v - \omega R}{v} = 1 - \frac{\omega R}{v} \quad (2.1.7.7)$$

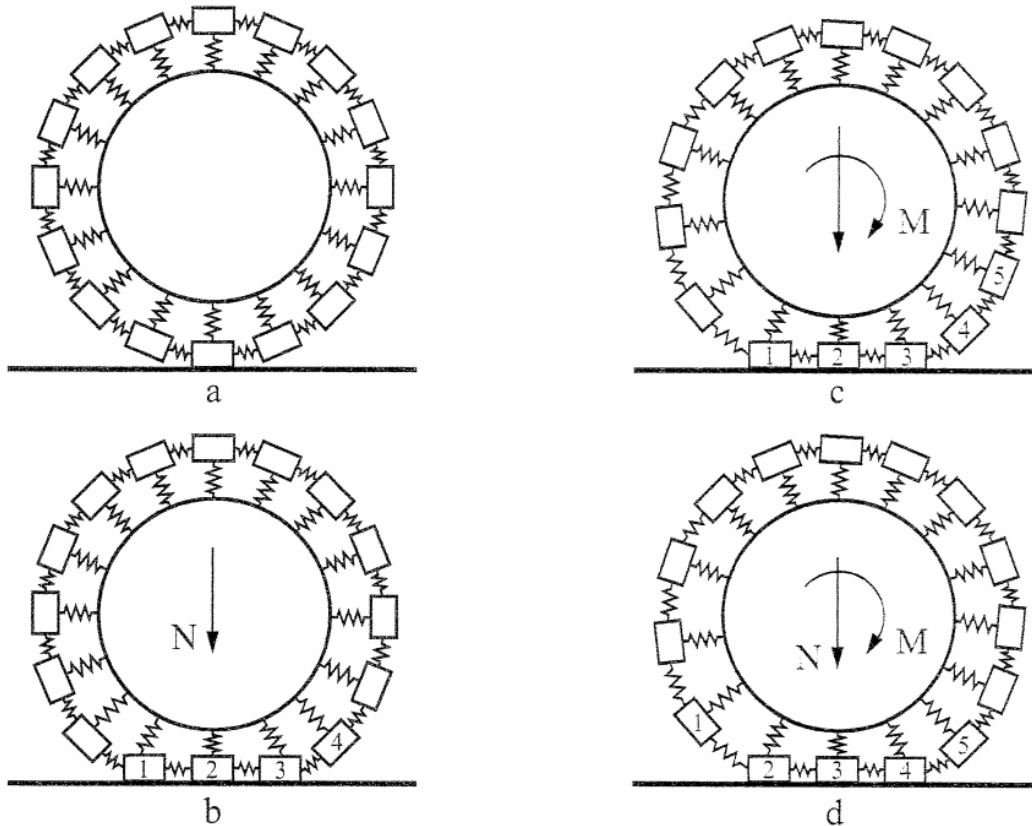


Figure 2.1.7.11. Simplification of creep phenomenon in rolling (based on Popov 2010)

The mass density in the contact area becomes $\rho_o/(1+\varepsilon_{xx})$ per a deformed length, and thus, the mass flow density is $v\rho_o/(1+\varepsilon_{xx})$, which must be equal to $\rho_o\omega R$ per conservation of mass. Satisfying the conservation of mass and substituting the resulting value for ωR into Eqn. 2.1.7.3, we have:

$$\xi = 1 - \frac{1}{1 + \varepsilon_{xx}} = \frac{\varepsilon_{xx}}{1 + \varepsilon_{xx}} \approx \varepsilon_{xx} \quad (2.1.7.8)$$

If the contact of two conforming bodies is considered, then the contact is made over contact points within a contact region that lies in different planes. Free rolling may take place at a number of points, but tractive rolling in combination with rolling (with slip) takes place at all other points (most likely the majority of contact points). To account for this slipping behavior, the sliding resistance at the interface has to be overcome and rolling friction must be present (Rabinowicz 1995). In this case, if adhesive bonds are formed (as explained earlier), the bonds would become disengaged at the trailing end of the rolling contact in tension (rather than shear as in a sliding contact). Thus, rolling friction may arise from the adhesion component of friction. Even for elastic contact during rolling, therefore, energy dissipation occurs. Such energy loss is called elastic hysteresis, which can be modeled as by accounting for rolling friction on two contacting spherical surfaces, with different radii of curvature (Bhushan 2013):

$$\mu_r = \xi\mu = \frac{4-3\nu}{4(1-\nu)} \frac{a}{R^*} \mu \quad (2.1.7.9)$$

where a is the half width of the contact (equivalent to the radius of Hertzian contact area), R^* is an effective radius, and the creep ratio ξ is re-written for 3D rolling contact with Poisson's effect. For practical modeling purposes, the following approximate is adopted in the current study: $\mu_r \approx 0.08\mu$. Combining Eqns. 2.1.7.6 and 2.1.7.9, we have:

$$\mu_r = \frac{1}{4} \tan \bar{\psi} + \xi\mu \quad (2.1.7.10)$$

Thus, depending on the normal deformation, the coefficient of rolling friction can vary over a wide range. For practical modeling purposes, and based on rigorous reviews of Johnson (1985), Popov (2010), and Bhushan (2013), the following approximate is adopted in the present study of contact models for monodisperse and bi-disperse systems: $\xi = [0.04, 0.10]$, assuming that Poisson's ratio varies between 0.17 and 0.3 per DSE diameters (Zheng et al. 2011). For example, if a monodisperse system of DSEs with a diameter of 5 mm is modeled using $\mu = 1.0$, the coefficient of rolling friction is approximately estimated as $\mu_r \approx 0.14 \sim 0.2$. Therefore, per use of Eqns. 2.1.2.3 and 2.1.7.1, i.e., stress superposition and decoupling techniques, the force mapping of Eqns. 2.1.7.6 and 2.1.7.10 (on rolling resistance at the grain level) is intended to collectively (and qualitatively) transform irregular shapes of angular particles to equivalent DSEs (as illustrated in Fig. 2.1.7.12).



Figure 2.1.7.12 Schematic of random assembly of eight angular particles (left) and transformed equivalent DSEs (right)

2.1.8 Macroscale Modeling Concepts

Having discussed the particle-level frictional mechanisms that are associated with particle geometry, interparticle interlocking, and rolling resistance, we now shift our attention to physical descriptions of macroscopic structural textures called soil fabrics. Subsequently, modeling concepts are discussed in relation to DEM simulations of macroscopic shear strengths of granular soil.

As presented earlier, surface roughness (microscopic) and shape (particle-level) of granular particles enhance the shear resistance of granular packing. Also, recall that initial particle arrangement is responsible for the evolution of anisotropy (macroscopic) during shearing processes (Santamarina and Cho 2004). The relative measure of the density state associated with a given initial particle arrangement is referred to as relative density. Further, relative density indicates the degree of particle interlocking and anisotropy, which in turn, influence volumetric behavior and corresponding macroscopic shear strength. For example, for initial particle arrangements under very dense states, the mobilization of frictional resistance reflects the evolution of internal anisotropy (particle contact orientation and contact forces), which produces an increment in volume (i.e., dilation). Relations emerge when considering DSE assemblies across various size scales. Namely, the evolution of contacts and contact anisotropy are strongly affected (or caused) by: 1) Micro-scale and particle-level frictional mechanisms; and, 2) Changes in contact orientation of multiple particles, which form chains of interconnectivity at macroscopic scales.

The characteristics of ‘relative densities’ from a macroscopic perspective are those of particle size distribution and the corresponding internal structure. An informative representation of internal structure (i.e., multi-grain fabrics) is found by examination of the polar histogram of contact normal and particle orientations. If contact between two adjacent particles is represented by a vector normal to the plane of the contact, then all contact normals can be plotted for each orientation angle in a polar coordinate system. In general, shapes of the polar histogram vary between a circle (isotropic distribution of contacts) and a ‘peanut-shell’ (anisotropic contact distributions for which the structure as a whole may maintain stability against the buckling of ‘internal columns’). For example, as shown in Fig. 2.1.8.1, preferential orientation angles can be seen where long axes for a large number of grains are oriented in the horizontal direction (Fig.

2.1.8.1c) in a cylinder sample prepared by pouring. Dynamic compaction, however, produces a more nearly random fabric (Fig. 2.1.8.1d). A completely random distribution of particles would yield the dashed circles shown in Fig. 2.1.8.1c and Fig. 2.1.8.1d. Non-spherical particles (ellipsoids) tend to align in a preferential direction during shearing processes. This preferential orientation of particles (i.e., interparticle contact orientation) and the particle distributions influence: deformation behaviors; strength properties; and, the propensity for anisotropy (with respect to macroscopic fabric characteristics). Thus, particle shapes also affect the internal structure, particularly pore size distribution. Packing of angular particles tends to produce less dense configurations than that of rounded particles. Maximum and minimum densities of packing, thus, depend on all of microscopic surface roughness, particle-level geometry, contact orientation, and particle size distribution (Arya and Paris 1981).

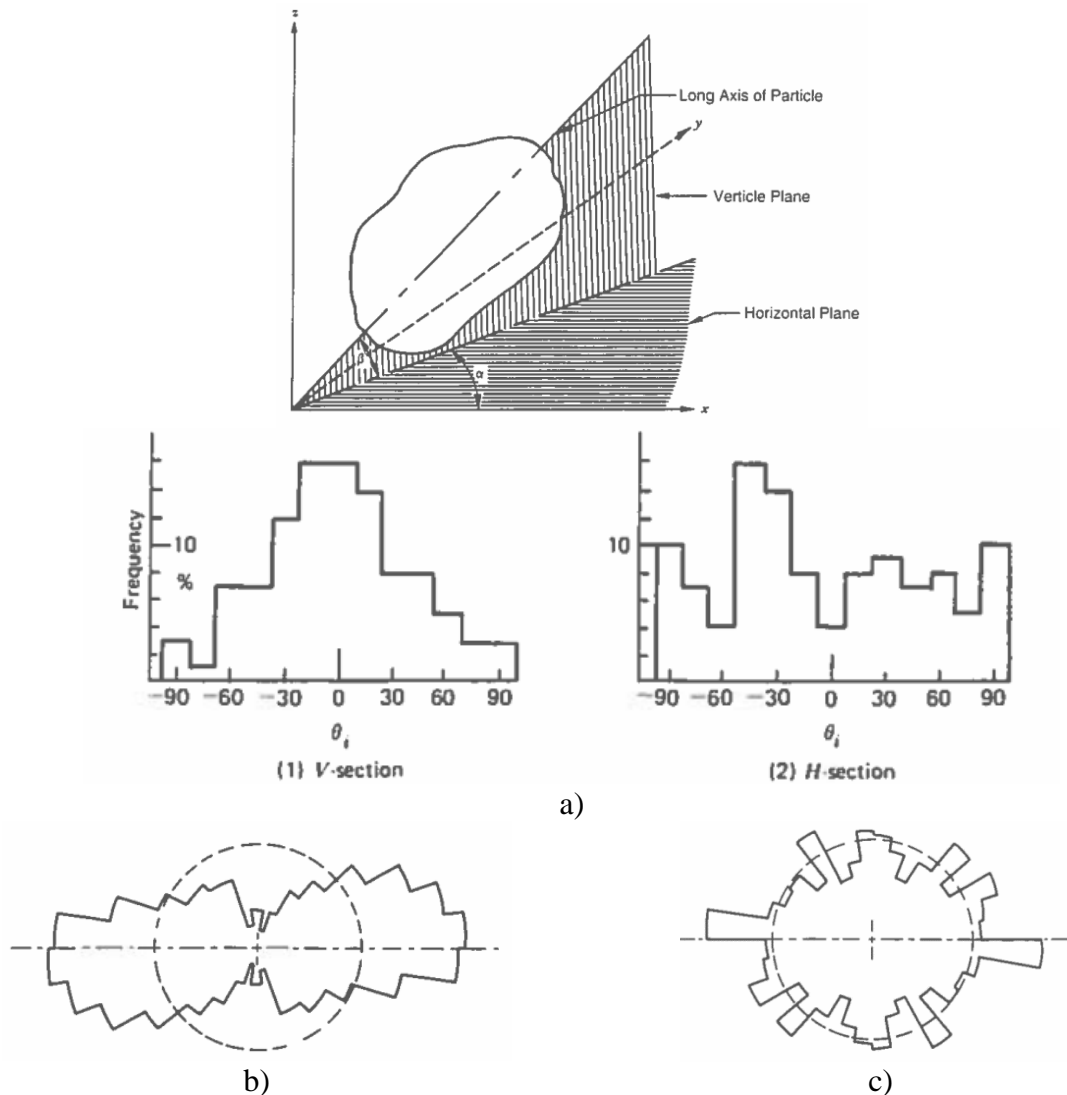


Figure 2.1.8.1. Polar histogram of coordination (from Mitchell and Soga 2005): a) 3D orientation of a crushed basalt particle (top); Frequency histogram of axis orientations (middle); b) Polar diagram of crushed basalt in a sample prepared by pouring (relative density is 62%); c) Polar diagram of crushed basalt in a sample prepared by dynamic compaction (relative density is 90%)

In DEM simulations, the internal structure of granular materials can be characterized using coordination numbers and packing methods of random particle distributions. The coordination number of an assembly of discrete particles is the average number of contacts per particle: more specifically in the context of DEM simulations, it is defined as the summation of the coordination number of each DSE divided by the number of DSE in a random packing assembly. The average coordination number of a packing assembly gives an idea of internal assembly and resulting structural stability.

Larger values of the coordination number indicate denser configurations and, thus, more stable internal structures. The possible range of packing of granular particles is also related to the maximum and minimum void ratios reflecting the loosest and densest states, respectively (Lambe and Whitman 1969). Limiting values of coordination number for structural instability (structural collapse) can be determined by equating the number of unknown contact forces and the number of force equilibrium equations (Rothenbug and Bathrust 1992). This is analogous to the structural determinacy of determinate truss systems; by removing one particle (member) from the internal structure (truss structure) at equilibrium, cascading collapse can occur among the remaining particles (members) (see Fig. 2.1.8.2 for examples of idealized internal structures).

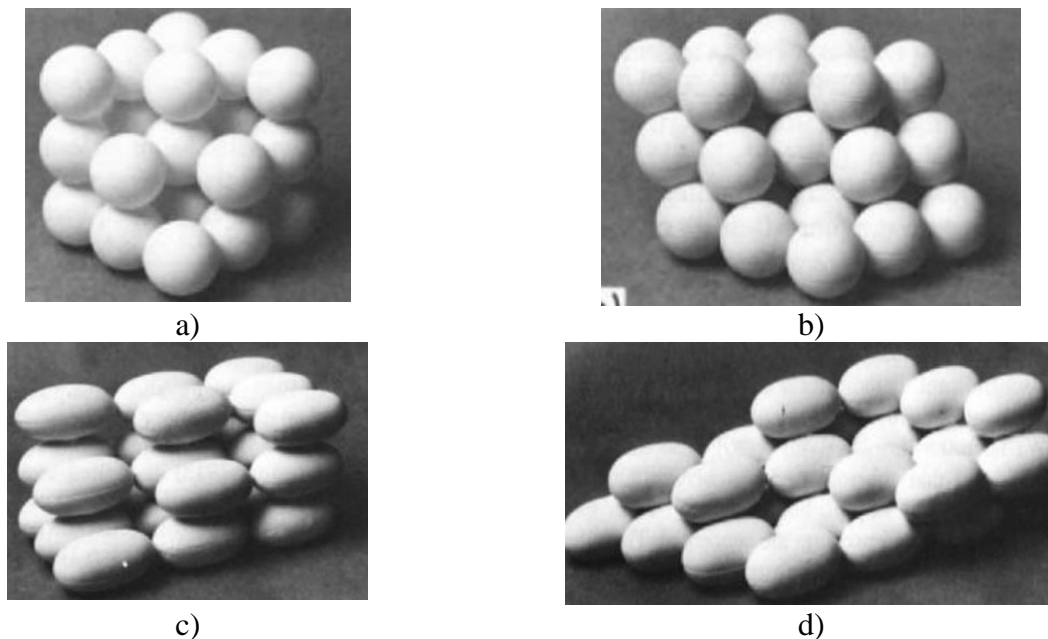
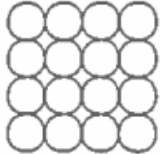
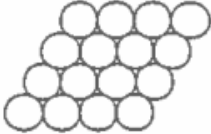
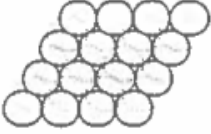
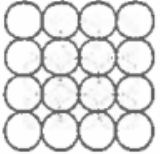
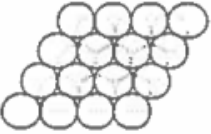


Figure 2.1.8.2. Physical representations of idealized packings (John 1982): a) Spheroids in cubic packing; b) Spheroids in tetragonal-spheroidal packing; c) Prolate spheroids in cubic packing; d) Prolate spheroids in tetrahedral packing

Experimental investigations (Scott and Kilgour 1969, Finney 1970) and numerical simulations (Moscinski et al. 1989, Jodrey and Tory 1981) on random DSE packing have been reviewed in detail. The experimental findings by Scott and Kilgour (1969) indicate that the mean packing density strongly depends on the method of packing, and the maximum for truly random experimental packing appears to be 0.64~0.67 (Scott and Kilgour 1969, Finney 1970, Moscinski et al. 1989). Based on the review findings, two primary packing methods are mainly adopted in DSE analysis of the present study. One algorithm begins with a very dense configuration of DSEs,

which overlap (Moscinski et al. 1989, Jodrey and Tory 1981). The DSEs are then spatially relocated (within the predetermined domain of a cylinder) in order to reduce the degree of overlapping. Dense packing structures can be obtained by using this method, which results in values close to 0.62. The second algorithm simulates the successive packing of a cylindrical container (for use in subsequent triaxial compression test simulations) with DSEs being subjected to a gravitational field (Tory et al. 1973). Once the DSEs settle down in the cylinder and reach a quasi-static force equilibrium state, the resulting packing is considered to be in its final position under gravity as a kinematically admissible (stable) state of granular mass. The computational procedures of the algorithm describe the actual process of packing generation in laboratory experiments (with or without a control drop height) to generate interacting forces among DSEs. Also, the procedures generally yield loose packing with densities of approximately 0.58 in the case of monodisperse systems. A comparison of theoretical properties for idealized packings is given in Table 2.1.8.1.

Table 2.1.8.1. Properties of uniform size sphere packings (from Santamarina et al. 2001)

Geometric arrangement	cn	Layer spacing	Porosity, n	Void ratio, e	Packing density, $1 - n$
Simple cubic (SC) 	6	d_g	0.476	0.908	0.524
Cubic - tetrahedral (CT) 	8	d_g	0.395	0.652	0.605
Tetragonal - sphenoidal (TS) 	10	$d_g/2\sqrt{3}$	0.302	0.432	0.698
Face-centered cubic (FCC) 	12	$d_g/2\sqrt{2}$	0.260	0.351	0.740
Tetrahedral (T) 	12	$d_g\sqrt{2/3}$	0.260	0.351	0.740

Notation: d_g is grain diameter, cn is coordination number.

As described in Fischer et al (2003), particles with uniform size distribution cannot be manufactured using current technologies. Therefore, Gaussian particle size distributions are suggested for the modeling of materials such as commercial powders. In contrast to the limitations of (physical) manufacturing, computational limitations come into play when attempting to model actual particle size distributions in DEM simulations. When populating (distributing) DSEs of various radii within a volume (according to either a prescribed probability density, or by use of a probability mass function to model distinct particle-size groups), the total number of DSEs can reach into the millions. This is particularly so when mathematically representing particles with diameters ranging from a few hundred micrometers to several millimeters. Even for cases where four particle-size groups are selected (e.g., per Murzenko’s sand sample 1965), packing procedures require approximately five million DSEs to populate a 100 mm by 200 mm (4 in. by 8 in.) cylinder. A discrete one-on-one description of multi-grain fabrics per an actual particle size distribution is therefore infeasible in consideration of the numerical experimentation necessary for developing various soil ‘unit’ models (i.e., the task-specific deliverables). Further, such a description is impractical for a single deterministic representation of heterogeneous fractal networks. However, the existence of multi-grain fabrics is evident in spatiotemporal changes in contact orientation of multiple particles (Fig. 2.1.8.3). More specifically, chains of interconnectivity form during shearing, and can produce amplification of local dilatancy as well as strain localization for very dense granular packings.

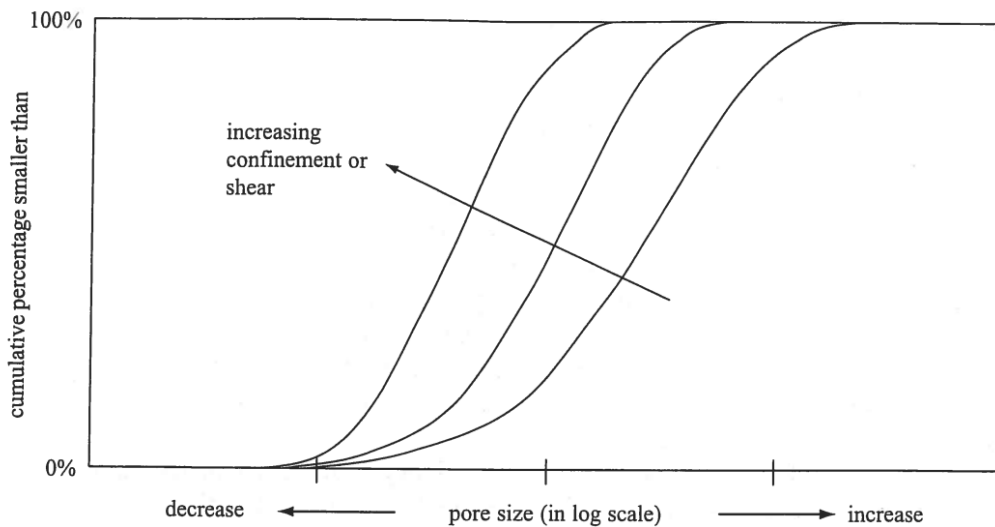


Figure 2.1.8.3. Evolution of pore size distribution with confinement: larger pores collapse before smaller pores (Santamarina et al. 2001)

A literature review focused on load transfer mechanisms in particulate materials reveals physical phenomena that may, in turn, provide a possible remedy in simulating the effects of relative density and local dilatancy (Hidalgo et al. 2002, Salot et al. 2009). During shearing processes, most of the applied load is transferred through chains of normal and tangential contact along “primary” particles. Particles in the vicinity of the chains play a secondary role in supporting the column-like chains of primary particles and increasing structural stability. This particulate behavior is depicted schematically in Fig. 2.1.8.4a, which is readily seen in: experimental studies using photoelasticity (Fig. 2.1.8.4b); and, numerical results obtained from non-uniform polygonal

discrete element analysis (Fig. 2.1.8.4c). Alternatively stated, there exist two representative groups of particles, where each group exhibits unique load-carrying mechanisms.

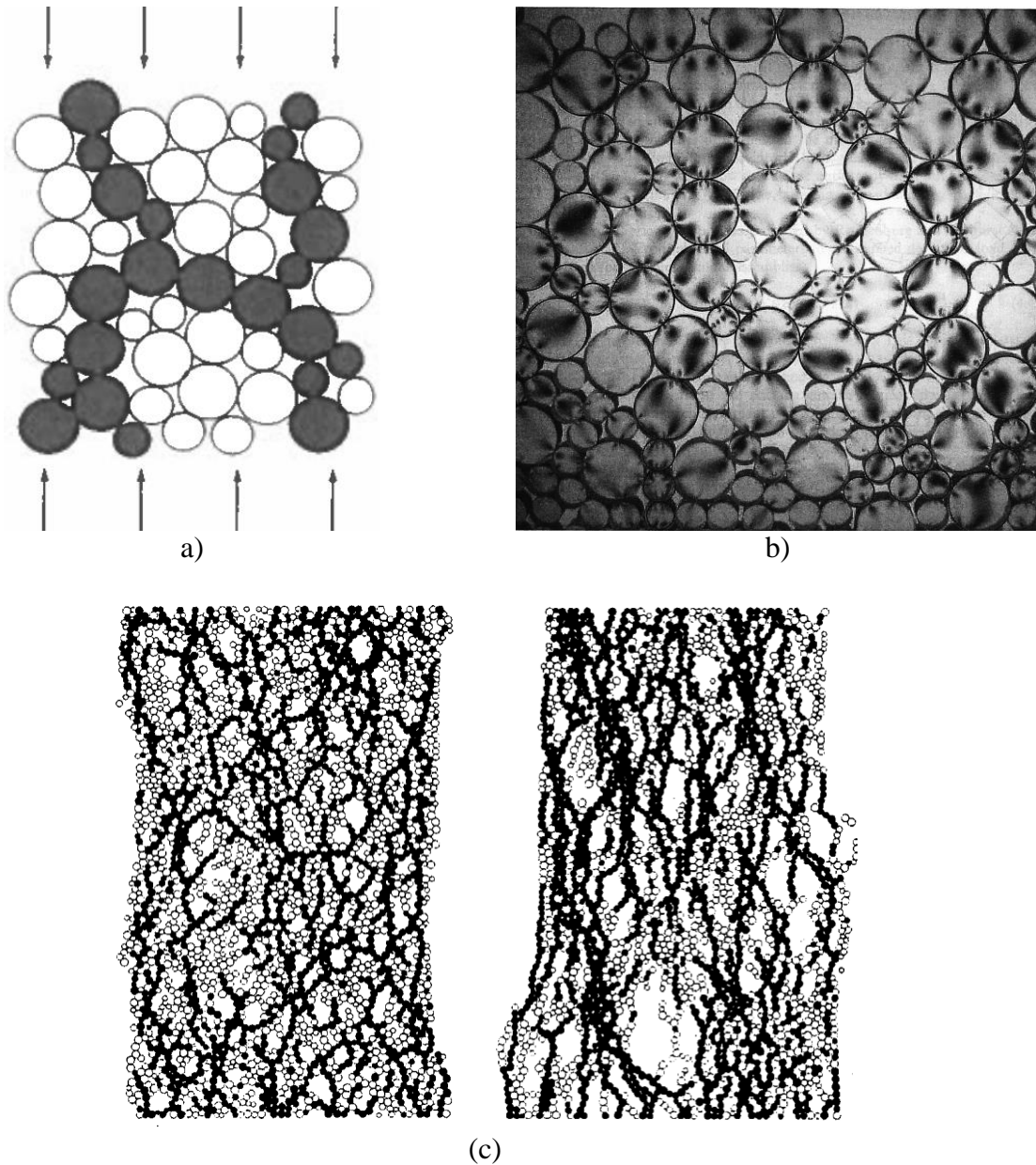


Figure 2.1.8.4. Force chains and granular fabrics: a) Force chains of the shaded particles carry larger contact forces than an average contact force. The remaining unshaded particles act as supports, playing a secondary yet important role in load-carrying mechanism (Santamarina et al. 2001); b) Photoelastic demonstration of force chains: Contact forces tend to be higher along particle chains. Particles that are not part of the force chains play the role of boundary supports preventing the chains from buckling (Mitchell and Soga 2005); c) Development of column-like force chains in 2D numerical tests on rolling resistance (left: free rolling, right: active rolling friction, Iwashita and Oda 1998).

It follows that large portions of particles in any real packing experience only gravity and local boundary forces, and remain relatively less affected (or unaffected) by external (shearing) forces. Guyont et al. (1987) first applied the modeling concept of fabrication of binary mixtures to macroscopic transport analysis of water percolation, and referred to it as *bimodal distributions of spheres*. These particles were later called spectators by physicists (Cates et al. 1998). Santamarina et al. (2001) explained this group of particles in a similar way: these mobile particles would follow the primary particles in shear flow, and are called the ‘mobile’ fraction of the packing (Fig. 2.1.8.5).

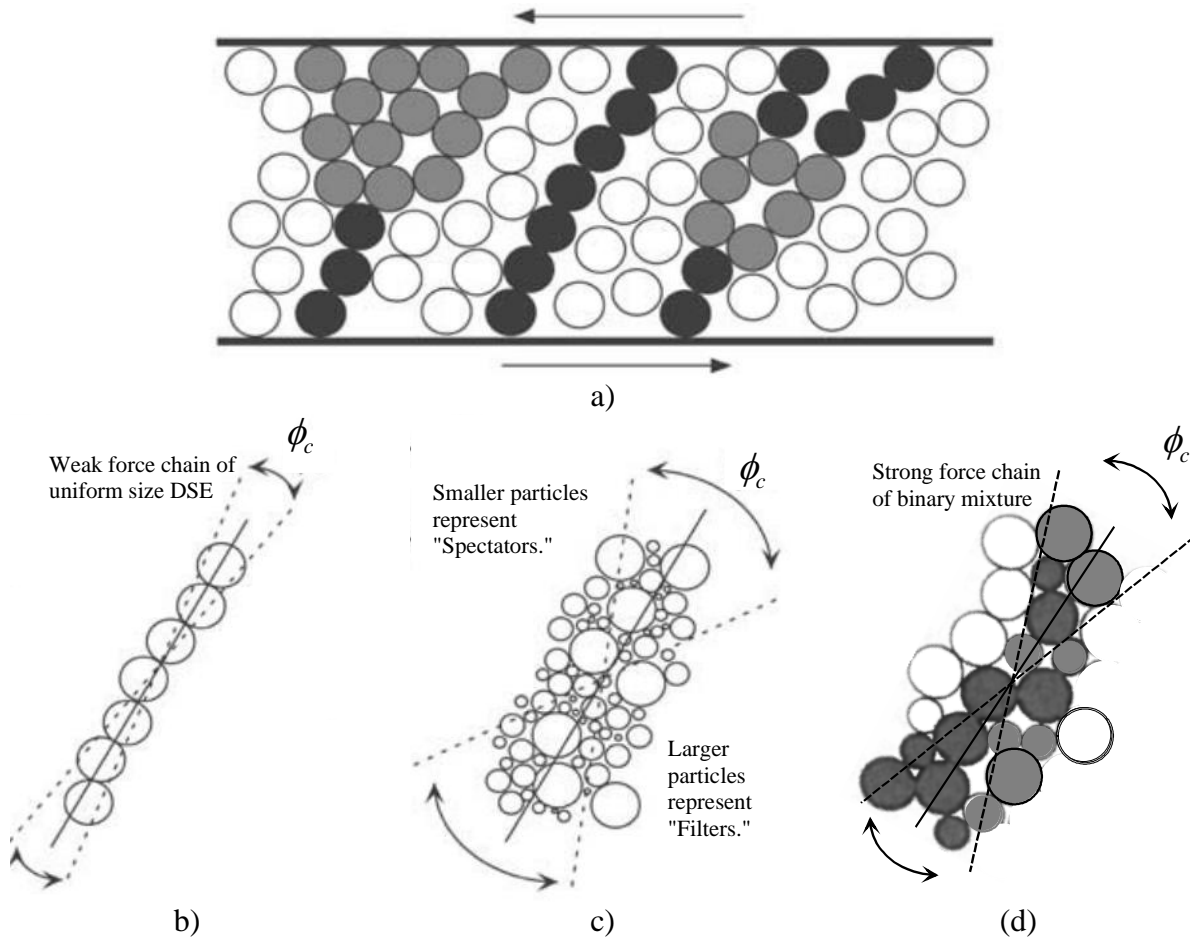


Figure 2.1.8.5. Illustration of possible force chain geometries for a granular layer subjected to shear. Solid lines indicate optimal chain orientation and dotted lines denote ranges of possible stable orientations; ϕ_c defines a critical angle of local dilatancy for stress chains; outside this range, stress chains fail by interparticle slip or rolling. Note that parts c and d have larger ϕ_c than that of part b. a) Force chains of a monodisperse system subjected to external shear forces (from Mair et al. 2002): dark gray particles bear high load; light gray particles carry moderate load; and white particles indicate spectators that do not contribute to appreciable load-carrying capacity; b) Force chain of uniform size DSEs; c) Multi-grain fabrics per particle size distributions; d) Modeling of jamming per binary mixtures of DSEs.

The coordination (number) in the evolving structure of these particles is minimal in interlocking, and more likely, biased by the local boundary forces that arise under gravity-induced static equilibrium conditions (e.g., geostatic stress states). In contrast, the other group of relatively larger particles (called ‘filters’; Santamarina et al. 2001) can be frustrated for both sliding and rolling motions, which are traversed by mobile, smaller particles. The spectators can also support the force chains of the filters, preventing them from buckling. Either way, as a larger shearing force would be required to displace (or buckle) the filters (or the chain), a greater degree of dilation could be simulated for a denser packing (as exemplified by comparing Figs. 2.1.8.5b-c). In general, contact forces are the greatest for shear jamming (such as that shown in Fig. 2.1.8.5d).

For a mixture of DSEs, generated based on a given volume fraction and subsequently packed, a successful “jamming” of the filters can be achieved (Majmudar et al. 2007, Salot et al. 2009). The density at which local force-chain systems jam is determined by many factors, including grain shape, the deformability of the particles, frictional interparticle forces, and pore structure network (called the degree of dispersivity) of the system. The overall degree of the jamming manifold may depend on the particle size distribution as well. For example, a particularly interesting feature of the jamming is the transition between loose packing states and interlocked denser states. Whether the jamming diverges (becomes ineffective) for high enough densities or low friction at the microscopic scale is uncertain. In this context, the degree of jamming under shear is a qualitative description used when simulating local dilatancy and accumulative effects in macroscopic dilative behaviors of granular systems (Bi et al. 2012). Thus, simulation of jamming effects during shearing process is to introduce a jamming coefficient μ_2 as a numerical parameter to simulate increased contact forces among DSE in shear jamming. Therefore, based on Eqn. 2.1.2.3: $\mu = \sum_i \mu_i$, a total coefficient of sliding friction becomes a DSE parameter, which tends to be greater than unity (Rotter et al. 1998, Yang et al. 2012; refer to Fig. 2.1.8.6):

$$\mu = \mu_0 + \mu_1 + \mu_2 \geq 1.0 \quad (2.1.8.1)$$

where μ_0 represent an intrinsic friction coefficient due to microscopic surface roughness, μ_1 is a numerical friction coefficient for shape effects, and μ_2 is a numerical jamming coefficient. Note that μ_2 is not a material parameter that holds a physical (frictional) meaning at the grain-level. Instead, this coefficient (an addition to the coefficient of friction) is to simulate shear jamming due to mesoscopic (intermediate scale) physical anisotropic fabrics of cohesionless granular materials.

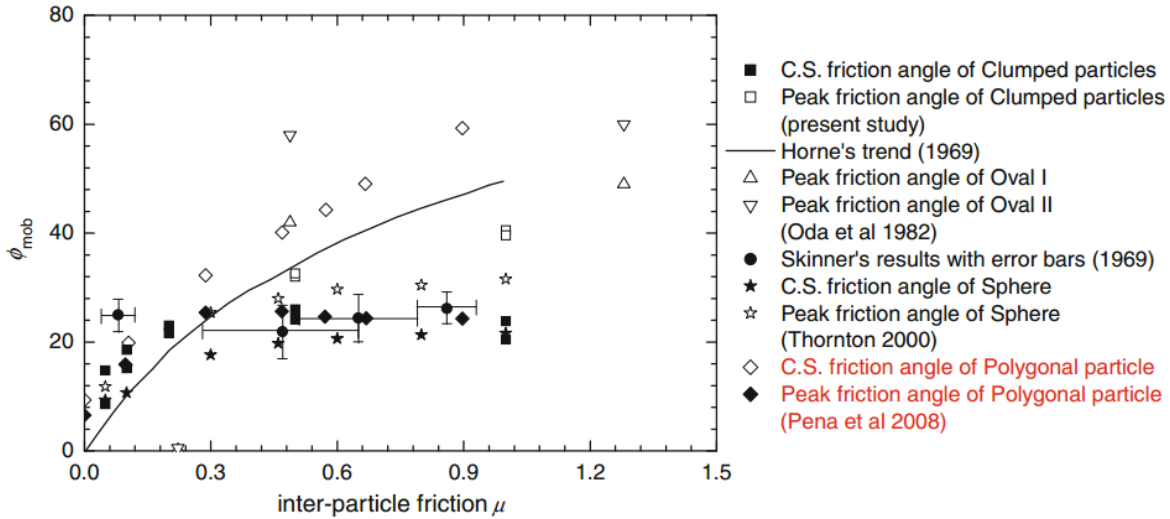


Figure 2.1.8.6. Comparison of mobilized macroscopic friction angles (from Yang et al. 2012): It is evident that polygonal discrete elements tend to produce shear jamming even with low values of interparticle friction coefficient. In contrast, uniform-size spherical and clustered discrete elements exhibit limited macroscopic mobilization of greater shear strengths regardless of the value of the coefficient. The effect of shear jamming phenomena needs to be simulated in spherical discrete element analysis.

In simulating the broad applicability of the “shear jamming” concept (Liu and Nagel 1998), the inclusion of secondary DSE (“spectators”) in the packings can play an important role in controlling the kinematics of DSE packings as a whole, such as when binary systems are modified to produce a higher, target shear strength of a very dense granular soil. Jamming apparently occurs because the particles form force chains along the compressional direction for spherical particles in an array or network of fractal structure. Alternatively described, the simulated lateral confinement on the force chains of the binary mixture enhances volumetric behaviors of the representative elementary volume (**REV**) as a whole. From a phenomenological standpoint, the volumetric behavior of the dense packing has to be consistent with the development of deviatoric stress observed in physical tests, and thus, the numerical results of both force and deformation become valid.

Although jamming states of granular matters have been intensively studied theoretically using both numerical and experimental tools in the power industry and field of granular physics, the nature of the jamming transition for cohesionless frictional grains has not yet been made clear from a quantitative standpoint. The degrees of jammed states and the fractions at which transitions occur from contraction to dilation (as part of reaching a critical state) are statistically independent of the mass density (Bi et al. 2011). Furthermore, ascertaining that states of cohesionless granular materials are macroscopically jammed is non-trivial in numerical analysis. As explored extensively in the soil mechanics literature (Lambe and Whitman 1966), increased packing (volume fraction of DSE) alone may not induce jamming at positive pressures as shear stress induces irreversible flow at the yield stress (black line as shown in Fig. 2.1.8.7a). The numerical parameter of jamming coefficient may depend on the protocol of preparing the jamming states as an initial condition. However, only a few experiments have investigated the Liu-Nagel jamming theory for physical systems consisting of spherical particles with friction. For example, under

isotropically confined conditions, the coordination number of DSE packings at jamming increases with interparticle frictional resistance (Majmudar et al. 2007). If the effect of multi-grain fabrics in the local (i.e., mesoscopic intermediate-scale) dilatancy is qualitatively accounted for per use of numerical “shear jamming” (i.e., a jamming coefficient), then the evolving fractal network of numerically-represented denser granular materials must satisfy the kinematics of volumetric behaviors under deviatoric loading. Therefore, whether or not the kinematic responses (obtained from DEM simulations) are consistent with the macroscopic dilation of REV would indicate an optimal inclusion of shear jamming effects. Thus, a limiting value of the shear jamming coefficient should be determined using numerical experimentation on kinematically admissible force-deformation relationships, based on the work-energy principle.

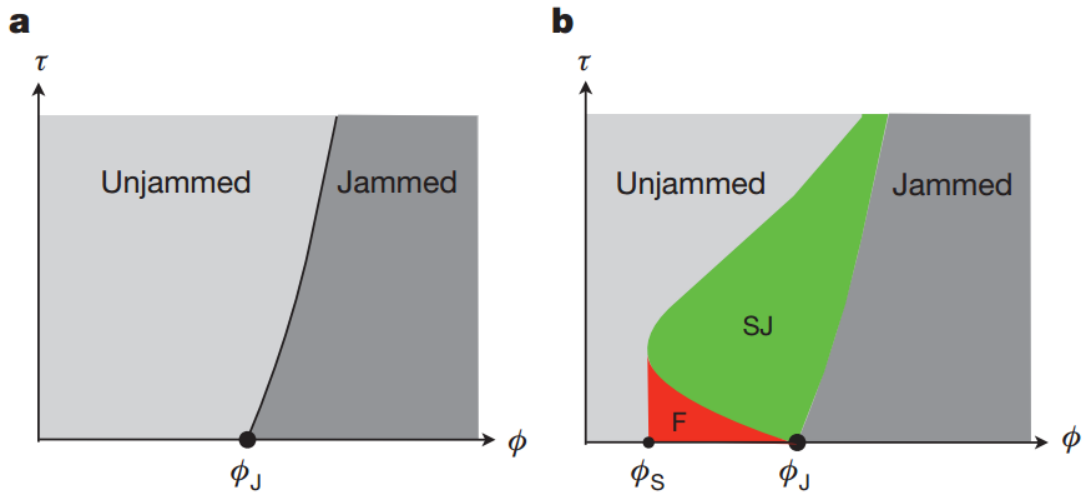


Figure 2.1.8.7. Jamming phase diagrams (from Bi et al. 2011): a) Original Liu–Nagel jamming phase diagram. The boundary between unjammed and jammed regions is the yield stress line. Unjamming can be induced by decreasing the packing fraction or increasing the shear stress; b) Generalized jamming diagram including the shear-jammed (SJ) and fragile (F) states. Along the ϕ axis, there are two special densities: ϕ_S , below which there is no shear jamming, and ϕ_J , above which isotropically jammed states exist. For $\phi_S \leq \phi \leq \phi_J$, jamming can occur with application of shear stress.

The smallest size of the particles in a DEM simulation also affects the efficiency of DSE analysis. To reduce computational costs yet to maintain the discrete nature of granular matter and the characteristics of inertial particle interactions in soft particle dynamics, many researchers across engineering disciplines use particle size up-scaling methods (e.g., O’Sullivan et al. 2004a, Lee et al. 2012). In general, the diameters of DSEs used in the past DEM simulations of triaxial compression tests on granular matters (from powders to sands) range between 2 mm and 25 mm (Thornton 1979, Jodrey and Tory 1981, Thomas 1997, Thornton 2000, Yimsiri and Soga 2001, O’Sullivan 2002). The maximum diameter of DSE selected for this study is a maximum particle size of sand (or a minimum size of gravel) based on soil composition and relevant mechanical properties given by Duncan (1994) (cited in Mitchell and Soga, 2005) and a chart given by Lee (1992); refer to Table 2.1.8.2 and Fig. 2.1.8.8, respectively. For these reasons, uniform size packings of DSE with a diameter of 5 mm allows for a benchmark system-level platform, where a binary mixture for “shear jamming” can additionally permit modeling of denser granular packings.

Using “mean-field theory” (Guyon et al. 1987, Moscinski et al. 1989), the critical volume fraction ratio of the filter to the mobile particles is explored as part of numerical experimentation in which the coordination number increases proportionally to the packing density of binary mixture.

Table 2.1.8.2. Compositional factors of granular soil (Mitchell and Soga 2005)

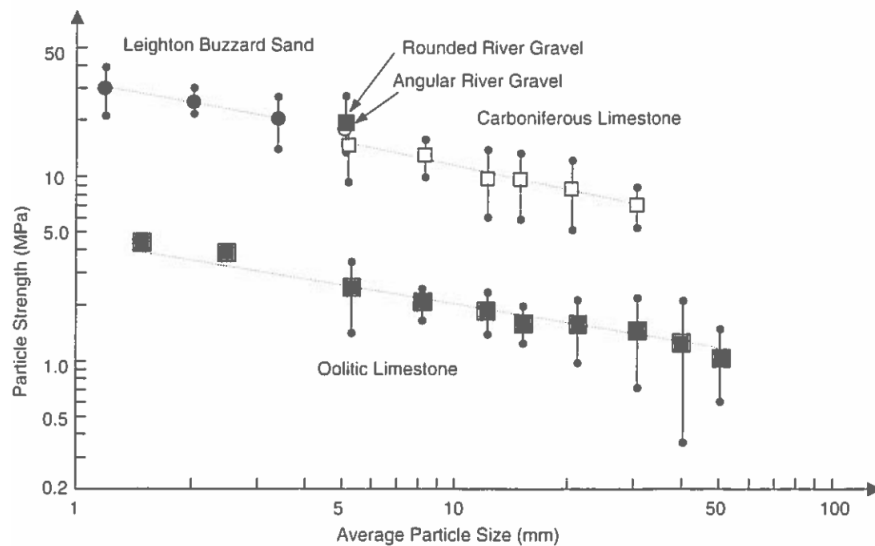
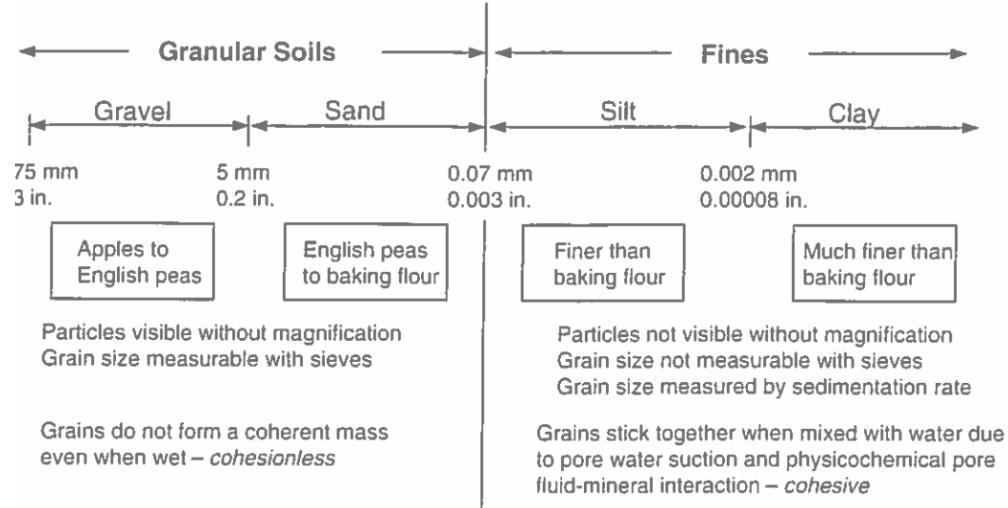


Figure 2.1.8.8. Relationship between tensile strength and particle size (Lee 1992)

2.2 Numerical Method for Soft Particle Dynamics

The study of molecular dynamics (e.g., packing structure, particle-particle interaction) greatly facilitates the development of numerical modeling methodologies for investigating the dynamic behaviors of particulate systems. One common formulation, which makes use of a “soft” contact approach is of relevance to the current study, and was first developed and applied in geotechnical mechanics by Cundall and Strack (1979). By definition (Crowe 1997), when

conducting simulations of bodies that utilize the soft-contact approach slight overlaps are permitted to develop at object-object contact interfaces. Contact forces are subsequently quantified based on the properties of the interacting objects (e.g., spherical particles) and the deformation history of the contact, which in turn, is driven by a force-displacement law. Molecular dynamics models that incorporate the soft contact approach effectively combine two theories (Newton's second law of motion and a force-displacement law) to trace the movement of discrete objects (particles) and the generation of boundary conditions throughout a given system. Further, applying the combined theories is amenable to forming repeatable, sequential (i.e., time-stepping) processes, with calculations including: 1) Forces at contact interfaces between two particles, or between particles and planar surfaces (such as finite element surfaces); and, 2) Motion (translation, rotation) of each particle and surface, based on mass-proportional acceleration. For each calculation cycle, the updated (end-of-cycle) positions of the particles enable calculation of updated contact forces, which in turn, drive the motion of the particles during the next calculation cycle. For such formulations, the time-step size is required to be sufficiently small so as to uphold the assumption that acceleration remains constant throughout a given time-step. Comprehensive literature reviews, which summarize the developments of discrete particle modeling over the past two decades, can be found in Zhu et al. (2007) and Zhu et al. (2008).

2.2.1 The Discrete Element Method (DEM)

The DEM consists of numerically modeling a number of separate (i.e., distinct, discrete) particles such that mechanically microscopic interactions, in aggregate, bring about meaningful phenomena at larger scales (e.g., macroscopic, megascopic). In the context of geomechanics, the DEM readily lends itself to replicating the particulate, discontinuous nature of soil. Indeed, the DEM is widely used to predict large-scale deformations of assembled particles: the DEM allows for the incorporation of highly irregular geometry; can capture evolving failure mechanisms (e.g., slip planes, cavity formation) that develop across a given collection of particles; and, permits statistical measures of the unique stresses and strains for a volume of interest. DEM parameters include physical parameters (e.g., particle size, topology, specific gravity, hardness), mechanical contact parameters (e.g., frictional coefficients, stiffness, viscous damping), and purely numerical parameters (e.g., derived numerical quantities of density, coordination number). The use of DEM, albeit computationally expensive, permits unprecedented insights to be made into the nature of particulate matter. For example, physical lab tests do not allow for the determination of internal stresses between soil grains, whereas the DEM is capable of modeling and cataloging of particle-particle interaction forces for every particle of a given numerical model. Hence, the DEM can be used to enrich those measurements obtained by manipulating soil specimens in laboratory settings.

The general computational algorithm that underlies DEM is comprised of two stages. Contact definitions are defined in the first stage. Interaction forces are then calculated via a force-displacement law at the boundaries of the individual particles in contact. This method captures the relative deformation of the particle boundaries, and is based on the particle-specific material properties as well as the particle-to-particle contact forces. The second stage involves the application of Newton's second law in terms of the forces generated for each discrete element, by which the induced accelerations of the particles are calculated. The collection of accelerations are then time-integrated to determine the updated positions of the particles. This overall algorithm is

then repeated across a pre-specified number of time-steps in order to give regularly updated forces, accelerations, and positions of the system of particles.

2.2.2 Advantages of Combined DEM-FEM

The most commonly employed and most highly developed numerical method that employs the continuum hypothesis is the FEM. It is this method which plays the part of modeling continua in the present study of driven SPWs and their effects on the apparent capacity of surrounding driven piles within granular media. The finite elements (FEs) which give this numerical method its name can be thought of as a small part of the continuous structure being modeled. As expected these “parts” (i.e., elements) are of finite size, separating them from the infinitesimal divisions made use of in calculus, and each element possesses definite geometric shape. The entire model of the physical structure under analysis is then a discretization of these finite elements, coupled to one another at points referred to as nodes, with the particular arrangement and shapes of these elements referred to as a mesh. Although the mesh is referred to as a discretization, it is important to distinguish between the continuous finite elements and discrete elements. Field quantities, such as axial stress or displacement under stresses, are allowed to have simple spatial variation in each finite element that makes up the mesh. Together, these result in the set of governing equations for the numerical model, given as a set of partial differential equations or integral equations. The field quantities which these equations represent are then piecewise interpolated over the finite elements, which can then be used to approximate the behavior of the physical system.

While the concept of a continuum problem can be readily adapted and applied (through FEM) to a powerful numerical method for modeling many physical systems, there are also physical systems for which the continuum hypothesis is not valid, especially once the extent of the available technology is considered. When considering the actions of granular materials like sands and clays, the particulate nature of the medium plays a much more pronounced role in the observable properties of the body as a whole. In this case, the most natural level for discretization of the medium is at the level of the grain, which is far larger than constituent atoms or molecules, but still far smaller than the body of which the grain (in turn) is a constituent. Physical properties of granular soils, like the volume of the voids within the soil body and the shapes of the individual grains, are very important to consider when studying the mechanics of granular bodies. It is clear that in applying a continuum hypothesis and assuming a body of continuous mass, the modeler fails to capture these properties.

The current research project requires the numerical modeling of the behaviors of different materials (SPW, individual driven piles, and a heterogeneous granular media) and their interactions with one another. For some of these entities, namely the structural elements and piles, the continuum hypothesis is a valid and effective modeling strategy. In contrast, granular material is more aptly modeled when its discontinuous particulate nature is taken directly into account. Hence, a combined numerical method is chosen in the current study, making use of both of the continuum and discrete approaches, and is referred to as DEM-FEM approach. Therefore, the models employed in the current study will consist of structural objects that are modeled as continuous (and formed as FEs), while the soil will consist of an assemblage of discrete spheres (and formed as DSEs).

2.2.3 Utility of DSE Libraries

In the current study, a standardized library of numerical parameter values is established, and from which, assemblies of DSEs can be formed such that said assemblies exhibit known macroscopic properties. This standardized library, or “soil unit” library is essential in building up megascopic DSE assemblies for use in the installation and removal of structural objects (SPWs, piles). For the remainder of this report, major considerations are given to characterize mechanical contact, friction, and viscous damping parameters associated with numerical modeling of individual DSE within a given assembly. Further, combined DEM-FEM models of laboratory test apparatuses are developed to facilitate assessment of macroscopic properties of DSE assemblies.

By combining: 1) Quantitative characterization outcomes associated with DSE rheological components and interaction behaviors (discussed in Ch. 2); and, 2) Benchmarked numerical (DEM-FEM) models of laboratory test apparatuses (discussed in Ch. 3), relevant input parameters to describe individual DSEs are calibrated and cataloged in forming the DSE library (Sec. 3.4). As detailed later in the report (Sec. 3.4), the DSE library developed for use in the current study contains a summary listing of input parameter values (obtained from simulations of laboratory tests on DSE assemblies) for collections of particles across a range of density states and shearing behaviors. The DSE library can be drawn upon to quickly build up, at will, homogenous or heterogeneous megascopic DSE assemblies. In turn, the megascopic assemblies constitute (for example) one realization of the possible soil conditions at a given pile installation site. The soil unit library will be subsequently (and heavily) employed in tandem with various pile-soil-SPW configurations in Task 3 of the overall research project, where the numerical modeling of driven structural members in granular soils will be explored in a direct fashion.

2.3 Governing Equation and Solution Approaches

In Sec. 2.3.1, the governing equation used in describing the motion at contacts between DSEs, in accordance with the DEM, is introduced. In particular, the equations of motion for both normal and tangential directions are derived for a system of two overlapping spheres. While translational motion is considered in the normal direction, both translational and rotational motions are of interest with respect to the tangential direction. In Sec. 2.3.2, a conceptual platform is established to contextualize the subsequent, comprehensive exploration of DSE modeling, rheology, and input parameter value determination for use in the multi-physics simulation software LS-DYNA (LSTC 2014b). In Sec. 2.3.3, relevant parameters of interest are introduced with focus given to the modeling of DSE assemblies in LS-DYNA.

2.3.1 Equation of Motion

The equation of motion for a dynamic system, based on D’Alembert’s principle, is an expression of “dynamic” equilibrium, where equilibrium must be satisfied at every instant of time (t). D’Alembert’s principle, which is dynamically analogous to the principle of virtual work for

applied forces in a static system, expresses that a system of rigid bodies satisfies dynamic equilibrium under a specific set of conditions. Namely, dynamic equilibrium is said to be achieved when the virtual work of both the sum of externally applied forces and inertial forces, and the sum of externally applied moments and moments of inertia are zero for any virtual displacement of the system. Enforcement of such conditions has proven useful in solving for the motion of particles during (and subsequent to) an arbitrary sequence of impacts and motions. The translational and rotational motion of an individual discrete particle i , with mass m and mass moment of inertia I_o , are expressed by the D'Alembert's principle as:

$$\begin{aligned} (F_i(t) - m_i a_i) \cdot \delta_{z_i} &= 0 \\ (M_i(t) - I_{o_i} \alpha_i) \cdot \theta_i &= 0 \end{aligned} \quad (2.3.1.1)$$

where the time-varying F_i and M_i quantities are the total applied force and the total applied moment (respectively) acting on particle i ; a_i and α_i are, respectively, the translational and rotational acceleration of particle i ; δ_{z_i} and θ_i are the translational and rotational virtual displacements of the particle i , respectively. Note the implicit presence of translational degree of freedom (DOF) z and a rotational DOF θ , in association with Eqn. 2.3.1.2. The relationship between forces (and moments) and motion can then be stated as:

$$\begin{aligned} F_i(t) - m_i a_i &= 0 \Leftrightarrow m_i a_i = F_i(t) \\ M_i(t) - I_{o_i} \alpha_i &= 0 \Leftrightarrow I_{o_i} \alpha_i = M_i(t) \end{aligned} \quad (2.3.1.2)$$

where the relations of Eqn. 2.3.1.2 are expressions of Newton's Second Law of motion in classical mechanics.

Consider a scenario where discrete particle i , undergoes a collinear collision with another individual discrete particle j in the z translational DOF. During impact, we can write the force equation of particles i and j as:

$$F(t) = m_i a_i = -m_j a_j \quad (2.3.1.3)$$

where $F(t)$ is the total force between the particles at any instant (t). Hence,

$$\begin{aligned} \frac{1}{m_i} F &= a_i \\ \frac{1}{m_j} F &= -a_j \\ -\left(\frac{1}{m_i} + \frac{1}{m_j} \right) F &= a_j - a_i = a \end{aligned} \quad (2.3.1.4)$$

where a is the relative acceleration of the system during impact and defined as $a = \ddot{\delta}_z$. The mass terms of Eqn. 2.3.1.4 are now defined as an effective mass m_{eff} , such that $\frac{1}{m_{eff}} = \frac{1}{m_i} + \frac{1}{m_j}$.

Therefore, (2.3.1.4) can be simplified to:

$$-F = m_{eff} a = m_{eff} \ddot{\delta}_z \quad (2.3.1.5)$$

If a linear contact model, consisting of a spring and a viscous damper, is used to model contact between particles i and j , then the normal force F can be rewritten as:

$$F = F_s^N + F_d^N \quad (2.3.1.6)$$

The normal spring force F_s^N is calculated based on the overlap between particles i and j , while and damping force F_d^N is proportional to the relative contact velocity:

$$\begin{aligned} F_s^N &= k_N \delta_z \\ F_d^N &= c_N \dot{\delta}_z \end{aligned} \quad (2.3.1.7)$$

where k_N and c_N are the spring stiffness and the damping coefficient, respectively. Thus, taking into account the particle-particle contact, the equation of motion for damped free vibration at the contact point is given as:

$$\begin{aligned} m_{eff} \ddot{\delta}_z &= -c_N \dot{\delta}_z - k_N \delta_z \\ \text{or} \\ m_{eff} \ddot{\delta}_z + c_N \dot{\delta}_z + k_N \delta_z &= 0 \end{aligned} \quad (2.3.1.8)$$

Similarly, for tangential motion (with both translation and rotation components), the damped free vibration of the contact point is described by:

$$\begin{aligned} m_{eff} \ddot{\delta}_x + c_T \left(\dot{\delta}_x + r \dot{\theta} \right) + k_T (\delta_x + r\theta) &= 0 \\ I_{0_{eff}} \ddot{\theta} + rc_T \left(\dot{\delta}_x + r \dot{\theta} \right) + rk_T (\delta_x + r\theta) &= 0 \end{aligned} \quad (2.3.1.9)$$

Taking the quantity $(\delta_x + r\theta)$ as a variable, it follows that:

$$m_{eff} I_{0_{eff}} \left(\ddot{\delta}_x + r \ddot{\theta} \right) + \left(I_{0_{eff}} + m_{eff} r^2 \right) c_T \left(\dot{\delta}_x + r \dot{\theta} \right) + \left(I_{0_{eff}} + m_{eff} r^2 \right) k_T (\delta_x + r\theta) = 0 \quad (2.3.1.10)$$

2.3.2 Conceptual Remarks on Geometry, Contact Mechanics, and Rheology

In the modeling of DSEs, spherical geometric descriptions are commonly assigned to individual particles. Alternatively stated, each individual sphere is defined (geometrically) as a center nodal point with a radius. In the multi-physics simulation software LS-DYNA (LSTC 2014a), rigid spherical particles are incorporated into the (numerical) DEM formulation. Consequently, for simulations in LS-DYNA, the radii of DSEs remain constant in the force and motion computations, regardless of the nature of DSE interactions. In general, each particle possesses three translational DOF and three rotational DOF.

Contact models are the physical basis of the DEM (Luding 2008). For DEM formulations that adopt the “soft” contact approach, there is a mapping between the contact forces generated during collision events and relatively more idealized dynamic systems. The elastic mechanism for the modeling of contact was first developed by Hertz (1882). Hertz’s quasi-static theory provides a very good approximation for collinear collisions between two nonconforming bodies, in which the contact region remains small in comparison to the size of either body. Further, the quasi-static theory holds explanatory value regarding the relationship between any two contacting spheres subjected to normal forces. Building upon Hertz’s normal force and the law of Coulombic friction, the relationship between contacting spheres subjected to tangential forces was derived by Mindlin (1949). As a result, the Hertz-Mindlin force-displacement law was proposed, and continues to play an important role in contact mechanics.

For example, Hertz-Mindlin theory is integral to the computational contact algorithms implemented for the LS-DYNA numerical linear contact model (LSTC 2014a). Specific to LS-DYNA simulations, mechanical parameters of particle-particle interaction can be defined using the keyword `*CONTROL_DISCRETE_ELEMENT`, which permits definitions of normal and tangential contact stiffnesses; damping coefficients; static and rolling friction coefficients; and, even liquid surface tension to account for capillary forces for modeling adhesion between saturated particles. As a fundamental assertion, these parameters are correlated to one another, where collectively, such parameters dictate the local deformation at any single contact between two particles. In turn, a given set of contact interactions can majorly affect the macroscopic behavior of the corresponding particulate system, even when said system is only subjected to (externally) quasi-static load conditions. Contact interactions also depend significantly on the material and material model type of particles, where the constitutive parameters dictate the intensity of contact stiffness.

2.3.3 Microscopic Constitutive Models and Parameters

Given the coordinates (x_1, y_1, z_1) and (x_2, y_2, z_2) , which represent the centroids of two particles, the position vectors P_1 and P_2 (with respect to the origin of the global coordinate system) are expressed as:

$$P_1 = x_1 \vec{i} + y_1 \vec{j} + z_1 \vec{k} \quad P_2 = x_2 \vec{i} + y_2 \vec{j} + z_2 \vec{k} \quad (2.3.3.1)$$

A penalty-based contact is used to capture the particle-particle interaction between these neighboring particles, and is expressed as:

$$d_{\text{int}} = R_1 + R_2 - |P_1 - P_2| \leq 0 \quad (2.3.3.2)$$

where R_1 and R_2 are the radii of particle 1 and particle 2, respectively.

When two spheres come into contact, a linear spring-dashpot system for both normal and tangential directions can be used to describe contact forces and the overlap (δ) between two particles. Such is the case for the DEM implementation in LS-DYNA (Fig. 2.3.3.1).

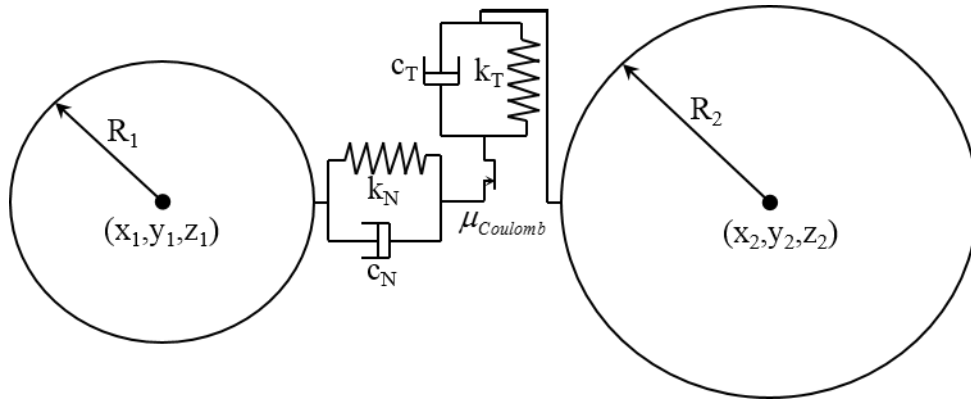


Figure 2.3.3.1. Particle-particle linear contact force model

In the stiffness model, the normal and tangential spring forces are calculated based on Hooke's law of linear elastic bodies, and operate on the particle-particle overlap distances:

$$\begin{aligned} F_N^S &= k_N \delta_N \\ F_T^S &= k_T \delta_T \end{aligned} \quad (2.3.3.3)$$

where k_N is normal spring stiffness, k_T is the tangential spring stiffness, δ_N and δ_T are, respectively, the normal and tangential overlap distances for the two interacting particles. To account for energy dissipation of the dynamic system (which commonly involves considerations for a coefficient of restitution), viscous damping forces are generated in parallel with those of the elastic spring stiffness. Thus, contact behavior is changed from elastic to viscoelastic, and further, this form of damping does not affect the equilibrium value of the resultant force. The damping mechanism does, however, reduce the number of calculation cycles needed to reach force equilibrium under at rest conditions. The normal and tangential damping forces are calculated based on normal and tangential components of relative contact velocity:

$$F_N^D = c_N \dot{\delta}_N \quad (2.3.3.4)$$

$$F_T^D = c_T \dot{\delta}_T$$

where c_N and c_T are normal and tangential damping constant respectively. Thus, the magnitude of the normal force is:

$$F_N = k_N \delta_N + c_N \dot{\delta}_N \quad (2.3.3.5)$$

For modeling slippage during particle-particle interactions, the various frictional forces that arise in association with mechanical contact can be modeled using Coulomb's law of dry friction. For the scenario of particle-particle (relative) translation, if the condition $F_T \leq \mu_{Coulomb} F_N$ is satisfied at any time during contact, then the contacting spheres are in a static friction condition. For this condition, the tangential force can be quantified based on Eqns. 2.3.3.3 and 2.3.3.4. Otherwise, sliding occurs and the tangential contact force reaches its maximum (limiting) value, F_{Tmax} :

$$F_{Tmax} = \mu_{Coulomb} F_N \quad (2.3.3.6)$$

where $\mu_{Coulomb}$ is the static friction coefficient. More generally, the magnitude of the tangential force, F_T , is given by:

$$F_T = \min \left(k_T \delta_T + c_T \dot{\delta}_T, \mu_{Coulomb} F_N \right) \quad (2.3.3.7)$$

Furthermore, the case of Coulomb friction is extended in LS-DYNA by the introduction of a rolling friction coefficient, $\mu_{rolling}$. For scenarios involving particle to particle contacts, resultant particle rotations are inhibited through introduction of the rolling resistance moment M_R , shown in equation 2.3.3.8.

$$M_T \leq M_R \quad (2.3.3.8)$$

$$M_R = F_T R = \mu_{roll} F_N R$$

A listing of the microscopic parameters, which are typical of numerical treatments of sphere-sphere contact interactions, is given in Table 2.3.3.1. In the context of modeling in LS-DYNA, parameter input values are specified using the keyword `*CONTROL_DISCRETE_ELEMENT` (LSTC 2014b).

Table 2.3.3.1. Contact parameters available in LS-DYNA for modeling sphere-sphere interactions

Parameter	Symbol
Normal damping coefficient	<i>NDAMP</i>

Tangential damping coefficient	<i>TDAMP</i>
Coefficient of static friction	μ_{static}
Coefficient of rolling friction	$\mu_{rolling}$
Normal stiffness factor	<i>NormK</i>
Shear stiffness factor	<i>ShearK</i>

2.4 Detailed Description of Rheological Model

A detailed description of the DSE rheological components is presented in Sec. 2.4, where care is taken to document how such components fit into the modeling of DSEs in LS-DYNA (LSTC 2014b). In Sec. 2.4.1 through Sec. 2.4.3, relevant contact stiffness parameters are defined (for both normal and tangential interactions), and the analytical network of relationships between the contact stiffness parameters are delineated. In Sec. 2.4.4, a similar treatment is applied to investigate those DSE rheological components dedicated to contact-dependent viscous damping. As a synthesis of the analytical derivations of Sec. 2.4.1 through Sec. 2.4.4, analytical expressions pertaining to contact stiffness and viscous damping are brought together in Sec. 2.4.5 as part of an examination of DSE restitution coefficients. In Sec. 2.4.6, a novel methodology is developed to map from the (analytical) nonlinear relationships of contact stiffness (introduced in Sec. 2.4.1 through Sec. 2.4.3) to the (numerical) linear contact spring-damper implementation in LS-DYNA. Finally, in Sec. 2.4.7, the concept of capillary suction pressure is introduced and the corresponding implementation in LS-DYNA is explored.

2.4.1 Microscopic Contact Parameters of LS-DYNA DSE Analysis

Recall that in Sec. 2.3.3, parameters were introduced in association with use of the linear contact force model implemented in LS-DYNA. In this context, one of the most important parameters for modeling penalty-based particle-particle interactions (i.e., mechanical contact) is the elastic spring stiffness. The formulation for normal spring stiffness k_N in LS-DYNA (LSTC 2014b) depends on two quantities: 1) Sphere radius (e.g., R_1 , R_2); and, 2) Compression modulus (e.g., K_1 , K_2). For any two interacting (contacting) spheres, a normal stiffness factor *NormK*, is then used to scale the normal contact stiffness:

$$k_N = \begin{cases} \frac{K_1 R_1 K_2 R_2}{K_1 R_1 + K_2 R_2} \text{NormK} : \text{if NormK} > 0 \\ |NormK| : \text{if NormK} < 0 \end{cases} \quad (2.4.1.1)$$

Specific to the LS-DYNA implementation of the DEM, tangential spring stiffness k_T is then calculated in proportion to the normal spring stiffness:

$$k_T = k_N \text{ShearK} \quad (0.1 \leq \text{ShearK} \leq 0.9) \quad (2.4.1.2)$$

The maximum overlap between particles is therefore strongly influenced (in LS-DYNA) by the magnitude of the normal contact stiffness. As a contributing factor in calculating the normal contact stiffness in LS-DYNA, the isotropic compression modulus is specific to the type of material being considered (e.g., steel, aluminum, granite, silica sand), as well as the material model (e.g., elastic, elastic-perfectly plastic) that is assigned to the DSEs. In the current study, a linear elastic treatment is elected for modeling of granular material using DSEs. Accordingly, the LS-DYNA keyword `*MAT_ELASTIC` is utilized, which requires input of three (constant) parameter values: mass density (ρ); Young's modulus (E); and Poisson's ratio (ν). Note that the Young's modulus can be approximated by making an equivalency between the normal spring stiffness and linearization of Hertz normal stiffness. In forming the normal contact stiffness, the (constant) bulk modulus for an individual DSE is calculated as:

$$K = \frac{E}{3(1-2\nu)} \quad (2.4.1.3)$$

Given the role of the bulk modulus in calculating the normal contact stiffness in LS-DYNA, bulk modulus necessarily affects the size of the critical time step for ensuring stability of the (explicit) time-stepping algorithms. More specifically, to ensure stability during the explicit numerical integration of the equations of motion in LS-DYNA, a critical time step $dt_{Cundall}$ (determined based on Cundall's approach; Cundall and Strack 1979) is defined as:

$$dt_{Cundall} = 0.2\pi \sqrt{\frac{(4/3)\rho\pi R_{sphere}^2}{K(NormK)}} \quad (2.4.1.4)$$

where R_{sphere} is the radius of a given sphere of interest.

For numerical models of DSE assemblies that utilize non-uniform spheres (i.e., spheres with differing radii), the critical time step should be calculated for each type of sphere being modeled, and the minimum should be specified for the analysis. The value of 0.2 in the calculation of Cundall's time step ($dt_{Cundall}$) in Eqn. 2.4.1.4 is included to limit relative errors in energy conservation for the linear elastic spring model to relative magnitudes of approximately less than five percent (Malone 2008). Specific to modeling in LS-DYNA, the time step size can be directly specified using the keyword `*CONTROL_TIMESTEP`.

An important consideration in the modeling of granular soil using DSE assemblies is the selection of primary and secondary sphere radii. As an example selection procedure, consider the grain size distribution in Fig. 2.4.1.1, which was derived from sieve analysis in a laboratory setting. Purely as furtherance of the example, the diameter of 100 percent finer by weight, D_{100} , is selected as a primary particle size for modeling a given coarse-grained soil. Having quantified the D_{100} , a shear jamming scheme would then potentially be adopted using either D_{50} or smaller size of secondary particles, depending on the application of interest (i.e., depending on the available computational resources and the number of spheres needed to populate the simulation space). Upscaling procedures are being developed as part of ongoing research efforts, and will be addressed in detail as part of the reporting for Task 3: simulations of jammed systems study particulate clustered configurations leading to jamming in both static systems and systems under

shear (refer to Section 2.1.8 for “shear jamming” modeling). Under shear stress, average cluster size may diverge after a finite amount of strain, leading to a jammed state. A particle configuration may exist in a jammed state with a stress required to “break” the force chains causing the jam.

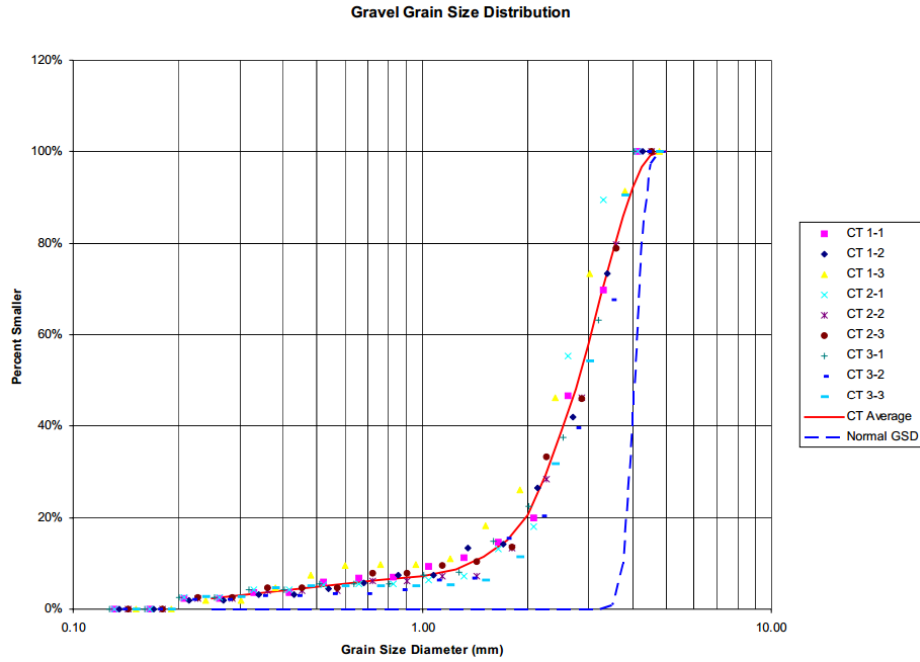


Figure 2.4.1.1. Example grain size distribution for a granular soil (Nielsen 2004)

Regardless of the means by which primary and secondary DSE radii are selected (and, as needed, upscaled), the stiffness factors *NormK* and *ShearK* are necessary in quantifying spring stiffnesses. Specific to the DSE stiffness formulation in LS-DYNA, the tangential to normal stiffness ratio k_T/k_N is analagous to the ratio of tangential to normal stiffness ($ShearK/NormK$). For a dense packing of particles in a mechanically stable state, the stiffness ratio most greatly influences the generation of those contact forces associated with relatively high levels of Coulombic friction (Cundall and Strack 1979). Furthermore, while shear stiffness can play a dominant role in driving the motions of interacting DSEs, as soon as particle-particle slippage occurs, the shear force reaches a maximum and subsequent variations in contact forces are determined solely by the normal particle-particle interactions. Considering undamped free vibration of an individual DSE in both the tangential and normal directions, the equations of motion (Eqn. 2.3.1.8 and Eqn. 2.3.1.10) are then expressed as:

$$\begin{aligned}
 m_{eff} \ddot{\delta}_z + k_N \delta_z &= 0 \\
 m_{eff} I_{0_{eff}} \left(\ddot{\delta}_x + R \ddot{\theta} \right) + \left(I_{0_{eff}} + m_{eff} R^2 \right) k_T (\delta_x + R\theta) &= 0
 \end{aligned}
 \tag{2.4.1.5}$$

where $I_{0_{eff}}$ is the effective moment of inertia of a given sphere-sphere pair. Likewise, the natural frequencies in the normal (ω_N) and tangential (ω_T) directions can be expressed as:

$$\omega_N = \sqrt{\frac{k_N}{m_{eff}}} \quad (2.4.1.6)$$

$$\omega_T = \sqrt{\frac{(I_{0_{eff}} + m_{eff}R^2)k_T}{m_{eff}I_{0_{eff}}}}$$

For the case of spheres of equal size and same material, the natural periods are calculated as:

$$T_N = \frac{2\pi}{\sqrt{\frac{k_N}{(m/2)}}} \quad (2.4.1.7)$$

$$T_T = \frac{2\pi}{\sqrt{\frac{(I_0 + mR^2)k_T}{(mI_0/2)}}}$$

where m is the mass of an individual sphere, and I_0 is the moment of inertia of an individual sphere. By equating the periods T_N (normal) and T_T (tangential), the relationship between k_N and k_T can be defined such that normal force and tangential force are simultaneously released:

$$\frac{k_T}{k_N} = \frac{I_0}{I_0 + mR^2} = \frac{2}{7} \quad (2.4.1.8)$$

since $I_0 = \frac{2}{5}mR^2$ for a solid sphere. Note that the ratio of k_T to k_N is set as the default value when modeling DSE using LS-DYNA (LSTC 2014b).

In addition, these two equations of motion can be solved for given initial conditions of velocity in normal direction $\dot{\delta}_{z_0}$ and tangential direction $\left(\dot{\delta}_{x_0} + R\dot{\theta}_0\right)$ as:

$$\delta_z(t) = \dot{\delta}_{z_0} \sqrt{\frac{m_{eff}}{k_N}} \sin\left(t \sqrt{\frac{k_N}{m_{eff}}}\right)$$

$$X(t) = \left(\dot{\delta}_{x_0} + R\dot{\theta}_0\right) \sqrt{\frac{m_{eff}I_{0_{eff}}}{(I_0 + m_{eff}R^2)k_T}} \sin\left(t \sqrt{\frac{(I_{0_{eff}} + m_{eff}R^2)k_T}{m_{eff}I_{0_{eff}}}}\right) \quad (2.4.1.9)$$

where $X(t)$ is the horizontal displacement as a function of time. By differentiating the horizontal displacement with respect to time t , horizontal velocity $\dot{X}(t)$ is obtained:

$$\dot{X}(t) = \left(\dot{\delta}_{x_0} + R \dot{\theta}_0 \right) \cos \left(t \sqrt{\frac{\left(I_{0_{eff}} + m_{eff} R^2 \right) k_T}{m_{eff} I_{0_{eff}}}} \right) \quad (2.4.1.10)$$

Contact durations ($T_{contact}$) corresponding to the condition that $\delta_z(T_{contact}) = 0$ can then be defined in accordance with Eqn. 2.4.1.9 such that:

$$T_{contact} = \pi \sqrt{\frac{m_{eff}}{k_N}} \quad (2.4.1.11)$$

Thus, the horizontal velocity just at the instant of contact termination is:

$$\dot{X}(T_{contact}) = \left(\dot{\delta}_{x_0} + R \dot{\theta}_0 \right) \cos \left(\pi \sqrt{\frac{m_{eff}}{k_N}} \sqrt{\frac{\left(I_{0_{eff}} + m_{eff} R^2 \right) k_T}{m_{eff} I_{0_{eff}}}} \right) \quad (2.4.1.12)$$

For interactions between spheres defined using identical geometric, constitutive, and rheological descriptions, the tangential coefficient of restitution (e_T) can be expressed in terms of k_T and k_N as (Fig. 2.4.1.2):

$$e_T = -\frac{\dot{X}(T_{contact})}{\left(\dot{\delta}_{x_0} + R \dot{\theta}_0 \right)} = -\cos \left(\pi \sqrt{\frac{7}{2}} \sqrt{\frac{k_T}{k_N}} \right) \quad (2.4.1.13)$$

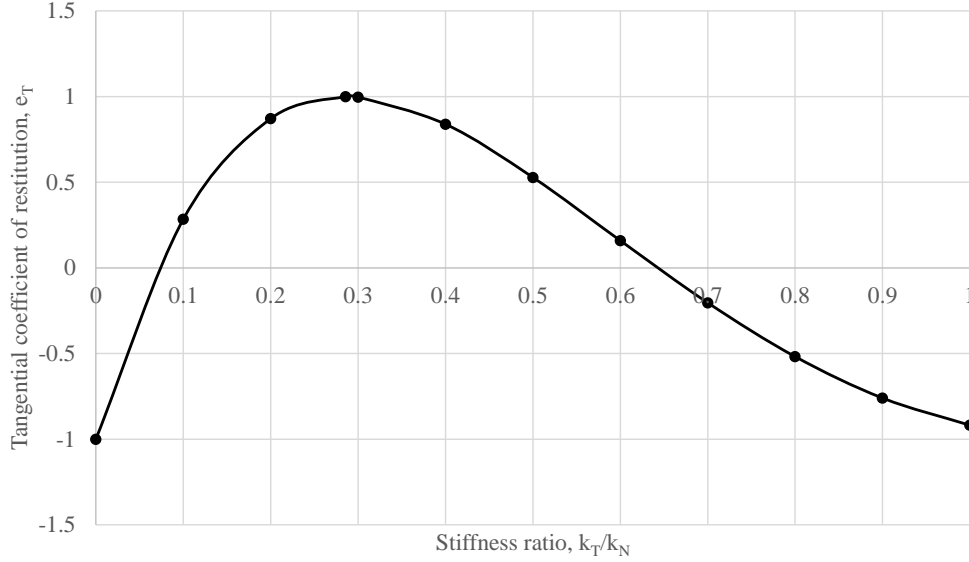


Figure 2.4.1.2. Tangential coefficient of restitution (e_T) versus stiffness ratio (k_T to k_N)

By employing the stiffness ratio of $2/7$ (recall Eqn. 2.4.1.8), the behavior of DSE is characterized as perfectly elastic. However, micromechanical behaviors of grains are viscoelastic, in which granular particle collision tests indicate energy loss per contact even with an elastic solid wall with smooth surfaces (Sommerfeld and Huber 1999). The degree of potential energy loss in collisions depends on particle size, shape, and surface roughness, which leads to both impact-velocity dependent damping (viscous) and friction-induced Coulombic damping (Abedi 2009). As we separately model an asymptotic limiting value per coefficients of friction as a model parameter, viscous damping is incorporated in the particle contact definition using numerical dampers. The determination of viscous damping requires analysis of natural frequency of DSE, which depends on the size of DSE, mass density, frictional parameters used in force mapping for shape transformation (see Section 2.1.8), and contact stiffnesses. In the following, we derive the correlations among the contact parameters in a step-by-step manner in order to increase confidence in computation of inter-particle shear forces and corresponding tangential stiffness (i.e., ratio of k_T to k_N).

In addition to considerations for spring stiffness, the mechanical penalty-based particle-particle contact formulation adopted in the current study is also sensitive to parameters that make up the coefficient of restitution. In LS-DYNA, the coefficient of restitution is treated through specification of some fraction of the normal and tangential critical damping forces. Regarding input parameters specific to LS-DYNA, the damping coefficients corresponding to the normal and tangential directions are referred to as *NDAMP* and *TDAMP*, respectively.

$$\begin{aligned}
 c_N &= (NDAMP)c_{cri_N} \\
 c_T &= (TDAMP)c_{cri_T}
 \end{aligned}
 \tag{2.4.1.14}$$

where $c_{cri_N} = 2m_{eff}\omega_N = 2\sqrt{m_{eff}k_N}$ and $c_{cri_T} = 2m_{eff}\omega_T = 2\sqrt{m_{eff}k_T}$; $0 \leq NDAMP, TDAMP \leq 1$.

In Sec. 2.4.4., the LS-DYNA input parameters *NDAMP* and *TDAMP* will be explored in detail, and a methodology will be established to ensure that (for varied values of *NDAMP*, *TDAMP*) damped vibrations hold matching frequency content in both the normal and tangential directions. Note that the damping effects associated with use of *NDAMP* and *TDAMP* are fundamentally different process from that of Coulombic damping (i.e., the Coulomb friction law). In particular, the two damping parameters (*NDAMP*, *TDAMP*) permit the modeling of viscous material behavior.

Two final parameters that are used to define particle-particle interactions in LS-DYNA are those of the static and rolling friction coefficients, μ_{static} and μ_{rolling} , respectively. For the DEM implementation available in LS-DYNA, frictional force generation is governed by Coulombic friction, where a detailed treatment of the physics underlying frictional phenomena was discussed in Sec. 2.1. From a numerical standpoint, friction forces that arise during particle-particle interactions depend on the input value of coefficient of static friction (μ_{static}) and the sum of all normal contact forces F_N . When the coefficient of static friction is input as zero, rotational DOF are removed from the associated DSEs. Furthermore, no tangential friction forces may be induced during periods of contact. For scenarios where non-zero values of static (sliding) friction are utilized (i.e., when rotational DOF are active for the DSEs), the rolling friction coefficient can additionally be specified to model particle-particle rolling resistance. The ratio of the rolling (μ_{rolling}) to static (μ_{static}) friction coefficients is further explored in Sec. 2.4.5.

2.4.2 Hertzian Normal Contact Stiffness

In 1880, Hertz developed the theory of elastic deformations localized near contact patches, and also, developed analytical procedures to predict stresses that arise due to contact between two elastic bodies. The work of Hertz has been shown to be well suited for explaining quasi-static mechanical contacts between two spheres (Johnson 1985; Stronge 2000). The concept of contacts between two spheres is complex, where for example, two spherical bodies can be said to be in contact when physically sharing some contact point (e.g., point O in Fig. 2.4.2.1a). Additionally, two spheres can be said to be in contact when pressed together such that the spherical geometries occupy a shared overlapping region (Fig. 2.4.2.1b).

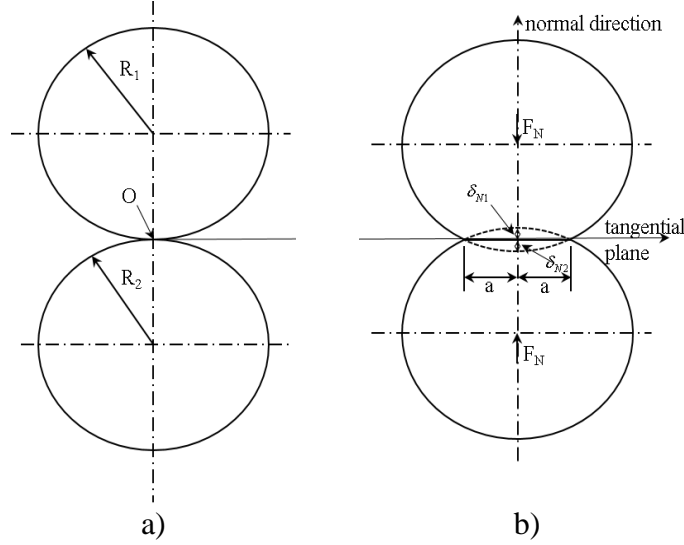


Figure 2.4.2.1. Contact between two spheres: a) With shared contact point O; b) With overlapping regions

In adopting the Hertzian theory on contact phenomena, the applied force at the contact between two nonconforming elastic bodies in the normal direction, F_N , can be written in terms of displacement as:

$$F_N = \frac{4}{3} E^* \sqrt{R} \delta_N^{3/2} \quad (2.4.2.1)$$

where $\frac{1}{E^*} = \frac{1-\nu_1^2}{E_1} + \frac{1-\nu_2^2}{E_2}$; E_1, E_2 are elastic moduli and ν_1, ν_2 are Poisson's ratios assigned to sphere one and sphere two, respectively. Likewise, $\frac{1}{R} = \frac{1}{R_1} + \frac{1}{R_2}$, where R_1, R_2 are significant radii of each spherical body and R is the relative radius of curvature or effective radius. Lastly, δ_N is the total overlap distance in the normal direction, $\delta_N = \delta_{N1} + \delta_{N2}$, and where δ_{N1}, δ_{N2} are the overlap distances specific to sphere one and sphere two, respectively. Note that, relative to the unreformed sphere geometries, the overlap distances (δ_{N1}, δ_{N2}) are treated as being equal to the displacements of the sphere centroids. Along these lines, δ_{N1} and δ_{N2} are referred to in terms of displacement in the following derivation.

By differentiating the force-displacement relationship (Eqn. 2.4.2.1) with respect to normal displacement (δ_N), the Hertz measure of normal stiffness (k_{N_Hertz}) can be expressed as:

$$\frac{dF_N}{d\delta_N} = k_{N_Hertz} = 2E^* \sqrt{R} \delta_N^{1/2} \quad (2.4.2.2)$$

Recalling Fig. 2.4.2.1b, the contact geometry along the tangential plane can be described as the area of a circle, where the associated radius (a) is related to the normal displacement (δ_N). Alternatively, the radius (a) can be defined in terms of applied force:

$$a = \sqrt{R\delta_N} = \left(\frac{3F_N R}{4E^*} \right)^{1/3} \quad (2.4.2.3)$$

Having defined a radius representing the contacting region, the maximum normal contacting pressure (p_0) is then given by:

$$p_0 = \frac{3F_N}{2\pi a^2} = \left(\frac{6F_N E^{*2}}{\pi^3 R^2} \right)^{1/3} \quad (2.4.2.4)$$

Combining Eqn. 2.4.2.1 and Eqn. 2.4.2.3 with Eqn. 2.4.2.4, the normal displacement (δ_N) can be expressed as a function of the maximum normal contacting pressure (p_0):

$$\delta_N = \left(\frac{\pi p_0 \sqrt{R}}{2E^*} \right)^2 \quad (2.4.2.5)$$

Maximum normal pressure at contact can then be obtained by incorporating a pertinent yield criterion. In the current study, the Von Mises yield criterion is adopted, leading to the following relationship between maximum normal pressure and yield stress (σ_{yield}):

$$p_0 = \frac{\sigma_{yield}}{\sqrt{3}} \quad (2.4.2.6)$$

2.4.3 Tangential Contact and Coulombic Friction

Consider two spherical elastic bodies, which are: 1) Initially pressed together by means of a Hertz normal force F_N ; and, 2) Subjected to an increasing tangential force F_T . Further, in this scenario, the normal contacting force is held constant while the tangential force is gradually increased from zero. Under these conditions, expressions relating the tangential direction force (F_T) and tangential displacement (δ_T) are of the form (Johnson, 1985):

$$\delta_T = \frac{3\mu F_N}{16aG^*} \left[1 - \left(1 - \frac{F_T}{\mu F_N} \right)^{2/3} \right] \quad (2.4.3.1)$$

$$F_T = \mu F_N \left[1 - \left(1 - \frac{16aG^* \delta_T}{3\mu F_N} \right)^{3/2} \right]$$

where μ is the Coulomb friction coefficient, $G = \frac{E}{2(1+\nu)}$, $\frac{1}{G^*} = \frac{2-\nu_1}{G_1} + \frac{2-\nu_2}{G_2}$, having G_1 and G_2 are the shear moduli associated with each spherical body.

The stick region of two interacting spherical bodies is defined as a circle of radius, c , and can be expressed as:

$$c = a \left(1 - \frac{F_T}{\mu F_N} \right)^{1/3} \quad (2.4.3.2)$$

recalling that a is the radius of the Hertz contact area. By differentiating force-displacement equation (2.4.3.1) with respect to tangential displacement, the tangential stiffness (referred to as $k_{T_Mindlin}$, as this quantity derives from the work of Mindlin) can be expressed as:

$$\frac{dF_T}{d\delta_T} = k_{T_Mindlin} = 8aG^* \left(1 - \frac{16aG^* \delta_T}{3\mu F_N} \right)^{1/2} \quad (2.4.3.3)$$

The ratio of the Mindlin tangential stiffness ($k_{T_Mindlin}$) and Hertz normal stiffness (k_{N_Hertz}) is:

$$\frac{k_{T_Mindlin}}{k_{N_Hertz}} = \frac{8G^* \left(1 - \frac{16aG^* \delta_T}{3\mu F_N} \right)^{1/2}}{2E^*} = \frac{4G^*}{E^*} \left(1 - \frac{4G^* \delta_T}{\mu E^* \delta_N} \right)^{1/2} \quad (2.4.3.4)$$

where the ratio expressed in Eqn. 2.4.3.4 is only valid when the condition $\delta_T \leq \frac{\mu E^* \delta_N}{4G^*}$ is satisfied.

When the tangential contact force component (F_T) is on the verge of being realized (i.e., $F_T \approx 0$), the area of the stick region equals the Hertz contact area (i.e., $c \approx a$). Therefore, slip area is very small and the contact approaches a no-slip condition. Also, due to the form of the relationship between force and displacement (Eqn. 2.4.3.1), tangential displacement is minimal ($\delta_T \approx 0$), which allows for a (conditionally valid) expression of Mindlin tangential stiffness:

$$\frac{dF_T}{d\delta_T} = k_{T_Mindlin} = 8aG^* \quad (2.4.3.5)$$

Consequently, when the above conditions are satisfied, the stiffness ratio given in Eqn. 2.4.3.4 becomes:

$$\frac{k_{T_Mindlin}}{k_{N_Hertz}} = \frac{4G^*}{E^*} = \frac{\frac{1-\nu_1}{G_1} + \frac{1-\nu_2}{G_2}}{\frac{1-\nu_1/2}{G_1} + \frac{1-\nu_2/2}{G_2}} \quad (2.4.3.6)$$

For scenarios where particle-particle sliding is imminent (i.e., when the stick region reduces to a single point, such that $c = 0$), the corresponding tangential displacement ($\delta_{T_sliding}$) and force (F_T) reduce to (relative to Eqn. 2.4.3.1):

$$\delta_{T_fully_sliding} = \frac{3\mu F_N}{16aG^*}$$

and

$$F_T = \mu F_N \quad (2.4.3.7)$$

For any time t in which the expressions given in Eqn. 2.4.3.7 hold, the system is said to have transitioned from quasi-static to transient conditions. It follows that, under transient conditions, the tangential component of sphere-sphere contacting force is limited to the Coulomb frictional force, and thus free sliding initiates. Also, under such conditions, the stiffness ratio (k_T/k_N) approaches zero.

Now, consider a scenario in which two spheres are engaged by means of applying equal and opposite oblique forces F_{ob} at each sphere centroid, where the forces are oriented at a constant angle of α , with respect to the normal direction (and where $0 < \alpha < 90$). The oblique force F_{ob} can be decomposed into the normal (F_{ob_T}) and tangential (F_{ob_N}) components:

$$F_{ob_N} = \Delta F_N = F_{ob} \cos(\alpha)$$

$$F_{ob_T} = F_{ob} \sin(\alpha) \quad (2.4.3.8)$$

Further, in this scenario, the total normal (F'_N) and tangential (F_T) forces are given by:

$$F'_N = F_N + \Delta F_N$$

$$F_T = F_{ob_T} = \tan(\alpha) \Delta F_N \quad (2.4.3.9)$$

For any time t , increases in the total normal force (F'_N) will correspond to increases in the radius of the circular contacting area (from a to b). According to Johnson (1985), the no-slip condition within the contact area holds as long as F_T does not exceed $\mu \Delta F_N$, from which it follows that:

$$\tan(\alpha) \leq \mu \quad (2.4.3.10)$$

As a result, the relative tangential displacement (δ_T) becomes:

$$\delta_T = \frac{F_T}{8bG^*} = \frac{\tan(\alpha)\Delta F_N}{8bG^*} \quad (2.4.3.11)$$

If the angle of the oblique force F_{ob} is greater than the resisting frictional force, then slip occurs.

For the scenario of oblique forces acting on two spheres, the force-displacement in the tangential direction is expressed as:

$$\delta_T = \frac{3\mu F'_N}{16bG^*} \left[1 - \left(1 - \frac{F_T}{\mu F'_N} \right)^{2/3} \right] \quad (2.4.3.12)$$

Similarly, the stick region of two spherical bodies (defined by a circle of radius, c) can be expressed as:

$$c = b \left(1 - \frac{F_T}{\mu F'_N} \right)^{1/3} = b \left(1 - \frac{F_{ob} \sin(\alpha)}{\mu(F_N + F_{ob} \cos(\alpha))} \right)^{1/3} \quad (2.4.3.13)$$

For any time t in which sliding may initiate (i.e., when the stick region approaches the condition $c = 0$), the oblique force is given by:

$$F_{ob} = \frac{\mu F'_N}{\cos(\alpha) [\tan(\alpha) - \mu]}, \tan(\alpha) > \mu \quad (2.4.3.14)$$

Further, under such conditions, the tangential displacement ($\delta_{T_sliding}$) and force (F_T) are given by:

$$\begin{aligned} \delta_{T_sliding} &= \frac{3\mu F'_N}{16bG^*} \\ F_T &= \frac{\mu F'_N}{1 - \mu \cot(\alpha)}, \tan(\alpha) > \mu \end{aligned} \quad (2.4.3.15)$$

2.4.4 Natural Frequencies and Critical Damping of Two Spheres in Contact

The second order differential equation governing two energy storage elements, including a spring and a dashpot, at the contact interface between two spheres (with non-zero masses) is defined as:

$$m_{eff} \ddot{x} + c \dot{x} + kx = 0 \quad (2.4.4.1)$$

where m_{eff} is effective mass, c is damping constant and k is stiffness of the contact point. Solutions to Eqn. 2.4.4.1 can consist of: 1) Two unique real-valued roots, in the overdamped case; 2) Two equal real-valued roots, in the critical damped case; or, 3) Two complex-valued roots (which form complex conjugates), in the underdamped case.

For the purposes of numerical modeling, it is convenient to consider system-wide viscous damping via specification of a damping coefficient ($DAMP$), which is equal to zero for no damping, and equal to unity for critical damping of a system. The underdamped condition is then imposed by specifying a value of $DAMP$ that falls within the range of zero and unity. Recalling Eqn. 2.4.4.1, the damping constant c can be defined as $c = 2m_{eff}\omega DAMP$, where $\omega = \sqrt{\frac{k}{m_{eff}}}$ is the

natural frequency of the system. By defining $x = e^{\lambda t}$, the characteristic equation can be written as:

$$\lambda^2 + 2\omega DAMP\lambda + \omega = 0 \quad (2.4.4.2)$$

The pair of complex conjugates, or eigenvalues (λ_1, λ_2), that constitute solutions to Eqn. 2.4.4.2 can be written in terms of the damping coefficient (c) and natural frequency (ω) as:

$$\lambda_{1,2} = -DAMP\omega \pm i\omega\sqrt{1 - DAMP^2} \quad (2.4.4.3)$$

where the real part of Eqn. 2.4.4.3 is the attenuation and the imaginary part is the damped natural frequency, ω_D . The solutions to Eqn. 2.4.4.3 can be plotted on the complex plane, as shown in Fig. 2.4.4.1. As a demonstration of how to interpret Fig. 2.4.4.1, consider a mid-plane angle θ is equal to 45° . For this scenario, Fig. 2.4.4.1 enables direct determination of the damping parameter

($DAMP$), which would be $\frac{\sqrt{2}}{2} = 0.707$.

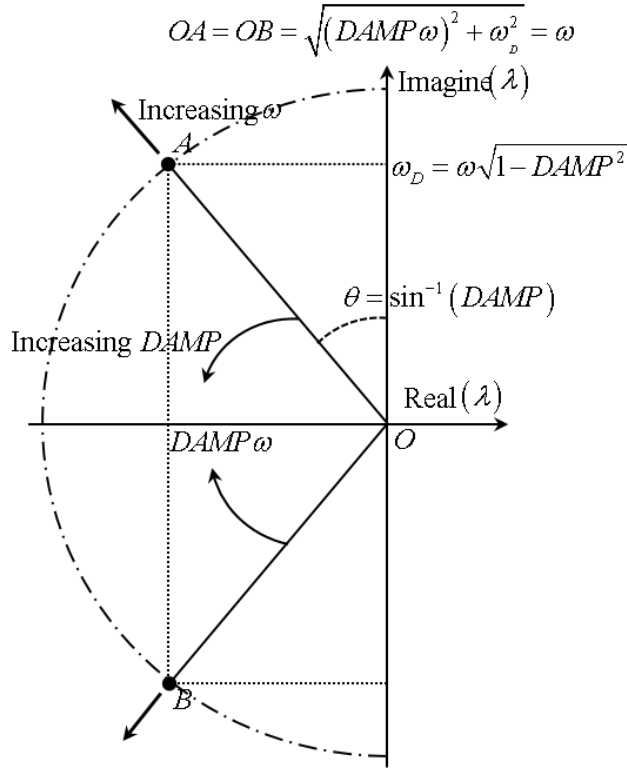


Figure 2.4.4.1. Solutions to the characteristic equation plotted in the complex plane

Now consider a system undergoing damped free vibration in association with two spheres that overlap one another in the normal direction. As an exploration of how stiffness and mass quantities of DSE relate to damping phenomena, additionally consider the system subject to initial conditions of $x(t) = 0$ and $\dot{x}(t) = 4.429$. The calculated displacement responses at the contact point are plotted in Fig. 2.4.4.2, where each curve represents a selected value of $NDAMP$ (ranging from 0.1 to 0.9 in increments of 0.1). The collected displacement histories (Fig. 2.4.4.2) indicate that contact duration increases in proportion to increasing values for the damping constant ($NDAMP$). Quantitatively, contact duration can be written in terms of the normal damping coefficient and natural frequency as:

$$T_{contact} = \frac{\pi}{\omega_N} \sqrt{\frac{1}{1 - NDAMP^2}} \quad (2.4.4.4)$$

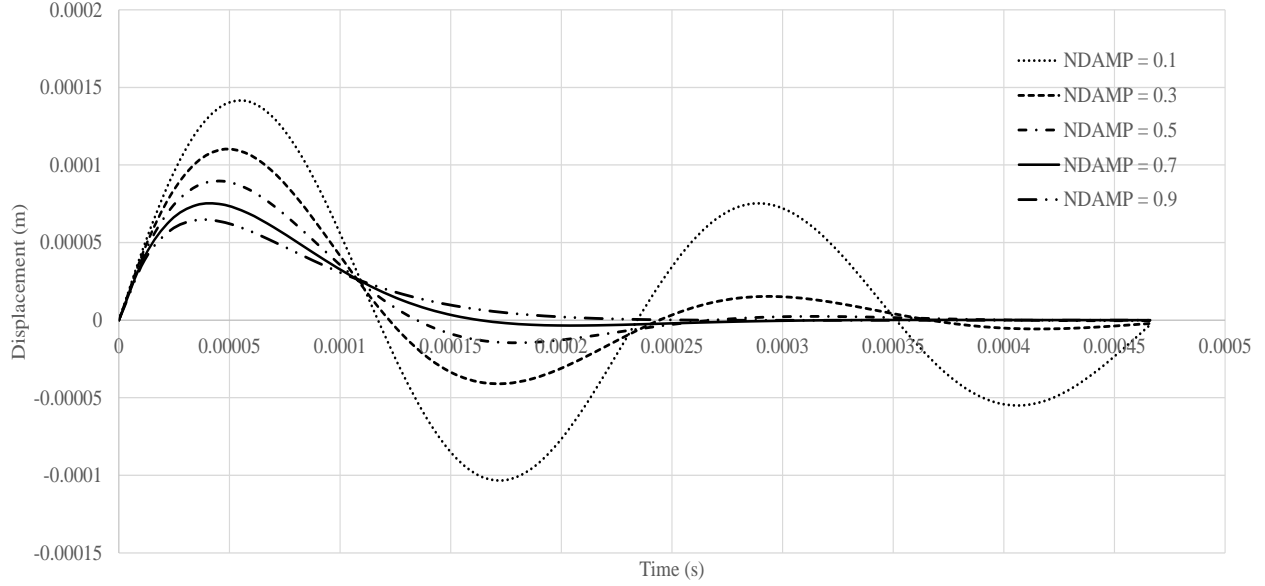


Figure 2.4.4.2. Displacement responses at the contact interface as damping is varied for two overlapping spheres

As indicated in Fig. 2.4.4.2, the local minima and maxima of displacements are attenuated for each cycle of oscillation. Further, the level of peak-displacement attenuation becomes more pronounced with increased damping. For the scenario considered, values of *NDAMP* that are equal to or greater than 0.7 correspond to (approximately) full attenuation of oscillatory displacements for times beyond the first half-cycle of response. The absence of such pronounced attenuation is referred to as “overshoot”, and is a decidedly non-physical phenomenon with respect to the motions of interacting granular particles. Therefore, in regards to the numerical modeling of granular particles, an *NDAMP* of 0.7 is adopted for carrying out simulations of DSE assemblies in the current study.

The ratio of tangential to normal natural frequencies of contact resonance (ω_T and ω_N , respectively) for an elastic impact between two spheres, based on Hertz-Mindlin contact theory, is defined as (Johnson 1985):

$$\frac{\omega_T}{\omega_N} = (2\chi)^{1/2} \quad (2.4.4.5)$$

where the parameter χ is defined by:

$$\chi = \frac{\kappa m_{eff}}{2m_{eff}^*} \quad (2.4.4.6)$$

and where κ is a stiffness ratio: $\kappa = \frac{\frac{1-\nu_1}{G_1} + \frac{1-\nu_2}{G_2}}{\frac{1-\nu_1/2}{G_1} + \frac{1-\nu_2/2}{G_2}}$; $m_{eff} = \frac{m_1 m_2}{m_1 + m_2}$;

$m_{eff}^* = \frac{m_1^* m_2^*}{m_1^* + m_2^*} = \frac{m_1 m_2}{m_1 \left(1 + \frac{R_2^2}{k_2^2}\right) + m_2 \left(1 + \frac{R_1^2}{k_1^2}\right)}$; and, the $k_i^2 = \frac{I_i}{m_i}$ values are the radii of gyration of the

spheres about their respective centers of mass. Given the moment of inertia for a solid sphere, $I_i = \frac{2}{5} m_i R_i^2$, the radius of gyration values become $k_i^2 = \frac{2}{5} R_i^2$ and $m^* = \frac{m_1 m_2}{m_1 \left(\frac{7}{2}\right) + m_2 \left(\frac{7}{2}\right)}$. Also, the

ratio of resonance frequencies (Eqn. 2.4.4.5) can then be expressed as:

$$\frac{\omega_T}{\omega_N} = (3.5\kappa)^{1/2} \quad (2.4.4.7)$$

In the context of modeling in LS-DYNA, the following relationship must be satisfied to ensure that damped vibrations hold matching frequency content in both the tangential and normal directions:

$$\frac{TDAMP}{NDAMP} = \frac{1}{(3.5\kappa)^{1/2}} \quad (2.4.4.8)$$

2.4.5 Restitution Coefficients

Coefficient of Normal Restitution (e_N)

For the modeling of granular media in industrial applications, the normal coefficient of restitution ($NDAMP$) is set to a relatively high value (approximately 0.5 to 0.9, Karajan et al. 2014). To gain a better understanding of viscous damping and restitution phenomena particular to the modeling of granular media in LS-DYNA (LSTC 2014b), a parametric set of simulations are carried out. Namely, ten ball drop simulations are conducted using LS-DYNA, where across the simulation set, the $NDAMP$ parameter is varied from 0.0 to 0.9 with an increment of 0.1. For these simulations, the model consists of two identical (and homogenous) elastic 50-mm-diameter spheres undergoing collinear impact (Fig. 2.4.5.1). Sphere 1 is located at an initial height of 1.1 m (center-to-center) above Sphere 2, which is fully restrained from motion. The top sphere is excited downward by the gravitational force. The contact analysis during the impact only considers the translational DOF in the normal direction of motion by setting $NormK = 1$ to fully use the normal spring stiffness k_N , and leaving other parameters of contact definition to zero.

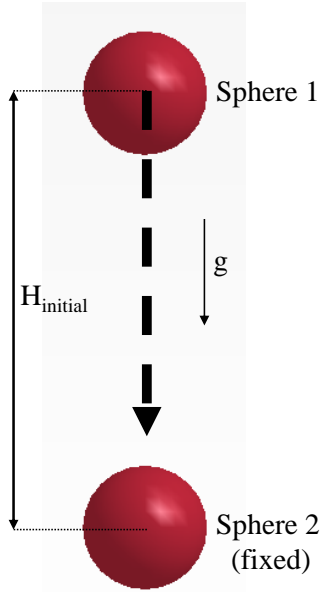


Figure 2.4.5.1. Schematic of ball-drop simulations

The time-varying height of Sphere 1, over the course of each of the ten simulations, is plotted in Fig. 2.4.5.2. For this test setup, the following definition of the coefficient of normal restitution defined in Ollagnier (2007) is adopted:

$$e_N = \frac{h_1}{h_0} \quad (2.4.5.1)$$

where h_0 and h_1 are the ball heights before and after impact, respectively. In addition, for the ball-drop scenario, the coefficient of normal restitution (e_N) can be used to arrive at a damping coefficient in the linear contact force model (Cleary and Prakash 2004; Navarro and de Souza Braun 2013):

$$NDAMP = -\frac{\ln e_N}{\sqrt{\ln^2 e_N + \pi^2}} \quad (2.4.5.2)$$

In Fig. 2.4.5.3, the coefficient of normal restitution (e_N) is plotted as a function of the $NDAMP$ parameter, where both Eqn. 2.4.5.2 and numerical results obtained from ball drop simulations using LS-DYNA are included. Agreement is observed between Eqn. 2.4.5.2 and the numerical results, which indicates that the preceding discussion is applicable for modeling sphere-sphere interactions in LS-DYNA. Also included in Fig. 2.4.5.3 is a plot of e_N versus $NDAMP$ when the full Cundall time step size is used in the simulations, and results are overlain with those associated with use of the Cundall time step factored at 20% (recall Eqn. 2.4.1.4). Note that use of the 20% factor (as recommended in Jensen et al. 2014) leads to even stronger agreement between the numerical results and Eqn. 2.4.5.2.

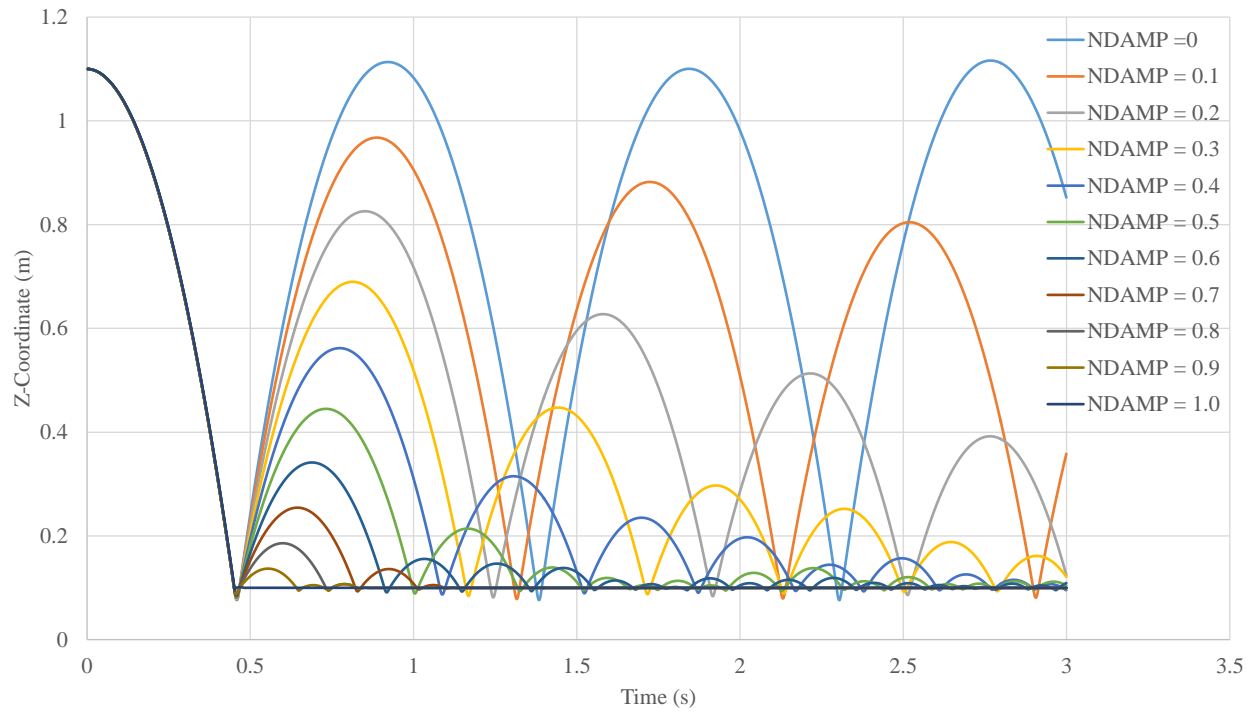


Figure 2.4.5.2. Time-varying vertical position of sphere over the range of damping values considered

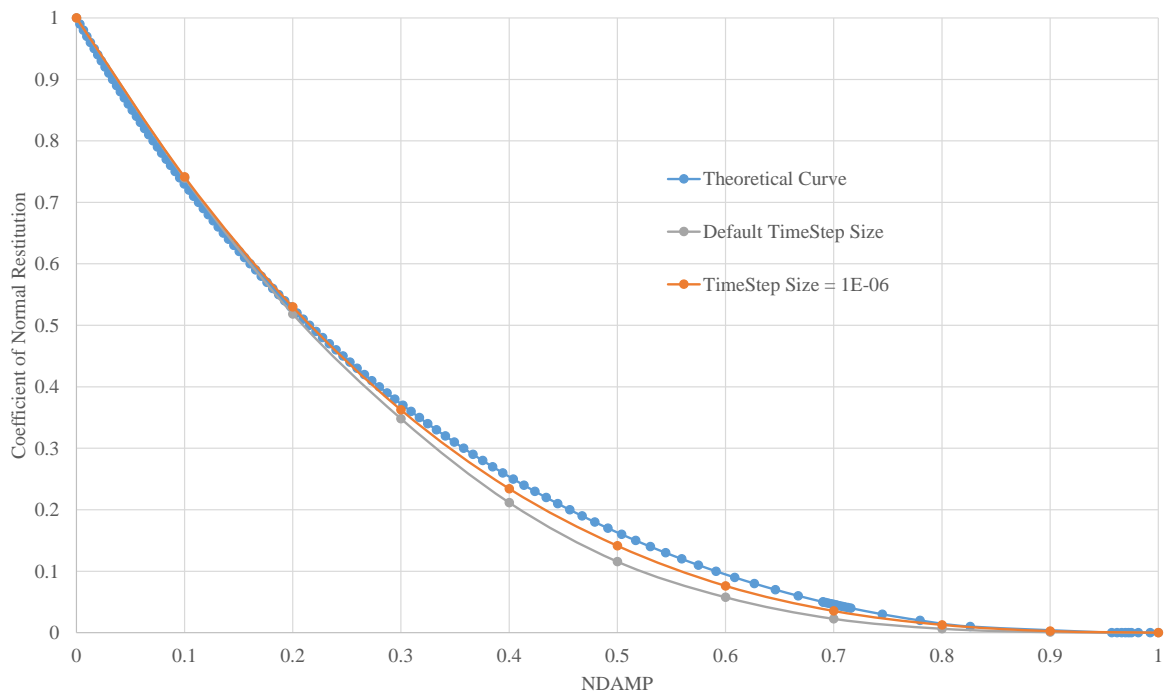


Figure 2.4.5.3. Coefficient of normal restitution versus normal damping

Coefficient of Tangential Restitution (e_T)

LS-DYNA simulations of two-sphere (DSE) systems undergoing oblique collision (Fig. 2.4.5.4) are carried out to gain insight into the interrelationships between the coefficient of tangential restitution (e_T), sliding friction (μ_{static}), and rolling friction (μ_{rolling}). As a given value of e_T affects both translational and rotational components of system response, oblique collision simulations are carried out for several angles of incidence (2° , 4° , 6° , 8° , 10° , 20° , 30° , 40° , 45° , 50° , 60° , 70° , and 80°). For all simulations conducted, Sphere 1 (Fig. 2.4.5.4) is initially positioned above and to the left of a fixed sphere (Sphere 2). Further, an initial velocity (v_{initial}) is imposed on Sphere 1, where the associated vector points from Sphere 1 directly toward Sphere 2. For each angle of incidence considered, an additional parametric dimension is investigated by varying (in separate simulations) the ratio of rolling (μ_{rolling}) to sliding friction (μ_{static}) at ratios of 0.1, 0.5, and 1.0 (with all other parameters remaining unchanged).

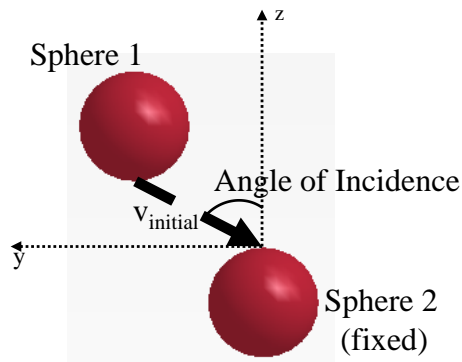


Figure 2.4.5.4. Schematic of oblique collision simulations

By making use of the time-histories of computed velocity components from the LS-DYNA simulations, in conjunction with the methodology given in Walton (1993), a selection process emerges for assigning meaningfully coupled values of sliding friction (μ_{static}) and rolling friction (μ_{rolling}). As the first step in this process, and for a given ratio of rolling to sliding friction, the tangent of the effective recoil angle, v'_y/v'_z is plotted against the tangent of the effective incident angle, v_y/v_z . Accordingly, shown in Fig. 2.4.5.5, are the v'_y/v'_z and v_y/v_z quantities obtained from oblique collision simulations across each of the thirteen aforementioned incidence angles, and where the ratio of rolling to sliding friction is maintained at 0.1. Similar plots are shown in Fig. 2.4.5.6 and Fig. 2.4.5.7 for rolling to sliding friction ratios of 0.5 and 1.0, respectively.

Consistent with Walton (1993), two pronounced slopes (approximately linear in form) are present among each of Fig. 2.4.5.5 through Fig. 2.4.5.7. To emphasize this, the collections of points associated with a negative slope are rendered as orange circles, while the collections of points associated with a positive slope are rendered as blue circles. For each collections of points, linear regression lines are formed (as shown in Fig. 2.4.5.5 through Fig. 2.4.5.7). The regression lines are referred to as “solution lines” (Walton 1993). With respect to the selection of parameter values for modeling DSE in LS-DYNA, and consistent with Walton (1993), the slopes of the regression lines for the orange-colored point data are characterized by the rolling friction coefficient (μ_{rolling}), while the slopes of the regression lines for the blue-colored point data are characterized by the sliding friction coefficient (μ_{static}). In this way, sliding and rolling friction are coupled, and

critically, such coupling is accounted for in the selection of the friction parameters for simulations conducted as part of the current study.

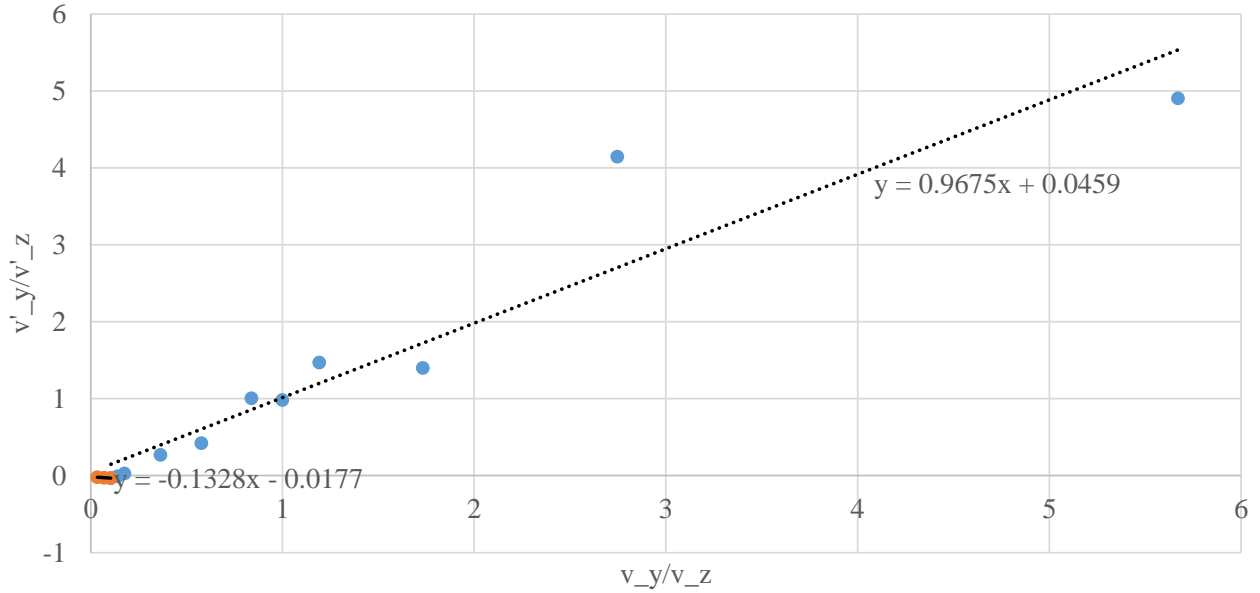


Figure 2.4.5.5. Tangent of effective recoil angle versus tangent of effective incident angle for a ratio of rolling to sliding friction equal to 0.1

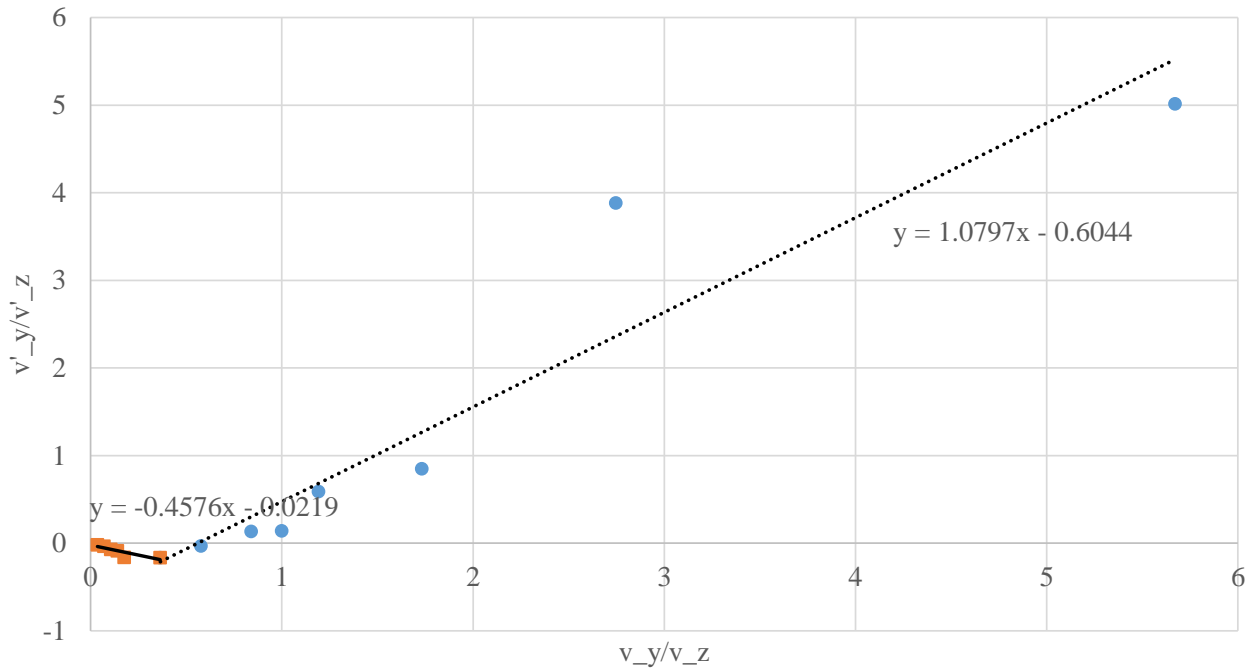


Figure 2.4.5.6. Tangent of effective recoil angle versus tangent of effective incident angle for a ratio of rolling to sliding friction equal to 0.5

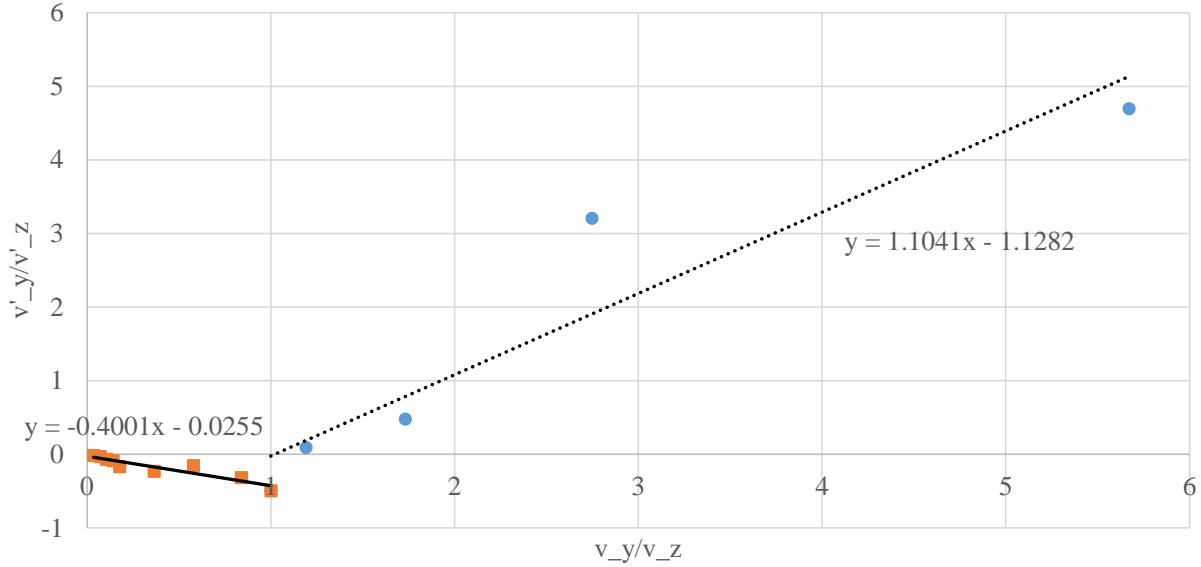


Figure 2.4.5.7. Tangent of effective recoil angle versus tangent of effective incident angle for a ratio of rolling to sliding friction equal to 1.0

2.4.6 Detailed Description of Rheological Model

For the DEM linear contact model implemented in LS-DYNA (LSTC 2014b), the normal stiffness of two interacting elastic spheres ($k_{N_LS-DYNA}$) is defined as:

$$k_{N_LS-DYNA} = \frac{K_1 R_1 K_2 R_2}{K_1 R_1 + K_2 R_2} \quad (2.4.6.1)$$

where the bulk modulus for sphere i is defined consistent with Eqn. 2.4.1.3. By incorporating Eqn. 2.4.1.3 into Eqn. 2.4.6.1 for each of the two spheres ($i = 1, 2$), the normal stiffness (Eqn. 2.4.6.1) can be written in terms of the sphere-specific values of modulus of elasticity (E), Poisson's ratio (ν), and radius (R) as:

$$k_{N_LS-DYNA} = \frac{E_1 E_2 R_1 R_2}{3(1-2\nu_1)E_2 R_2 + 3(1-2\nu_2)E_1 R_1} \quad (2.4.6.2)$$

Recall Eqn. 2.4.2.1, which expresses the Hertz normal force (F_N) as a nonlinear function of, in part, normal displacement (δ_N). Given the implementation of a linear contact DEM model in LS-DYNA, additional considerations are required to map from the previously discussed (nonlinear) Hertzian expressions to the (linearized) input parameters available in LS-DYNA. Namely, a quantity referred to as Hertz's secant stiffness ($k_{N_Hertz_secant}$) is introduced (Fig. 2.4.6.1), and is introduced:

$$k_{N_Hertz_secant} = \frac{F_N}{\delta_N} = \frac{4}{3} E^* \sqrt{R} \delta_N^{1/2} \quad (2.4.6.3)$$

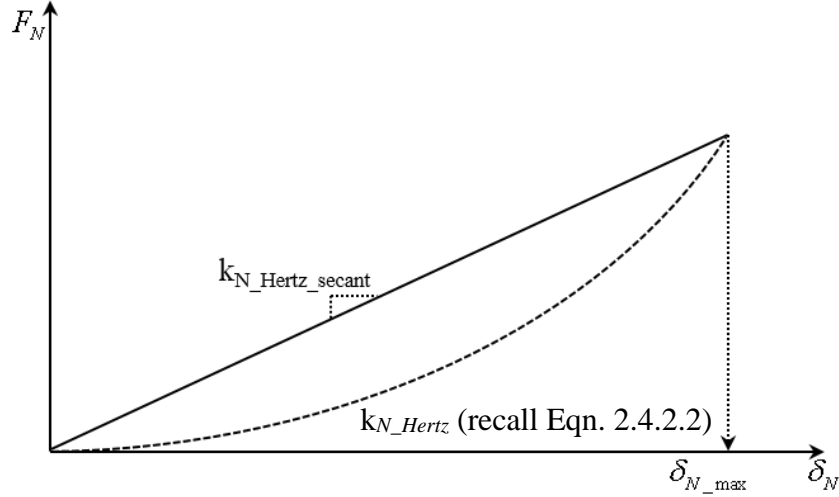


Figure 2.4.6.1. Nonlinear stiffness and Hertz secant stiffness for modeling normal contact between spheres

$$k_{N_Hertz_secant} = \frac{F_N}{\delta_N} = \frac{4}{3} E^* \sqrt{R} \delta_N^{1/2} \quad (2.4.6.3)$$

For two elastic spheres in contact, the Hertz secant stiffness ($k_{N_Hertz_secant}$) can be expressed in terms of the constituent values of elastic moduli (E_i^H), Poisson's ratios (ν_i), and radii (R_i):

$$k_{N_Hertz_secant} = \frac{4}{3} \left(\frac{E_1^H E_2^H}{E_1^H (1-\nu_2^2) + E_2^H (1-\nu_1^2)} \right) \sqrt{\frac{R_1 R_2}{R_1 + R_2}} \delta_N^{1/2} \quad (2.4.6.4)$$

Note that the elastic moduli in Eqn. 2.4.6.4 are strictly associated with Hertzian theory, whereas the elastic moduli of Eqn. 2.4.6.2 are strictly associated with numerical input for modeling in LS-DYNA.

As a measure of upholding Hertzian theory, numerical parameter selection for normal contact stiffness modeling in LS-DYNA is driven by equating Eqn. 2.4.6.4 and Eqn. 2.4.6.1:

$$k_{N_Hertz_secant} = k_{N_LS-DYNA} \quad (2.4.6.5)$$

$$\frac{4}{3} \left(\frac{E_1^H E_2^H}{E_1^H (1-\nu_2^2) + E_2^H (1-\nu_1^2)} \right) \sqrt{\frac{R_1 R_2}{R_1 + R_2}} \delta_N^{1/2} = \frac{E_1 E_2 R_1 R_2}{3(1-2\nu_1)E_2 R_2 + 3(1-2\nu_2)E_1 R_1}$$

To facilitate manipulation of Eqn. 2.4.6.5, the following three constants are defined:

$$\begin{aligned}
C_1 &= (1 - 2\nu_2)R_1 \\
C_2 &= (1 - 2\nu_1)R_2 \\
C_3 &= 4 \frac{E_1^H E_2^H}{E_1^H (1 - \nu_2^2) + E_2^H (1 - \nu_1^2)} \frac{1}{\sqrt{R_1 R_2 (R_1 + R_2)}} \delta_N^{1/2}
\end{aligned} \tag{2.4.6.6}$$

Consequently, the equality in Eqn. 2.4.6.5 simplifies to: $C_3 C_1 E_1 + C_3 C_2 E_2 = E_1 E_2$. By additionally making an assumption of the relationship between E_1 and E_2 (namely, $E_1 = r E_2$), the elastic modulus associated with numerical modeling in LS-DYNA can be expressed in terms of Hertzian quantities. For example, in a two-sphere collision scenario, the LS-DYNA input parameter for the elastic modulus of Sphere 2 is determined as:

$$E_2 [r E_2 - (C_3 C_1 r + C_3 C_2)] = 0 \rightarrow E_2 = \frac{C_3 C_1 r + C_3 C_2}{r} \tag{2.4.6.7}$$

A similar methodology is adhered to in selecting numerical parameter values to model tangential components of contact stiffness in LS-DYNA. Specifically, for any instant within a simulation wherein oblique contact forces arise, a secant definition of the tangential contact stiffness ($k_{T_Mindlin_secant}$) can be expressed as:

$$k_{T_Mindlin_secant} = \frac{16aG^*}{3[1 - \mu \cot(\alpha)]}, \tan(\alpha) > \mu \tag{2.4.6.8}$$

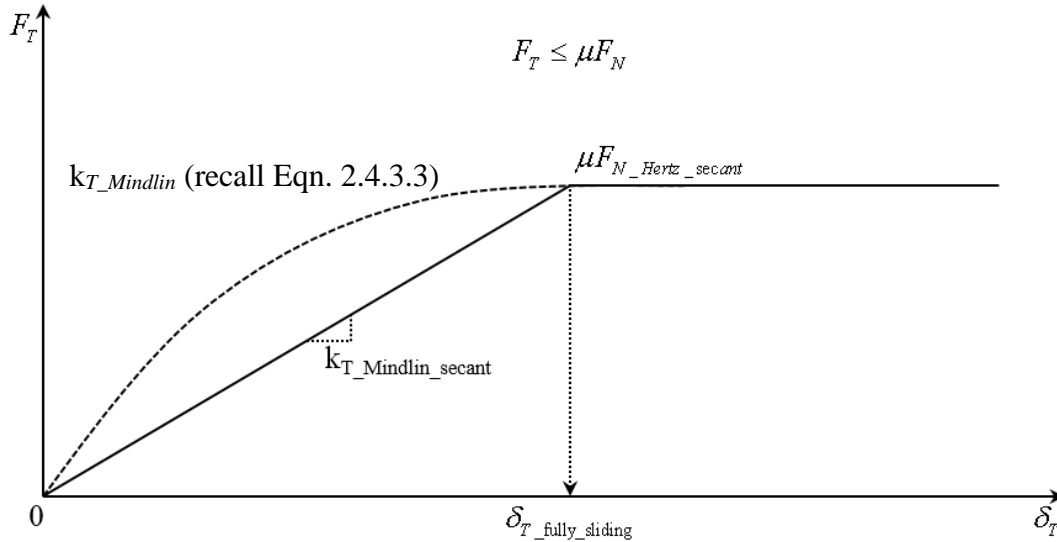


Figure 2.4.6.2. Nonlinear tangential stiffness per Mindlin's Theory and an approximate secant stiffness approach for use in tangential contact modeling between DSE

For the LS-DYNA implementation of the DEM, tangential contact stiffness ($k_{T_LS-DYNA}$) is defined as the product of normal stiffness ($k_{N_LS-DYNA}$) and the *ShearK* coefficient (LSTC 2014b):

$$k_{T_LS-DYNA} = k_{N_LS-DYNA} ShearK \quad (2.4.6.9)$$

Given the relationship between normal and tangential contact stiffness (Eqn. 2.4.6.9), the numerical input value selection process for modeling tangential contact stiffness in the current study is driven by ensuring that the following stiffness ratio is maintained:

$$\frac{k_{T_Mindlin_secant}}{k_{N_Hertz_secant}} = \frac{4G^*}{E^* [1 - \mu \cot(\alpha)]} \quad (2.4.6.10)$$

2.4.7 Boundary Model of Capillary Suction Pressure

Capillarity, or capillary action is defined as the ability of a liquid to flow in narrow spaces without being influenced by the effects of external forces. Capillary action is a result of cohesion pressure as well as adhesion, which may cause the liquid to work against gravity. With respect to granular material, capillary action induces inter-particle forces via the pores of granules, which contributes positively to shear and tensile strengths for any collection of neighboring granules. The applicability of capillary forces in industrial applications is well established. One such previously developed treatment is that of the “liquid bridge” concept, which is used in numerical models to mimic the (physical) introduction of liquid throughout the pore spaces of granules. Due to surface tension of the liquid, the surface area of the “bridge” tends toward a minimal value, hence, exerting a pulling (attraction) force on the affected particles.

The work of Rabinovich et al. (2005) was adopted in implementing a numerical model of capillary action in LS-DYNA (Karajan et al. 2012), and therefore, is of interest for the current study. Rabinovich et al. (2005) explored pressure differences that arise when making use of the liquid bridge concept to, in turn, develop analytical expressions for determining capillary suction force. Further, Rabinovich et al. (2005) analyzed the geometry of sphere-plate interactions, and then made extrapolations in developing expressions pertaining to sphere-sphere interactions (Fig. 2.4.7.1). Along these lines, capillary forces between two spheres separated by a liquid bridge were estimated using the analytical expressions and their predictions were compared against experimentally measured values of capillary force, obtained using an atomic force microscope (AFM).

The analytical expressions developed by Rabinovich et al. (2005) stem from the seminal work of Derjaguin. Namely, the Derjaguin approximation can be used to calculate the suction force F between two spheres separated by a distance H :

$$F = \pi R U \quad (2.4.7.1)$$

in which R is the radius of the sphere upon which the adhesion force acts, and U is the specific energy (per unit area) of interaction of two flat surfaces at a separation distance of H . The specific energy U acting through the liquid layer is:

$$U = -2\gamma \cos \theta \quad (2.4.7.2)$$

where γ is the liquid surface tension and θ is the tangent angle between the liquid volume and a given sphere (as annotated in Fig. 2.4.7.1).

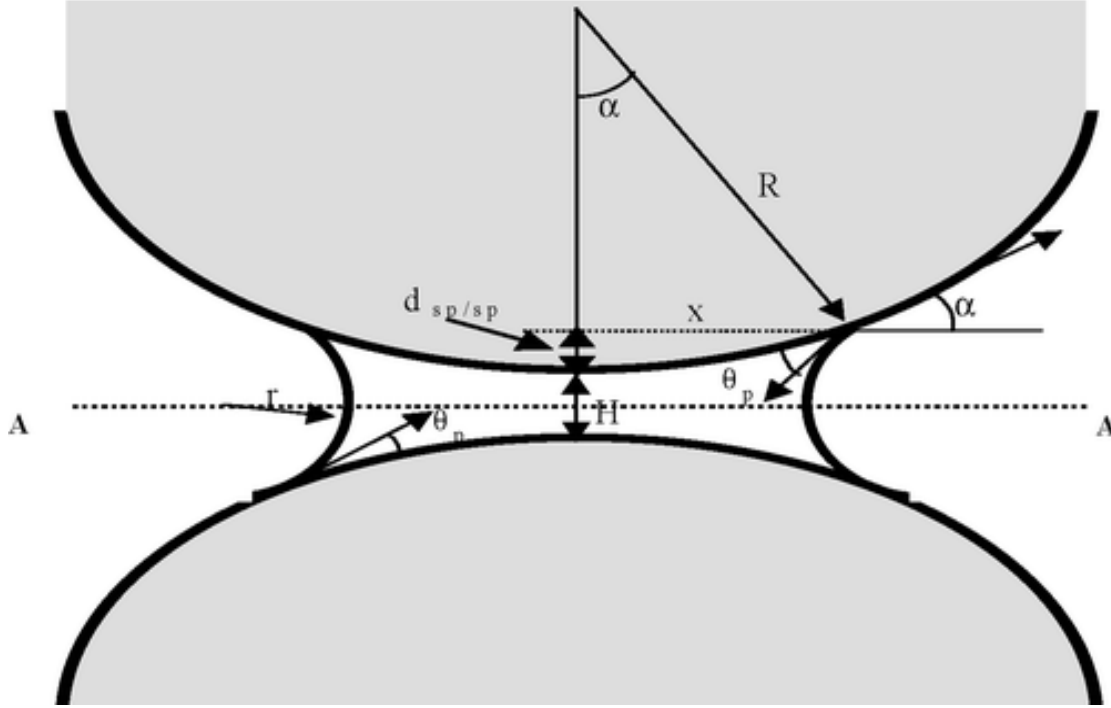


Figure 2.4.7.1. Schematic of the liquid bridge concept for two neighboring spheres (Rabinovich et al. 2005)

At $H=0$, the suction force is given by:

$$F = -2\pi\gamma R \cos \theta \quad (2.4.7.3)$$

However, the Derjaguin' approximation is only valid when $H=0$, and therefore, it cannot be used to determine the suction force when $H \neq 0$. As an alternative, Rabinovich et al. (2005) proposed that the capillary suction force can be determined by taking the derivative of total energy (W) with respect to separation distance H :

$$F(H,V) = -\frac{dW}{dH} = 4\pi R^2 \alpha \gamma \cos \theta \frac{d\alpha}{dH} \quad (2.4.7.4)$$

where, in this context, α is the angle between a given sphere center and the edge of the liquid volume (recall Fig. 2.4.7.1). Further, Rabinovich et al. (2005) defined the volume of a liquid bridge between two spheres as:

$$V = \pi R^2 \alpha^2 H + 0.5\pi R^3 \alpha^4 \quad (2.4.7.5)$$

For a fixed volume of liquid bridge, $dV/dH = 0$, and from Eqn. 2.4.7.5, the corresponding derivative of the parameter α is:

$$\frac{d\alpha}{dH} = \frac{-1}{2H/\alpha + 2R\alpha} \quad (2.4.7.6)$$

Thus, from equations 2.4.7.4 and 2.4.7.6., capillary suction force is given by:

$$F(H, V) = -\frac{2\pi R\gamma \cos \theta}{1 + \left[\frac{H}{2d_{sp/sp}(H, V)} \right]} \quad (2.4.7.7)$$

where the distance $d_{sp/sp}(H, V)$ (as shown in Fig. 2.4.7.1) can be obtained using the following expression:

$$d_{sp/sp}(H, V) = \frac{H}{2} \left[-1 + \sqrt{1 + \frac{2V}{\pi R H^2}} \right] \quad (2.4.7.8)$$

Taking into account the attraction force due to transverse components of the liquid bridge, the formula for capillary suction force proposed in Rabinovich et al. (2005) is then given by:

$$F(H, V) = -\frac{2\pi R\gamma \cos \theta}{1 + \left[\frac{H}{2d_{sp/sp}(H, V)} \right]} - 2\pi\gamma R \sin \alpha \sin(\theta + \alpha) \quad (2.4.7.9)$$

The capillary suction force expression given in Eqn. 2.4.7.9 was demonstrated to show good agreement with experimentally measured suction forces in Rabinovich et al. (2005).

As noted previously, the LS-DYNA DEM implementation makes use of the capillary suction force model proposed by Rabinovich et al. (2005). In LS-DYNA, numerical treatment of capillarity is activated by setting the parameter $CAP \neq 0$ under the keyword `*CONTROL_DISCRETE_ELEMENT`. Along with activation of the capillary model, the following parameters must be specified: *GAMMA*, which corresponds to the previously defined parameter γ ; *VOL*, which gives the initial volume fraction of the liquid bridge with respect to the volume of any interacting spheres; and, *ANG* which corresponds to the previously described parameter θ (recall Fig. 2.4.7.1). A schematic of the capillary force model implemented in LS-DYNA is given in Fig. 2.4.7.2.

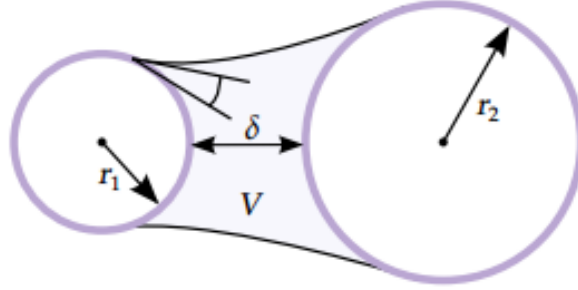


Figure 2.4.7.2. Schematic representation of capillary force model (LSTC 2014b)

For the two neighboring particles shown in Fig. 2.4.7.2 (with radii r_1 and r_2), the volume of a liquid bridge V is calculated as:

$$V = \frac{4}{3} \pi (r_1^3 + r_2^3) \frac{1}{10} VOL \quad (2.4.7.10)$$

In addition, an effective radius, R , is determined as:

$$R = \frac{2r_1r_2}{r_1 + r_2} \quad (2.4.7.11)$$

where Eqn. 2.4.7.10 and Eqn. 2.4.7.11 can be combined with the separation distance (δ) to calculate an effective distance parameter, d (analogous to Eqn. 2.4.7.8):

$$d = \frac{\delta}{2} \left(-1 + \sqrt{1 + \frac{2V}{\pi R \delta^2}} \right) \quad (2.4.7.11)$$

Finally, the capillary suction force (F) is computed (for each calculation cycle within the LS-DYNA simulation) as:

$$F = - \frac{2\pi\gamma R \cos(\theta)}{1 + \frac{\delta}{2d}} \quad (2.4.7.10)$$

To study the effect of capillary suction force on the response of a particle, a demonstration simulation was carried out using LS-DYNA. The demonstration model consists of three identical spheres (Fig. 2.4.7.3). A linearly increasing upward force was applied to the top sphere, which acted to oppose the automatically computed capillary suction forces. The parameter values specified for the LS-DYNA capillary model, as part of the demonstration simulation, are listed in Table 2.4.7.1.

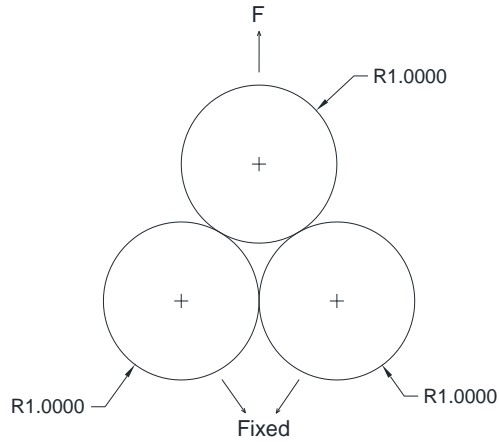


Figure 2.4.7.3. LS-DYNA model to study the effects of capillary suction force

Table 2.4.7.1. LS-DYNA input parameters for modeling capillarity

Parameter	Value	Units
<i>GAMMA</i>	0.264	N/m
<i>VOL</i>	0.66	--
<i>ANG</i>	10	°

Numerical results obtained from the LS-DYNA simulation, pairing sphere-sphere distance to capillary suction force, are plotted in Fig. 2.4.7.4. Also shown in Fig. 2.4.7.4 is Eqn. 2.4.7.10, when supplied with values used in the demonstration simulation. Excellent agreement is observed between the purported capillary suction force model and the numerical simulation results.

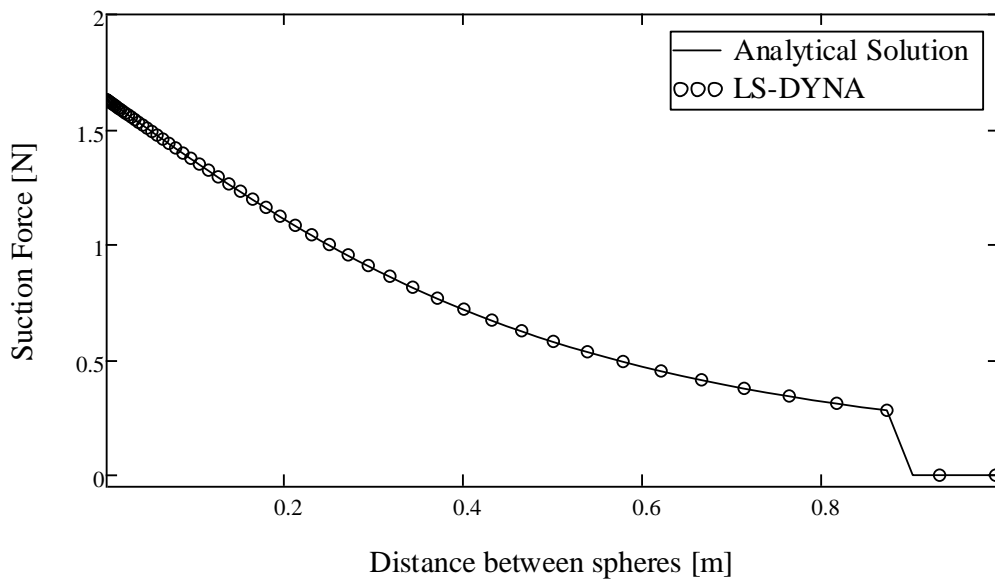


Figure 2.4.7.4. Sphere-sphere distance versus capillary suction force

CHAPTER 3

NUMERICAL MODELING OF STANDARD LABORATORY TESTS FOR ASSESSING MACROSCOPIC PROPERTIES OF DSE ASSEMBLIES

3.1 Overview

Presented in Chapter 3 are the development efforts and numerical parameter listings that, when applied to standardized volumes of randomly packed DSE, make up a “soil unit” library. The catalog of microscopic (i.e., individual-sphere) parameters facilitates manifestations of pertinent macroscopic properties (over practical ranges) for simulations involving granular media. As part of the overall research program, standardized volumes of DSE, or “soil units”, are ultimately going to be used in populating megascopic assemblies of DSE. In this context, a given megascopic assembly constitutes one realization of the possible site conditions (i.e., the soil medium) that may be encountered at a construction site. As part of Task 3 of the current research project, megascopic assemblies (site realizations) will be subjected to simulated installation and removal of SPW and pile objects.

Paramount to the overall investigations of installation and removal of structural objects into granular media is that the megascopic assemblies investigated are composed of volumes possessing known macroscopic properties. Just as physical laboratory testing of soils yields physical measurements of macroscopic properties (e.g., internal friction angle), numerical models for simulating controlled manipulations of DSEs are integral to assessing macroscopic properties of the standardized DSE volumes. Accordingly, the development of robust, benchmarked numerical models for carrying out selected laboratory procedures on granular soil specimens makes up a key component of establishing a soil unit library. The two laboratory tests considered as part of the current research are the direct shear test and the triaxial compression test, which are discussed in detail in Sec. 3.2 and Sec. 3.3, respectively. As a culmination of the Chapter 2 investigation into fundamental behaviors of DSE, and based on utilization of the numerical models for simulating laboratory-scale testing of granular soils (Secs. 3.2-3.3), the quantitative parameter listings for the soil unit library are presented along with the corresponding ranges of soil-unit macroscopic properties in Sec. 3.5.

3.2 Direct Shear Test

Presented in Sec. 3.2 are considerations made toward numerical modeling of granular materials subjected to direct shear testing. To establish a datum for numerical modeling of the test apparatus components, a standard test protocol is identified, as summarized in Sec. 3.2.1. Numerical model counterparts to the essential components of the direct shear test apparatus are detailed in Sec. 3.2.2, where adherence is maintained relative to the required laboratory equipment listed in the testing standard. Further, as derived from the testing standard, each stage of the numerical testing procedure is discussed in Sec. 3.2.3. As a benchmarking measure, in Sec. 3.2.4, it is demonstrated that the test apparatus and testing procedure, as modeled, give numerical predictions of macroscopic specimen response quantities that are in line with those measured as part of previously completed (physical) laboratory testing. The final two portions of Sec. 3.2 are dedicated to exploring fundamental properties of DSE assemblies by making use of the

benchmarked (numerical) direct shear test apparatus: in Sec. 3.2.5, geometrically regular packings of DSE are investigated; in Sec. 3.2.6, the phenomenon of apparent cohesion (in association with capillarity) is explored for randomly packed DSE specimens.

3.2.1 Description of Physical Test Procedure

To contextualize the numerical modeling techniques discussed in Sec. 3.2.2. and 3.2.3, salient aspects of the physical laboratory test procedure are first described. The ASTM D3080 (ASTM 2012) testing standard is selected as the basis in developing a numerical model for simulating direct shear testing on DSE assemblies. As detailed in ASTM D3080, the direct shear test involves placement of a specimen (e.g., a relatively small volume of granular soil, sampled from a construction site) into a disc-shaped test chamber (Fig. 3.2.1.1). Importantly, the specimen volume is such that the specimen mid-height is aligned with the horizontal boundary between the lower frame and upper frame of the test apparatus. Further, the regions of contact between the lower and upper frames (i.e., all frame-to-frame interfaces) are lubricated. Following initial placement of the specimen, a disc made of porous stone and piston are positioned directly atop the specimen such that the specimen is encapsulated between the lower frame, upper frame, and stone discs.

After the specimen and apparatus components are put into place, a normal force is gradually applied to the piston, which (due to encapsulation by the rigid frame) imposes a normal pressure throughout the specimen. The lower frame does not move throughout the entire procedure. Subsequent to imposing the normal pressure, a controlled shearing (horizontal motion at a constant rate) is imposed on the upper frame, which in turn, forces the specimen to shear along the horizontal boundary between the lower and upper frames. Importantly, no appreciable frame-to-frame sliding forces arise during the shearing stage because all lower and upper frame interfaces have been lubricated prior to placement of the specimen.

During the shearing stage, the horizontal force needed to maintain the constant rate of horizontal motion (i.e., shearing) is recorded. Additionally, the vertical position of the piston is recorded throughout the test. Typically, in physically measuring macroscopic properties for a given soil, the overall procedure will be repeated across three or more levels of imposed normal pressure, where a fresh specimen is taken from a larger soil sample for each run of the direct shear test. In this way, the normal force and peak shearing force can be paired and plotted across the three (or more) test runs, which in turn, permits estimation of a Mohr-Coulomb failure envelope for the soil. This overall process (as modeled) is demonstrated for a benchmark case in Sec. 3.2.4.

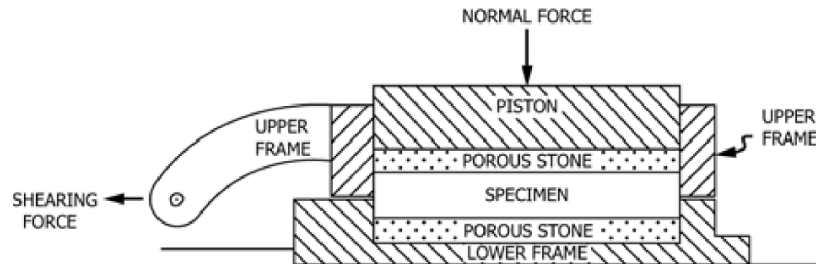


Figure 3.2.1.1. Schematic of a direct shear test (ASTM 2012)

3.2.2 Numerical Model of Test Apparatus

With consideration of ASTM D3080 (ASTM 2012), the numerical model for simulating direct shear tests on DSE assemblies is shown in Fig. 3.2.2.1. The numerical model consists of rigid finite element entities, which act to encapsulate the DSE assembly at all times. Namely, rigid top and bottom plates, modeled using eight-node rigid solid elements, bound the top and bottom portions of the test chamber. The vertical surfaces of the test chamber consist of two independent open-ended cylinders, modeled using four-node rigid shell elements. Rigid extender plates are also modeled using four-node rigid shell elements, and prevent the escape of individual DSEs during the shearing stage of the simulation. Importantly, each apparatus component is modeled to permit independent motions. For example, the top half of the rigid cylinder is permitted to translate independent (i.e., without inducing stresses) of the bottom half of the rigid cylinder.

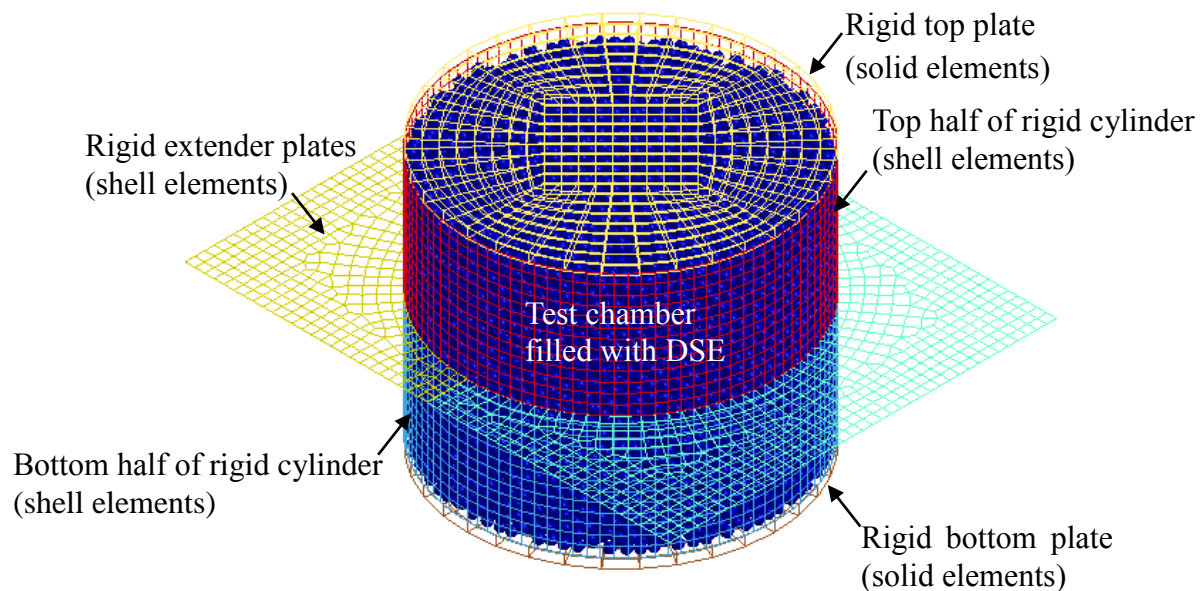


Figure 3.2.2.1. Combined DEM-FEM model of direct shear test apparatus

3.2.3 Numerical Test Procedure

Consistent with testing standard ASTM 3080 (ASTM 2012), the numerical direct shear test procedure is divided into three stages: 1) Specimen placement; 2) Application of normal pressure; and, 3) Shearing of the specimen. The initial configuration of the direct shear test model is shown in Fig. 3.2.3.1. In the initial configuration, all test apparatus components are restrained, with the exception that the top plate is permitted to undergo vertical translation. Also, initially, the collection of DSEs extend a small distance vertically above the top half of the test chamber cylinder. This initial overage is deliberate, where the intention is that the initial configuration of DSEs reaches a mechanically stable state that approximately fully populates the test chamber volume in response to the gradual introduction of gravitational acceleration (Fig. 3.2.3.2). While this approach to specimen placement necessitates iterations on the number of DSEs to include in the assembly, it ensures that the tenants of the ASTM standard are upheld. Specifically, this

approach provides a means of packing the assembly of DSEs such that the assembly possesses a mechanically stable mid-height in alignment with the horizontal boundary between the lower and upper halves of the direct shear test apparatus.

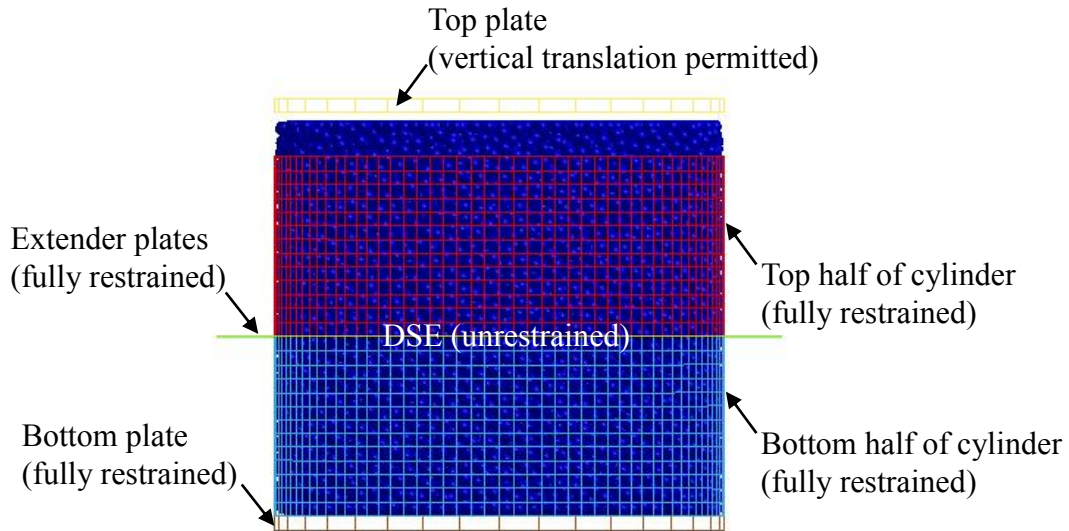


Figure 3.2.3.1. Initial configuration with unpacked specimen

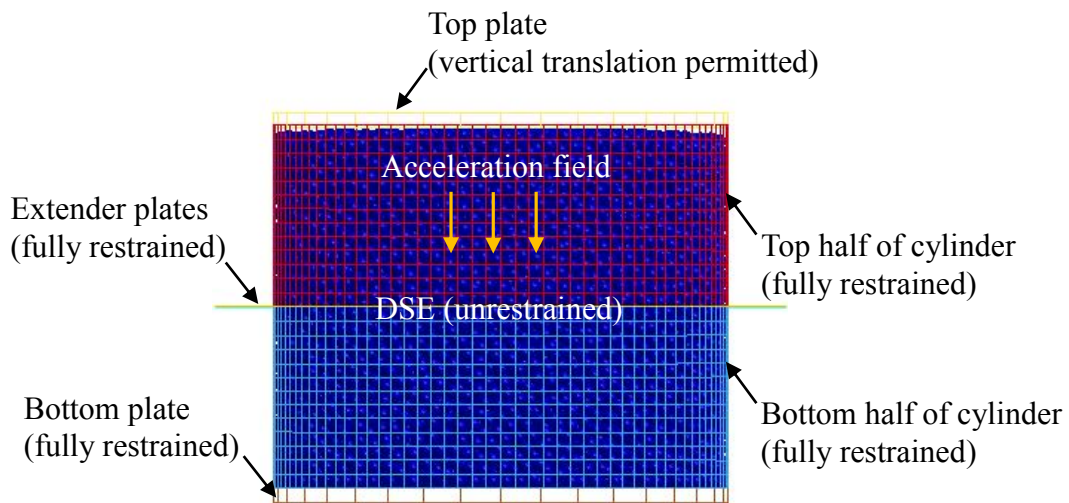


Figure 3.2.3.2. Application of acceleration field

Subsequent to specimen placement (i.e., random packing of the DSEs within the test chamber using gravitational acceleration), a normal pressure is gradually imposed on the top plate (Fig. 3.2.3.3). Those boundary conditions that are initially imposed on the test apparatus components are maintained throughout the first two stages of the direct shear test simulation (specimen placement, application of normal pressure). Consequently, the DSE assembly (representing the specimen) is encapsulated in a manner that is consistent with the ASTM standard: the bottom and top plates bound the bottom and top portions (respectively) of the DSE assembly;

the bottom and top halves of the test chamber cylinder bound the vertical perimeter of the DSE assembly.

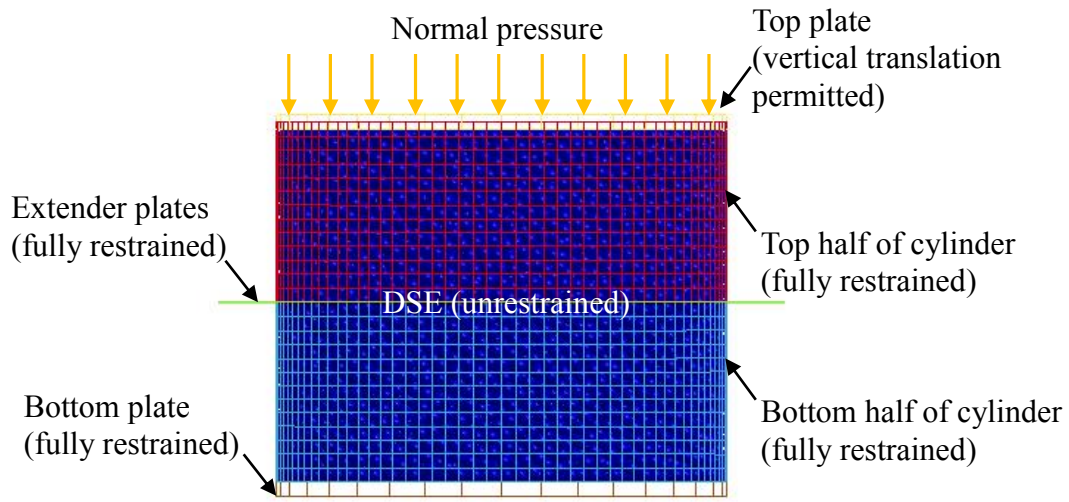


Figure 3.2.3.3. Application of normal pressure

The final stage of the direct shear test consists of imposing a prescribed shearing of the DSE assembly (Fig. 3.2.3.4). To facilitate the shearing process, modifications are made to the boundary conditions of the test apparatus components upon reaching the final simulation stage. In particular, the top half of the test chamber cylinder and the trailing extender plate are subjected to prescribed horizontal translation. Regarding the top plate, the top-surface normal pressure is maintained and the top plate remains free to undergo vertical translation. In addition, the top plate is subjected to a prescribed horizontal translation that matches that imposed upon the top half of the test chamber cylinder and trailing extender plate. Consequently, the top plate, top half of the test chamber cylinder, and the trailing extender plate all undergo the same prescribed horizontal translation. During the shearing process, the lead extender plate remains fully restrained. As an ensemble, the as-imposed boundary conditions prevent the escape of DSE from the test chamber.

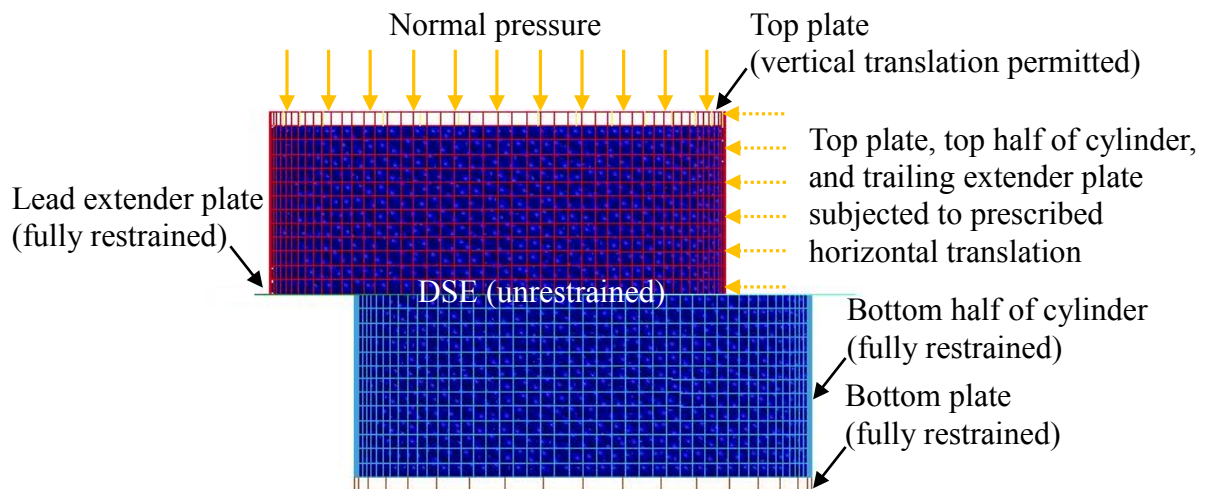


Figure 3.2.3.4. Prescribed horizontal translation of top half of apparatus

3.2.4 Validation

To gauge the overall efficacy of the previously described numerical model (Sec. 3.2.2) and simulation stages (Sec. 3.2.3) for the direct shear test, care was taken in identifying a benchmark study from among the literature. More specifically, O’Sullivan et al. (2004b) is selected as a benchmark study because the data reported therein permit focused assessments of the numerical direct shear test apparatus and testing procedure, exclusive of the complications that arise when attempting to model granular soil specimens using DSE assemblies.

As part of O’Sullivan et al. (2004b), stainless steel spheres of diameter 1 mm were manufactured, subjected to (physical) direct shear testing, and the test results were reported. The use of highly uniform monodisperse assemblies of stainless steel spheres for benchmarking the direct shear test numerical model in the current study substantially reduces the uncertainty associated with supplying microscopic (i.e., individual-sphere) properties for the constituent DSEs. In contrast, if benchmarking of the (numerical) test apparatus were to be carried out based on physical testing of granular soil specimens, then difficulties would arise in attributing the source of any observed differences between the physically measured benchmark data and the numerical modeling results. Stated alternatively, it would be difficult to ascertain the proportion of any observed differences that was caused by deficiencies in the test apparatus components and what proportion was caused by the deficiencies in the numerical description of the DSEs.

For the benchmark simulations of the current study, three direct shear tests were simulated using randomly packed monodisperse assemblies, representing the highly uniform stainless steel spheres. A single set of properties, listed in Table 3.2.4.1, were supplied for all DSEs included in the benchmark simulations. The simulations proceeded in accordance with the staging specified in Sec. 3.2.3. Consistent the physical test conditions documented in O’Sullivan et al. (2004b), a single benchmark direct shear test simulation was completed for applied normal pressures of 54.5 kPa, 109 kPa, and 163.5 kPa. Plots of shear stress and horizontal displacement, as obtained from the benchmark simulations, are given in Fig. 3.2.4.1. Superimposed on the numerical results of Fig. 3.4.2.1 are the test-specific peak shear stresses measured by O’Sullivan et al. (2004b), where three separate runs of the (physical) direct shear tests were carried out for each applied normal pressure. Plots of peak shear stress versus applied normal pressure are shown in Fig. 3.4.2.2. Note that the 95th percentile values of shear stress are reported in association with the benchmark simulation results. Also shown in Fig. 3.4.2.2. envelopes of the physical test data, as compared to a linear regression of the peak shear stresses obtained from the numerical simulations. Overall, the physical test measurements successfully validate benchmark numerical results.

Table 3.2.4.1. Numerical parameters listed for DSEs in O’Sullivan et al. (2004b)

Parameter	Value	Units
Radius	0.9922	mm
Mass density	7.8334E-06	kg/mm ³
Shear modulus	7.945E+07	kg/(mm-s ²)
Poisson’s ratio	0.28	--
Friction coefficient	5.5	°

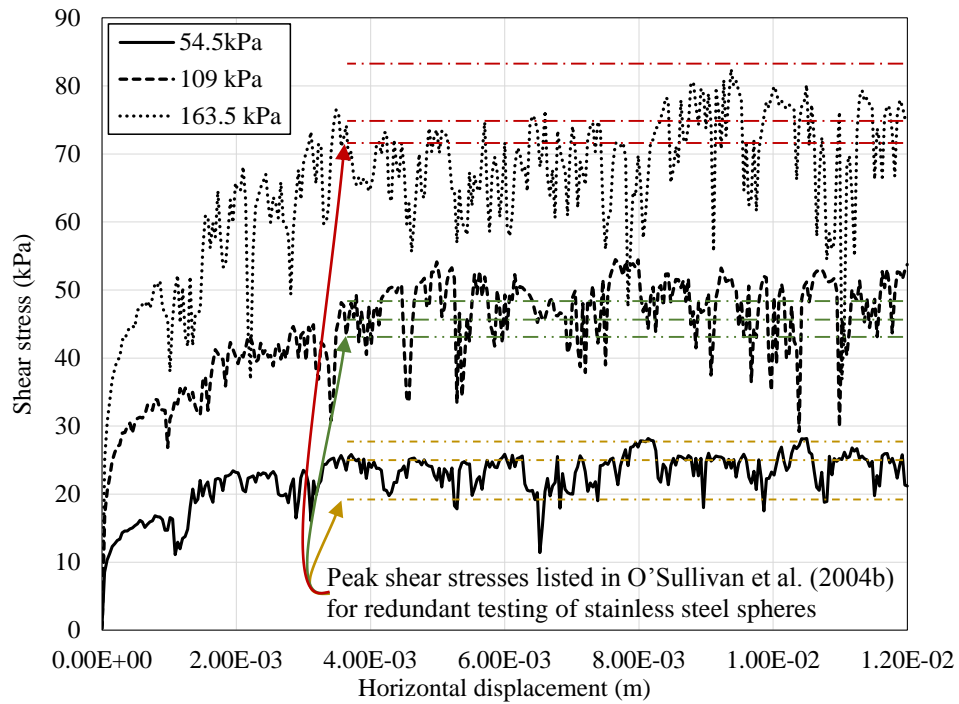


Figure 3.2.4.1. Shear stress versus horizontal displacement for direct shear test simulations using random packings of stainless steel spheres

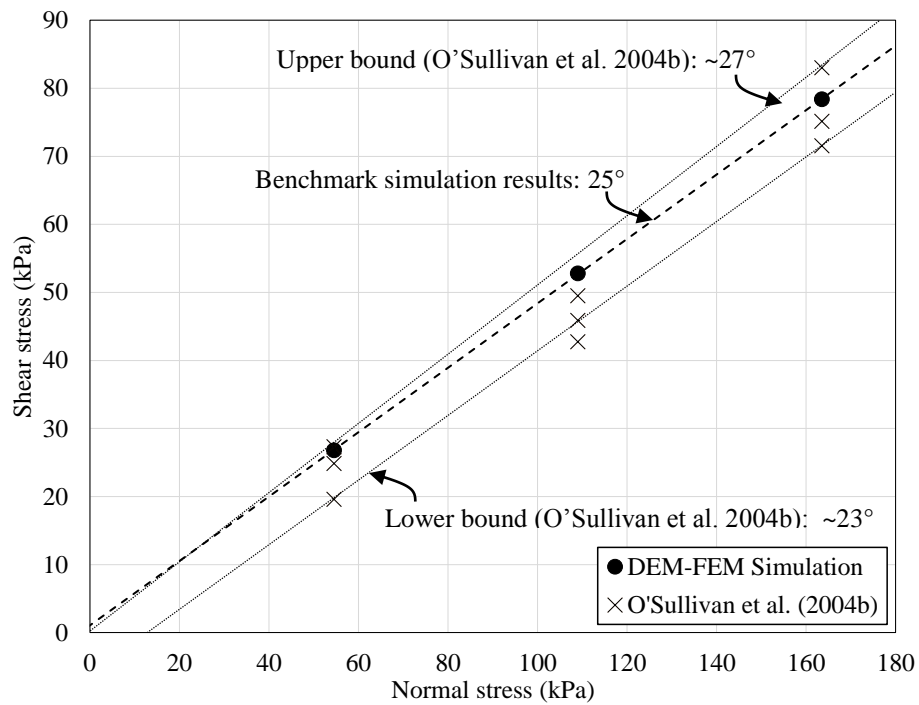


Figure 3.2.4.2. Peak shear stress versus normal stress for direct shear test simulations using random packings of stainless steel spheres

3.2.5 Shearing Resistance of Geometric Packings

This section presents an analysis of shearing resistance of DSE models whose particles are packed in a regular geometric assembly. The theoretical description of granular materials in assemblies of microscopic particles is a challenging task. The particle assemblies characterize in-situ initial and boundary conditions. In turn, the conditions are used in solving the equations of motion of the particulate system under stress equilibrium states (via a network of particle contact forces and various degrees of dissipative interparticle friction). Using the DEM implementation of LS-DYNA (LSTC 2014b), the influence of packing on contact stress distributions within an explicit time domain is investigated using idealized DSE assemblies and contact penalty springs. The validity of idealized geometric packings, as to whether uniformity can simulate granular fabrics, is still a matter of debate. However, the present section strictly focuses on the effects that micromechanical structures (idealized by assemblies of spherical discrete elements) can have on the macroscopic shear strength of the entire assembly. In this context, the macroscopic scale is associated with the size of samples used for direct shear experiments in laboratory settings.

The four packing assemblies used for this investigation are shown in Fig. 3.2.5.1, where the gray circles represent an individual row of spheres and the black circles represent the arrangement of spheres on the level above the gray set. The assembly schematics of Fig. 3.2.5.1 represent the unit cell for each packing, or the basic structure that repeats itself throughout the assembly. The packing assemblies shown in Fig. 3.2.5.1a and Fig. 3.2.5.1b are the face centered cubic (FCC) and Rhombic (also referred to as tetrahedral or hexagonal close packing). These two packing arrangements are theoretically considered to be the densest arrangement for uniformly sized spheres.

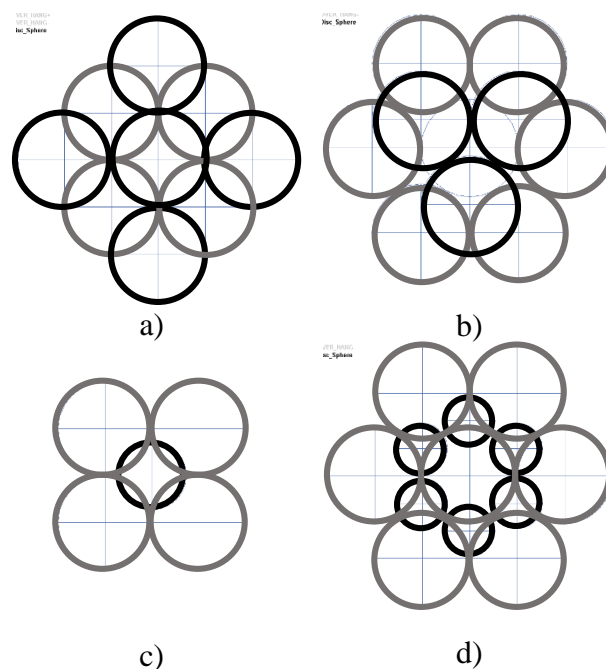


Figure 3.2.5.1. Geometric packings considered: a) Face-centered cubic; b) Rhombic; c) Simple cubic binary; d) AB binary

The packing assemblies shown in Fig. 3.2.5.1c and Fig. 3.2.5.1d are referred to as binary packing structures since two different sets of radii are present. The binary packing shown in Fig. 3.2.5.1c is called the simple cubic binary, which is based on the simple cubic packing structure with the addition of smaller spheres (with radius R_{\min}) located within the available space between layers of the larger sphere set (R_{\max}). The binary packing structure shown in Fig. 3.2.5.1d is referred to as AB Binary. This packing was developed using the cubical-tetrahedral packing structure with the addition of smaller spheres located within the available space between layers of larger spheres. Summaries of the geometric packing assemblies are listed in Table 3.2.5.1. The coordination number is defined as the average number of contacts per sphere. It can be seen that the addition of a smaller sphere set increases the density of packing (corresponds to a smaller void ratio), but the coordination numbers of such binary packings remain at values of 12 or less.

Table 3.2.5.1. Properties of geometric packings

Type of Packing	Coordination Number	Layer Spacing	Porosity [%]	Void Ratio	R_{\min}/R_{\max}
FCC	12	$\sqrt{2}R$	25.95	0.35	1
Rhombic	12	$2\sqrt{2/3}R$	25.95	0.35	1
Simple Cubic BINARY	11.1	$2R$	23.83	0.31	$\sqrt{3}-1$
AB BINARY	10.7	$2R$	22.65	0.29	$\sqrt{7/3}-1$

In the present study of macroscopic-scale shear behaviors of idealized packings, discrete element analysis models are developed using LS-DYNA. The motion of each sphere is computed using Newton's laws of motion, allowing for both translations and rotations at the centroid. Interactions between spheres are controlled through specification of frictional coefficients, along with spring and damping constants, which are defined in both normal and tangential directions to the plane of spherical surface contact (Karajan et al. 2012). A penalty-spring method is used by populating the LS-DYNA keyword `*CONTROL_DISCRETE_ELEMENT`. Material properties such as mass density and bulk modulus are defined using material definition cards (e.g., `*MAT_ELASTIC`). A summary of the DEM input parameters used for the direct shear test simulations on idealized packing is listed in Table 3.2.5.2. Note that capillary forces were not utilized in the investigation.

Table 3.2.5.2. DSE Parameters for direct shear testing of idealized packings in LS-DYNA

Parameter	Value
Radius	5 mm
<i>NDAMP</i>	0.70
<i>TDAMP</i>	0.40
<i>FRIC</i>	0.1, 0.3, 0.5
<i>FRICR</i>	0
<i>NORMK</i>	1.0
<i>SHEARK</i>	0.5
Mass Density	3,000 kg/m ³
Elastic Modulus	300 MPa
Poisson's Ratio	0.33333

Three values of *FRIC*, the interparticle sliding friction coefficient, are used in a parametric study (with values of 0.1, 0.3, and 0.5) to develop a range of values in conjunction with the aforementioned packing structures. Normal and tangential damping parameters, *NDAMP* and *TDAMP* respectively, are used to ensure numerical stability and are based on recommended values from Karajan et al. (2012). The focus of this investigation is placed solely on the effects that the packing assemblies and *FRIC* values have on macroscopic behavior, thus the frictional rolling coefficient *FRICR* is set to zero. The normal-contact spring scale factor, *NORMK*, is set 1.0 and the ratio of tangential to normal stiffness, *SHEARK*, is set to 0.5 as used by Cil and Alshibli (2014). Mass density and modulus values are selected to prevent significant particle overlapping for the magnitudes of pressure imposed during the direct shear and chamber tests, while also promoting practical computational times.

Direct shear tests are simulated to quantitatively characterize the macroscopic shear behaviors of packings with latticed geometry (i.e., regular, repeated arrangements). A square shaped test apparatus is used that is 200 mm in width by 100 mm in height (see Faraone et al. 2015 for details of the numerical test apparatus model development). Each packing assembly can have a different sized unit cell for the same specified radius, thus not all packing assemblies can fill the respective, specified domains without gaps developing between spheres and the apparatus walls. Any gaps between arrays of spheres and the walls of the direct shear test apparatus are not ideal. When initial gaps are present, application of gravitational accelerations or applied normal stress may cause significant rearrangement of the sphere arrays due to absence of lateral confinement. To account for such gaps, apparatus dimensions in the horizontal directions are scaled so as to encase the assembly, (i.e., initial gaps are approximately equal to 0 mm). Contact between the discrete spheres and shell elements is specified using the `*CONTACT_AUTOMATIC_NODES_TO_SURFACE` keyword. The coefficient of sliding friction used in the shell-spheres contact is set equal to *FRIC* (Table 3.2.5.2).

To estimate the frictional resistance of the packing, normal stresses are applied, and the corresponding maximum shear stresses are plotted. Shear stresses on the samples are calculated by first measuring lateral forces (in the direction of shearing) acting on the top box and plate. These forces are recorded using the `*DATABASE_RCFORC` card and are divided by the cross sectional area of the sample. An example of the results obtained from this process is depicted in Fig. 3.2.5.2a, which consists of shear stress versus shear strain for testing of the Rhombic packing assembly, *FRIC* = 0.3, and under normal stresses of 50 kPa, 100 kPa, and 150 kPa. Peak shear stress values are found for each normal stress and then plotted in Fig. 3.2.5.2b, for which a regression line is then fitted using a least-squares approximation. The angles of internal friction (φ) are determined per the slope of the fitted line. For the Rhombic packing example, using the fitted line from Fig. 3.2.5.2b, $\varphi = \tan^{-1}(1.1535) = 49.1^\circ$.

Results from the parametric study for various combinations of packing assemblies and coefficients of friction are shown in Fig. 3.2.5.3. For the rhombic and FCC packing, there is a relationship between coefficient of friction and φ . For the binary packing assemblies, a relationship is not as readily apparent (φ does not increase as prominently for increasing values of *FRIC*).

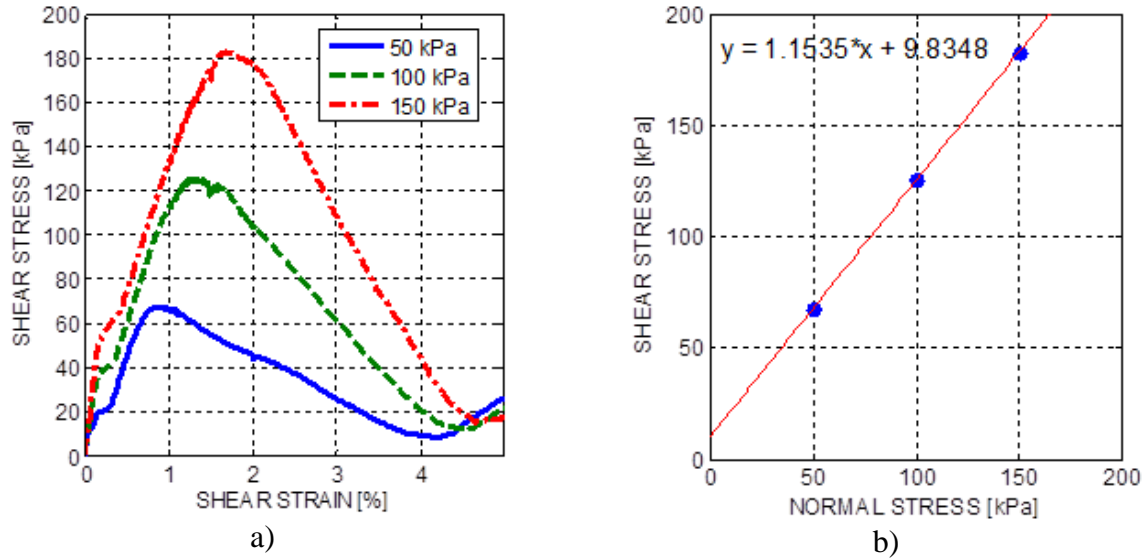


Figure 3.2.5.2. Numerical simulation of direct shear tests for rhombic packings $FRIC = 0.3$: a) Shear stress versus shear strain; b) Peak shear stress versus normal stress

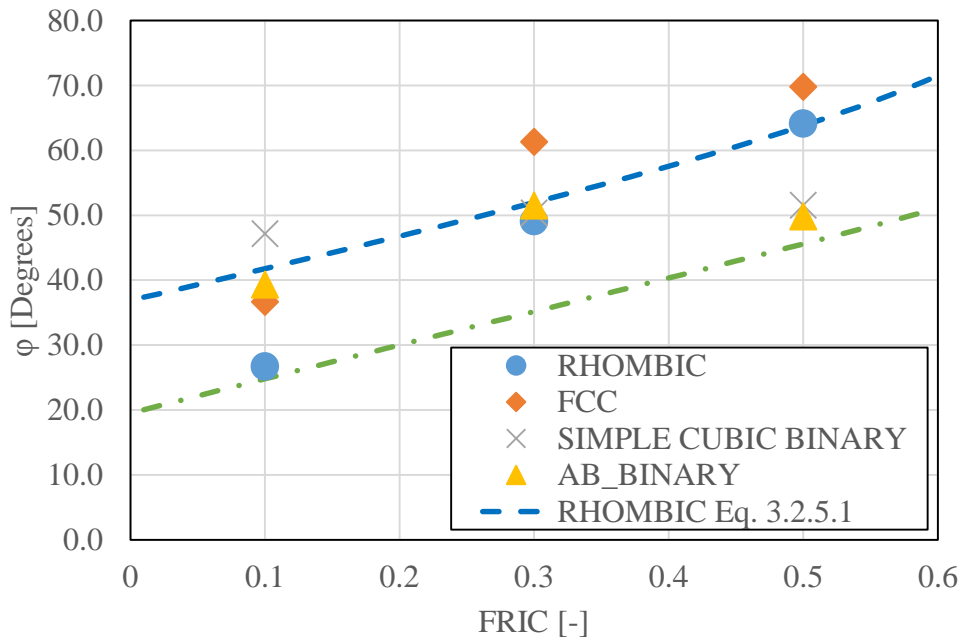


Figure 3.2.5.3. Parametric results from direct shear test simulations of idealized packings

It is also observed that φ for the FCC packing is greater than that of the Rhombic packing. As reported by O’Sullivan (2004a), for two physical triaxial compression tests of 12.7 mm diameter steel spheres, φ values of 41.6° and 24.6° were measured for Rhombic and FCC packings, respectively. O’Sullivan (2004a) also reported comparable results for DEM modeling of

the triaxial compression tests using a *FRIC* value of 0.096, resulting in ϕ values of 42° and 23.5° for Rhombic and FCC packings, respectively. Additionally, theoretical expressions to estimate the peak strength of Rhombic packings (Rowe 1962) and FCC packings (Thorton 1979) show agreement in that for any value of interparticle friction, the Rhombic packing will have a higher peak strength than that of the FCC packing. These theoretical expressions are shown in Eqn. 3.2.5.1 and Eqn. 3.2.5.2 for Rhombic (Rowe 1962) and FCC (Thorton 1979) packings, respectively.

$$\frac{\sigma_1}{\sigma_3} = \frac{(4 + 2\sqrt{2}FRIC)}{(1 - \sqrt{2}FRIC)} \quad (3.2.5.1)$$

$$\frac{\sigma_1}{\sigma_3} = \frac{2(1 + FRIC)}{(1 - FRIC)} \quad (3.2.5.2)$$

where σ_1 is the major principle stress and σ_3 is the minor principle stress. Using Eqn. 3.2.5.3, ϕ can be evaluated using principal stresses, and can be combined with Eqns. 3.2.5.1-3.2.5.2, to evaluate ϕ as a function of *FRIC* (recall Table 3.2.5.2):

$$\phi = \sin^{-1} \left[\frac{(\sigma_1 - \sigma_3)}{(\sigma_1 + \sigma_3)} \right] \quad (3.2.5.3)$$

Results of this combination are shown in Fig. 3.2.5.3 as dashed lines. Validation of the previously discussed direct shear test apparatus was carried out by comparing results from numerical direct shear tests to results reported in O’Sullivan (2004b). The validation consisted of modeling steel spheres arranged in a random packing. The numerical used to investigate geometric packings in the current study produced a ϕ of 21.1°, where over the course of repeated testing, O’Sullivan (2004b) measured ϕ values ranging from 22.7° to 26.2°. The comparable benchmarking results (for randomly distributed spheres) suggest that geometrical arrangement of the packing assemblies may lead to significant differences in ϕ values observed in triaxial versus direct shear testing. Future research is needed to explore such differences.

3.2.6 Apparent Cohesion

Cohesion by definition means the act (stress) of sticking together. In soil mechanics, cohesion refers to the shear strength under zero applied normal stress. Cohesion is a property associated with cohesive soils (e.g., clayey silt, sandy clay). However, under certain saturation conditions, cohesion can be observed in otherwise cohesionless soils. This increase in initial shear strength in cohesionless soils is known as apparent cohesion. Apparent cohesion is the result of negative pore water pressure, caused by capillary suction at the scale of individual granules. Recall that the micromechanics of capillary suction force was previously discussed in Sec. 2.4.7.

Apparent cohesion depends on the degree of saturation of the granules making up a given soil mass. It has been observed that as degree of saturation of the soil mass increases, apparent cohesion decreases. Depending on the saturation level, a soil mass is said to belong to one of three

regimes: capillary, funicular, and pendular. During desaturation of a soil mass, both the large pores and small pores can become saturated with water. This regime is called the capillary regime (Fig. 3.2.6.1). As desaturation continues, shrinkage of pore spaces is observed. At some point of time, air begins to occupy the pore spaces, and liquid bridges or menisci are formed between soil particles. This regime is called the funicular regime (Fig. 3.2.6.1b). As desaturation continues further, liquid is present only in the form of thin films surrounding the soil particles. This regime is called the pendular regime (Fig. 3.2.6.1c). Apparent cohesion is most prominent in soil masses exhibiting saturation under the pendular regime.

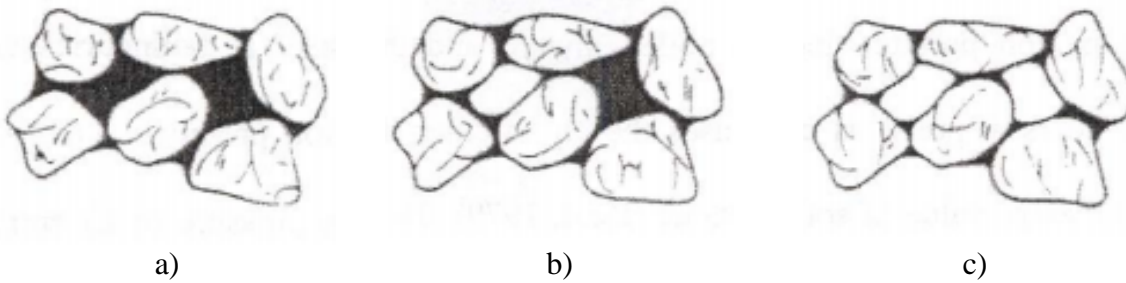


Figure 3.2.6.1. States of saturation in for granular soils (Kim 2001): a) Capillary; b) Funicular; c) Pendular

To study apparent cohesion at the macroscopic level, and as brought about by microscopic capillary suction forces, two direct shear test simulations were performed using the LS-DYNA DEM-FEM model. The combined DEM-FEM model of the direct shear test described in Sec. 3.2.2 was used, and the procedure described in Sec. 3.2.3 was followed. Additionally, the parameter values listed in Table 3.2.6.1 were utilized in modeling the randomly packed DSE assemblies. The only difference between the two simulations was in the numerical treatment of particle-particle contact. Namely, one simulation was carried out without consideration of capillary suction force calculations (i.e., unsaturated conditions were simulated), and one simulation was carried with consideration of capillary suction force calculations (i.e., partially saturated conditions were simulated).

Table 3.2.6.1. DSE parameter values for direct shear test simulations

Parameter	Value	Units
<i>NDAMP</i>	0.70	--
<i>TDAMP</i>	0.40	--
<i>FRIC</i>	0.1	--
<i>FRICR</i>	0.001	--
<i>NORMK</i>	1.0	--
<i>SHEARK</i>	0.28	--
Surface Tension	0.072	N/m
Initial volume fraction	0.5	--
Contact Angle	20	°

For each run of the direct shear test simulation (under applied normal stresses of 54.5 kPa, 109 kPa, and 163.5 kPa), the corresponding peak shear stresses (as obtained from the LS-DYNA results) are listed in Table 3.2.6.2. To highlight the apparent cohesion phenomenon, the quantities

listed in Table 3.2.6.2 are plotted in Fig. 3.2.6.2. Additionally plotted in Fig. 3.2.6.2 are linear regression lines (i.e., estimates of Mohr-Coulomb failure envelopes) for the three test runs with, and separately, without calculation of capillary forces. As denoted in Fig. 3.2.6.2, a non-zero intercept (3.23 kPa) is present in the failure envelope pertaining to the model utilizing the LS-DYNA capillary force module. In contrast, no such intercept is present for the failure envelope of the simulations that did not make use of the capillary force calculation module. It is important to note that the DSE assemblies used in the simulations are modeled after stainless steel spheres. For granular material, like sand, the apparent cohesion phenomenon may be even more pronounced. To better characterize the modeling of apparent cohesion for DSE assemblies representing granular media, further investigation is required, and is currently underway.

Table 3.2.6.2. Direct shear test simulation results

Normal stress (kPa)	Shear stress without Capillary Suction (kPa)	Shear stress with capillary suction (kPa)
54.5	22.87	24.59
109	45.32	48.12
163.5	68.5	70.5

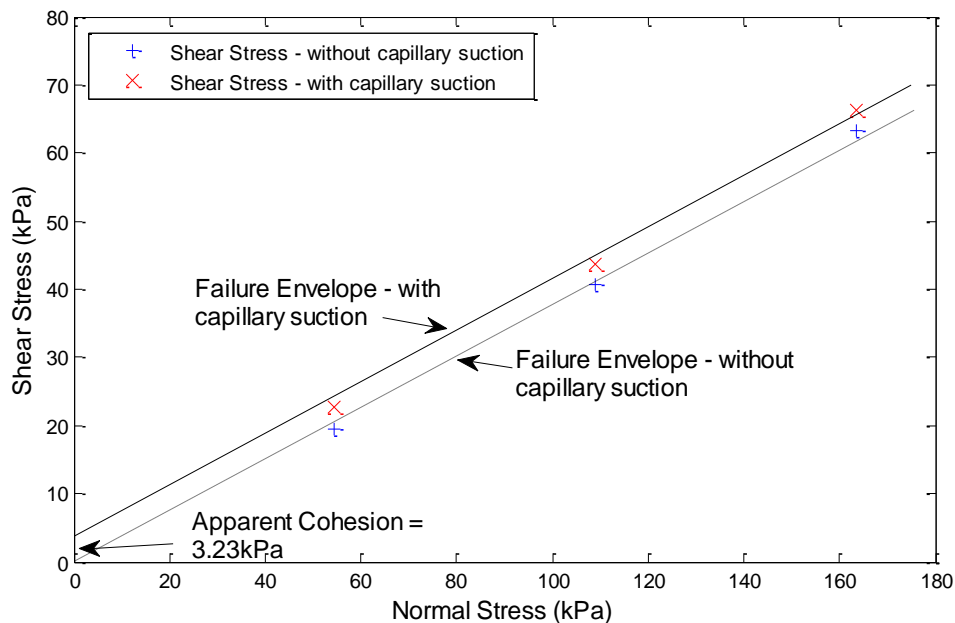


Figure 3.2.6.2. Direct shear test simulations with and without use of capillary force calculations

3.3 Triaxial Compression Test

In Sec. 3.3, focus is placed on development and benchmark testing for numerical modeling of granular materials subjected to triaxial compression tests. As with the numerical modeling of the direct shear test (recall Sec. 3.2), a testing standard is first identified to establish a datum for the triaxial compression test numerical model development. Pertinent aspects of the selected test standard are summarized in Sec. 3.3.1. Considerations for components of the (physical) triaxial

compression test that are included in the (numerical) testing of the current study are detailed in Sec. 3.3.2. Each stage of the triaxial compression test simulation is discussed in Sec. 3.3.3., including the manner in which assemblies of DSE are introduced (i.e., packed) into the test chamber. For all stages of the testing, efforts are made to maintain consistency with the processes delineated in the physical test standard. A benchmarking scenario, involving previously conducted physical testing, is reported in Sec. 3.3.4. Additionally, physical test measurements are compared to results obtained using the triaxial compression test model of the current study. Lastly, presented in Sec. 3.3.5 are the findings from a preliminary exploration into the effects of scaling DSE radii in conjunction with use of the (numerical) triaxial compression test procedure.

3.3.1 Description of Physical Test Procedure

As motivation for the numerical modeling approach and test staging described in Sec. 3.3.2 and Sec. 3.3.3., respectively, relevant facets of the (physical) triaxial compression test are first summarized. While several extant ASTM testing standards are dedicated to triaxial compression testing (e.g., standards specific to drained consolidated conditions, undrained consolidated conditions), the equipment and procedures listed in ASTM D2850 (ASTM 2007) are adopted for the purposes of model development in the current study. An example schematic of a triaxial compression test is shown in Fig. 3.3.1.1, where the highlighted region denotes the scope of the numerical model for the current study.

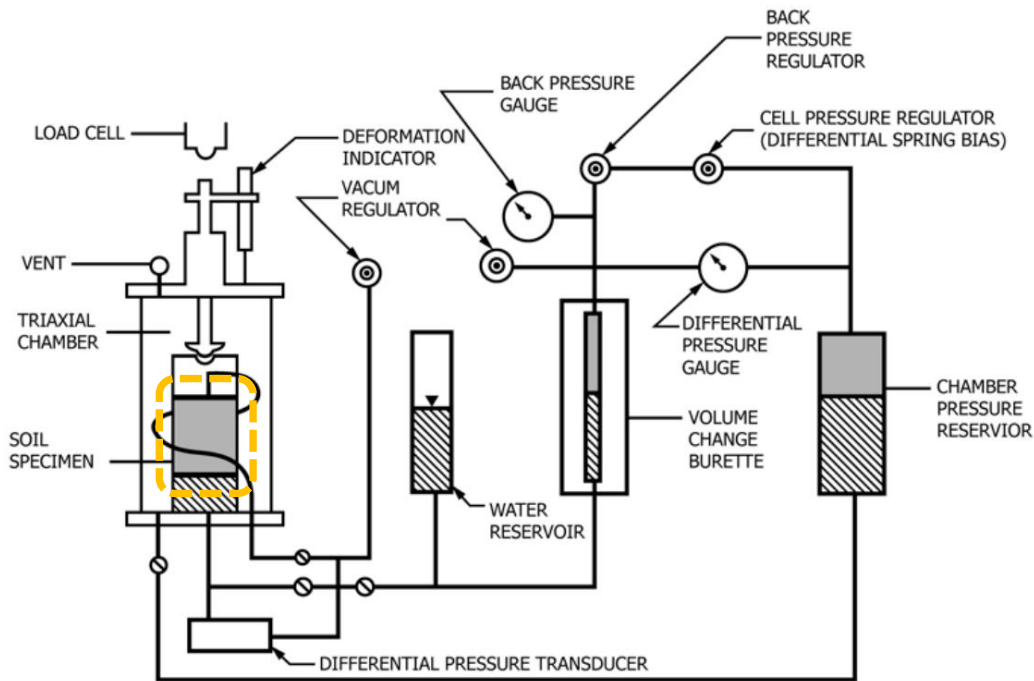


Figure 3.3.1.1. Schematic of a triaxial compression test (ASTM 2011) with indication of numerical model scope for the current study

Physically, test preparation is initiated directly within the triaxial chamber (Fig. 3.3.1.1) by placing a cylindrical soil specimen directly atop the chamber bottom plate. While in position atop

the bottom plate, a thin rubber membrane sleeve (e.g., with thickness of approximately 0.6 mm, 0.025 in., or less) is slid over the specimen and secured along the bottom plate perimeter using O-rings (or other positive seals). A top plate is then brought down to bear directly atop the partially encased cylindrical specimen, and in a consistent fashion, O-rings (or comparable sealing implements) are used to affix the membrane and top plate. These preparations ensure that the specimen is entirely sealed along its vertical surfaces via the rubber membrane, and further, that the specimen bottom and top surfaces are bounded by the bottom and top plates, respectively. As a result, the volume occupied by the specimen is isolated within a sub-region of the triaxial chamber, and any substances subsequently introduced into the triaxial chamber (e.g., water) are precluded from adulterating the specimen.

After completing the specimen encasement process, the triaxial chamber (Fig. 3.3.1.1) is hermetically sealed. Then, the entire chamber is pressurized to a predetermined pressure level using either (typically) water or air. In order for the test to be carried out under triaxial compression, by definition, vertical stresses and horizontal stresses of equal magnitude must be simultaneously imposed on the specimen during the pressurization (confining) stage. Therefore, pressures that develop within the chamber, along with those that arise along the top and bottom plate interfaces, are monitored during the pressurization stage. In the event that, during pressurization, stresses along the top or bottom plate begin to deviate from the chamber pressure, then an actuator (with load cell, Fig. 3.3.1.1) is used to impose a corrective translation to the top plate.

The final stage of the triaxial compression test consists of shearing the specimen, which is enacted by imposing controlled vertical translations to the top plate, relative to (i.e., directly toward) the bottom plate. During the controlled shearing process, the triaxial chamber pressure is otherwise maintained at the pre-determined level of confining pressure. Also, as the top plate translates toward the bottom plate, the force required to maintain a constant displacement rate is recorded. The volume of the specimen is monitored and recorded throughout the final stage of testing. Triaxial compression test runs are typically carried out on three or more fresh (previously untested) specimens taken from a relatively larger sample of material. For each test run, a unique confining pressure is imposed. Data recorded during the testing permits quantification of: 1) Deviatoric stress versus axial strain; and, 2) Volumetric strain versus axial strain. Ultimately, such quantities facilitate the generation of Mohr-Coulomb failure envelopes, as well as the characterization of macroscopic properties.

3.3.2 Numerical Model of Test Apparatus

Taking into consideration the apparatus components and procedures listed in ASTM D2850 (ASTM 2007), a numerical model for simulating triaxial compression tests on DSE assemblies is shown in Fig. 3.3.2.1. The apparatus components of the numerical model derive from both finite element and discrete element entities, which together, act in a complimentary manner to maintain encasement of the DSE assembly throughout the confining and shearing stages of simulation. Within the context of detailing the apparatus components of the numerical model, the volume contained within (i.e., bounded by) the components is referred to as the test chamber. Rigid plates bound the top and bottom boundaries of the (numerical) test chamber, and both the bottom and top

plate are modeled using eight-node rigid solid elements. The vertical surfaces of the test chamber are bounded by set of bonded DSE, initialized in a hexagonal array, to form a flexible, cylindrical boundary spanning between the bottom and top plates. Properties for individual DSEs making up the cylindrical boundary are listed in Table 3.3.2.1. This particular means (and parameter values) of modeling the triaxial compression test apparatus membrane, originally proposed by Cil and Alshibli (2014), is demonstrated in Sec. 3.3.4 to give numerical test results that show agreement with physical test measurements.

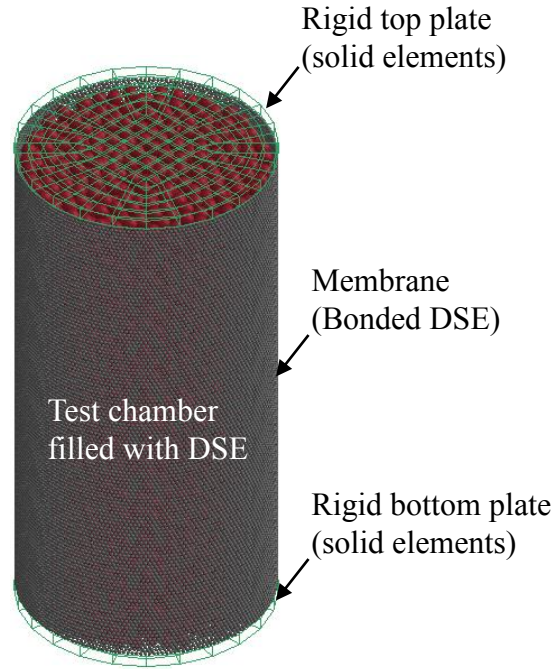


Figure 3.3.2.1. Combined DEM-FEM model of triaxial compression test apparatus

Table 3.3.2.1. Numerical parameters for the bonded DSE membrane (adapted from Cil and Alshibli 2014)

Parameter	Value	Units
Radius	0.85	mm
Density	7.85	kN/m ³
Normal contact stiffness	0.5E+01	kN/m
Tangential contact stiffness	0.5E+01	kN/m
Normal bond stiffness	1.0E+06	kPa
Shear bond stiffness	1.0E+06	kPa
Friction coefficient	0.26	--

3.3.3 Numerical Test Procedure

As adherence to testing standard ASTM D2850 (ASTM 2007), the numerical procedure for simulation triaxial compression testing is divided into the following stages: 1) Specimen preparation (packing); 2) Placement (mapping) of the specimen within the test chamber; 2) Application of hydrostatic (confining) pressure; and, 3) Shearing of the specimen. The initial unprepared (i.e., unpacked) configuration for an example DSE assembly is shown in Fig. 3.3.3.1. For the initial (unpacked) configuration, the DSE assembly is bounded along all outermost vertical surfaces by an open-ended cylinder of four-node rigid shell elements, where the inner diameter of the cylinder is equal to the unpressurized diameter of the test chamber. The bottom surfaces of the unpacked DSE assembly (Fig. 3.3.3.1) are bounded by a rigid bottom plate (made up of eight-node rigid solid elements), and all nodes of the bounding finite element entities are fully restrained from motion.

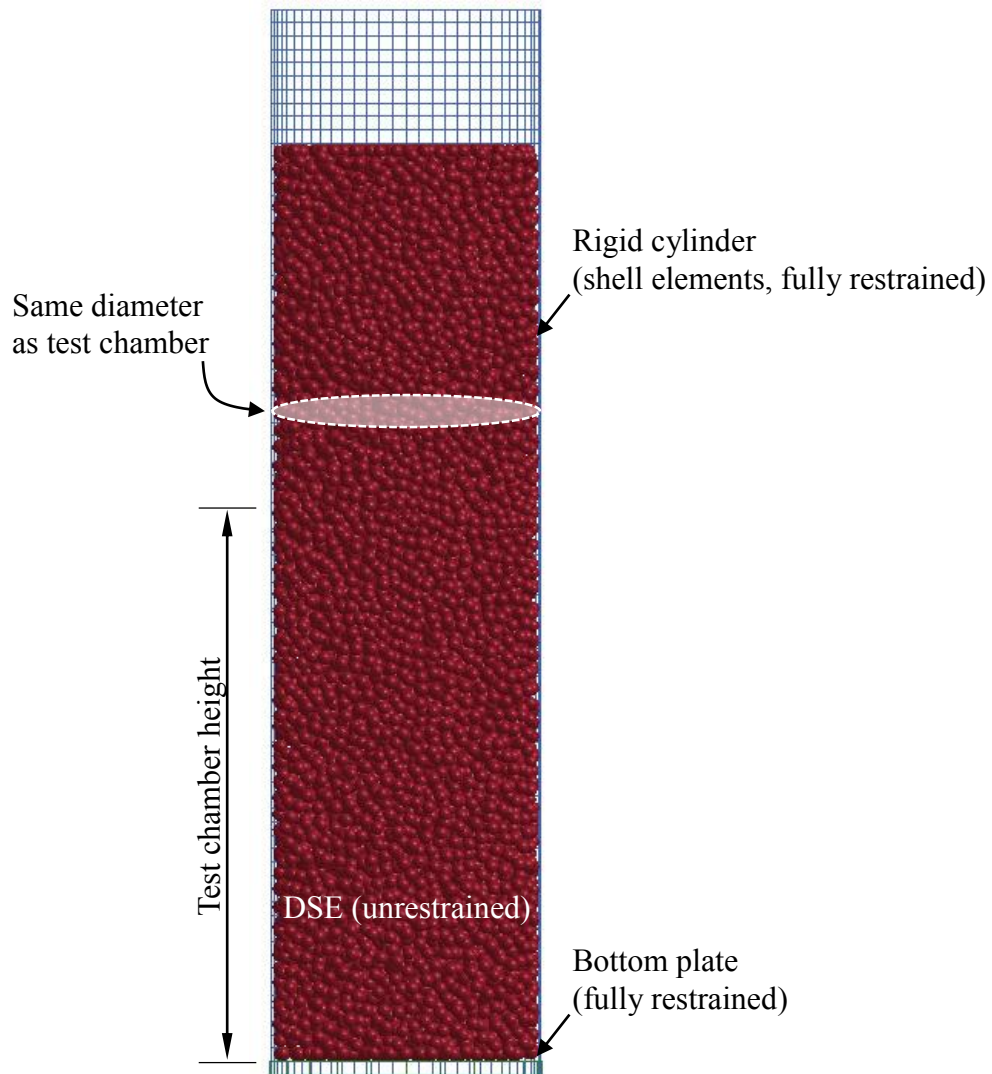


Figure 3.3.3.1. Unpacked specimen within a rigid cylinder

Prior to packing of the DSE assembly, the spheres extend a significant vertical distance above the height of the test chamber (Fig. 3.3.3.1). However, upon application of an acceleration field (Fig. 3.3.3.2), the DSE assembly reaches a mechanically stable state with overall height that (approximately) equals that of the test chamber. The process of introducing an acceleration field (e.g., gravitational acceleration) to bring about the random packing shown in Fig. 3.3.3.2 is iterative. In transitioning from one iteration to the next, the number of spheres included in the unpacked assembly (recall Fig. 3.3.3.1) may be either increased or decreased. This iterative packing process is considered to have reached convergence when the height of the assembly, when exhibiting a mechanically stable state, approximately equals the height of the test chamber.

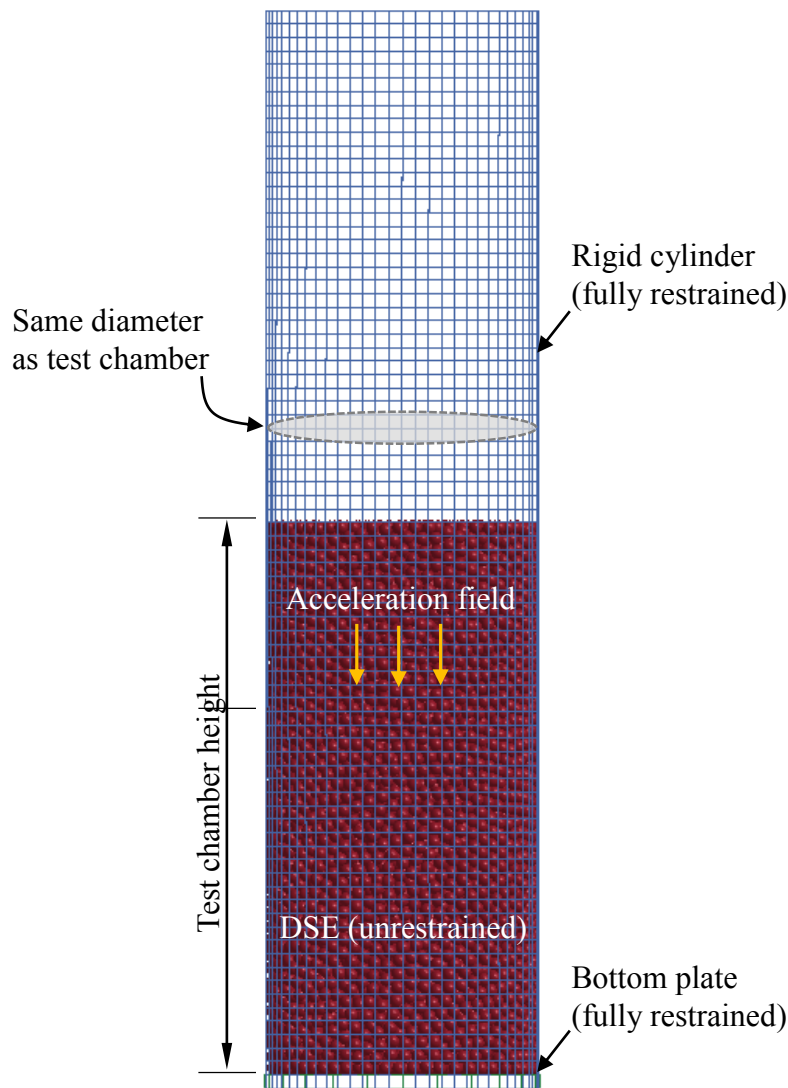


Figure 3.3.3.2. Packed specimen within a rigid cylinder

The second stage of the triaxial compression test simulation begins with coordinate mapping of the DSE assembly, after said assembly has reached a mechanically stable state, into a

model containing the rigid bottom and top plates of the triaxial compression test apparatus (Fig. 3.3.3.3). While the bottom plate shown in Fig. 3.3.3.3 is fully restrained from motion, the top plate is permitted to undergo vertical translation. To temporarily hold the packed DSE assembly in place, an open-ended cylinder of four-node rigid shell elements is again modeled. Furthermore, the rigid cylinder is fully restrained from motion and possesses an inner diameter equal to that of the test chamber. As an ensemble, the rigid bottom plate, top plate, and cylinder ensure that the packed DSE assembly maintains an overall shape that approximately conforms to the geometry (diameter and height) of the test chamber.

At the onset of the third stage of the triaxial compression test simulation (i.e., application of confining pressure), the bonded DSE membrane (recall Table 3.3.2.1) is introduced into the model (Fig. 3.3.3.4). Care is taken regarding the manner in which the bonded DSE membrane, with inner diameter equal to the test chamber diameter, interacts with other portions of the model. Accordingly, contact definitions are defined for interactions between the membrane spheres and: 1) Specimen DSEs; 2) Top plate; and, 3) Bottom plate. At the instant in which application of the confining pressure is initiated (Fig. 3.3.3.5), the boundary conditions of the model are simultaneously modified such that the DSE assembly (specimen) is held in place by the bottom plate, top plate, and bonded DSE membrane. Upon reaching the pre-determined level of confining pressure, the rigid cylinder is removed from the simulation. In the final stage of the simulation, the top and bottom plates undergo prescribed translations towards one another (Fig. 3.3.3.6).

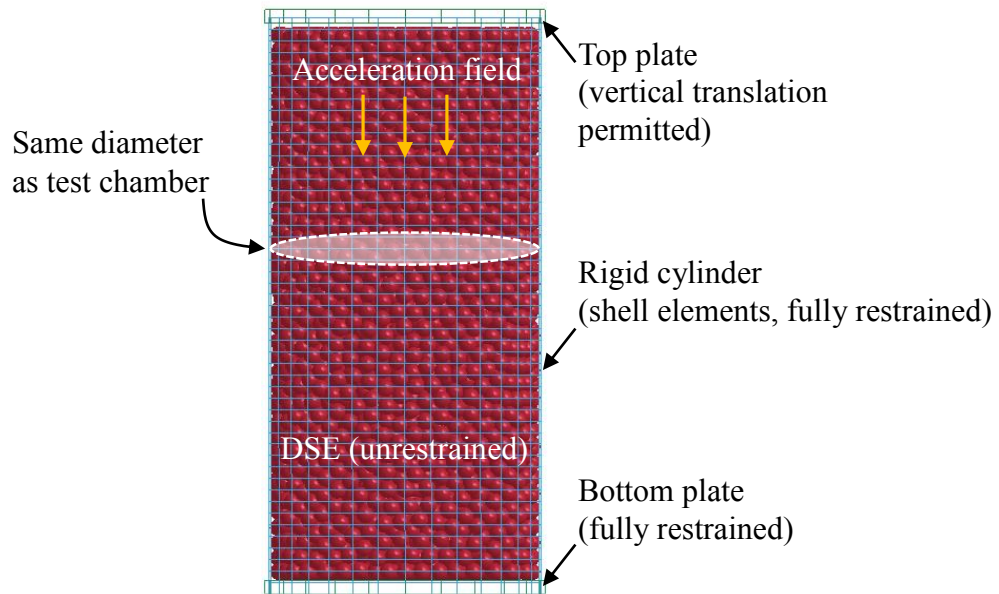


Figure 3.3.3.3. Random packing of specimen into the test chamber

Throughout the shearing stage of the triaxial compression test simulation (Fig. 3.3.3.6), the pre-determined confining pressure is maintained across the bonded DSE membrane. Also, the forces necessary to maintain constant translations of the bottom and top plate is monitored. Likewise, the total volume bounded by the bottom plate, top plate, and membrane is monitored. Monitoring of such quantities facilitates the making of direct comparisons between simulation results and physical test measurements, as demonstrated for a benchmark case in Sec. 3.3.4.

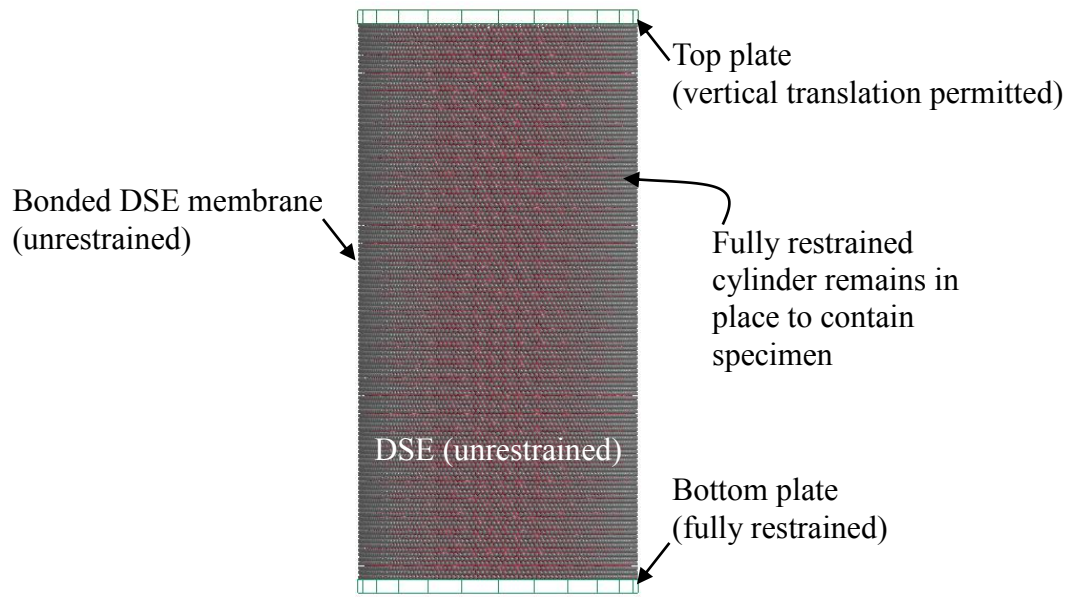


Figure 3.3.3.4. Introduction of bonded DSE membrane

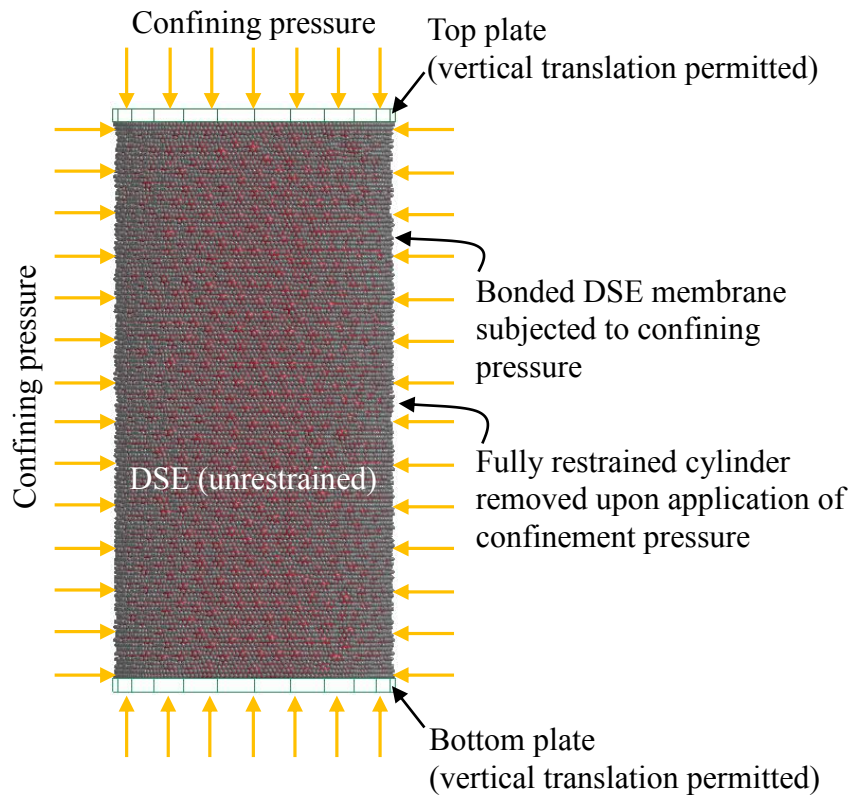


Figure 3.3.3.5. Application of confining (hydrostatic) pressure to bonded DSE membrane, bottom plate, and top plate

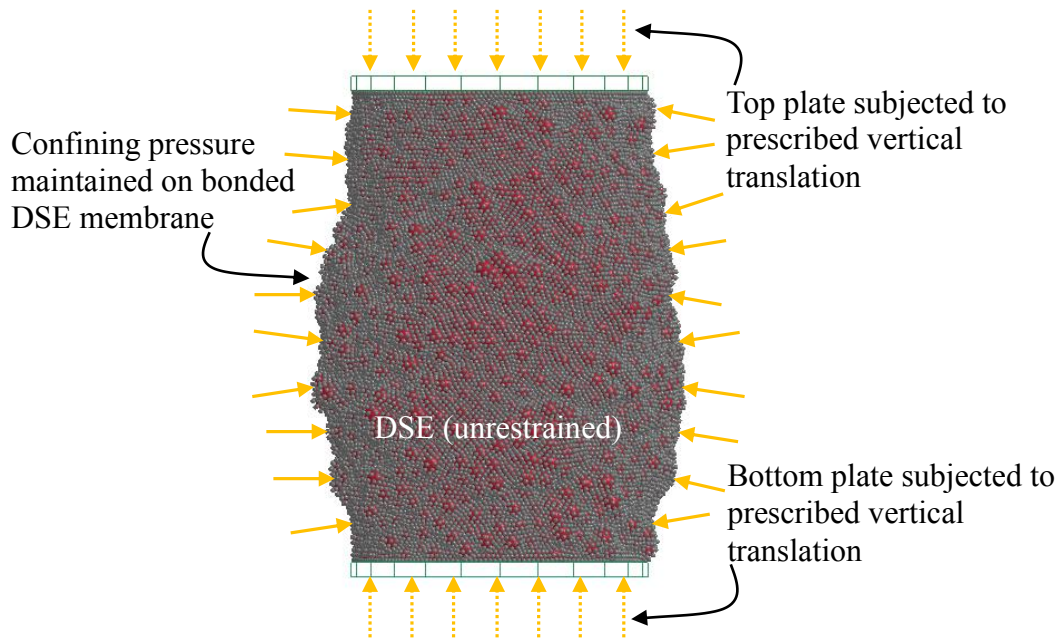


Figure 3.3.3.6. Prescribed motion of apparatus top and bottom plates

3.3.4 Validation

The triaxial compression test model and simulation stages (discussed in Sec. 3.3.2 and Sec. 3.3.3, respectively) are validated against physical measurements reported in Cil and Alshibli (2014), where plastic pearls were utilized in conducting physical triaxial compression tests. While numerous studies pertaining to triaxial compression testing of granular media are available in the literature, the work of Cil and Alshibli (2014) holds particular relevance in benchmarking the triaxial compression test model of the current study. In particular, the physical test measurements reported in Cil and Alshibli (2014) correspond to specimens (random packings of plastic pearls) with uniform properties. Consequently, the uncertainty attributed to the properties of the specimen constituents (i.e., each plastic pearl) is relatively small (as compared to the uncertainties that arise when modeling granular soil using DSE assemblies). By drastically reducing the uncertainties associated with the test specimen properties, the focus of the triaxial compression test benchmarking remains squarely on judging the capabilities of the numerical apparatus components and simulation stages.

Properties excerpted from Cil and Alshibli (2014) for defining the (numerical) benchmarking specimen (corresponding to the plastic pearls), are listed in Table 3.3.4.1. A qualitative comparison of the previously conducted physical testing and numerical simulations of the current study (each carried out for confining pressures of 25 kPa, 50 kPa, and 100 kPa) can be made by reviewing Fig. 3.3.4.1. One of the physical specimens used in the previously conducted physical testing is shown just prior to shearing (Fig. 3.3.4.1a), and in the post-sheared state (Fig. 3.3.4.1b). As comparison, a corresponding benchmark model (generated as part of the current

study) is shown just prior to, and just after, the shearing stages in Fig. 3.3.4.1c and Fig. 3.3.4.1d, respectively.

Table 3.3.4.1. Numerical parameters for DSEs representing the plastic pearls (after Cil and Alshibli 2014)

Parameter	Value	Units
Radius	3.25	mm
Density	9.03	kN/m ³
Normal contact stiffness	2.00E+06	kN/m
Tangential contact stiffness	1.00E+06	kN/m
Bond strength	1.00E+10	kN/m
Friction coefficient	0.26	--

With focus on comparing Fig. 3.3.4.1b to Fig. 3.3.4.1d, both the physical test and numerical model indicate a barrel-shaped failure (i.e., yielding) of the specimen. As a quantitative assessment of the capabilities of the triaxial compression test model, comparative data plots of axial strain versus deviatoric stress are shown in Fig. 3.3.4.2. Across the three confining pressures considered (25 kPa, 50 kPa, and 100 kPa), excellent agreement is observed between the physical test data and the simulation results: the (benchmark) physical test data encompass the numerical data for both the initial curve portions (i.e., for axial strains less than 1%) as well as for the asymptotic curve portions (i.e., after the specimens have yielded).

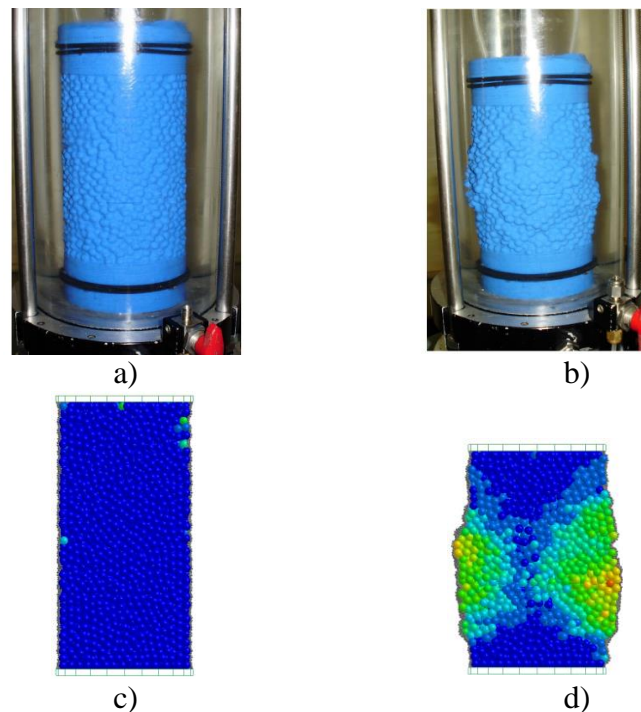


Figure 3.3.4.1. Triaxial compression testing of plastic pearls: a) Physical specimen prior to shearing; b) Physical specimen after shearing (Cil and Alshibli 2014); c) Numerical model prior to shearing; d) Numerical model after shearing (displacement field shown)

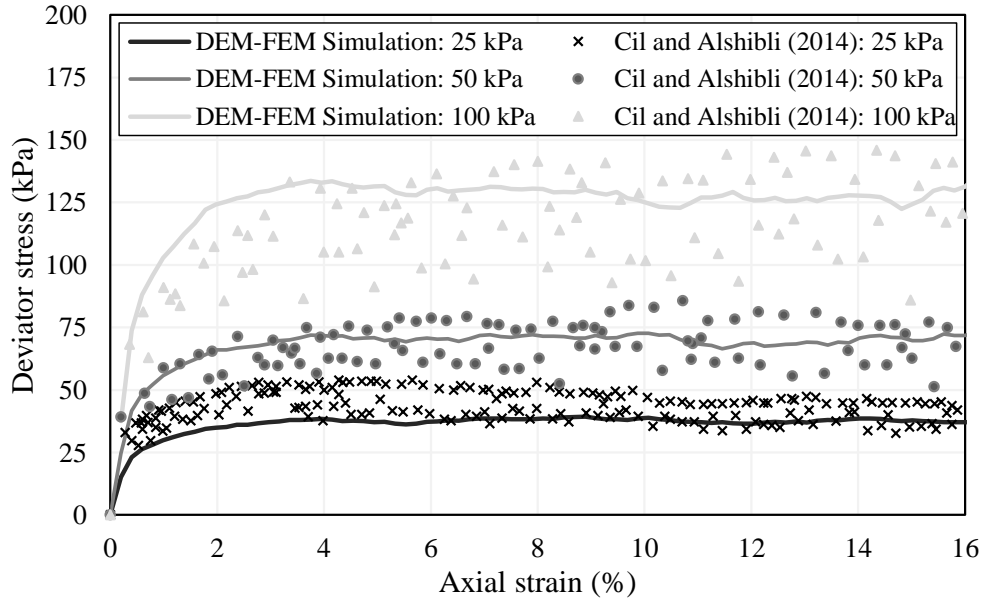


Figure 3.3.4.2. Comparison between numerical simulation and physical triaxial compression tests using random packings of plastic pearls

3.3.5 Preliminary Investigation of Scale Invariance with respect to DSE Size

A preliminary investigation is carried out to explore how size scaling of individual DSE radii within an assembly affects the macroscopic properties for a monodisperse mesh. Critically, the investigation of the overall upscaling process is ongoing, and will be completed as part of Task 3 of the research project. For the preliminary investigation into the effects of scaling DSE radii, a monodisperse assembly of 5 mm DSEs are generated within a 200 mm by 400 mm (cylindrical) triaxial test chamber using the gravitational packing procedure discussed in Sec. 3.3.3. Parameters for the DSE assembly are shown in Table 3.3.5.1. A corresponding (scaled) assembly of DSE is created by increasing the radii of all spheres by a factor of five, resulting in a triaxial specimen consisting of 25 mm DSEs. In addition, the triaxial test chamber volume (and surrounding components of the numerical test apparatus) are scaled by a factor of five. Importantly, equal-valued contact and material parameters (from Table 3.3.5.1) are used to simulate triaxial compression testing on the 5 mm and 25 mm assemblies.

Three triaxial compression tests are simulated as part of the preliminary investigation: the 5 mm assembly with an equivalent strain rate of shearing of 10 mm/sec; the 25 mm assembly with an equivalent strain rate of shearing of 10 mm/sec; and, the 25 mm assembly with an equivalent displacement rate of 2 mm/sec. For all DSE assemblies considered, a confining pressure of 140 kPa is applied and the specimens are tested up to a shear strain of 5% or greater. Computed values of deviatoric loading and volumetric strain are shown in Fig. 3.3.5.1. Clearly, the three test simulations show strong agreement with respect to both changes in stress, as well as volumetric behavior. Further interpretation, and the overall methodology for upscaling of DSE for use in large-scale simulations (e.g., megascopic assemblies that represent site conditions for installing piles), are reserved for Task 3 of the ongoing research.

Table 3.3.5.1. Properties of DSE used in demonstrating scale invariance

LS-DYNA Discrete Element Analysis Parameter	Value
Radius	5 mm and 25 mm
<i>NDAMP</i>	0.70
<i>TDAMP</i>	0.40
<i>FRIC</i>	0.6
<i>FRICR</i>	0
<i>NORMK</i>	1.0
<i>SHEARK</i>	0.29
Mass Density	2,600 kg/m ³
Elastic Modulus	700 MPa
Poisson's Ratio	0.15

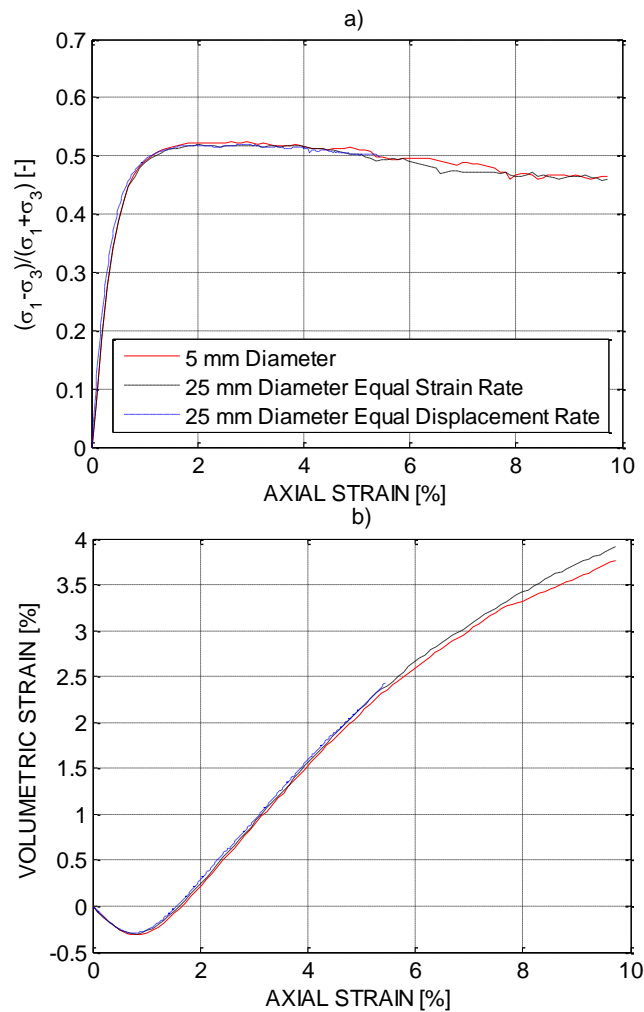


Figure 3.3.5.1. Comparison of numerical results for triaxial compression tests of 5 mm and 25 mm DSE assemblies: a) Deviatoric stress versus shear strain; b) Volumetric strain versus shear strain

3.4 Calibration of DSE Library Rheological Components

As a culmination of the efforts made toward: 1) Characterizing DSE rheology components in Ch. 2; and, 2) Developing and validating the combined DEM-FEM laboratory test models (Ch. 3), a standardized DSE library is formed. In establishing the library entries (i.e., the quantitative listings of parameter input values for DSEs), numerous DSE assemblies are utilized in triaxial compression test simulations. Assemblies are considered for configurations representing (physical) granular materials across an extensive range of (numerical) density states. Parameter values assigned to DSEs (making up the assemblies) included in the triaxial compression test simulations are additionally calibrated to bring about desired macroscopic (volumetric, stress-strain) responses under each of the numerical density states considered. Consequently, the collection of standardized DSE input parameter values (i.e., the DSE library) permits the modeling of DSE assemblies that are known *a priori* to exhibit desired macroscopic behaviors.

Density distribution plays a significant role in the manifestations of macroscopic strength of particulate systems (e.g., resistance to forming slip planes; stability of a given configuration). In Sec. 3.4.1, the range of macroscopic behaviors (volumetric, stress-strain) that can be exhibited by monodisperse systems subjected to random packing under gravitational acceleration is determined. Note that “monodisperse system” is defined as a DSE assembly where a single radius is assigned to all spheres within said assembly. In Sec. 3.4.2, to facilitate the modeling of granular materials under relatively more dense states, binary (bidisperse) systems (DSE assemblies containing a mixture of spheres with two unique radii) are introduced. In Sec. 3.4.3, widely adopted density state descriptors (pertaining to physical, granular soil masses) are identified as part of introducing strictly numerical density state descriptors for DSE assemblies. Additionally, for the newly defined (numerical) density state descriptors, conceptual pairings are made with the ranges of values for the macroscopic quantity known as the angle of internal friction. In this way, quantitative benchmarks of desired macroscopic behavior are established, which give focus to the DSE parameter calibration efforts (also discussed in Sec. 3.4.3). Finally, presented in Sec. 3.4.4 is a catalog of DSE input parameter values, which constitutes the DSE library.

3.4.1 Simulation of Macroscopic Granular Behaviors using Monodisperse Systems

Shown in Fig. 3.4.1.1 is a combined DEM-FEM model for generating mechanically stable configurations for monodisperse systems. The model is divided into two regions: the top portion of the model consists of a relatively voluminous funnel; and, the bottom portion of the model consists of a cylindrical chamber. Both the (top) funnel and (bottom) cylinder components are modeled using four-node rigid shell elements, the nodes of which are fully restrained from motion at all times. The dimensions of the rigid cylinder match those of the (numerical) triaxial compression test chamber (recall Sec. 3.3). A bottom plate, modeled using eight-node rigid solid elements, is positioned at the bottom end of the cylinder, and similarly, the nodes of the solid elements are fully restrained from motion throughout the simulation. As a final model component, a collection of DSEs are initialized at incipient contact (but non-overlapping) positions within the funnel region of the model.

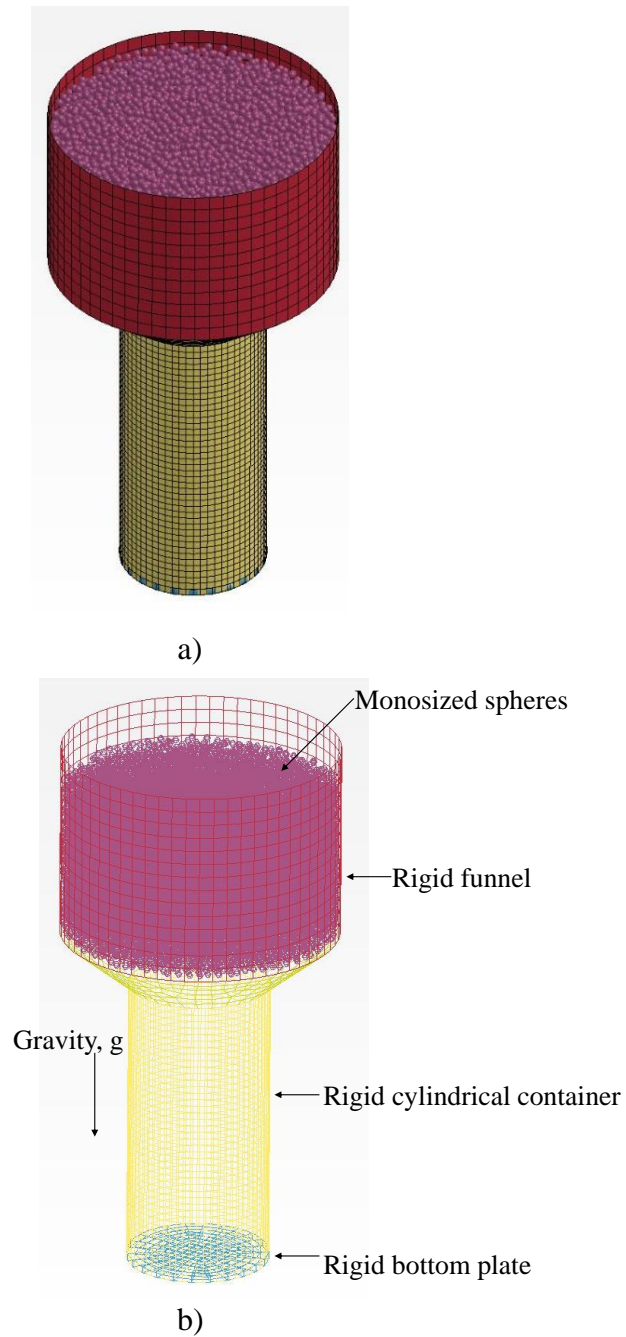


Figure 3.4.1.1. A DEM-FEM model for generating various density states of monodisperse systems: a) Isometric view; b) Wireframe view

Using the model shown in Fig. 3.4.1.1, the generation of a mechanically stable assembly consists of imposing gravitational accelerations on the set of (initially) suspended DSEs. Being unrestrained from motion, the spheres react to the gravitational acceleration (i.e., respond to the action of body forces) and fall from the funnel downward into the rigid cylindrical container. As

the spheres collect within the cylindrical container, a network of contact forces arises, and some finite time thereafter, a mechanically stable state is reached. This state, whereby the body forces are equilibrated by the network of sphere-sphere and sphere-surface contact forces, constitutes a random packing of the DSE assembly under gravitational acceleration.

To facilitate generation of mechanically stable, randomly packed DSE assemblies for modeling configurations under various density states, the rheological input parameter values assigned to DSEs of the monodisperse systems are manipulated. Note that, for Sec. 3.4.1, the extent to which the topic of density is discussed is intentionally limited to that of void ratios (i.e., the ratio of the volume of voids to the volume of solids for a given collection of granules, or DSEs). Density (and more specifically, relative density) is revisited in Sec. 3.4.3.

As listed in Table 3.4.1.1, the normal and tangential damping coefficients, rolling and sliding friction coefficients, and tangential stiffness all contribute to changes in the simulation of granular materials. For example, to generate a DSE assembly (a 2.5 mm monodisperse system) exhibiting a void ratio of 0.88 (Table 3.4.1.1), relatively high magnitudes of friction coefficients, tangential contact stiffness, and viscous damping are supplied. In contrast, parameter values corresponding to ideally smooth spheres are utilized to (numerically) generate a DSE assembly with void ratio of 0.64 (using DSEs with 2.5 mm radii).

Table 3.4.1.1. Parameter values of random packing simulations and resulting void ratios

Spherical radius (m)	0.0025	0.0025	0.0025
Elastic material properties:			
Mass density (kg/m ³)	2650	2650	2650
Young's modulus (N/m ²)	1.724E+08	1.724E+08	1.724E+08
Poisson's ratio	0.17	0.17	0.17
Parameters of contact definition used:			
Normal damping	1.0	0.7	0.7
Tangential damping	1.0	0.4	0.001
Coefficient of sliding friction	1.0	0.48	0.001
Coefficient of rolling friction	0.1	0.048	0.0001
Normal stiffness factor	1.0	1.0	1.0
Tangential stiffness factor	0.9	0.9	0.9
Number of spheres in the cylinder	13346	13759	15347
Void ratio	0.88	0.82	0.64

Subsequent to the generation of random packings for uniform DSE assemblies, collectively exhibiting a range of void ratios, triaxial compression test simulations are conducted. More specifically, the packings are subjected to confining pressures of 140 kPa and then sheared to quantify corresponding stress-strain and volumetric behaviors at the macroscopic scale. As an important step in initializing each packed DSE assembly within the numerical triaxial compression test chamber, the originally supplied DSE input parameter values (Table 3.4.1.1) are replaced by making use of the parameter values listed in Table 3.4.1.2. Stated alternatively, one set of parameters is used for the packing simulations solely for the purpose of bringing about a target void ratio. Then, parameter values consistent with the methodologies reported in Ch. 2 are utilized for all subsequent simulations.

Table 3.4.1.2. Summary of input parameter values for triaxial compression tests simulations

Elastic material properties:	
Mass density (kg/m ³)	2650
Young's modulus (N/m ²)	1.724E+08
Poisson's ratio	0.17
Parameters of contact definition used:	
Normal damping	0.7
Tangential damping	0.4
Coefficient of sliding friction	1.0
Coefficient of rolling friction	0.1
Normal stiffness factor	1.0
Shear stiffness factor	0.9

In Fig. 3.4.1.2, conceptual plots of deviatoric stress and volumetric strain (versus axial strain) are displayed for loose and dense granular soils, when said (physical) soils are subjected to triaxial compression testing. As indicated for the dense specimen, a global maximum occurs in the peak value of deviatoric stress (σ_{peak}) at the same axial strain level in which the volumetric strain exhibits an inflection point. In contrast, for the loose specimen, no such correlation is observed. For relatively large values of axial strain, both the loose and dense specimens reach critical states, wherein the deviatoric stresses converge to the same asymptotic stress value. In addition, upon reaching the critical states, the volumetric strains develop uniquely valued asymptotes. Specific to the loose physical specimen (Fig. 3.4.1.2), volumetric contraction is generally the dominant behavior. For the dense (again, physical) specimen, volumetric contraction is observed at relatively small strain levels, but dilatatory behavior becomes more dominant for increasing axial strains.

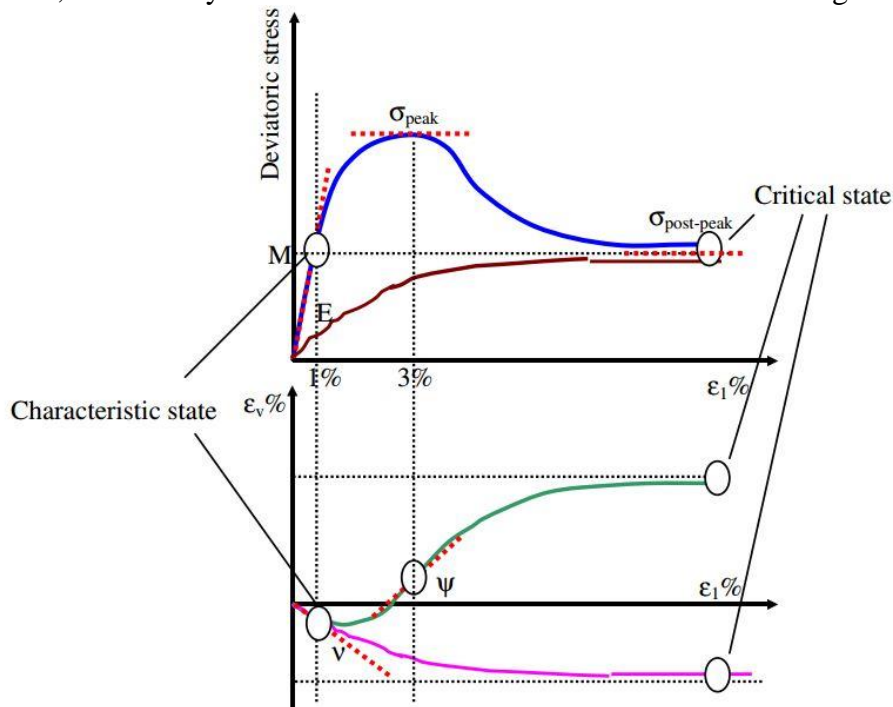


Figure 3.4.1.2. Illustration of deviatoric stress and volumetric strain per relative density states (Belheine et al. 2009)

Numerical results obtained from conducting triaxial compression test simulations on monodisperse systems (with model parameters of contact definition listed in Table 3.4.1.2) are plotted in Fig. 3.4.1.3 through 3.4.1.5. Results specific to the DSE assembly exhibiting the lowest (numerical) void ratio (i.e., the least dense assembly) are intended to more aptly represent (physical) coarse-grained soil in a loose state. Along these lines, the numerical results of a packing with an initial void ratio of 0.88 illustrate the macroscopic shear behavior of loose granular soils in Fig. 3.4.1.3, both with respect to the qualitative shapes of deviatoric stress (Fig. 3.4.1.3) and volumetric strain (Fig. 3.4.1.4).

Numerical results specific to a monodisperse system (with void ratio equal to 0.82) exhibit a mixture of the conceptual behaviors depicted in Fig. 3.4.1.3, with emphasis on initial conditions of a loose state. On the other hand, the volumetric behavior of a dense monodisperse system with void ratio equal to 0.64, which appears to be a limit density state that can be simulated by means of random packing under gravitational acceleration, is in good agreement with the conceptual plot of Fig. 3.4.1.3. However, a discrepancy is observed for the strain level at which the peak deviatoric stress occurs, with respect to the inflection point in the volumetric strain (conceptual Fig. 3.4.1.3 versus Fig. 3.4.1.4). Numerical treatment in kinematic control may be necessary to reduce the discrepancy using “shear jamming” and inclusion of secondary DSE in the packing. Nevertheless, the force-displacement relationship observed in the simulation is reasonable within an acceptable margin of error.

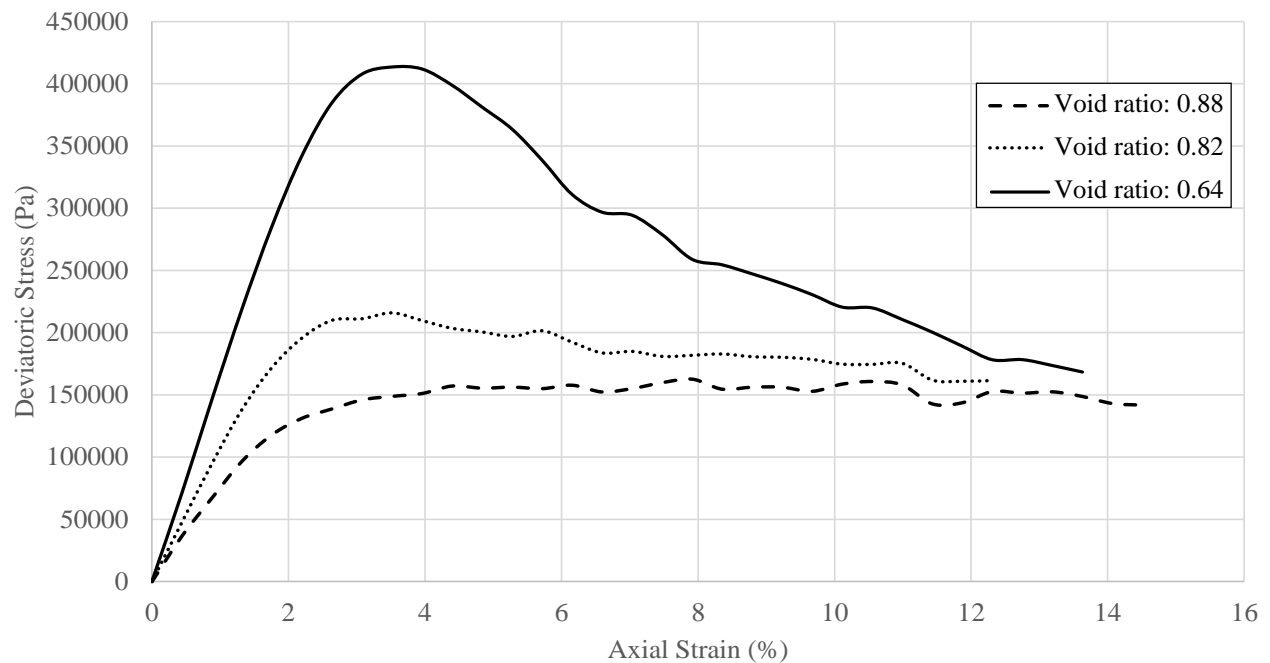


Figure 3.4.1.3. Deviatoric stress versus axial strain for triaxial compression test simulations on monodisperse systems

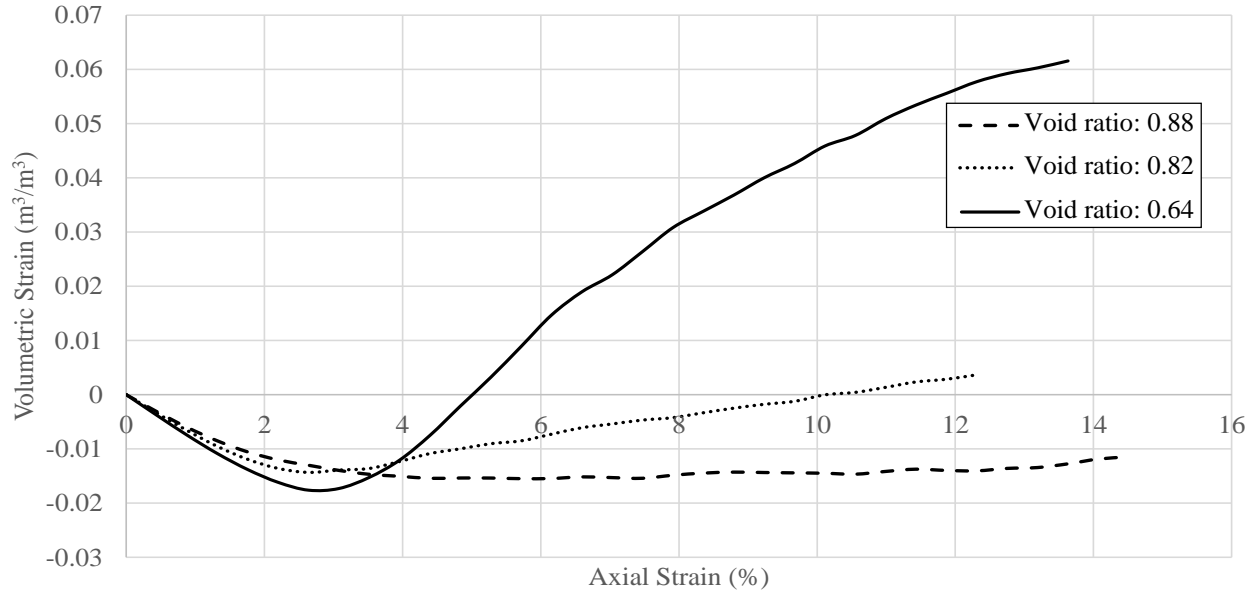


Figure 3.4.1.4. Volumetric stress versus axial strain for triaxial compression test simulations on monodisperse systems

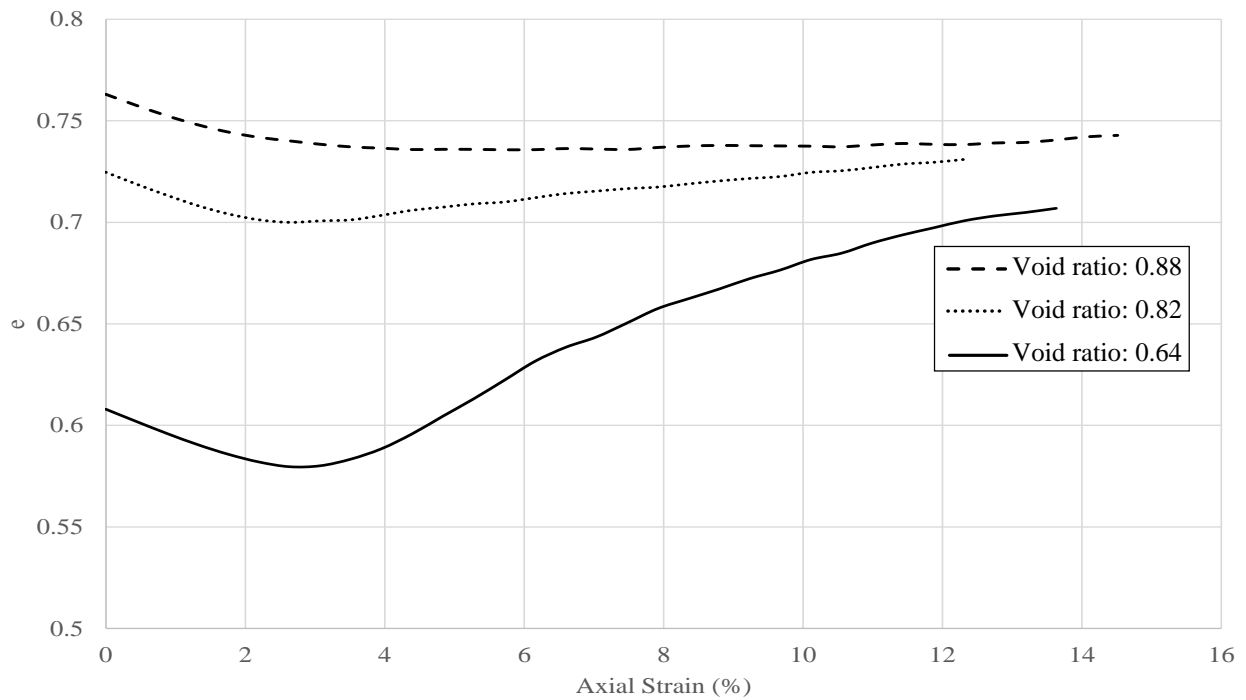


Figure 3.4.1.5. Void ratio versus axial strain for triaxial compression test simulations on monodisperse systems

3.4.2 Simulation of Shear Jamming Effects on Macroscopic Granular Behaviors using Binary Systems

To facilitate numerical simulation of DSE assemblies that are more capable of exhibiting dilative behaviors of (physical) granular media under relatively denser density states, binary (bi-disperse) systems are introduced. Recalling Section 2.1.8, where the modeling concept of “shear jamming” was introduced, this “binary system” constitutes a packing assembly composed of both primary and secondary DSEs. A numerical packing procedure for the binary system is shown in Fig. 3.4.2.1 and follows the same simulation stages as that discussed previously in Sec. 3.4.1 (i.e., random packing under gravitational acceleration).

Characterization of binary systems with various density states is reserved for Sec. 3.4.3, whereas, in Sec. 3.4.2, focus is placed on demonstrating the utility of binary systems in comparison to monodisperse systems. Accordingly, two random packings of DSE assemblies are shown in Fig. 3.4.2.2: a binary system (Fig. 3.4.2.2a); and, a monodisperse system (Fig. 3.4.2.2b), where the latter packing is achieved by removing the smaller sized spheres from the former. The ratio of sphere radii in Fig. 3.4.2.2a is assigned as 1.6, and is selected such that the binary spheres are classified as “similar-sized” (O’Toole and Hudson 2011). Alternatively stated, if the larger sized spheres (of radius 5 mm) were to be assembled in a simple cubic packing (recall Fig. 3.4.1.2a), then the smaller size spheres (of radius 3 mm) would not fit within the octahedral interstices between the larger spheres.

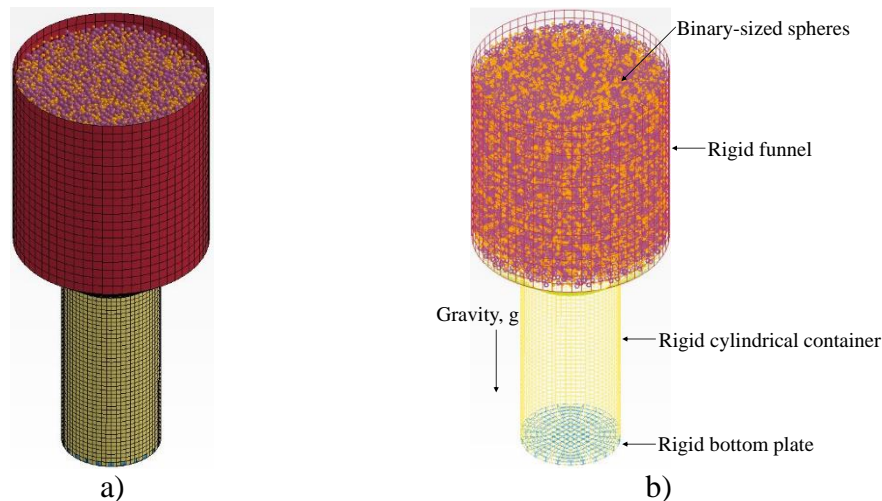


Figure 3.4.2.1. A DEM-FEM model for generating density states of binary-sized sphere systems: a) Isometric view; b) Wireframe view

The packed binary system (Fig. 3.4.2.2a) and corresponding monodisperse system (Fig. 3.4.2.2b), with input parameter values listed in Table 3.4.2.1, are utilized in triaxial compression test simulations. A confining pressure of 70 kPa is prescribed in each simulation, where this level of confinement is selected solely to maintain comparability between the numerical results. Comparative plots of deviatoric stress versus axial strain and volumetric strain versus axial strain are shown in Fig. 3.4.2.3. As expected, the binary system exhibits behavior that more closely resembles that of a physical, granular material under a relatively more dense state (recall Fig. 3.4.1.3). Also, the monodisperse system exhibits behaviors that align with those of (physical)

granular materials in a loose state. Such pronounced differences in behavior are observed even though the two as-configured DSE assemblies each occupy spaces of approximately equal volume. As a final observation for these demonstration simulations, the binary system response (with respect to macroscopic volumetric behavior) is consistent with that previously discussed for granular material under relatively more dense density states. Summarily, the two sets of triaxial compression test results indicate that loose and dense states of cohesionless granular materials can be simulated by making judicious use of monodisperse and binary systems.

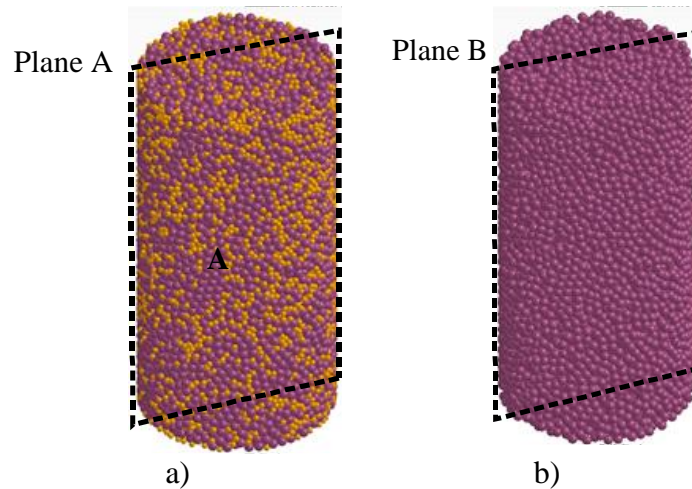
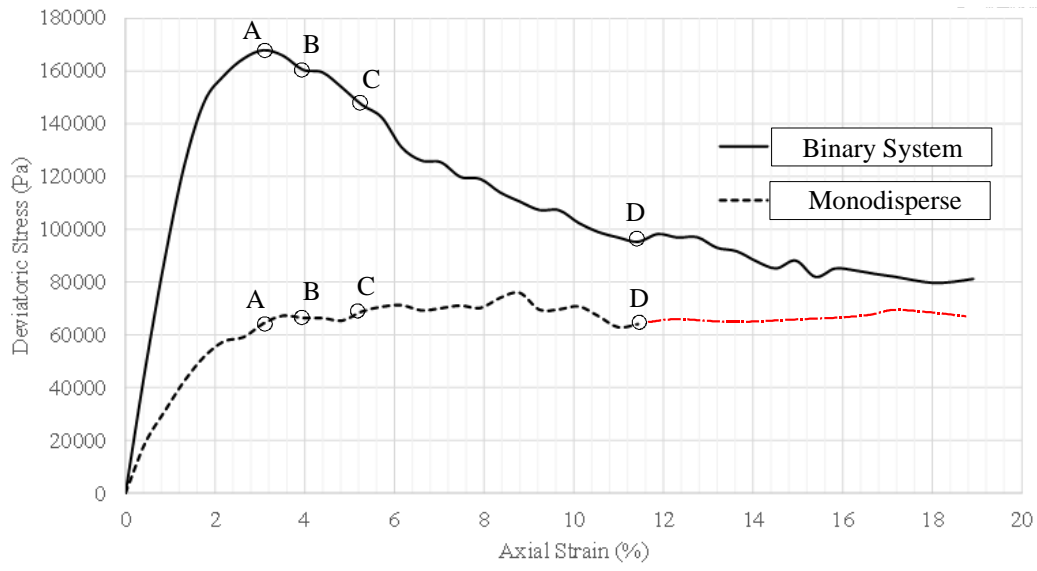


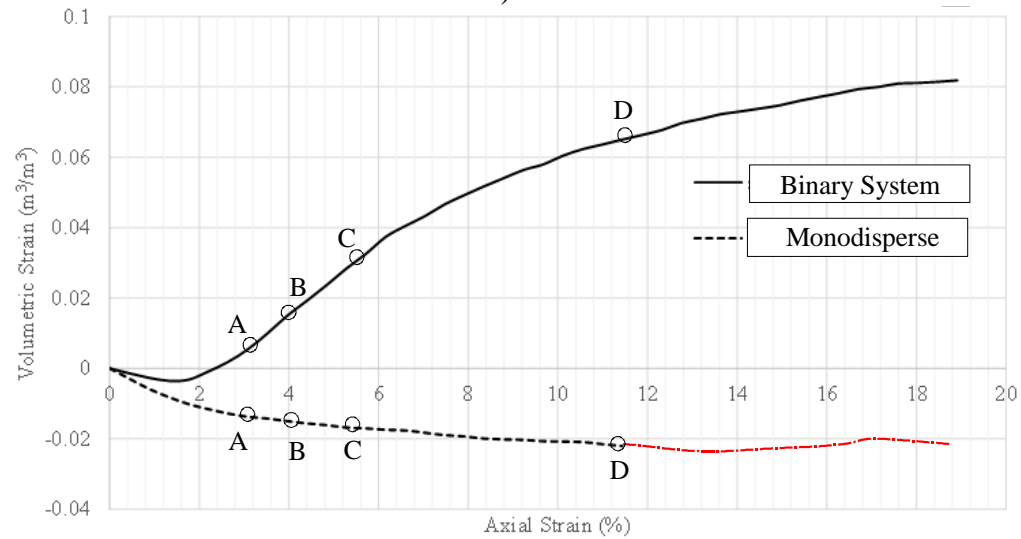
Figure 3.4.2.2. Random packings of DSE assemblies: a) Binary system (with a cut plane across the center of the section, Plane A); b) Monodisperse system created via removal of smaller spheres (with a cut plane across the center of the section, Plane B)

Table 3.4.2.1. Summary of input parameters used for comparing behaviors between monodisperse and binary systems

Diameters:	
Primary DSE (m)	0.005
Secondary DSE (m)	0.003
Elastic material properties:	
Mass density (kg/m ³)	2650
Young's modulus (N/m ²)	1.724E+08
Poisson's ratio	0.17
Parameters of contact definition used:	
Normal damping	0.7
Tangential damping	0.4
Coefficient of sliding friction	1.0
Coefficient of rolling friction	0.1
Normal stiffness factor	1.0
Shear stiffness factor	0.9
Configuration data:	
Ratio of primary to secondary (by volume)	4:1
A total number of DSE	26108
Primary DSE	12938
Secondary DSE	13170



a)



b)

Figure 3.4.2.3. Triaxial compression test simulations of monodisperse and binary systems: a) Deviatoric stress versus axial strain; b) Volumetric strain versus axial strain

Two distinct shear failure mechanisms are observed among the monodisperse and binary systems (with respect to Plane A and Plane B, Fig. 3.4.2.2). As shown in Fig. 3.4.2.3, during the early stages of the triaxial compression tests, both systems contract in compression while supporting the development of homogeneous deformation fields. As the tests progressed however, volumetric behaviors diverge between the two systems. The monodisperse system continues to undergo contraction while the binary system reaches an asymptotic contraction, and subsequently reverses from contraction to expansion. The binary system clearly dilates (i.e., the net volume change becomes positive) as the applied load exceeds an approximate yield limit. The post-peak strain softening behavior of the binary system is pronounced (Fig. 3.4.2.3a), as indicated by the development of in-plane displacements among the DSEs: sequential, pictorial depictions of evolving in-plane displacement fields are given at various deformed states (i.e., at various levels

of axial strain) in Fig. 3.4.2.4. The progressive formation of strain localization is quite obvious as axial strain increases. Corresponding shear bands of displaced DSEs are forming inward. In contrast, the evolution of deformation field in the monodisperse system is rather homogeneous throughout the shearing process. Overall, a minimal deformation is observed in the bottom region of the binary system: “spectators” appear in a conical region near the bottom of the cylindrical volume.

The effect of shear jamming is successfully simulated, as modeled, to be more predominant in the binary system (during shearing process). Further, for the binary system, networks of force chains strengthen as surrounding secondary particles become increasingly engaged in supporting the main (strong) force chains (Fig. 3.4.2.5a). This process continues as the applied load spreads across the principal axis of the cylinder with the steady growth of contact forces and (concurrent) weakening confinement. Jamming of the primary particles’ motions in the networks hinder the already-formed force chains from buckling during the ensuing dynamic rearrangements of secondary particles (Fig. 3.4.2.5a). A collective release of frictional engagements, accumulated via contact forces, induces outward buckling of the force chains. Consequently, elastic unloading propagates from the circumference toward the shear bands (i.e., cascading buckling occurs). Further, the force chains collapse is responsible for the nonaffine deformation mode (i.e., a sudden reduction in deviatoric stress, which constitutes the onset of post peak strain softening). In contrast, we notice fragmented (strong) force chains in the monodisperse system at early loading stages. The fragmented force chains sporadically form, with lack of interconnectivity. Even at an axial strain of 12% (which is near the constant volume state), no formation of coherent force-chain networks is observed (Fig. 3.4.2.5b, bottom row).

The effects of inter-granular contact play an important role in the elastic behavior of granular materials. Relative displacements between particles in contact can be processed using a kinematic averaging operator to define macroscopic strain fields. Static localization of contact forces is averaged over a control volume (this process can also be applied to macroscopic stresses). The corresponding elastic constants at the macroscopic scale are then estimated for each spherical particle of equal diameter. In this way, the constants can be given in terms of the ratio of the tangential to normal stiffness, an average coordination number, and/or the number of particles of control volume (Cambou et al. 2009). The elasticities of binary or polydisperse systems have not been well documented in existing literature (with respect to averaging operators), the study of which requires mathematical descriptions of the anisotropic contact structures. Contact stiffnesses among various sizes of particles in polydisperse (or binary) systems are randomly distributed, and the corresponding direction-dependent elasticity at the macro scale can vary. This variation necessitates a stochastic analysis to quantify the elasticity across various composition ratios (volume fractions). A rigorous probabilistic characterization of elasticity is beyond the scope of the current study. Instead, the elastic constants of the monodisperse and binary systems are qualitatively assessed in comparison to effective compression moduli calculated from an averaging theory of transition from micro mechanics to continuum mechanics (Walton 1987). There are a number of methods to approximate the elasticity of granular materials at the macroscopic scale. Although other theories may give a value of effective compression modulus more closely matched with the numerical result for the monodisperse system, the investigators elect to present analytical calculations based on Walton’s theory for simplicity and comprehensiveness, based on Hertzian Contact Theory (Walton 1987):

$$K_{eff} = \frac{1}{6} \left[\frac{3 \cdot \eta^2 \cdot n^2 \cdot p}{\pi^4 B^2} \right]^{\frac{1}{3}} \quad (3.4.2.1)$$

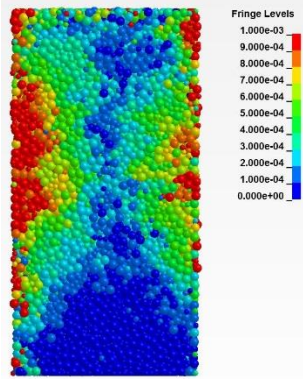
where K_{eff} is an effective compression (bulk) modulus; η represents a volume fraction of solid; n denotes an average coordination number (the average number of contacts per discrete sphere) at a stress equilibrium state, under hydrostatic pressure; p is an effective mean stress (Pa) responsible for an averaged volumetric strain; and, $B = \frac{1}{4} \left\{ \frac{1}{\lambda} + \frac{1}{\lambda + \xi} \right\}$ for which λ and ξ are

Lamè constants (Pa). For example, consider a monodisperse system with $n \approx 3.5$:

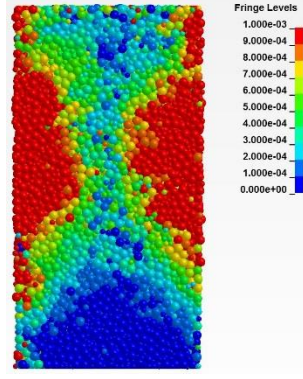
$$K_{eff} = \frac{1}{6} \left[\frac{3 \cdot \eta^2 \cdot n^2 \cdot p}{\pi^4 B^2} \right]^{\frac{1}{3}} = \frac{1}{6} \left[\frac{3 \cdot 0.545^2 \cdot 3.5^2 \cdot 92770}{\pi^4 (1.684E-9)^2} \right]^{\frac{1}{3}} = 2.6 \text{ MPa}$$

A comparative agreement between the values of effective compression modulus numerically simulated (3.0 MPa) and theoretically calculated (2.6 MPa) indicates a degree of validity among both numerical and theoretical predictions (see Fig. 3.4.2.6a). For the case of the binary system, a doctoral student is currently formulating a mathematical derivation for analytically quantifying the compression modulus; despite an exhaustive literature search, the investigators have not been able to find an existing theoretical solution as of yet. In a preliminary analysis based on Walton's theory of monodisperse systems, a compression modulus of 7.8 MPa is approximated as a lower bound of $n = 4.4$ and $B = 4.138E-10$ in favor of the numerically-simulated value of 10.0 MPa. Also, as shown in Fig. 3.4.2.6b, stress paths of both the monodisperse and binary systems are almost identical during contraction. As the monodisperse system approaches an ultimate state, the binary system further mobilizes dilative shear resistance. However, the stress paths of the both systems converge to a point in the p-q space as they approach constant volume states. Thus, the system models simulate a type of granular material, which exists at various density states as initial conditions yet self-organize to reach consistent critical states of constant volume.

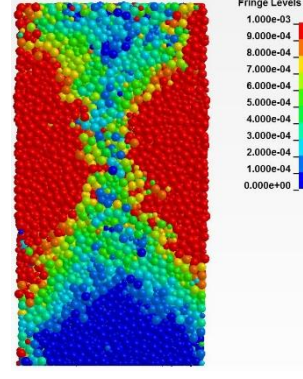
Point A of Fig. 3.4.2.3a
axial strain = 3.2%



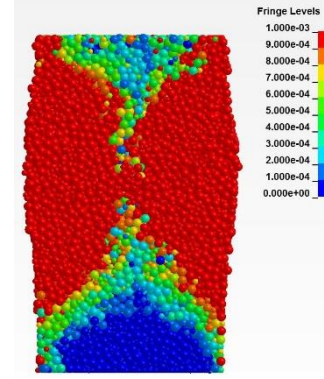
Point B of Fig. 3.4.2.3a
axial strain = 4%



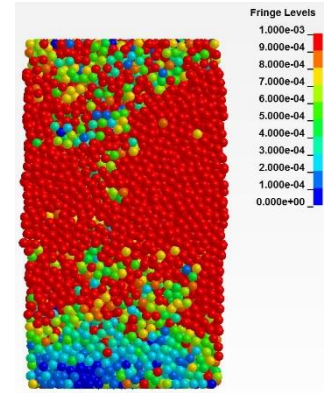
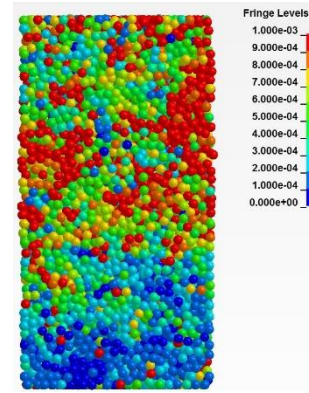
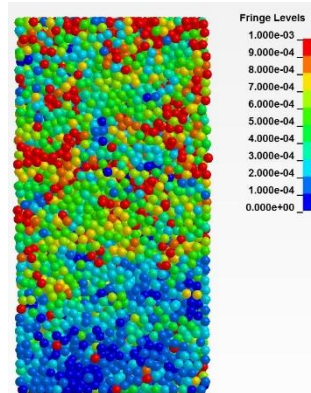
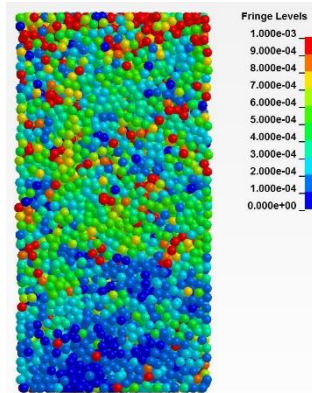
Point C of Fig. 3.4.2.3a
axial strain = 5.6%



Point D of Fig. 3.4.2.3a
axial strain = 11.5%



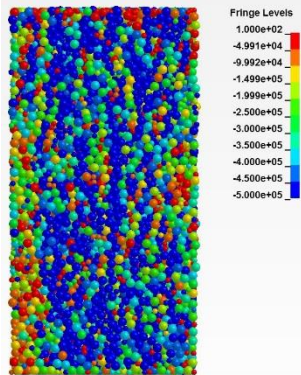
a)



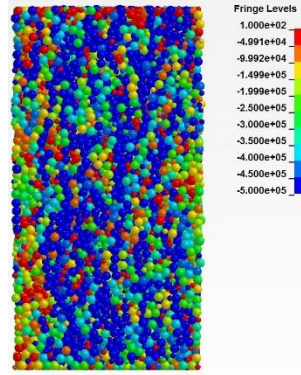
b)

Figure 3.4.2.4. Evolution of particle rearrangement and in-plane displacement using the cut planes from Fig. 3.4.2.2: a) Sequence of shear deformation patterns in the binary system; b) Formation of homogeneous deformation fields in the monodisperse system

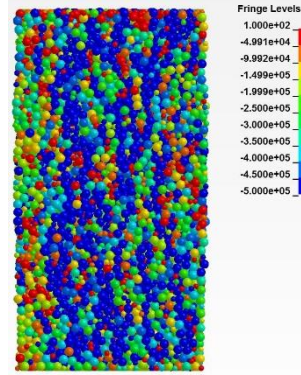
Point A of Fig. 3.4.2.3a
axial strain = 3.2%



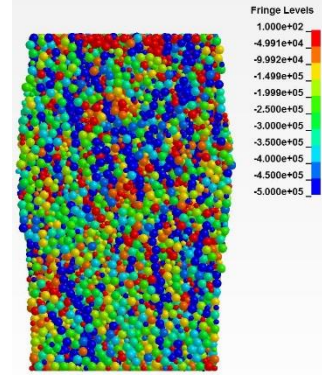
Point B of Fig. 3.4.2.3a
axial strain = 4%



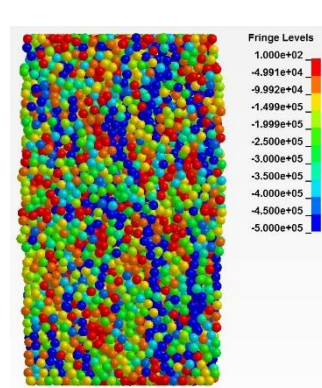
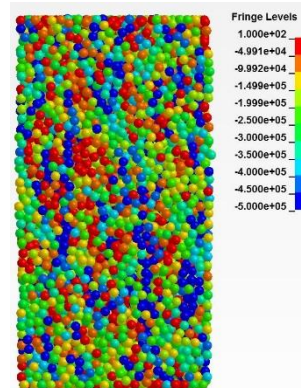
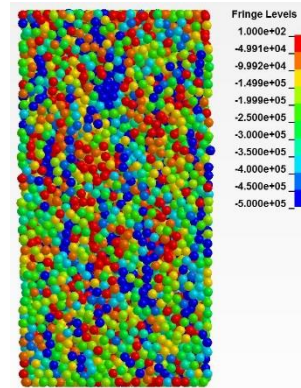
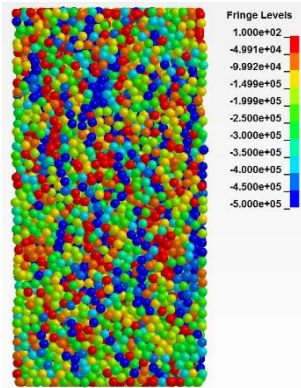
Point C of Fig. 3.4.2.3a
axial strain = 5.6%



Point D of Fig. 3.4.2.3a
axial strain = 11.5%



a)



b)

Figure 3.4.2.5. Development of force chains in the cut planes of Fig. 3.4.2.2: networks in color of blue are strong contact forces; green and red particles are spectators: a) Vertical force chains in the binary system; b) Weaker force chains in the monodisperse system

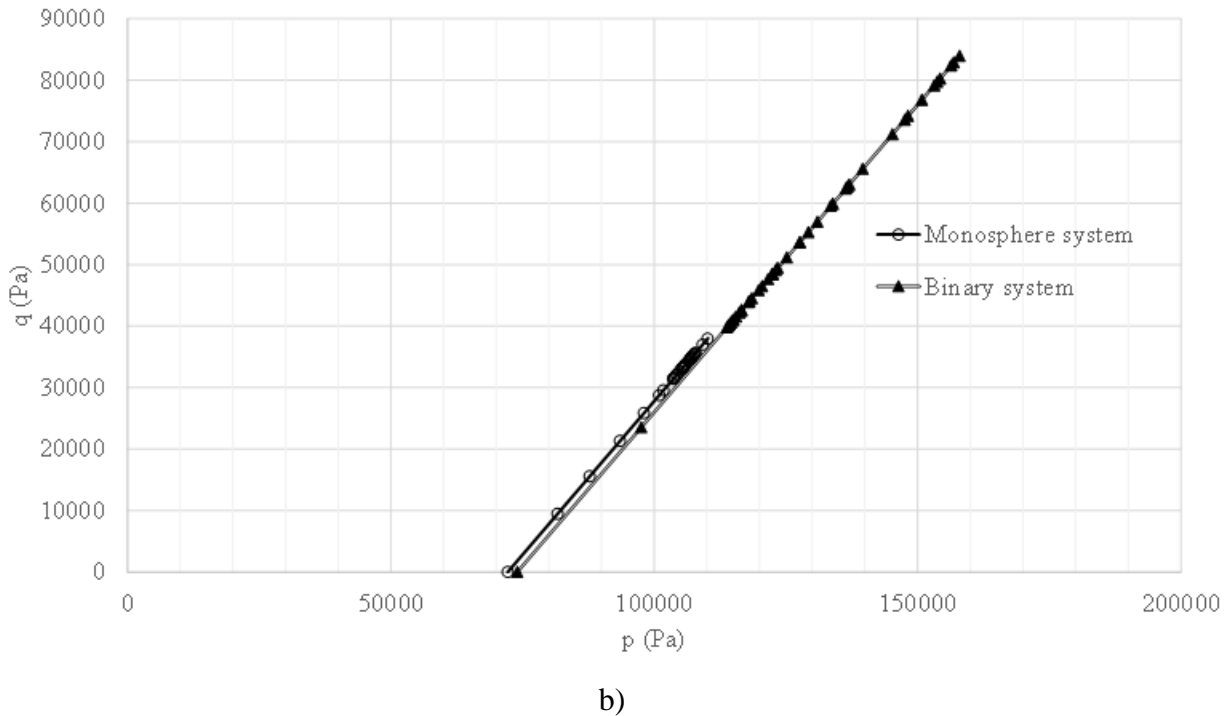
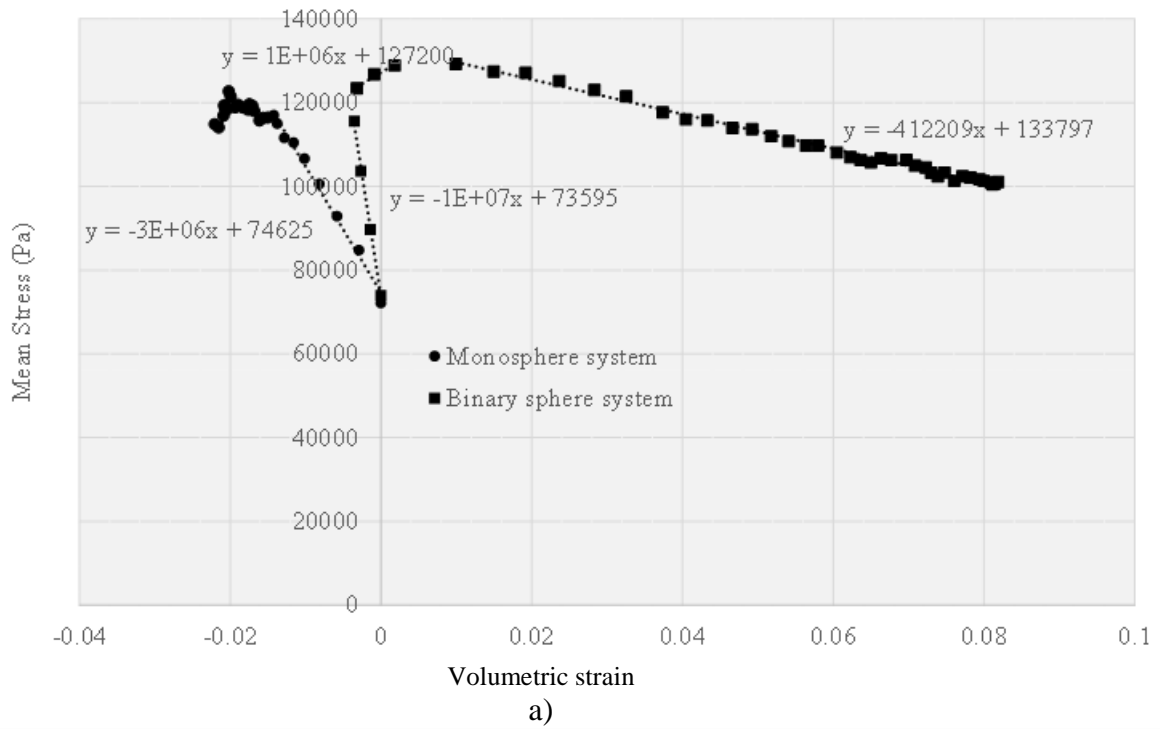


Figure 3.4.2.6. Comparison of elasticity and stress paths for the monodisperse and binary systems: a) Compression (and extension) moduli; b) Stress paths

Summarily, when macroscopic unjamming nucleates from the buckling of a few to several force chains of primary particles, bands begin to form (shear bands). The formation of shear bands, in turn, triggers the spectators and surrounding weak network particles to become mobile. The

mobilized particles (and concurrent weakening confinement at the local-level) destabilize more adjacent force chains, and induce cascading structural failures (simultaneous buckling). The process continues, and spreads along the band until the two outer regions on either side of the cylinder are unloaded elastically (e.g., post peak strain-softening, Fig. 3.4.2.3a). Shear jamming in numerical simulation occurs at two length scales: the friction at the DSE scale and irreversible structural changes in the mesoscopic “jammed” textures, formed by the network of force chains.

Therefore, as discussed in Ch. 2, the coupling (and superposition) of frictional resistances at multiple scales is demonstrated in the numerical experimentation, where such coupling enables the modeling of increased shear strength at the macroscopic scale. On the other hand, the dichotomy between brittle fracture (with a clear formation of failure slip plane) and conventional forms of elastoplasticity may not adequately capture the mesoscopic shear behavior of jammed granular particles. At least for the two cases representing (physical) relative density states, particles are not perfectly rigid (e.g., fragility emerges as the limiting behavior for rigid particles), and no physicochemical bonding exists between particles (e.g., cemented sand, rock). Overall, the prediction of system behaviors is consistent with previous studies: more complex descriptors of particle shapes were used to model random interparticle anisotropic contact angles (Ishikawa and Oda 1998, Cheng et al. 2003, Hosseininia and Mirghasemi 2006, Lee et al. 2012). However, such increases in complexity (for higher degrees of dimensional constraints) have limited previous work to relatively smaller sizes of system models, given practical time limits and finite computational resources.

3.4.3 Representative DSE Models for Relative Density States

In forming the ‘soil unit’ library (presented in Sec. 3.4.4), both monodisperse and binary systems are developed for mechanically stable granular assemblies under gravity. In turn, macroscopic shear behaviors of the DSE systems may be consistent with those observed in laboratory testing on granular soils. To enable standard, quantitative characterizations of density states associated with the DSE systems, the bounds of numerical void ratios are established in reference to the void ratios of monodisperse systems. As given in Lambe and Whitman (1966), for uniform spheres in a mechanically stable configuration, the maximum indexed value of void ratio (e_{max}) is 0.92. This idealized packing of uniform spheres corresponds to the simple cubic packing shown in Fig. 3.4.3.1a. The lower bound value of void ratio (e_{min}) is given as 0.35, which corresponds to an idealized hexagonal close packing (Fig. 3.4.3.1b).



Figure 3.4.3.1. Ordered packings of monodisperse systems: a) Simple cubic assembly; b) Hexagonal assembly

Based on the bounding e_{min} and e_{max} , relative mass-density states of binary systems are computed. It is noted that a theoretical limit of the maximum void ratio for binary systems (e_{max})

is not known. Therefore, in the current study, for binary systems composed of primary and secondary DSEs (distributed according to a given volume fraction), the upper bound void ratio (e_{max}) is equated to that of a monodisperse system. The corresponding lower bound value of numerical void ratio (e_{min}) for binary systems was parametrically determined in Kummerfeld et al. (2008). Accordingly, e_{min} is taken as 0.35. Based on these two extremes of void ratio values, numerical relative densities of binary systems are used to provide a qualitative sense of the degree of packing density for a given assembly (and corresponding coordination numbers). Therefore, the numerical relative density (D_{rel}) is defined as:

$$D_{rel} = \frac{e_{max} - e}{e_{max} - e_{min}} \times 100\% \quad (3.4.3.1)$$

where e is the ratio of void volume to total volume of DSEs, as defined for a REV (taken as the volume of a 100 mm by 200 mm cylinder in the current study).

Presented in Table 3.4.3.1 are correlations that relate relative density, density state, and angle of internal friction. The naming conventions for the density states, and the paired values of angle of internal friction, are intentionally defined to maintain distinctions between: 1) Previously established density state descriptors for (physical) granular soil (e.g., Meyerhof 1976); and, 2) Numerical modeling of granular materials using DSE assemblies in the current study. Nonetheless, the content in Table 3.4.3.1 aids in characterizing macroscopic behavior of random packings of DSE assemblies. Stated alternatively, the density state categories and angles of internal friction constitute benchmarks for calibrating macroscopic quantities that, in turn, are obtained from simulations involving random packings of DSE assemblies.

Descriptive categories representing the range of density states defined in the current study vary from loose to dense (Table 3.4.3.1), and correlate positively with numerical (i.e., not physically measured) values of relative density. Recall that in Sec. 3.4.1 limitations of achieving very dense states of granular matrices exist (to an extent) when conducting numerical simulations using monodisperse systems. Among the categories defined in Table 3.4.3.1, the loose and medium density states are exclusive to categorization of monodisperse systems. Further, the medium-dense and dense density states are exclusive to categorizing binary systems, and where shearing jamming schemes are employed. Two different packing methods are extensively studied in transition states from loose to dense. With respect to creating medium density states, a broader range of numerical relative-density is needed to (approximately) model upper limits for random packings of DSE that satisfy post-simulation assessments of kinematic behavior (recall Fig. 3.4.1.3). Namely, the “medium-mono” descriptive category is specific to monodisperse systems while the “medium-binary” category is specific to binary systems (where, again, various degrees of shear jamming schemes are employed in conjunction with calibrated contact definitions).

Numerical generation of DSE assemblies necessitates usage of not only the numerical internal structure (recall the random packing procedures discussed in Sec. 3.4.1 and 3.4.2), but also the calibration of DSE rheological parameters. It is important to note that input parameters used in packing simulations (i.e., simulations of static equilibrium states of DEM packing under gravity prior to application of external forces) do not hold physical meaning, and further the parameters are not unique in transitioning from one descriptive category to the next. For example,

for monodisperse systems considered in the present study, an upper limit of numerical relative density is found to be approximately 17.5%. For monodisperse systems that are packed at greater relative density states, the predicted macroscopic volumetric behaviors would not satisfy benchmarks of kinematic behavior (recall Sec. 3.4.1). Thus, discrete representation of granules and collective internal structures at this point is solely a physics-based numerical model that consistently predicts macroscopic force-displacement phenomena. The DSE assemblies should be neither presented nor implied as physical geometries of any real fractal networks of granular soils, (e.g., pore/particle size distributions).

Table 3.4.3.1. Numerical characteristics of DSE assemblies across descriptive density categories and angles of internal friction

Numerical relative density (%)	Descriptive category	Angle of internal friction (°)
7.0	Loose	19 - 24
17.5	Loose-medium	24 - 28
17.5	Medium (monodisperse)	28 - 33
56.0	Medium (binary)	28 - 33
56.0	Medium-dense	33 - 37
56.0	Dense	~38

For each density state listed in Table 3.4.3.1, an iterative procedure is carried out to calibrate the rheological parameters supplied for modeling individual spheres within a corresponding DSE assembly. For a given random packing of a DSE assembly that falls within one of the listed density states, the iterations are initiated by supplying input values for the DSE rheological parameters (with adherence to the methodologies detailed in Ch. 2). Then, the DSE assembly is subjected to (simulated) triaxial compression testing. Numerical results from the simulation are then used to calculate the angle of internal friction for the DSE assembly. If the macroscopic behavior of the DSE assembly is not consistent with the pairings listed in Table 3.4.3.1, then the next iteration is carried out: individual DSE rheological parameter values are adjusted (per the Ch. 2 methodologies); a subsequent triaxial compression simulation is conducted; the simulation results are used to calculate a macroscopic angle of internal friction; and, Table 3.4.3.1 is consulted to ascertain whether or not the paired density and shearing behaviors are observed. These iterations are repeated as needed until a given DSE assembly satisfies all descriptors and quantities within a given (targeted) row of Table 3.4.3.1.

Plots of deviatoric stress versus axial strain and volumetric strain versus axial strain, as obtained from the final-iteration triaxial compression test simulations at confinement of 140 kPa, are shown in Fig. 3.4.3.2 and Fig. 3.4.3.3 (respectively) for each of the numerical density states defined in the current study. Recalling the conceptual plot of loose versus dense (physical) macroscopic behaviors (recall Fig. 3.4.1.3), the respective results of (numerical) macroscopic behaviors exhibited by the DSE assemblies representing loose and dense density states show good qualitative agreement. Further, for (numerical) density states that fall between loose and dense, gradual transitions (from loose to dense behaviors) are observed.

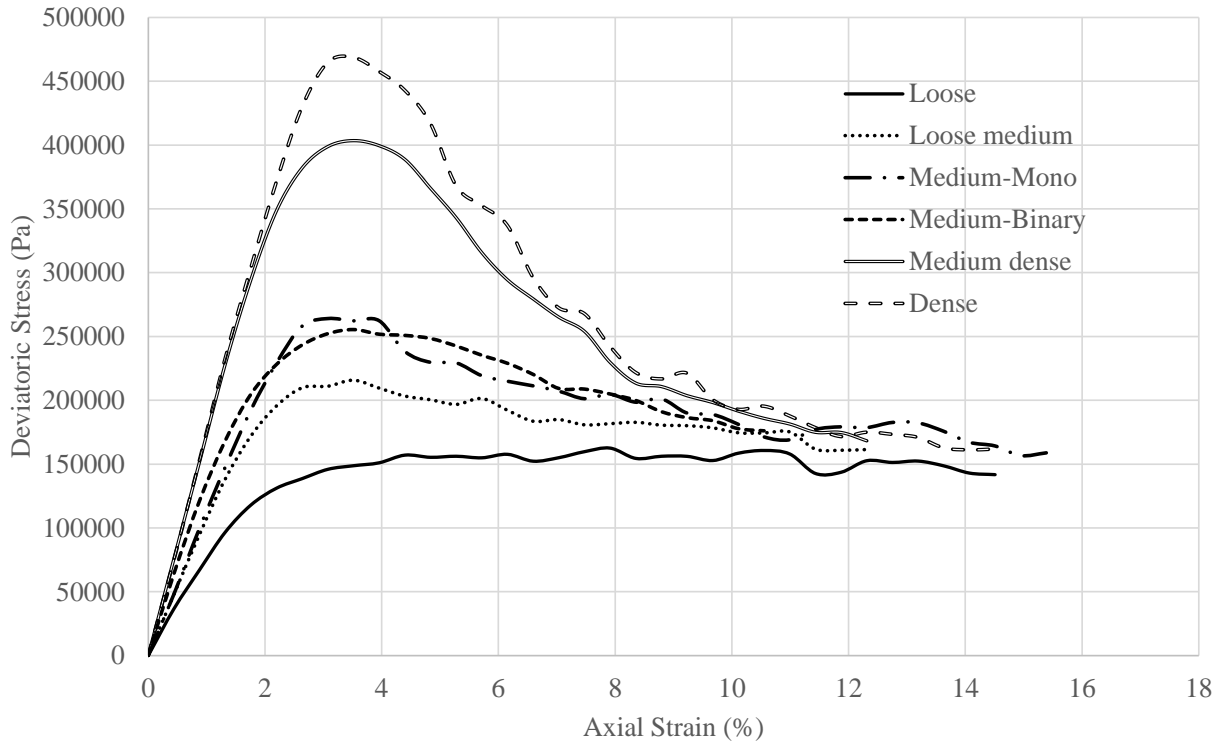


Figure 3.4.3.2. Deviatoric stress versus axial strain for DSE assemblies under initial numerical density states

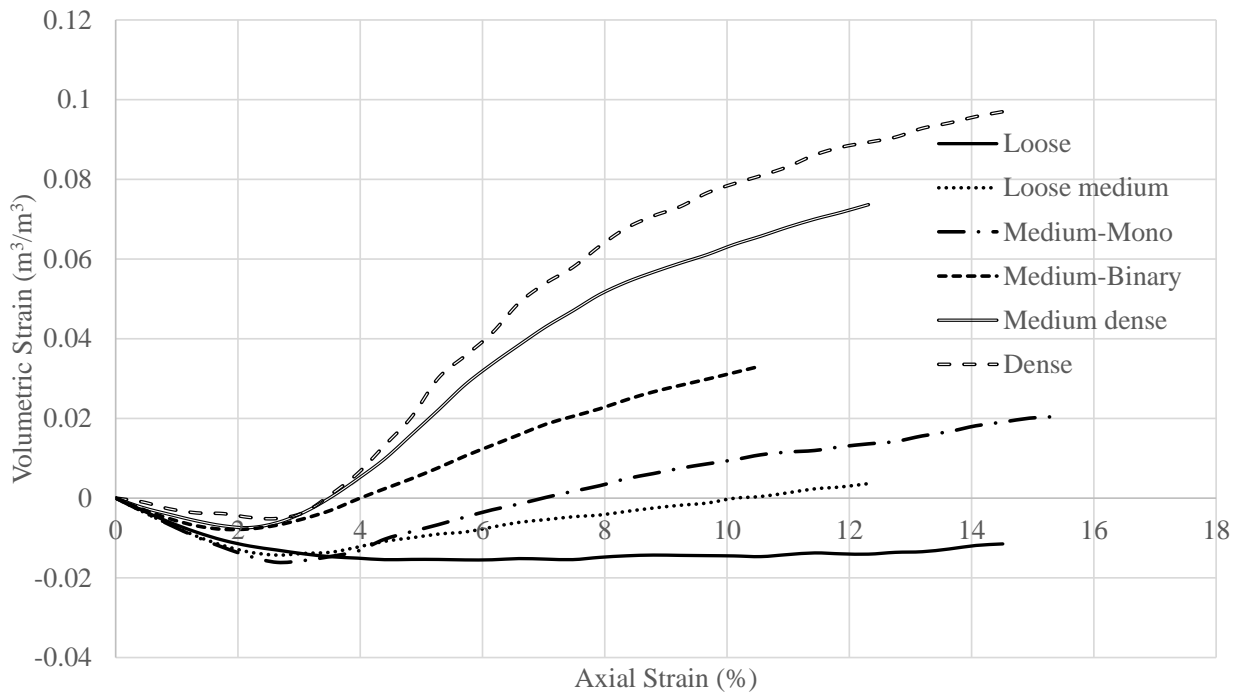


Figure 3.4.3.3. Volumetric strain versus axial strain for DSE assemblies under initial numerical density states

3.4.4 Summary of Numerical Results

Contact parameters of primary-to-primary, primary-to-secondary, and secondary-to-secondary DSE contacts are defined to bring about desired (numerical) relative density states, as listed in Table 3.4.4.1. As part of this process, rheological parameters are calibrated to generate each of a set of corresponding DSE packings within a 100 mm by 200 mm cylinder (recall Table 3.4.3.1). Subsequently, the cylinders are subjected to tri-axial compression at two various confinements of 70 kPa and 140 kPa. The resulting angles of internal friction are estimated per secant slope of Mohr-Coulomb failure envelopes. To calculate maximum angles of internal friction, the K_f lines are constructed, and subsequently, the peak angles of internal friction are calculated:

$$\sin(\phi_{peak}) = \text{slope of } K_f \text{ line} \rightarrow \phi_{peak} = \arcsin(\text{slope of } K_f \text{ line}) \quad (3.4.4.1)$$

Further, to increase the versatility of the soil unit library, macroscopic shear strengths associated with a coarse-grained soil in a medium density state are accounted for using both monodisperse and binary systems.

Table 3.4.4.1 Library for discrete element analysis models with simulated macroscopic behaviors

Density state being modeled:	Loose	Loose-medium	Medium-mono	Medium-binary	Medium-dense	Dense
Particle size distribution:	Mono-spheres	Mono-spheres	Mono-spheres	Binary-spheres	Binary-spheres	Binary-spheres
Spherical radius 1 (m)	0.0025	0.0025	0.0025	0.0025	0.0025	0.0025
Spherical radius 2 (m)	-	-	-	0.0015	0.0015	0.0015
Number of spheres created:	1.335E+04	1.376E+04	1.376E+04	2.611E+04	2.611E+04	2.611E+04
Large spheres (n_1)	-	-	-	1.294E+04	1.294E+04	1.294E+04
Small spheres (n_2)	-	-	-	1.317E+04	1.317E+04	1.317E+04
Void ratio	0.88	0.82	0.82	0.60	0.60	0.60
Numerical mass density (kg/m ³)	1.406E+03	1.456E+03	1.456E+03	1.651E+03	1.651E+03	1.651E+03
Numerical relative density (%)	7.0	17.5	17.5	56.0	56.0	56.0
Elastic material properties:						
Mass density (kg/m ³)	2.650E+03	2.650E+03	2.650E+03	2.650E+03	2.650E+03	2.650E+03
Young's modulus 1 (N/m ²)	1.724E+08	1.724E+08	1.724E+08	1.724E+08	1.724E+08	1.724E+08
Young's modulus 2 (N/m ²)	-	-	-	7.00E+08	7.00E+08	7.00E+08
Poisson's ratio 1	0.17	0.17	0.17	0.17	0.17	0.17
Poisson's ratio 2	-	-	-	0.17	0.17	0.17
Rheological model parameters:						
Normal damping	0.7	0.7	0.7	0.7	0.7	0.7
Tangential damping	0.4	0.4	0.4	0.53	0.4	0.4
Coefficient of sliding friction	1.0	1.0	1.0	0.5	1.0(1) & 1.0(2)	1.0(1) & 1.0(2)
Coefficient of rolling friction	0.1	0.1	0.2	0.05	0.2(1) & 0.1(2)	0.2(1) & 0.1(2)
Coefficient of shear jamming	0.0	0.0	1.0	0.0	1.0(1) & 0.0(2)	4.0(1) & 0.0(2)
Normal stiffness factor	1.0	1.0	1.0	1.0	1.0	1.0
Shear stiffness factor	0.9	0.9	0.9	0.5	0.9	0.9
Shear behavior under triaxial compression testing:						
At 70 kPa confinement						
Peak shear strength (N/m ²)	-	9.53E+04	1.18E+05	1.14E+05	1.70E+05	1.98E+05
Ultimate shear strength (N/m ²)	7.66E+04	7.63E+04	7.60E+04	7.61E+04	8.42E+04	8.50E+04
At 140 kPa confinement						
Peak shear strength (N/m ²)	-	2.14E+05	2.62E+05	2.55E+05	3.57E+05	4.65E+05
Ultimate shear strength (N/m ²)	1.56E+05	1.56E+05	1.56E+05	1.58E+05	1.61E+05	1.62E+05
Angle of internal friction						
Peak angle (°)	-	27.1	30.7	29.0	38.2	40.6
Secant angle (°)	21.8	24.0	28.0	28.0	35.0	38.0
Constant volume angle (°)	21.0	21.0	21.0	21.0	21.0	21.0

The diameter ratio between primary and secondary DSEs associated with Table 3.4.4.1 is 1.6, where approximately equal numbers of primary and secondary DSEs are used for each assembly of binary spheres. The volume fractions of primary and secondary DSEs are 80% and 20%, respectively. This mixture composition is selected based on Shi and Zhang (2006) to maximize both the packing density and coordination number (Table 3.4.4.2) in consideration of computational cost. The computed void ratio and relative density of the binary system are 60% and 56%, respectively. The shear jamming effects are simulated using jamming coefficients of 1.0 and 4.0 for the medium-dense and dense cases, respectively (in addition to the constant coefficients of sliding friction).

Table 3.4.4.2. Simulation of random packing of spherical particles with two different size distributions (top: packing density, bottom: coordination number) (Shi and Zhang 2006)

	$n_2/n_1=2:8$	4:6	5:5	6:4	8:2
$d_2/d_1=1.1$	0.578	0.579	0.578	0.579	0.578
1.5	0.585	0.584	0.586	0.582	0.577
2.0	0.600	0.595	0.594	0.587	0.581
3.0	0.625	0.597	0.596	0.585	0.578
	$n_2/n_1=2:8$	4:6	5:5	6:4	8:2
$d_2/d_1=1.1$	5.947	5.934	5.940	5.948	5.940
1.5	5.925	5.890	5.911	5.923	5.903
2.0	5.904	5.846	5.824	5.872	5.830
3.0	5.781	5.626	5.611	5.683	5.579

In dilative soils (e.g., dense sands or overly-consolidated clays), the angle of peak shear resistance ϕ_{peak} is known to be related to the critical state angle of shearing resistance at constant volume ϕ_{cv} and the peak angle of dilation ψ (Bolton 1986):

$$\phi_{peak} = \phi_{cv} + 0.8\psi \quad (3.4.4.2)$$

This relation highlights the scale-dependency of friction, particularly at the macroscopic scale where the characteristics of dense packing, i.e., shear jamming, attributes to the dilative behavior. Given the role of the peak angle of dilation on peak strength, a semi-empirical correlation is drawn upon for the cases presented in Table 3.4.4.1:

$$\phi_{peak} = \phi_{cv} + 0.789\psi \quad (3.4.4.3)$$

which is based on a linear regression as shown in Figure 3.4.4.1.

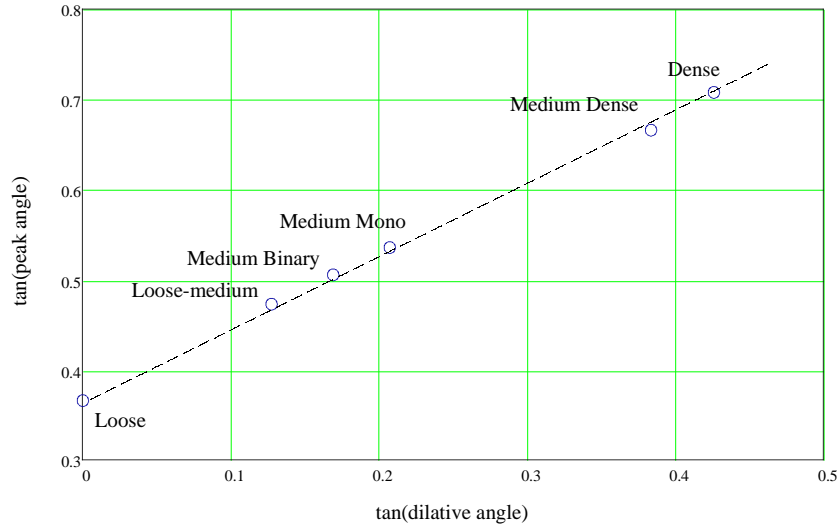


Figure 3.4.4.1 Linear regression of flow rule

It should be noted that the flow rule of Eqn. 3.4.4.3 is applied to expression of the relationship between the peak friction angle and the maximum dilation rate for numerical tests on the same granular material per simulations for six various states of relative density. This numerically-simulated correlation is in good agreement with Bolton's observation, i.e., Eqn. 3.4.4.2. More specifically, from a macroscopic prospective, the intermediate principal stress can significantly change dilative shear resistance; for example, plane strain conditions leads to higher angles of shear resistance than axis-symmetric conditions (two-four degrees in medium sands and four to six degrees in dense sands). The empirical correlation of Bolton's flow rule (and similar to Rowe's observation in idealized dense packings in 1962) is based on experimental tests conducted under plane strain conditions. That being considered, the modelling of shear jamming effects constrains the ability of particle assembly to rearrange, and effectively simulates localized constraints. Thus, Eqn. 3.4.4.3 is in a close match with Bolton's correlation (Eqn. 3.4.4.2), yet indicates development of less intermediate principal stress in a three-dimensional stress state than in a plane strain condition at the macroscopic scale.

It is clear from the above discussion and other literature (e.g., Houlsby's interpretation of the relationship between the angle of dilation and the distance to the critical state line; Houlsby 1991) that peak shear resistance is related with dilation. Although the flow rule per simulation results may not possibly covers all types of granular soils, the broad conclusion per completion of this task is same as others both experimental and theoretical by various researchers. Therefore, qualitative modelling schemes have been established for the variation of dilation rate with density.

CHAPTER 4 SUMMARY AND CONCLUSIONS

4.1 Summary of Task 2 Work Completed

The overall objective of this research project is to use computational methods and laboratory-scale testing to characterize the effect of driven sheet pile walls (SPWs) on the resistance of subsequently driven (nearby) piles in a granular medium. The focus of the current report is on Task 2 of the overall study. Further, the Task 2 deliverable report is concerned with four objectives: 1) Development of a numerical model for the purpose of simulating direct shear tests on granular soil; 2) Development of a numerical model for the purpose of simulating triaxial compression tests on granular soil; 3) Creation of a standardized discrete spherical element (DSE) library that relates individual sphere properties to (when assembled in random packings) macroscopic properties of DSE assemblies; and, 4) Evaluation of Mohr-Coulomb envelopes based on numerical simulations of DSE assemblies, as representations of granular soils.

Specific to the first objective listed above, a standard test method was identified and used as a datum in developing the (numerical) direct shear test apparatus. Additionally, the testing standard was used in defining the stages of the direct shear test simulation. The numerical model and simulation stages were then used in a set of benchmark simulations. Comparisons of the numerical results to previously measured physical properties of corresponding specimens were made and found to be favorable.

In accomplishing the second objective listed above, the numerical modeling was preceded by the identification of a standard test method for carrying out triaxial compression tests. Key components from among the full complement of triaxial test equipment listed in the standard were identified. Subsequently, the selected apparatus components were modeled with adherence to the descriptions given in the standard. Likewise, the step by step procedure listed in the testing standard was used in forming the triaxial compression test simulation stages. Having formed the triaxial compression test model and simulation stages, benchmark simulations were carried out to demonstrate that the numerical model is capable of generating numerical results that show agreement with physical test measurements.

As a precursor to forming the library of parameter values for random packings of DSE assemblies, a comprehensive investigation was made, both conceptually and quantitatively, into the rheological components making up individual DSEs, the motions of DSEs, and interactions among DSEs. This comprehensive exploration of the underlying physics that drive simulations involving DSE assemblies was carried out to inform the selection of parameter values in the DSE library. In this way, novel correlations have been discovered, and were included in the current report, across the various DSE rheological components. Further, the collection of correlations have permitted the quantification of practical bounds (minimum and maximum values) for modeling DSE using multi-physics simulation software.

In building upon insights gained from the investigation into the fundamental behaviors of DSEs, and by making use of the numerical models for simulating laboratory tests, the DSE library was formed by: 1) Developing methodologies for simulating density states in monodisperse and

binary assemblies; 2) Making comparisons of macroscopic properties exhibited by monodisperse and binary systems to macroscopic properties associated with size-distributed assemblies; 3) Establishing representative DSE assemblies to represent, for a given assembly, a given density state; and, 4) Calibration of the rheological parameter values for individual DSE such that corresponding DSE assemblies exhibit one of a range of macroscopic property values.

4.2 Conclusions

Using the combined DEM-FEM modeling approach, it has been demonstrated that the numerical models and procedures established in the current study are capable of simulating direct shear tests and triaxial compression tests such that agreement is observed between physical test measurements and numerical results. Considerations that were made in developing the models ensure that the DSE assemblies are prepared in ways that are consistent with specimen preparation provisions listed among selected testing standards. In addition, specific considerations were made to ensure fidelity between testing standards and those numerical model components corresponding to the laboratory test equipment. For both the direct shear test and triaxial compression test models, concerted efforts were made to ensure that the (numerical) apparatus components do not unduly influence the DSE assemblies at any time during the simulation staging. Also, the numerical models were shown to produce simulation results that are in line with physical test measurements made in laboratory settings. These numerical tools are integral to the formation of a library DSE, which in turn, can be used (in conjunction with in-development upscaling methods) in forming megascopic DSE assemblies.

Force chain evolution is key to shear band formation and failure of granular materials. Force chains are quasi-linear, particle chains through which above average contact forces are transmitted within a deforming granular medium. These chains may be only a few DSE in length, or they may extend for tens of primary DSE diameters. Physical experiments collected from the literature have shown that force chains form to resist deformation, and that these “columnar structures” of particles preferentially align in the direction of maximum compressive stress in the system (the direction where the soil “feels” the greatest compression). Force chains exist amidst a network of secondary particles (i.e. particles bearing low load) as well. Under continued compression, the force chain columns ultimately buckle under lateral confinement from their weak neighbors. Depending on the degree of shear jamming (i.e., a DEM modeling strategy to simulate higher density states of particles that interlock and restrain each other in motions under lateral confinement), a coordinated release of the stored potential energy (locked-in frictions at grain-level) manifest on the macroscale via a sudden drop in deviatoric stress and a concurrent peak in shear strength. Thus, this meso-structural mechanism of force chain buckling and concurrent lateral confinement of weak networks of (secondary) particles is found to be a predominant mode of failure.

Buckling of force chains is a highly nonaffine mode of deformation. Mounting experimental evidence suggests that this confined buckling event is responsible for the formation of shear bands – the key mechanism for failure in granular materials. Shear bands are recognizably highly complex processes, and slip events in idealized DSE packings (i.e. a cycle of successive frictional phenomena known also as “stick-slip”) are linked to force chain buckling. For the simulations shown in the present study, several experimentally observed nonaffine modes that

emerge within a deforming coarse-grain soil have been captured by the measure of DEM models. Primary particles have undergone high deformation, which sustained very high nonaffine deformation (i.e., elastoplasticity). The modes include: 1) Shear jamming and unjamming by surrounding secondary particles, which in turn, form micro-bands (local crisscrossing planes where the particles re-organize themselves in ‘stick-slip’); and, 2) Shear bands that form within the buckled regions of the strong force chains. Once fully developed, the shear band effectively divides the REV into two regions that can move (or slide) past one another in rigid body motion; at this point, the granular matrix can no longer support load, and thus, has failed.

By making use of insights into the intrinsic characteristics of granular geometries and micromechanical behaviors of grains, the numerical bounds of parameter values for DEM contact rheological components, and the validated (numerical) laboratory test apparatuses, a library of DSE analysis models have been developed. This library constitutes an advance in the application of DEM to soil-structure interaction analysis, and permits the development of models of unprecedented scope. As a result, various in-situ conditions can be discretely simulated (as opposed to approximated using a continuum assumption). Drawing from the DSE model library such that a given spatially varying field of macroscopic properties is exactly satisfied, we can simulate large-scale geostatic stress states that are commensurate with overall pile and SPW dimensions (as part of Task 3). The collective DEM modeling procedures and DSE analysis models themselves have not been previously gathered and synthesized (as of August 2015) to the extent that spatial variability can be simulated at multiple scales, where the scales range from individual DSE, across the mesoscopic scale (clustered DSEs), and across control-volume (soil-unit) scales.

As part of the remaining tasks of the current study, the selected computational approach (the combined discrete element and finite element methods) will be used to initiate explorations of the relationships between many candidate parameters (identified in Task 1) and the performance of displacement-driven piles that are located near SPWs.

4.3 Preliminary Progress for Task 3

Simulation of Geostatic Stresses

Numerical models capable of capturing geostresses that develop throughout megascopic DSE assemblies may require the modeling of thousands or even millions of spheres. Efforts made toward assessing volume-averaged stresses across macroscopic subsets of spheres within megascopic assemblies are reported as part of the preliminary progress made toward completion of Task 3. In addition, the effect of Coulombic friction is explored for otherwise identical simulations of quasi-static stress development in randomly packed (megascopic) DSE assemblies. Additional details of this investigation are reported in Davidson et al. (2015).

Using the microscopic properties listed in Table 4.3.1.1, and for eight values of Coulombic friction (from 0.1 to 0.8), eight corresponding rigid cylindrical containers are populated with approximately 1.26 million spheres (Fig. 4.3.1.1). Note that the algorithm implemented in LS-PREPOST (Han et al. 2012) was utilized in initially populating the cylindrical containers with uniform DSEs. All spheres within the rigid cylindrical containers are then subjected to body forces

(via gravitational acceleration, 9.81 m/s^2) in generating random packings. Across the set of eight simulations, only the Coulombic friction coefficient is varied. Upon reaching mechanically stable states, stresses that develop throughout the uniform DSE assemblies are investigated.

Table 4.3.1.1. Input parameter values for modeling megascopic DSE assemblies

Property	Value	Unit
Radius	2.5E-03	m
Density (by weight)	25.51	kN/m ³
Bulk modulus	3.33E+07	kPa
Spring stiffness (normal contact)	4.17E+04	kN/m
Coulombic friction coefficient	0.1 to 0.8	--

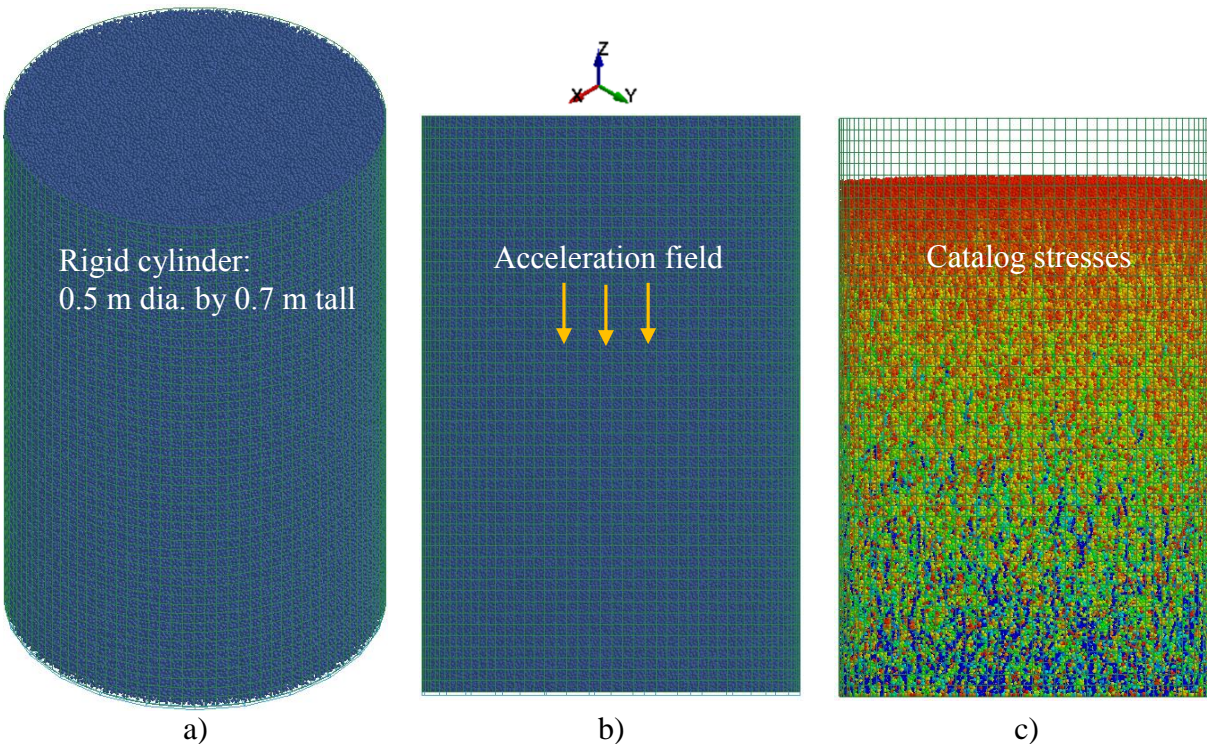


Figure 4.3.1.1. Simulation of geostatic stresses in a megascopic DSE assembly: a) Isometric view of model; b) Application of acceleration field; c) Cataloging of stresses

Volumetric properties of the random packings of the DSE assemblies are listed for each of the eight simulations in Table 4.3.1.2: height (H_s), total volume (V_{total}), volume of solids (V_{solid}), volume of voids (V_{void}), and porosity (η). As expected, the full assembly height (H_s) and porosity (η) increase in proportion to increasing coefficients of Coulombic friction. Three separate but consistent **representative elementary volumes** (REV_1 , REV_2 , REV_3) are defined within the full assemblies, as shown in Fig. 4.3.1.2. Note that the dimensions of REV_1 , REV_2 , and REV_3 match that of the REV associated with the triaxial compression test model (recall Ch. 3). Specifically, for the eight simulations, each cylindrical REV is defined as 0.1 m in diameter and 0.2 m long. As a means of minimizing boundary effects (due to the presence of the rigid cylinder container), the REVs are sampled end-to-end along the vertical central axis of the rigid cylinder container (Fig. 4.3.1.2).

Computed (volume-averaged) values of horizontal (X-direction) and vertical (Z-direction) stresses that develop across the REVs are depicted in Fig. 4.3.1.3 through Fig. 4.3.1.5. As expected, the computed horizontal and vertical stress components indicate that the volume-averaged stresses become more compressive in proportion to increasing depth. Further, as expected, the ratios of horizontal to vertical stress indicate consistent decreases in proportion to increasing levels of microscopic friction.

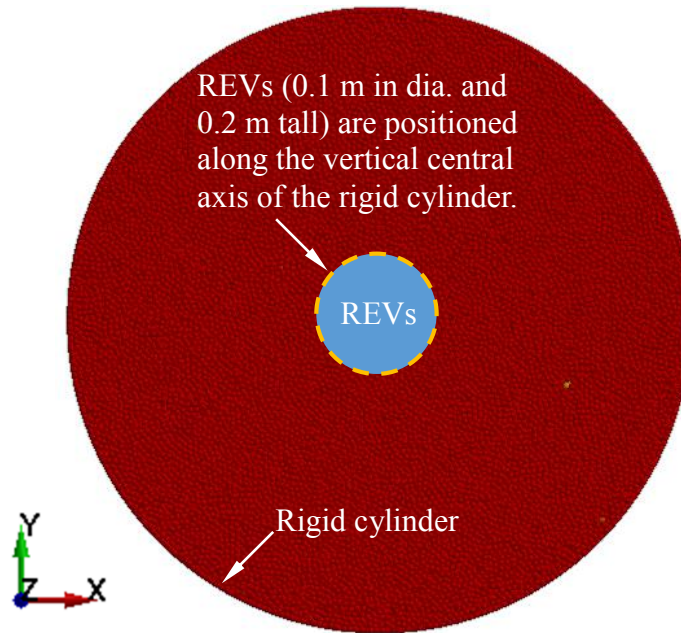


Figure 4.3.1.2. Locations of REVs in the random packings of DSE assemblies (plan view)

Table 4.3.1.2. Volumetric properties of the random packings of DSE assemblies over the range of Coulombic friction coefficients considered

Sliding friction coefficient	H _s (m)	V _{total} (m ³)	V _{solid} (m ³)	V _{void} (m ³)	η
0.1	0.695	1.36E-01	8.24E-02	5.41E-02	0.396
0.2	0.706	1.39E-01	8.24E-02	5.61E-02	0.405
0.3	0.712	1.40E-01	8.24E-02	5.74E-02	0.411
0.4	0.713	1.40E-01	8.24E-02	5.76E-02	0.411
0.5	0.715	1.40E-01	8.24E-02	5.80E-02	0.413
0.6	0.715	1.40E-01	8.24E-02	5.80E-02	0.413
0.7	0.718	1.41E-01	8.24E-02	5.85E-02	0.415
0.8	0.723	1.42E-01	8.24E-02	5.96E-02	0.420

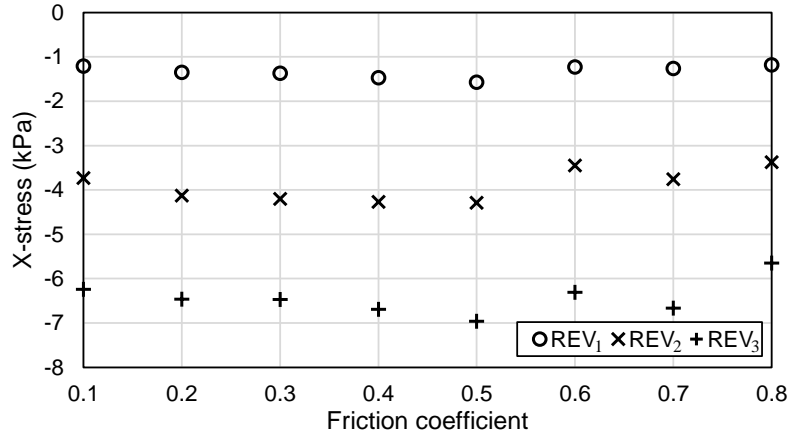


Figure 4.3.1.3. Macroscopic horizontal stresses over the range of Coulombic friction coefficients considered

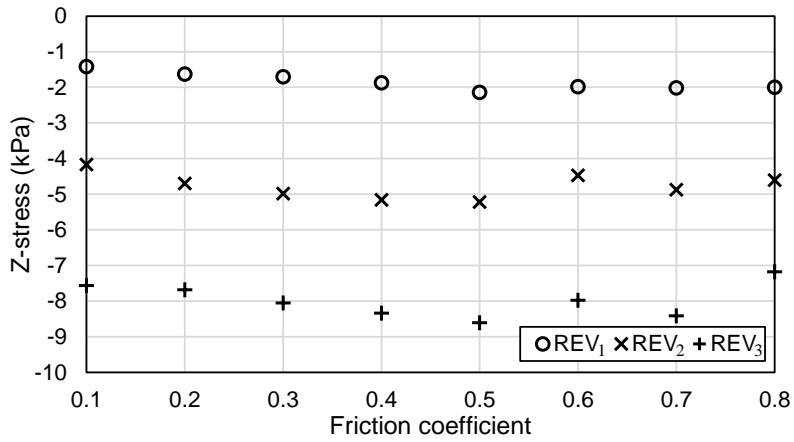


Figure 4.3.1.4. Macroscopic vertical stresses over the range of Coulombic friction coefficients considered

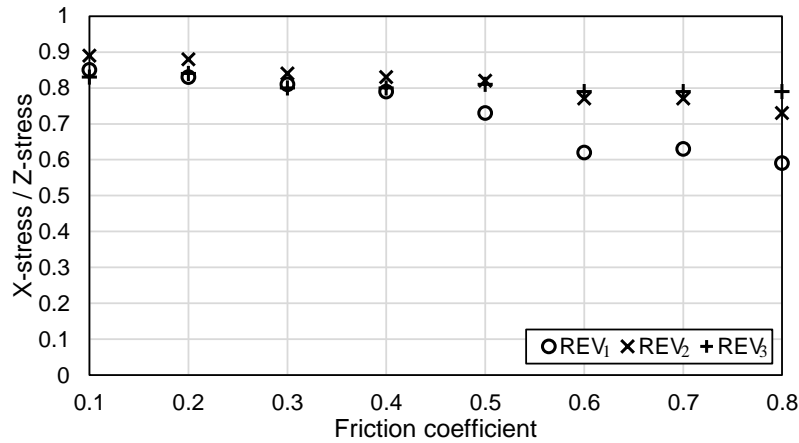


Figure 4.3.1.5. Macroscopic horizontal versus vertical stresses over the range of Coulombic friction coefficients considered

Simulation of Pile Driving into Megascopic DSE Assemblies

Numerical models for simulating the driving of structural objects into granular media are currently being developed. Consider the combined DEM-FEM model shown in Fig. 4.3.1.6, which is discussed purely for demonstration purposes. The model contains a 0.61 m square concrete pile (composed of eight-node elastic solid elements) and a megascopic DSE assembly, which is 2 m wide (square) and 1 m tall. The megascopic DSE assembly is built up using sixteen distinct regions. In turn, each region corresponds to a macroscopic DSE assembly of random packing (under gravitational acceleration). In the context of this demonstration model, all spheres are of 12.7 mm radius, and all perimeter spheres of the DSE assembly are fully restrained from motion. Triaxial compression test simulations of any macroscopic volume within the megascopic assembly would correspond to a calculated peak angle of internal friction of approximately 30° . As a final demonstration-model component, the top surface of the pile object is subjected to a periodic triangular pulse load, intended to approximately represent a 10,320 kg hammer with 3.24 m rated stroke, operating at 44 blows per minute.

Shown in Figs. 4.3.1.7 through 4.3.1.12 are profiles of the vertical compression stresses that arise (over the range of 0 MPa to 1 MPa) throughout one cycle of the periodic pile-top loading. Namely, stress profiles are provided at instants in which: the pile is resting near the top of the DSE assembly under the influence of self weight (Fig. 4.3.1.7); force transfer is initiated between the pile and DSE assembly (Fig. 4.3.1.8); the intensity of the driving force transfer increases (Fig. 4.3.1.9); the force transfer reaches peak intensity (Fig. 4.3.1.10); the intensity of the force transfer decreases as the pile object begins to rebound (Fig. 4.3.1.11); and, at maximum rebound (Fig. 4.3.1.12).

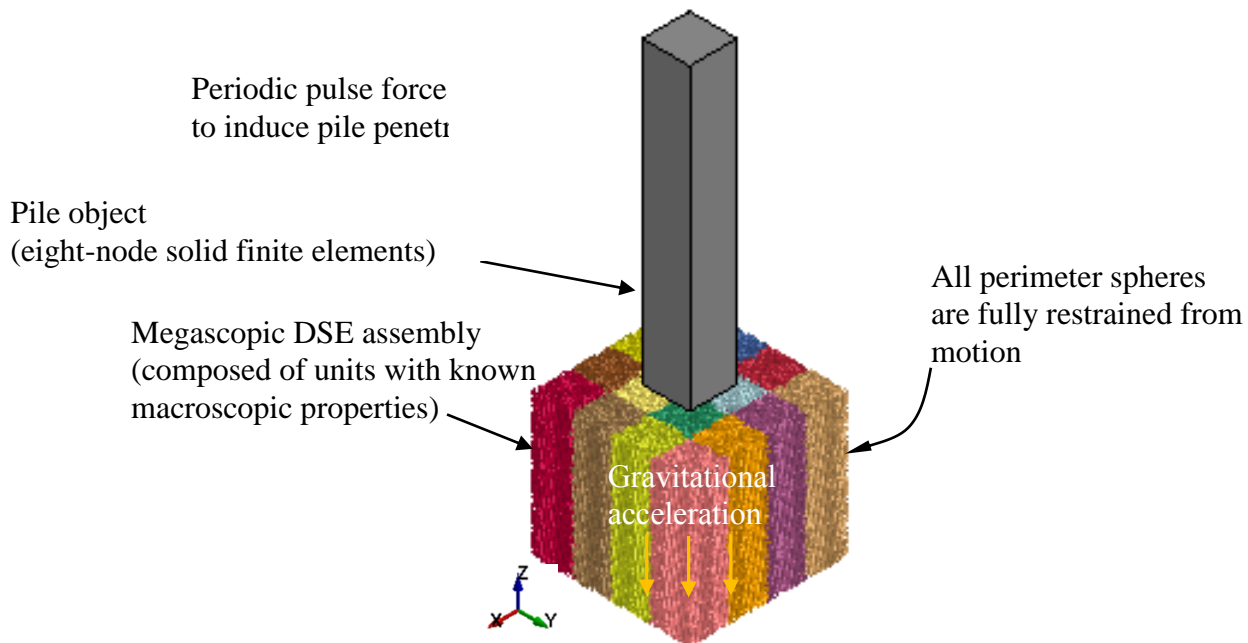


Figure 4.3.1.6. Demonstration of combined DEM-FEM models; preliminary contact-model testing purposes only per simulated driving of pile objects into granular media

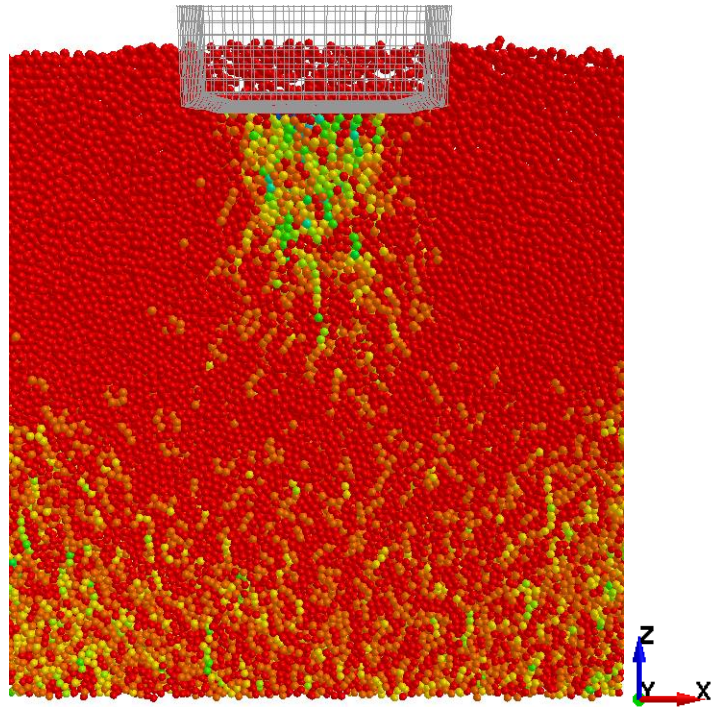


Figure 4.3.1.7. Vertical compressive stresses (0 MPa to 1 MPa) that arise due to gravitational acceleration and driving of the pile object: penetration due to self weight

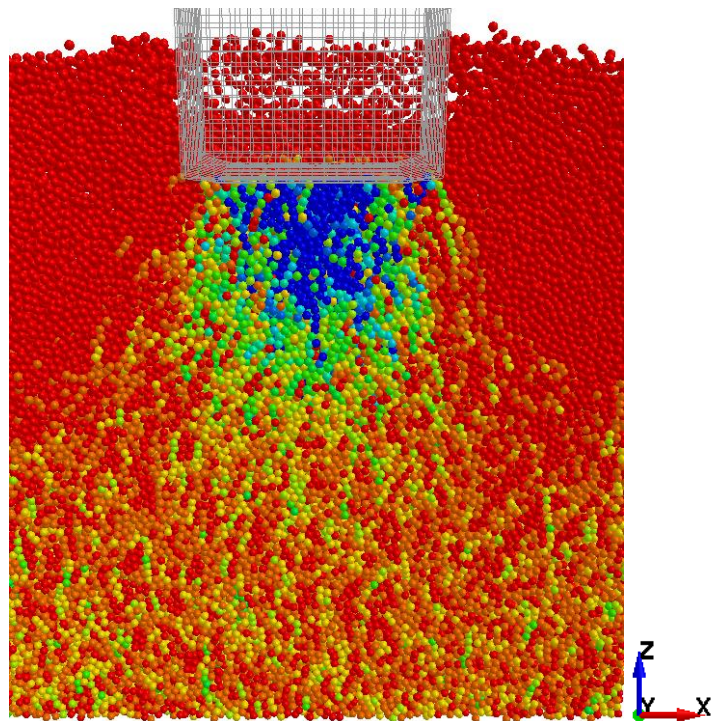


Figure 4.3.1.8. Vertical compressive stresses (0 MPa to 1 MPa) that arise due to gravitational acceleration and driving of the pile object: onset of driving force transfer

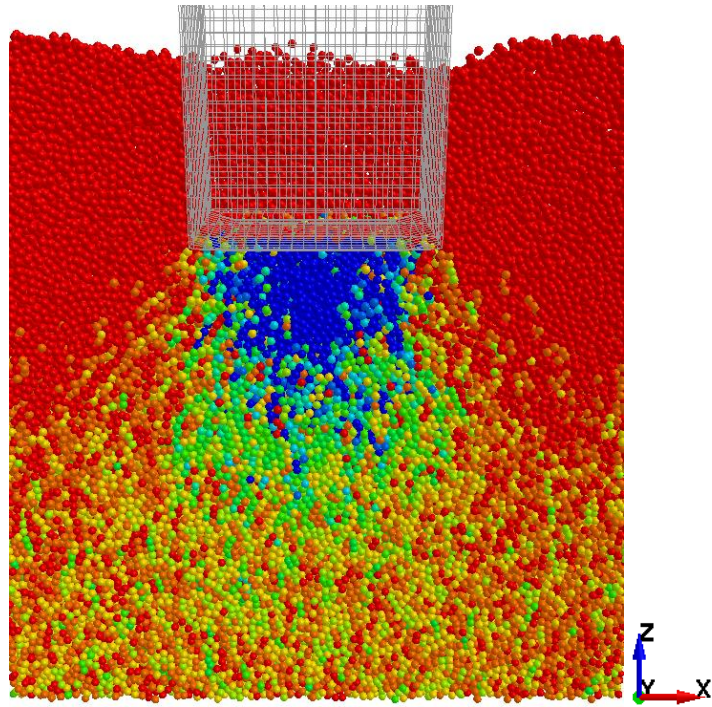


Figure 4.3.1.9. Vertical compressive stresses (0 MPa to 1 MPa) that arise due to gravitational acceleration and placement of the pile object: increased transfer of driving force

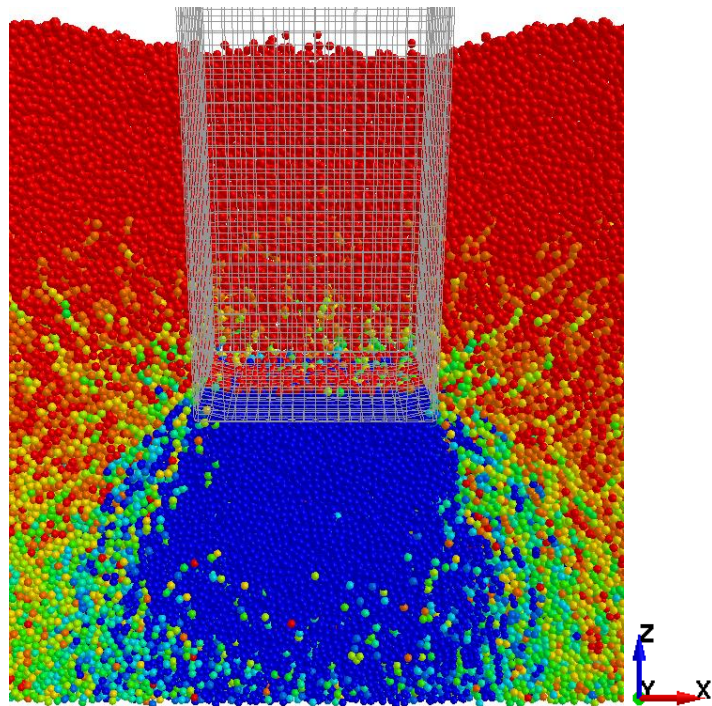


Figure 4.3.1.10. Vertical compressive stresses (0 MPa to 1 MPa) that arise due to gravitational acceleration and driving of the pile object: peak transfer of driving force

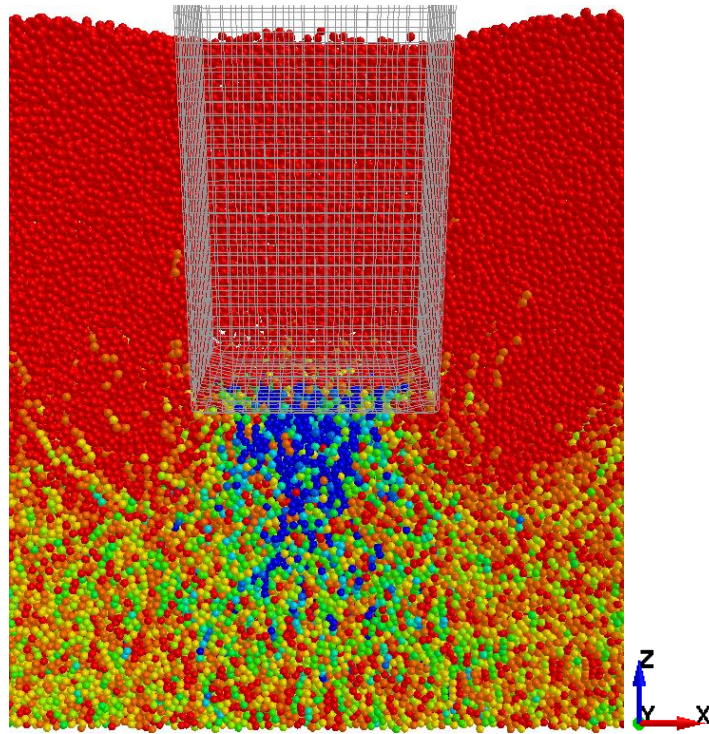


Figure 4.3.1.11. Vertical compressive stresses (0 MPa to 1 MPa) that arise due to gravitational acceleration and placement of the pile object: onset of rebound

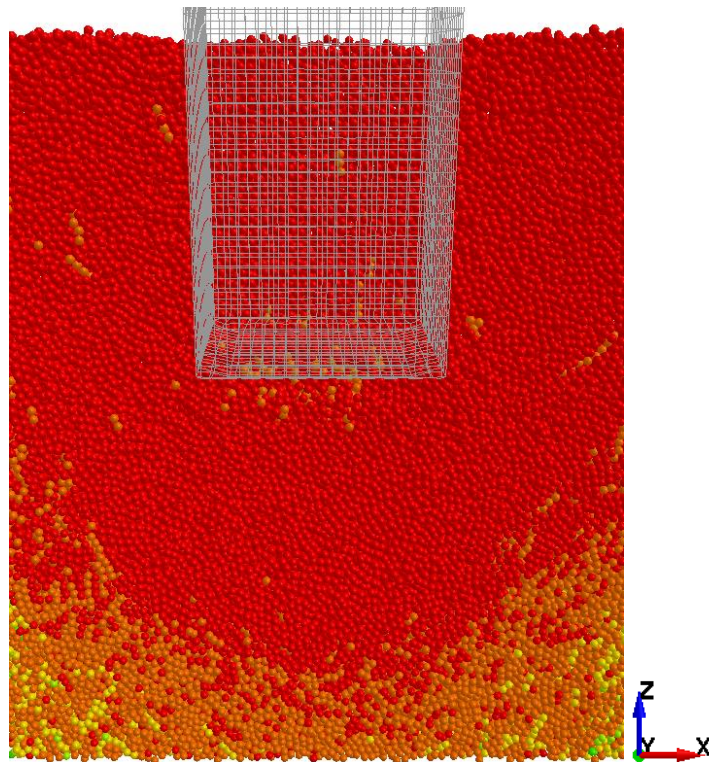


Figure 4.3.1.12. Vertical compressive stresses (0 MPa to 1 MPa) that arise due to gravitational acceleration and driving of the pile object: maximum rebound

CHAPTER 5 REFERENCES

- Abedi, M. (2009). Effect of Restitution Coefficient on Inertial Particle Separator's Efficiency. Mechanical Engineering, Northeastern University, Boston, MA, M.S. Thesis.
- Adams, G.G. and Nosonovsky, M., (2000). "Contact modeling-forces", *Tribology International*, 33, pp. 431-442.
- Alshibli, K. A. and Alsaleh, M. I. (2004). "Characterizing surface roughness and shape of sands using digital microscopy." *Journal of Computing in Civil Engineering*, Vol. 18, No. 1, pp. 36-45.
- Anthony, J. L. and Marone, C. (2005). "Influence of particle characteristics on granular friction." *Journal of Geophysical Research*, Vol. 110, B08409.
- Arasan, S., Akbulut, S., and Hasiloglu, A. S. (2011). "The Relationship between the Fractal Dimension and Shape Properties of Particles." *KSCE Journal of Civil Engineering*, Vol. 15, No. 7, pp. 1219-1225.
- Archard, J.F., (1957). "Elastic Deformation and the Laws of Friction", *Proceedings of the Royal Society of London. Series A, Mathematical and Physical*, 243, 1223, pp. 190-225.
- Arya, L. M. and Paris, J. F. Paris. (1981). "A Physicoempirical Model to Predict the Soil Moisture Characteristic from Particle-Size Distribution and Bulk Density Data." *Journal of Soil Science Society of America*, Vol. 45, pp. 1023-1030.
- ASTM. (2007). "Standard test method for unconsolidated-undrained triaxial compression test on cohesive soils". *ASTM Designation D2850-03a*, ASTM International, West Conshohocken, Pennsylvania, USA.
- ASTM. (2011). "Standard test method for consolidated drained triaxial compression test for soils". *ASTM Designation D7181*, ASTM International, West Conshohocken, Pennsylvania, USA.
- ASTM. (2012). "Standard test method for direct shear test of soils under consolidated drained conditions". *ASTM Designation D3080/D3080M*, ASTM International, West Conshohocken, Pennsylvania, USA.
- Belheine, N., Plassiard, J.-P., Donze F.-V., Darve, F., Seridi A. (2009). "Numerical simulation of drained triaxial test using 3D discrete element modeling". *Computers and Geotechnics*, 36, pp. 320-331.
- Bi, D., Zhang, J., Chakraborty, B, and Behringer, R. P. (2011). "Jamming by Shear." *Nature*, Vol. 480, pp. 355-358. doi:10.1038/nature10667

- Bowden, F. P. and Tabor, D. (1950) *Friction and lubrication of solids*. Oxford University Press.
- Briaud, J. L. and Tucker, L. (1985). "Piles in Sand – A Method Including Residual Stresses." *Journal of Geotechnical Engineering*, ASCE 110, No. 11, pp. 1666-1679.
- Bromwell, L.G. (1966). *The friction of quartz in high vacuum*. Department of Civil Engineering, Massachusetts Institute of Technology, Cambridge, Mass. Research report R66-18.
- Bhushan, B. (2013) *Introduction to Tribology*. 2nd Ed. John Wiley & Sons, New York.
- Carter, J. P. and Kulhawy, F. H. (1992). "Analysis of Laterally Loaded Shafts in Rock." *Journal of Geotechnical Engineering*, ASCE 118, No. 6, 839-855.
- Cates, M. E., Wittmer, J. P., Bouchaud, J.-P., and Claudin P. (1998). "Jamming, Force Chains, and Fragile Matter." *Physical Review Letters*, Vol. 81, No. 9, pp. 1841-1844.
- Chan, C. Y. and Page, W. P. (1997). "Particle fractal and load effects on internal friction in powders." *Powder Technology*, Vol. 90, No. 3, pp.259-266.
- Cheng, Y. P., Nakata, Y., and Bolton, M. D. (2003). "Discrete Element Simulation of Crushable Soil." *Geotechnique*, Vol. 53, No. 7, pp.633-641.
- Cil, M. B., & Alshibli, K. A. (2014). "3D analysis of kinematic behavior of granular materials in triaxial testing using DEM with flexible membrane boundary". *Acta Geotechnica*, 9(2), 287-298.
- Cleary, P., Prakash, M. (2004). "Discrete-element modelling and smoothed particle hydrodynamics: potential in the environmental sciences". *Philosophical Transactions of the Royal Society of London*, 362, 1822, pp. 2003-2030, 2004.
- Crowe, C., Sommerfeld, M. and Tsuji, Y. (1997). *Multiphase flows with droplets and particles*. CRC Press, Boca Raton.
- Cundall, P.A. & Strack, O.D.L. (1979). "A discrete numerical model for granular assemblies", *Geotechnique*, 29, No. 1, pp. 47-65.
- Daphalapurkar, N. P., Wang, F., Fu., B., Lu, H. and Komanduri, R. (2011). "Determination of Mechanical Properties of Sand Grains by Nanoindentation". *Experimental Mechanics*, 51, pp. 719-728.
- Das, M. B. (2007). *Principles of Foundation Engineering*. Seventh edition, Cengage Learning, USA.
- Davidson, M., Chung, J., and Le, V. (2015). "Volume-averaged stress states for idealized granular materials using unbonded discrete spheres in LS-DYNA", *15th LS-DYNA European Conference*, Wurzburg, Germany, June 15-17.

- Dowson, D. (1979). *History of tribology*. Longman, London.
- Duncan, M. J., Wright G. S. (2005). "Soil Strength and Slope Stability". John Wiley & Sons Inc., printed in USA.
- Estrada, N., Azéma, E., Radjai, F., and Taboada, A. (2013). "Comparison of the effects of rolling resistance and angularity in sheared granular media." *Powder and Grains*, Sydney, Australia. pp. 891-894.
- Faraone, M., Chung, J., and Davidson, M. (2015). "Discrete element analysis of idealized granular geometric packing subjected to gravity", *15th LS-DYNA European Conference*, Wurzburg, Germany, June 15-17.
- Finney, J. L. (1970). "Random Packings and the Structure of Simple Liquids I. the Geometry of Random Close Packing." *Proc. R. Soc. London, Ser. A*, Vol.319, pp.479.
- Fischer, P., Romano, V., Weber, H. P., Karapatis, N. P., Boillat, E., Glardon, R. (2003). "Sintering of Commercially Pure Titanium Powder with a Na:YAG Laser Source," *Acta Materialia*, Vol. 51, pp.1651-1662.
- Greenwood, J.A. and Williamson, J.B.P., (1966). "Contact of nominally flat surfaces", *Proc. R. Soc. London A*, 295, pp. 300-319.
- Guyont, E., Oger, L., and Plona, T. J. (1987). "Transport Properties in Sintered Porous Media Composed of Two Particle Sizes." *Journal of Physics. D:Applied Physics*, Vol. 20, pp. 1637-1644.
- Han, Z., Teng, H., and Wang, J. (2012). "Computer Generation of Sphere Packing for Discrete Element Analysis in LS-DYNA", *12th International LS-DYNA Conference*.
- Hanna, T. H. and Tan, R. H. S. (1973). "The Behavior of Long Piles under Compressive Loads." *Canadian Geotechnical Journal*, 10, No. 3, 311-340.
- Hardy, W. and Doubleday, I. (1922). "Boundary Lubrication. The Temperature Coefficient", *Proceedings of the Royal Society of London. Series A, Containing Papers of a Mathematical and Physical Character*, 1922-09-01. 101, 713, pp. 487-492.
- Helland, P. E. and Holmes, M. A. (1997). "Surface Textural Analysis of Quartz Sand Grains from ODP Site 918 Off the Southeast Coast of Greenland Suggests Glaciation of Southern Greenland at 11 Ma." *Palaeogeography, Palaeoclimatology, Palaeoecology*, Vol. 135, pp. 109-121.
- Helland, P. E., Huang, Pei-Hua, and Diffendal, R. F. (1997). "SEM Analysis of Quartz Sand Grain Surface Textures Indicates Alluvial/Colluvial Origin of the Quaternary "Glacial"

- Boulder Clays at Huangshan (Yellow Mountain), East-Central China." *Natural Resources, Quarterly Research*, Vol. 48, pp. 177-186.
- Hertz, H. (1882). "On the contact of elastic solids". *Journal für die Reine und Angewandte Mathematik*, Vol. 92, pp. 156-171.
- Hidalgo, R. C., Grosse, C., Kun, F., Reinhardt, H. W., and Herrmann, H. J. (2002). "Force Chains in Granular Packings." *Physical Review Letters*, 89:205501.
- Holloway, M., Clough, G. W., and Vesic, A. S. (1978). "A Rational Procedure for Evaluating the Behavior of Impact-Driven Piles." *ASTM Symposium on Behavior of Deep Foundations*, ed. R. Lundgren, Special Technical Publication STP 670, 335-357.
- Horn, H.M. (1961). *An investigation of the frictional characteristics of minerals*. Department of Civil Engineering, University of Illinois, Urbana, Illinois. Ph.D. Dissertation.
- Horn, H.M. and Deere, D.U. (1962). "Frictional characteristics of minerals", *Geotechnique*, 12, 4, pp. 319-335.
- Hosseiniia, E. S. and Mirghasemi, A. A. (2006). "Numerical simulation of breakage of two-dimensional polygon-shaped particles using discrete element method." *Powder Technology*, Vol. 166, pp. 100–112.
- Houlsby, G. T. (1991). How the Dilatancy of Soils Affects Their Behavior. The 10th European Conference on Soil Mechanics and Foundation Engineering, Florence, Italy, May 28.
- Israelachvill, J.N. (2011). *Intermolecular and Surface Forces*, Elsevier: Waltham, MA.
- Iwashita, K. and Oda, M. (1998). "Rolling Resistance at Contacts in Simulation of Shear Band Development by DEM." *ASCE Journal of Engineering Mechanics*, Vol. 124, No.3, pp. 285–292.
- Jodrey, W.S. and Tory, E.M. (1981). "Computer Simulation of Isotropic, Homogeneous, Dense Random Packing of Equal Spheres, *Powder Technology*, Vol. 30, pp.111-118.
- John, R. L. A.: Editor (1982). *Sedimentary Structures, Their Character and Physical Basis Volume 1*. Elsevier, New York.
- Johnson K.L. (1985). *Contact mechanics*. Second Edition, Cambridge University Press, New York.
- Jensen, A., Fraser, K., and Laird, G. (2014). "Improving the precision of discrete element simulations through calibration models". *13th International LS-DYNA Users Conference*, Michigan.

- Karajan, N., Han, Z., Teng, H., and Wang, J. (2012). "Particles as discrete elements in LS-DYNA: interaction with themselves as well as deformable or rigid structures" *11th LS-DYNA Forum*, Ulm, October 10.
- Karajan, N., Han, Z., Teng, H., and Wang, J. (2014). "On the parameter estimation for the discrete-element method in LS-DYNA." *13th International LS-DYNA Users Conference*, Michigan.
- Kim, Tae-Hyung. (2001). "Moisture-Induced Tensile Strength and Cohesion in Sand." Doctoral dissertation, University of Colorado.
- Kishida, H. (1967). "Ultimate Bearing Capacity of Piles Driven into Loose Sand." *Soil and Foundations*, 7, No. 3, 20-29.
- Krinsley, D.H. and Doornkamp, J.C. (1973). *Atlas Of Quartz Sand Surface Textures*. Cambridge University Press.
- Kolay, E. and Kayaball, K. (2006). "Investigation of the effect of aggregate shape and surface roughness on the slake durability index using the fractal dimension approach." *Engineering Geology*, Vol. 86, No. 4, pp. 271-284
- Konopinski, D.I., Hudziak, S., Morgan, R.M., Bull, P.A., and Kenyon A.J. (2012). "Investigation of Quartz Grain Surface Textures by Atomic Force Microscopy for Forensic Analysis". *Forensic Science International*, Vol. 223, pp. 245-255.
- Krumbein, W. C. (1941). "Measurement and Geological Significance of Shape and Roundness of Sedimentary Particles." *Journal of Sedimentary Petrology*, 11, pp. 64-72.
- Krumbein, W. C. and Silos, L. L. (1963). *Stratigraphy and Sedimentation*. 2nd Ed., W. H. Freeman, San Francisco.
- Kummerfeld, J. K., Hudson, T. S., and Harrowell, P. (2008). "The Densest Packing of AB Binary Hard-Sphere Homogenous Compounds across all Size Ratios", the *Journal of Physical Chemistry C*, 115, 19037-19040.
- Lambe, T. W. and Whitman, R. V. (1969) *Soil Mechanics*, John Wiley & Sons, New York.
- Lieu, K.P. (2013). *Sediment Diagenesis and Characteristics of Grains and Pore Geometry in Sandstone Reservoir Rocks from a Well of the North German Basin*. Crystallography Section, Ludwig Maximilians University of Munich, Munich, Germany Ph.D. Dissertation.
- LSTC. (2014a). *LS-DYNA Theory Manual*. Livermore Software Technology Corporation, Livermore CA.

- LSTC. (2014b). *LS-DYNA Keyword User's Manual, Volume I*. Livermore Software Technology Corporation, Livermore CA.
- Lee, M. D. (1992). *The Angles of Friction of Granular Fills*. Department of Civil Engineering, University of Cambridge, UK. Ph.D. Dissertation.
- Liu, A. and Nagel, S. (1998). "Jamming is not just cool any more." *Nature*, 396, pp. 21-22.
- Luding, S. (2008). "Introduction to discrete element methods: basic of contact force models and how to perform the micro-macro transition to continuum theory". *European Journal of Environmental and Civil Engineering*, 12 (7-8). pp. 785-826.
- Mair, K., Frye, K. M., and Marone, C. (2002). "Influence of grain characteristics on the friction of granular shear zones." *Journal of Geophysical Research*, 107 (B10-2219), 4-1 to 4-9.
- Majmudar, T. S., Sperl, M., Luding, S., and Behringer, R. P. (2007). "Jamming Transition in Granular Systems." *Physical Review Letters*, Vol. 98: 058001.
- Malone, F.K., Xu, B.H. (2008). "Determination of contact parameters for discrete element method simulations of granular systems". *Particuology* 6, 521-528.
- Meyerhof, G. G. (1959). "Compaction of Sands and Bearing Capacity of Piles." *Journal of the Soil Mechanics and Foundation Division*, ASCE 85; SM 6; 1-29.
- Meyerhof, G. G. (1963). "Some Recent Research on the Bearing Capacity of Foundations." *Canadian Geotechnical Journal*, 1, No. 1, 16.
- Meyerhof, G. G. (1976). "Bearing capacity and settlement of pile foundations." *Journal of Geotechnical Engineering*, ASCE, 102(3), 195-228.
- Mindlin, R.D. (1949). "Compliance of elastic bodies in contact". *ASME Journal of Applied Mechanics* 16, pp 259-268.
- Mitchell, J. K., and Soga K. (2005). *Fundamentals of Soil Behavior, 3rd Ed.*, John Wiley & Sons.
- Moscinski, J., Bargie, M., Rycerz, Z. A., Jacobs, P. W. M. (1989). "The Force-biased Algorithm for the Irregular Close Packing of Equal Hard Spheres.", *Molecular Simulation*, Vol. 3, pp. 201-212.
- Murzenko, Y. N. (1965). "Experimental results on the distribution of normal contact pressure on the base of a rigid foundation resting on sand", *Soil Mechanics and Foundation Engineering*, Volume 2, Issue 2, pp 69-73.

- Nadukuru, S.S. (2013). *Static Fatigue: A Key Cause of Time Effects in Sand*. Department of Civil Engineering, University of Michigan, Michigan. Ph.D. Dissertation.
- Navarro, A. H., de Souza Braun, P. M. (2013). “Determination of the normal spring stiffness coefficient in the linear spring-dashpot contact model of discrete element method”. *Powder Technology* 246, 707-722.
- Nielsen, B. D. (2004). *Nondestructive Soil Testing Using X-Ray Computed Tomography*. Department of Civil Engineering, Montana State University, Montana. M.S. Thesis.
- Obermayr, M., Vrettos, C., Kleinaert, J., Eberhard, P. (2013). “A Discrete Element Method for assessing reaction forces in excavation tools.” *Congreso de Métodos Numéricos en Ingeniería*, 25-28 June, Bilbao, Spain.
- Ollagnier A., Doremus P., and Didier Imbault. (2007). “Contact particles calibration in a discrete element code”. <http://people.3sr-grenoble.fr/users/fdonze/articles/GED_2007/Article-C.pdf>.
- O’Sullivan, C., Bray, J. D., & Riemer, M. (2004a). “Examination of the response of regularly packed specimens of spherical particles using physical tests and discrete element simulations”. *Journal of engineering mechanics*, 130(10), 1140-1150.
- O’Sullivan, C., Cui, L., & Bray, J. D. (2004b). “Three-dimensional discrete element simulations of direct shear tests”. *Numerical Modeling in Micromechanics via Particle Methods*, 373-382.
- O’Toole, P. I. and Hudson, T. S. (2011). “New High-Density Packings of Similiarly Sized Binaries”, the *Journal of Physical Chemistry C*, 115, 19037-19040.
- Parks, G.A. (1984). “Surface and Interfacial Free Energies of Quartz”. *Journal of Geophysical Research*, Vol. 89, No. B6, pp. 3997-4008.
- Plassiard, J. P., Belheine, N., and Donz, F. V. (2009). “A spherical discrete element model: calibration procedure and incremental response.” *Granular Matter*, Vol. 11, pp. 293–306.
- Popov, V.L. (2010). *Contact Mechanics and Friction*, Springer, Berlin.
- Popov, V. L. and Gray, J. A. T. (2012). “Prandtl-Tomlinson model: History and applications in friction, plasticity, and nanotechnologies.” *Journal of Applied Mathematics and Mechanics*, Vol. 92, No. 9, pp. 683-708.
- Powers, M. C. (1953). “A New Roundness Scale for the Sedimentary Particles.” *Journal of Sedimentary Petrology*, 23, pp. 117-119.

- Rabinovich, Y. I., Esayanur, M. S., and Moudgil, B. M. (2005). "Capillary forces between two spheres with a fixed volume liquid bridge: theory and experiment". *Langmuir*, 21(24):10992-7.
- Rabinowicz, E. (1995). "The intrinsic variables affecting the stick-slip process." *Proc. R. Soc. London*. Vol. 71, pp. 668-675.
- Radchik, V.S., Ben-Nissan, B., and Muller, W.H. (2002). "Theoretical Modeling of Surface Asperity Depression Into an Elastic Foundation Under Static Loading", *Journal of Tribology*, 124, pp. 852-877.
- Randolph, M. F., Carter, J. P., and Wroth, C. P. (1979). "Driven Piles in Clay – the Effects of Installation and Subsequent Consolidation." *Géotechnique*, 29, 361-393.
- Randolph, M. F., Dolwin, J., and Beck, R. (1994). "Design of Driven Piles in Sand." *Géotechnique*, 44, 427-448.
- Rogers, C. A. (1958). "The Packing of Equal Spheres." Proceedings of the Royal Society of London. Mathematical Society, Vol. 3, No. 8, pp. 609-620.
- Rotter, J. M., Holst, F. G., Ooi, J. Y., and Sanad A. M. (1998). "Silo pressure predictions using discrete-element and finite-element analyses." Philosophical Transactions of the Royal Society of London. A, Vol. 356, pp. 2685-2712.
- Rowe, P. W. (1962). "The stress-dilatancy relation for static equilibrium of an assembly of particles in contact". *Proceedings of the Royal Society of London A: Mathematical, Physical and Engineering Sciences*, Vol. 269, No. 1339, pp. 500-527.
- Russell, R. D. and Taylor, R. E. (1937). "Roundness and shape of Mississippi River sands." *Journal of Geology*, Vol. 45, No. 3, pp.225-267.
- Salot, C. Gotteland, P., and Villard, P. (2009). "Influence of relative density on granular materials behavior: DEM simulations of triaxial tests." *Granular Matter*, Vol. 11, pp. 221–236.
- Santamarina, J. C. and Cho, G. C. (2004). "Soil behaviour: The role of the particle shape." *Proceedings Skempton Conference*, March, London.
- Santamarina, J.C., Klein, K.A., and Fam, M.A. (2001). *Soils and Waves – Particulate Materials Behaviors, Characterization and Process Monitoring*. Wiley, New York, NY.
- Shi, Y. and Zhang, Y. (2006). "Simulation of Random Packing of Spherical Particles with Different Size Distributions." *Proceedings of 2006 ASME International Mechanical Engineering Congress & Exposition*, November 5-10, Chicago, IL.

- Scott, G. D. and Kilgour, D.M. (1969). "The Density of Random Close Packing of Spheres." *Journal of Physics D*, Vol.2, pp.863.
- Sjaastad, G.D. (1963). *The Effect of Vacuum on the Shearing Resistance of Ideal Granular Systems*, Princeton University, Princeton, New Jersey, Ph. D. Thesis.
- Skempton, A. W. (1959). "Cast in situ bored piles in London Clay." *Géotechnique*, 9:153–173.
- Sommerfeld, M. and Huber, N. (1999). "Experimental Analysis and Modelling of Particle-Wall Collisions." *International Journal of Multiphase Flow*, Vol. 25, pp.1457-1489.
- Stronge, W.J. (2000). *Impact mechanics*. First Edition, Cambridge University Press, printed in USA.
- Sukumaran, B. and Ashmawy, A. K. (2001). "Quantitative Characterization of the Geometry of Discrete Particles." *Geotechnique*, Vol. 51, No. 7, pp. 171-179.
- Terzaghi, K. (1925). *Erdbaumechanik*, Franz Deuticke, Vienna.
- Thomas, P. A. (1997). *Discontinuous deformation analysis of particulate media*. PhD dissertation, Dept. of Civil Engineering, Univ. of California at Berkeley, Berkeley, Calif.
- Thornton, C. (1979). "The conditions for failure of a face-centered cubic array of uniform rigid spheres". *Géotechnique*, 29(4), 441-459.
- Thornton, C. (2000). "Numerical simulations of deviatoric shear deformation in granular media." *Geotechnique*, 50(4), 43-53.
- Tory, E. M., Church, B. H., Tam, M. K., Ratner, M. (1973). "Simulated Random Packing of Equal Spheres." *The Canadian Journal of Chemical Engineering*, Vol. 51, pp. 484-493.
- Vallejo, L. E. (1995). "Fractal analysis of granular materials." *Geotechnique*, Vol. 45, pp. 159-163.
- Vesic, A. S. (1972). "Expansion of Cavities in Infinite Soil Mass." *Journal of the Soil Mechanics and Foundation Division*, ASCE 98, 265-290.
- Wadell, H. (1932). "Volume, Shape, and Roundness of Rock Particles." *Journal of Geology*, 40, pp. 443-451.
- Walton, K. (1987). "The Effective Elastic Moduli of a Random Packing of Spheres." *Journal of Mechanics and Physics of Solids*, Vol. 35, No. 2, pp. 213-226.
- Walton, O.R. (1993). "Numerical simulation of inelastic frictional particle-particle interactions". *Particulate Two-Phase flow*, edited by M.C. Roco.

- Walton, O.R. (1994). "Force Models for Particle-Dynamics Simulations of Granular Materials." *North American Treaty Organization: Advanced Study Institute for Mobile Particulate Systems*, July 13-15, Cargese, Corsica.
- Yang, Z. X., Yang, J., and Wang, L. Z. (2012). "On the influence of inter-particle friction and dilatancy in granular materials: a numerical analysis." *Granular Matter*, Vol. 14, pp. 433-447.
- Yimsiri, S., and Soga, K. (2001). "Effects of soil fabric on undrained behavior of sands." *Proc., 4th Int. Conf. on Recent Advances in Geotechnical Earthquake Engineering and Soil Dynamics*, Editor: S. Prakash, San Diego, CA.
- Yu, H. S. and Holsby, G. T. (1991). "Finite Cavity Expansion in Dilatant Soil: Loading Analysis." *Géotechnique*, 41, 173-183.
- Zheng, Q.J., Zhu, H.P., and Yu, A.B. (2011). "Finite element analysis of the rolling friction of a viscous particle on a rigid plane." *Powder Technology*, Vol. 207, pp. 401-407.
- Zhu, H.P., Zhou, Z.Y., Yang, R.Y. and Yu, A.B. (2008). "Discrete particle simulation of particulate systems: A review major application and findings". *Chemical Engineering Science*, Vol. 63, No. 23, pp. 5728-5770.